DISSERTATION

COMPUTATIONAL MODELING OF BIOREMEDIATION OF ACID MINE DRAINAGE IN BIOCHEMICAL PERMEABLE REACTIVE BARRIERS

Submitted by

Paulo Scarano Hemsi

Department of Civil Engineering

In partial fulfillment of the requirements

For the Degree of Doctor of Philosophy

Colorado State University

Fort Collins, CO

Fall 2005

COLORADO STATE UNIVERSITY

September 27, 2005

WE HEREBY RECOMMEND THAT THE DISSERTATION PREPARED UNDER OUR SUPERVISION BY PAULO SCARANO HEMSI ENTITLED "COMPUTATIONAL MODELING OF BIOREMEDIATION OF ACID MINE DRAINAGE IN BIOCHEMICAL PERMEABLE REACTIVE BARRIERS" BE ACCEPTED AS FULLFILLING IN PART THE REQUIREMENTS FOR THE DEGREE OF DOCTOR OF PHILOSOPHY.

COMMITTEE ON GRADUATE WORK

Dr. Kenneth H. Carlson

Dr. James W. Warner

Dr. Thomas R. Wildeman, Colorado School of Mines

Co-Advisor: Dr. Linda A. Figueroa, Colorado School of Mines

Advisor: Dr. Charles D. Shackelford

Department Head: Dr. Sandra L. Woods

ABSTRACT OF DISSERTATION

COMPUTATIONAL MODELING OF BIOREMEDIATION OF ACID MINE DRAINAGE IN BIOCHEMICAL PERMEABLE REACTIVE BARRIERS

Biochemical, sulfate (SO_4^{2-}) reducing permeable reactive barriers (PRBs) containing decomposable solid organic materials can be used for *in-situ* bioremediation of ground water impacted by acid mine drainage (AMD). A new biochemical model for bioremediation of AMD based on SO_4^{2-} reduction and precipitation of metals coupled to, and limited by, the decomposition of solid organic materials (e.g., leaf mulch compost, wood chips, sawdust, alfalfa) was formulated and integrated either as a stand-alone algorithm or coupled to flow and multi-species contaminant transport (i.e., MODFLOW with RT3D). The model combines the primary processes of (i) decomposition of polysaccharides in solid organic materials, (ii) SO_4^{2-} reduction based on lactate, (iii) precipitation of insoluble metal sulfides, (iv) partial volatilization of hydrogen sulfide (H_2S) to the gas phase, and (v) reversible dissolution-precipitation of calcite ($CaCO_{3(s)}$) and metal carbonates (e.g., siderite, $FeCO_{3(s)}$). The model was evaluated and calibrated using experimental data from the literature pertaining to four batch-equilibrium (no-flow) tests, two closed-system column tests, three open-system bioreactor tests, and a full-scale PRB. The comparisons with experimental data are performed in terms of both effluent and resident concentrations and cumulative mass, and provide insight into the effects of different model kinetics, slow solid decomposition, multiple-phase precipitation, and

temperature and seasonality, as well as the appropriate ranges of values for a variety of model parameters.

Additionally, as common to all PRBs, heterogeneity in aquifer hydraulic conductivity (K) also influences the performance of biochemical PRBs, with preferential flow and contaminant transport exposing the PRB to spatially variable groundwater seepage velocities at the location of the PRB, with localized values that may be sufficiently high such that the required PRB thickness is greater than that evaluated for homogenous aquifer. Also, heterogeneity induces divergent flow patterns such that the PRB length required to capture or encompass the contaminant plume at the location of the PRB is greater than that for homogenous aquifer. New probabilistic factors of safety related to scaling the PRB thickness and length amidst heterogeneity were quantified using flow and particle tracking (i.e., MODFLOW with MODPATH) in conjunction with 650 synthetic stochastic heterogeneous aquifers (Turning Bands method) for different levels of aquifer heterogeneity, correlation structure anisotropy ratios, and distances from source zone to PRB. The significant magnitudes of such scaling factors emphasize the importance of site characterization as a prerequisite to PRB design.

Paulo Scarano Hemsi
Department of Civil Engineering
Colorado State University
Fort Collins, CO 80523
Fall 2005

ACKNOWLEDGEMENTS

I would like to express my sincere gratitude to my advisor, Dr. Charles D. Shackelford, for continuous support, encouragement, availability, and insightful exchange of ideas in so many occasions. I would never have accomplished this objective without his guidance and support. I would like to express my sincere gratitude to my co-advisor, Dr. Linda A. Figueroa (Colorado School of Mines), for important orientation, advice, and exchange of ideas. I also would like to thank Drs. Kenneth H. Carlson, James W. Warner, and Thomas R. Wildeman (Colorado School of Mines) for agreeing to participate in my Graduate Committee.

I would like to extend thanks to many people in the Department of Civil Engineering, including Drs. Wayne A. Charlie and Marvin Criswell for helping me during my initial semesters as a Graduate Teaching Assistant, as well as Ms. Laurie Howard, Ms. Linda Hinshaw, and Ms. Bernie Sheppard. I also thank Mr. Joe Wilmetti for all his help with computers and equipment.

In addition, I would like to extend my appreciation to many fellow graduate students and friends in particular, for past couple of years, Elizabeth and David Castelbaum, Margarete and Marcelo Galdos, Aida Jimenez-Esquilin, Ernesto Trujillo, Jorge Gironás, John Edgerly, Roberto Arranz, Fernando Ramirez, Aaron Ogorzalek, Jin-Chul Joo, Dr. Jae-Myung Lee, Dr. Jong Beon Kang, Gabriel Iltis, Kristin Sample, Giovanni Leoncini, and Christophe Attard.

This research was funded by the United States Environmental Protection Agency's (US EPA's) Science to Achieve Results (STAR) Program under Grant No. R-82951501-0, as part of the US EPA's Rocky Mountain Regional Hazardous Substance Research Center (HSRC). Dr. Mitch Lasat is the US EPA program manager for the HSRC.

Finally, I would like to thank my family in Brazil for missing me for so long, my parents, and my brother Cyro S. Hemsi. This effort is dedicated to my parents and to my aunt and godmother.

Paulo Scarano Hemsi
Department of Civil Engineering
Colorado State University

TABLE OF CONTENTS

LIST OF TABLES

LIST OF FIGURES

Chapter 6

Chapter 7

CHAPTER 1

INTRODUCTION

1.1 BACKGROUND

1.1.1 Definition of Acid Mine Drainage

Acid mine drainage (AMD) is an inorganic waste solution affecting groundwater quality in coal and metalliferous mine sites and generated when sulfidic ores, waste rock dumps, and tailings are oxidized by air or infiltrating water. Acid mine drainage is characterized by high concentrations of sulfate (SO_4^{2-}) and metals (e.g., aluminum, Al^{3+}, cadmium, Cd^{2+}, cobalt, Co^{2+}, copper, Cu^{2+}, ferrous iron, Fe^{2+}, lead, Pb^{2+}, manganese, Mn^{2+}, mercury, Hg^{2+}, nickel, Ni^{2+}, and zinc, Zn^{2+}, among others), and low pH (e.g., Alexander 1999, Roane et al. 1996, Ludwig et al. 2002, Benner et al. 2002). These toxic heavy metals in AMD generally are in a state of high mobility (e.g., Sposito 1989, Drever 1997). Additionally, as AMD percolates through the disposed materials and adjacent soils, further mineral dissolution tends to occur due to the low solution pH, increasing the concentrations of toxic heavy metals and contributing non toxic alkali and alkaline-earth metals (e.g., sodium, Na^{+}, calcium, Ca^{2+}, magnesium, Mg^{2+} and potassium, K^{+}) to AMD.

1.1.2 Genesis of Acid Mine Drainage

Sulfidic minerals occur as metal ores that can be present in most types of geological formations (Langmuir 1997). The most abundant metal sulfide in nature is

pyrite (FeS_2), and additional examples include chalcopyrite ($CuFeS_2$), chalcocite (Cu_2S), galena (PbS), and sphalerite (ZnS), among others (e.g., Pough 1996). Pyrite forms in reducing environments where ferric iron (Fe^{3+}), for example from goethite (α-FeOOH), can be reduced to ferrous iron (Fe^{2+}), subsequently combining with hydrogen sulfide (i.e., HS^- or H_2S) to spontaneously form an amorphous mono-sulfide intermediate, FeS, as follows:

$$2FeOOH + 3H_2S \rightarrow 2FeS + S^0 + 4H_2O \qquad (1.1)$$

where the reduction of Fe^{3+} to Fe^{2+} is paired to the half-reaction of oxidation of one mole of S^{2-} to S^0. Once amorphous FeS is formed, sequential Fe-S replacements progressively generate FeS_2, based on different mechanisms and intermediate species as described elsewhere (e.g., Furukawa and Barnes 1995, Langmuir 1997). Sulfidic minerals, such as FeS_2, remain stable in anoxic environments with oxidation-reduction potentials, E_h, less than zero for pH ranging from 2 to 12 (Langmuir 1997), but undergo oxidation when exposed to an aerobic environment.

Mining of FeS_2 and other sulfidic minerals for the extraction of sulfur (S) and various metals of interest exposes large amounts of these minerals to oxygen ($O_{2(g)}$) and water, as superficial layers are stripped to reach near-surface ores (surface mining) or as shafts and tunnels are excavated to reach deep ores (underground mining), resulting in *in-situ* oxidation of sulfidic minerals. Additionally, refuse materials such as waste rock and tailings (i.e., finely-ground waste rock) frequently stored in disposal units such as waste rock dumps and tailings impoundments located near the mineral processing plant remain

exposed to the environment for long periods of time, resulting in the *ex-situ* oxidation of sulfidic minerals, and significantly contributing to AMD.

The oxidation of ores containing sulfide (e.g., FeS_2) can be abiotic or biotic. Purely chemical oxidation of FeS_2 occurs spontaneously, but progresses at very slow rates. The presence and activity of chemoautotrophic bacteria *Thiobacillus ferroxidans* may increase the rate of the purely chemical oxidation of FeS_2 by a factor ranging from 10^5 to 10^6 (e.g., Singer and Stumm 1970, Brierley and Brierley 1997, Langmuir 1997, Alexander 1999). The oxidation of FeS_2 begins with an abiotic step releasing SO_4^{2-} and Fe^{2+} (Singer and Stumm 1970):

$$FeS_{2(s)} + 3.5O_{2(g)} + H_2O \rightarrow Fe^{2+} + 2SO_4^{2-} + 2H^+ \qquad (1.2)$$

Subsequently, *T. ferroxidans* convert the generated Fe^{2+} into Fe^{3+} as follows:

$$4Fe^{2+} + O_{2(g)} + 4H^+ \rightarrow 4Fe^{3+} + 2H_2O \qquad (1.3)$$

where produced Fe^{3+} acts as oxidant for further FeS_2 oxidation (Singer and Stumm 1970, Drever 1997), as follows:

$$FeS_{2(s)} + 14Fe^{3+} + 8H_2O \rightarrow 15Fe^{2+} + 2SO_4^{2-} + 16H^+ \qquad (1.4)$$

which constitutes a cyclic process, since Fe^{2+} is re-generated in Eq. 1.4, re-entering Eq. 1.3 to produce more Fe^{3+}, which, in turn, further oxidizes FeS_2 (Eq. 1.4), and so on. Due to this cyclic behavior, Fe^{3+} is commonly considered the major oxidant of metal sulfides (Singer and Stumm 1970, Drever 1997).

A fraction of the Fe^{3+} released in solution (Eq. 1.3) may precipitate in the form of $Fe(OH)_{3(s)}$ as the migrating AMD discharges into a stream or when the solution reaches a more aerobic zone in the subsurface (Drever 1997). The precipitation of $Fe(OH)_{3(s)}$ is responsible for the typical reddish pigmentation occurring on the bottom and along the sides of streams affected by AMD discharges. Additionally, the coating with $Fe(OH)_{3(s)}$ in such streams generally results in death of vegetation (Harris and Ragusa 2000).

1.1.3 Prevention and Active Neutralization

Prevention is a fundamental way of dealing with AMD, and simply consists of limiting or restricting the exposure of sulfidic wastes (such as waste rock and tailings) to oxygen and water using soil covers or employing a sub-aquatic disposition of waste rock dumps. However, the applicability of soil covers may be limited by high installation costs in large areas, as well durability concerns, such as those related to cracking of the cover and chemical compatibility. Also, the applicability of sub-aquatic disposition of waste rock dumps may be considered limited by the possibility of harmful ecological impacts (Thomas 2001). In theory, the use of bactericides to restrain the growth of *T. ferroxidans* also can be used as a preventive approach to AMD (Singer and Stumm 1970).

Active neutralization of AMD is an intuitive approach in which AMD is chemically treated (i.e., active approach) by admixing the AMD solution with a

compound releasing alkalinity, such as limestone ($CaCO_{3(s)}$) or anhydrous or hydrated lime (CaO or $Ca(OH)_2$), to neutralize the acidity of AMD and promote the precipitation of metals. Besides raising the solution pH and precipitating metals, the addition of limestone or lime promotes the removal of sulfate (SO_4^{2-}) by precipitating gypsum ($CaSO_4.2H_2O$). However, this active approach is limited by the high cost of chemical reactants, by the need for continuous re-applications of the chemicals, and by the large volumes of sludge produced by the reactions and requiring disposal (Webb et al. 1998, Thomas 2001).

1.1.4 Passive Treatment in Wetlands

Remediation of AMD in natural and constructed wetlands is a significant passive-treatment technology. For example, more than 300 constructed wetlands were built in the U.S.A. from 1984 to 1990 (Webb et al. 1998). The simplest mechanisms leading to AMD treatment in wetlands are dilution, plant uptake, and sorption. The majority of existing wetlands are predominantly aerobic systems in which heavy metals from the influent AMD are removed by oxidation, hydrolysis, and precipitation promoted within the wetland.

In addition to aerobic wetlands, anaerobic wetlands are designed to emphasize microbial sulfate reduction, based on different types of sulfate reducing bacteria (SRB) that are capable of oxidizing organic molecules of general form CH_2O (carbon and energy sources) using SO_4^{2-} as the electron acceptor and releasing hydrogen sulfide (H_2S), and alkalinity (HCO_3^-) as follows:

$$2CH_2O + SO_4^{2-} \rightarrow H_2S + 2HCO_3^- \quad (1.5)$$

Readily usable organic molecules for Eq. 1.5 include methanol (CH_3OH), ethanol (CH_3CH_2OH), acetate (CH_3COO^-), lactate ($CH_3CH(OH)COO^-$), pyruvate (CH_3COCOO^-), and propionate ($CH_3CH_2COO^-$), among others (e.g., Postgate 1984, Nagpal et al. 2000). Also, dissolved hydrogen (H_2) in equilibrium with the gas phase, $H_{2(g)}$, can be effectively employed by several groups of SRB (Postgate 1984). For example, the reduction of sulfate based on the oxidation of ethanol, lactate, and acetate can be written as follows (Postgate 1984, Nagpal et al. 2000):

$$\underbrace{2CH_3CH_2OH}_{\text{ethanol}} + SO_4^{2-} \rightarrow H_2S + 2H_2O + \underbrace{2CH_3COO^-}_{\text{acetate}} \quad (-66 \text{ kJ/mol}) \quad (1.6)$$

$$\underbrace{2CH_3CH(OH)COO^-}_{\text{lactate}} + SO_4^{2-} \rightarrow H_2S + 2HCO_3^- + \underbrace{2CH_3COO^-}_{\text{acetate}} \quad (-79 \text{ kJ/mol}) \quad (1.7)$$

$$\underbrace{2CH_3COO^-}_{\text{acetate}} + SO_4^{2-} \rightarrow H_2S + 2HCO_3^- \quad (-47 \text{ kJ/mol}) \quad (1.8)$$

where the energy produced (kJ) is expressed in terms of one mole of organic substrate oxidized.

The dissolved utilizable organic substrates for SRB (e.g., ethanol, lactate, or acetate) are released in the wetland upon decomposition and fermentation of emplaced solid organic materials. These materials generally consist of low-cost natural products and wastes such as spent mushroom compost, horse and cow manure, peat, wood chips, and sawdust, among others (Gazea et al. 1996). Several studies involving field

applications of sulfate reducing systems for remediation of AMD in wetlands and large-scale bioreactors have been reported. These studies include the sulfate reducing wetlands constructed near the Big Five Tunnel in Idaho Springs, Colorado (Mechemer and Wildeman 1992) and the Wheal Jane mine in Cornwall, UK (Webb et al. 1998, Whitehead and Prior 2005), and the passive SRB bioreactors filled with organic matter and limestone for AMD remediation constructed at an abandoned mine site (Calliope mine) near Butte, Montana (MSE, 2002). A review of AMD treatment in distinct types of wetlands is provided by Gazea et al. (1996).

1.1.5 Passive Treatment in Permeable Reactive Barriers

As shown in Fig. 1.1, permeable reactive barriers (PRBs) are subsurface emplacements of reactive materials designed to intercept a contaminant plume, provide a flow path through the reactive media, and transform the contaminants into environmentally acceptable forms to achieve remediation goals down gradient of the barrier (US EPA 1998). Remediation goals typically include contaminant effluent concentrations in compliance with prescribed maximum contaminant levels (i.e., MCLs).

Properly designed and constructed PRBs have minimal impact on the natural groundwater gradient (i.e., unimpeded flow), as well as low operational and maintenance costs for extended periods of time (i.e., except for the costs associated with monitoring). Zero-valent iron (Fe^0) has been used as the reactive material for the majority of constructed PRBs to promote the reductive dehalogenation of volatile organic compounds (VOCs), reduce mobile and toxic oxyanions of chromium (CrO_4^{2-}), arsenic ($H_2AsO_4^-$), and selenium ($HSeO_4^-$) into immobile precipitates, and treat radionuclide and nitrate bearing ground waters (e.g., US EPA 1998, O'Hannesin and Gilham 1998, US EPA

2002).

Biochemical systems based on the activity of microbial consortia and the decomposition of emplaced solid (particulate) organic materials have been used as PRBs oriented towards the remediation of nitrate and AMD. For example, a denitrifying PRB (University of Waterloo) oriented towards the remediation of nitrate was installed in the field to intercept drainage from a farm (e.g., Robertson et al. 2000). Sulfate reducing PRBs oriented towards the remediation of SO_4^{2-}, heavy metals, and acidity in AMD effluents have been installed in some AMD sites (e.g., Thombre et al. 1997, US EPA 1998, Benner et al. 1997, 1999, 2002, McGregor et al. 1999, Blowes et al. 2000, Ludwig et al. 2002, US EPA 2002, Groudev et al. 2003). For example, a sulfate reducing PRB containing 50 % gravel, 20 % municipal compost, 20 % leaf mulch, 9 % wood chips, and 1 % limestone (all by volume) was constructed in 1995 at the Nickel Rim mine in Ontario, Canada (Benner et al. 1997, 1999, 2002). Also, a sulfate reducing PRB containing 15 % leaf mulch, 84 % pea gravel, and 1 % limestone (all by volume) was employed for remediation of AMD containing SO_4^{2-}, Cu^{2+}, Co^{2+}, Ni^{2+}, and Zn^{2+} emanating from an industrial site used to store ore concentrates in British Columbia (Ludwig et al. 2002). Additionally, a sulfate reducing PRB containing leaf detritus, spent mushroom compost, cow manure, and sawdust was constructed in 1997 in central Bulgaria to intercept the discharge from a former copper mine and remove high concentrations of Fe^{2+}, Cu^{2+}, Cd^{2+} and arsenic from AMD (Groudev et al. 2003).

The interest on sulfate reducing field-scale systems based on solid substrates (such as anaerobic wetlands and PRBs) for AMD remediation is based on the facts that such systems result generally more cost effective than active remediation systems, and

that the technical efficacy of treating AMD *via* sulfate (SO_4^{2-}) reduction mediated by SRB, precipitation of metal sulfides, and amelioration of pH has been widely demonstrated in the laboratory (e.g., Tuttle at al. 1969, Wakao et al. 1979, Dvorak et al. 1992, Hammack and Edenborn 1992, Bechard et al. 1994, Waybrant et al. 1998, Groudev et al. 1999, Prasad et al. 1999, Chang et al. 2000, Waybrant et al. 2002, Gibert et al. 2003, Hulshof et al. 2003, Gibert et al. 2004, Luptakova and Kusnierova 2005).

1.1.6 Effects of Aquifer Heterogeneity on Permeable Reactive Barriers

In the field, heterogeneity in aquifer hydraulic conductivity (K) will inherently affect the performance of PRBs. Several modeling studies have focused on aspects of the effects of aquifer heterogeneity on flow and contaminant transport (e.g., Poeter and Gaylord 1990, Moreno and Tsang 1994, Eykholt 1997, Zheng and Jiao 1998, Gavaskar et al. 1998, Eykholt et al. 1999, Bilbrey and Shafer 2001, Elder et al. 2002, Zheng and Bennett 2002).

Heterogeneity induces preferential pathways of flow and contaminant transport (channeling) that expose the PRB to spatially variable groundwater seepage velocities with localized values that may be sufficiently high such that the required PRB thickness is greater than that for a homogenous aquifer. Additionally, aquifer heterogeneity may induce divergent flow patterns that require the length of the PRB to be greater than that for a homogenous aquifer in order to capture or encompass the plume as the plume arrives at the location of the PRB. Finally, the potential significance of aquifer heterogeneity on PRB design and performance emphasize the importance of site

characterization (e.g., Pfleiderer and Moltyaner 1993, Gavaskar et al. 1998, Zheng and Bennett 2002).

1.1.7 Modeling Sulfate Reducing Remediation of AMD in Heterogeneous Aquifers

1.1.7.1 Existing Models for the Biochemical Processes

Differences exist among previous models for sulfate reduction or used for simulating AMD remediation in sulfate reducing systems. Westrich and Berner (1984) and Bourdeau and Westrich (1984) considered the aerobic degradation of seawater plankton as precursor to sulfate (SO_4^{2-}) reduction in marine environments. In their model, the rate of SO_4^{2-} reduction was assumed equal to conversion factors multiplied by the rate of plankton decomposition (which was modeled using first-order kinetics with respect to carbon), multiplied by a hyperbolic term to account for SO_4^{2-} limitation. Drury (2000) considered anaerobic solid-substrate sulfate reducing bioreactors in which the rate of SO_4^{2-} reduction was assumed equal to conversion factors multiplied by the rate of decomposition of the biodegradable solid waste materials, multiplied by the concentration of SO_4^{2-} to account for SO_4^{2-} limitation. In this model, the degradation of solid materials was modeled using first-order kinetics with a declining rate coefficient, based on an empirical declining rate function accounting for the aging of the solid materials (Janssen 1984, Middelburg 1989).

The aforementioned models (i.e., Westrich and Berner 1984, Bourdeau and Westrich 1984, Drury 2000) do not model the bacterial populations (i.e., decomposers and SRB), or the effects of bacterial growth and decay. Also, these models do not include dissolved organic substrates existing as decomposition products and utilizable by SRB (e.g., Gujer and Zehnder 1983, Chynoweth and Pullammanappallil 1996).

Schafer et al. (1998a,b) developed a bioremediation model that includes aerobic reactions, fermentation, nitrate-, manganese-, iron-, and SO_4^{2-} reduction, and Prommer et al. (2001) describe the conceptual framework of a reactive transport model that includes geochemical equilibrium and kinetically controlled bioremediation using sulfate reduction. In both of these cases, Monod kinetics (Monod 1949) was used for modeling the growth of SRB on a dissolved substrate. However, in both cases, bioremediation in the models is assumed to be sustained by the direct injection of a dissolved organic substrate (e.g., lactate-propionate, ethanol, or sucrose), and not by solid decomposable organic material.

Mayer et al. (2002) describe the conceptual framework for a reactive transport model including AMD genesis, transport (impacted by equilibrium with a number of alumino-silicates, carbonates, and gypsum), and bioremediation partly based on kinetically controlled SO_4^{2-} reduction. However, the model described by Mayer et al. (2002) does include bacterial populations (e.g., decomposers and SRB) or the effects of bacterial growth and decay, and also does not include solid decomposable organic materials. Additionally, the actual kinetic expressions for modeling SO_4^{2-} reduction and the assumptions with respect to dissolved organic substrates required for SO_4^{2-} reduction are not given.

Benner et al. (2002) and Amos et al. (2004) describe a model based on SO_4^{2-} reduction for AMD remediation in which the rate of SO_4^{2-} reduction is assumed equal to a constant value multiplied by a hyperbolic term accounting for SO_4^{2-} limitation. The constant rate of SO_4^{2-} reduction in this model is determined by fitting SO_4^{2-} experimental data, for example from a previous column test. Bacterial populations and the effects of

bacterial growth and decay, as well as the existence of solid or dissolved organic substrates that may limit the extent of SO_4^{2-} reduction, are not considered by the model. As a result, the model potentially oversimplifies sulfate reducing systems in which the rate of SO_4^{2-} reduction is critically limited by the presence of dissolved organic substrates generated as a result of decomposition and fermentation of solids and critically linked to bacterial growth and decay (e.g., Boudreau and Westrich 1984, Westrich and Berner 1984, Dvorak et al. 1992, Bechard et al. 1994, Drury 2000, Chang et al. 2000, Logan et al. 2003).

When dealing with no-flow systems, the differential equations in the new biochemical model will be solved with a stand-alone algorithm (Compaq Visual Fortran 6.0) formulated for this research on the basis of a Runge-Kutta-Fehlberg numerical method (Chapra and Canale 2002). When dealing with flowing systems, the model will be coupled in time to flow (i.e., U.S. Geological Survey MODFLOW 2000, version 1.7, Harbaugh et al. 2000) and multi-species contaminant transport (i.e., U.S. Department of Energy RT3D, version 2.5, Clement 1997, 2003).

1.1.7.2 Modeling the Influence of Aquifer Heterogeneity on PRBs

In terms of previous studies focusing on PRB design and performance amidst aquifer heterogeneity, Eykholt (1997) performed a Monte Carlo analysis of a closed-form analytical solution to determine the minimum PRB thickness based on steady-state one-dimensional advective (plug flow) transport with first-order decay kinetics (e.g., VOC in contact with Fe^0) on the basis of a large number of combinations of values for the input variables related to aquifer and PRB. The final values for a factor of safety for scaling the

PRB thickness ranged from about 2 to 6, with the higher values being associated with higher standard deviations of input groundwater seepage velocity, as expected.

Also, Eykholt et al. (1999) evaluated the impacts of aquifer heterogeneity on effluent VOC concentrations leaving a Fe^0 PRB using both modeling of flow and particle tracking and a Monte Carlo analysis and different levels of aquifer heterogeneity, as represented by standard deviations of the logarithm of K, σ_{lnK}, ranging from 0.5 to 2.0. Different compensatory factors for reducing the vulnerability of PRBs induced by aquifer heterogeneity are provided, although the study by Eykholt et al. (1999) was based on a small number of aquifer realizations for each simulation case (i.e., < 5).

Elder (2000) and Elder et al. (2002) performed numerical modeling of flow and contaminant transport in three-dimensional synthetic heterogeneous aquifers generated using a Turning Bands algorithm (Tompson et al. 1989) in conjunction with first-order contaminant degradation kinetics within the PRB (i.e., VOC in contact with Fe^0), and considering different simulation scenarios in terms of aquifer and PRB heterogeneity. Elder (2000) and Elder et al. (2002) concluded that the standard deviation of lnK, i.e., σ_{lnK}, is the aquifer parameter with the greatest impact on the distributions of PRB influent and effluent concentrations, and more significantly affecting the PRB performance. However, the number of aquifer realizations per simulation scenario used by Elder (2000) and Elder et al. (2002) also appears to be relatively small (i.e., ~ 10).

Bilbrey and Shafer (2001) performed numerical modeling of flow and particle tracking in 15 moderately heterogeneous aquifers (i.e., aquifers with σ_{lnK} = 1.0) containing a funnel-and-gate PRB system to evaluate the variability in the downstream capture width of the funnel-and-gate amidst aquifer heterogeneity. Simulated pathlines

connecting the downstream capture zone to the funnel-and-gate resulted mandering and varied not only in size but also shifted positions within the aquifer, such that Bilbrey and Shafer (2001) proposed factors of safety for increasing the length of the funnel-and-gate amidst heterogeneity.

In addition, Benner et al. (2001) performed numerical modeling of flow and particle tracking to study the spatial variability of contaminant residence time within a PRB considering layered aquifer systems (i.e., discretely heterogeneous aquifers) formed by approximately four adjacent homogeneous layers. The results showed the expected behavior of critical contaminant residence times occurring in conjunction with scenarios where aquifer layers with high K are intercepted by the PRB. Also in this case, the total number of simulations was limited, i.e., equal to 18.

For the purpose of quantifying the effects of aquifer heterogeneity on PRB design and performance, the U.S. Geological Survey models MODFLOW 2000 and MODPATH, version 4.2 (Pollock 1994) can be employed for modeling flow and particle tracking, respectively, in conjunction with synthetic stochastic heterogeneous aquifers generated using either the Turning Bands method (Tompson et al. 1989) recently employed by Elder (2000) and Elder et al. (2002), or the sequential Gaussian simulation (sgsim) program (Deutsch and Journel 1998) recently employed by Bilbrey and Shafer (2001). Since Elder (2000) recommended the use of the Turning Bands method, and this was a reference followed more closely in this research, the Turning Bands method was selected for generating all stochastic aquifers in this research. Also, MATLAB® version 6.5 (The MathWorks, Inc., Natick, MA) will be chosen to develop algorithms for handling output data from MODFLOW and MODPATH, and perform calculations on the

basis of that data.

1.2 GOAL AND OBJECTIVES OF RESEARCH

Based on aforementioned discussion, the following observations can be made regarding the limitations existing with respect to modeling permeable reactive barriers (PRB) for treatment of acid mine drainage (AMD). With respect to the existing models for biochemical reactivity in sulfate reducing systems:

- None of the existing models concomitantly models decomposable solid (particulate) organic materials, dissolved bacterial substrates, and growth and decay of bacterial populations (decomposer bacteria and SRB), and
- None of the existing models has been as extensively evaluated and calibrated against experimental data as proposed for this research.

With respect to the existing studies dealing with the influence of aquifer heterogeneity on PRB design and performance:

- None of the existing studies includes the study of plume patterns in heterogeneous aquifers. Also, none of the existing studies quantifies the PRB length required to capture the entire contaminant plume in heterogeneous aquifers,
- None of the existing studies defines the probabilistic factors of safety for scaling the required thickness and length of a PRB in heterogeneous aquifers defined in this research,
- None of the existing studies uses more than 18 aquifer realizations per simulation case, whereas this research is based on 45 to 200 aquifer realizations per simulation case, desirable for obtaining probabilistic

distributions of results, such as probabilistic factors of safety, and

- The studies reported by Eykholt (1997), Eykholt et al. (1999), Elder (2000), and Elder et al. (2002) are based on first-order contaminant degradation kinetics within the PRB, which are not likely to be applicable in the case of biological PRBs, whereas the results in this research are intended to be independent of the type of degradation kinetics.

As a result of these observations, the two primary goals of this research are:

(1) To develop a new biochemical model representing the primary biochemical processes accounting for the bioremediation of AMD in sulfate reducing systems. The model will concomitantly include decomposition of solid (particulate) organic materials, dissolved organic substrates, and bacterial populations with bacterial growth and decay, and will be numerically solved both as a stand-alone algorithm and coupled to flow and multi-species reactive contaminant transport. In addition, the model will be evaluated and calibrated by comparing modeled results (simulated results) to measured experimental data from several bench-scale experiments and a field-scale PRB; and

(2) To quantify the influence of aquifer heterogeneity on PRB performance and design, including plume patterns and new probabilistic factors of safety for scaling the required thickness and length of PRBs in heterogeneous aquifers. This quantification will be based on numerical modeling of flow and particle tracking in conjunction with a total of 650 synthetic stochastic heterogeneous aquifers.

These goals will be achieved by accomplishing the following objectives:

Objective 1: To formulate the concepts, assumptions, and mathematics for a new biochemical model representing the primary biochemical processes accounting for the bioremediation of AMD in sulfate reducing systems coupled to, and limited by, decomposition of solid organic materials (Chapter 2);

Objective 2: To evaluate and calibrate the new model using the experimental results pertaining to four batch-equilibrium (no-flow) tests previously reported in the literature (Chapter 3);

Objective 3: To evaluate and calibrate the new model using the experimental results pertaining to two closed-system column tests previously reported in the literature (Chapter 4);

Objective 4: To evaluate and calibrate the new model using the experimental results pertaining to three open-system bioreactor tests previously reported in the literature (Chapter 5);

Objective 5: To study plume patterns and quantify new probabilistic factors of safety for scaling required length and thickness of PRBs in heterogeneous aquifers considering different levels of aquifer heterogeneity, different correlation structure anisotropy ratios, and different distances from the contamination source zone to the PRB (Chapter 6); and

Objective 6: To evaluate extending the modeling capability to the field-scale (full-scale PRB reported in the literature), including adjustment of model parameter values to account for the effects of temperature, seasonality, and particle size of organic materials (Chapter 7).

1.3 POTENTIAL IMPACT OF RESEARCH

The results of this research may have significant ramifications with respect to the potential applicability of the new biochemical model for simulating and predicting the behavior of biological systems for the passive treatment of AMD, as well as the results of this research may have significant ramifications with respect to quantifying useful probabilistic factors of safety for scaling thickness and length of PRBs amidst aquifer heterogeneity.

1.4 REFERENCES

Alexander, M. (1999). Biodegradation and Bioremediation. 2nd Edition, Academic Press, San Diego, CA.

Amos, R.T., Mayer, K.U., Blowes, D.W., and Ptacek, C.J. (2004). Reactive transport modeling of column experiments for remediation of acid mine drainage. *Environmental Science and Technology*, 38(11): 3131-3138.

Bechard, G., Yamazaki, H., Gould, W.D., and Bedard, P. (1994). Use of cellulosic substrates for the microbial treatment of acid mine drainage. *Journal of Environmental Quality*, 23(1): 111-116.

Benner, S.G, Blowes, D.W., Ptacek, C.J., and Mayer, K.U. (2002). Rates of sulfate reduction and metal sulfide precipitation in a permeable reactive barrier. *Applied Geochemistry*, 17(1): 301-320.

Benner, S.G., Blowes, D.W., and Molson, J.W. (2001). Modeling preferential flow in reactive barriers: implications for performance and design. *Ground Water*, 39(3): 371-379.

Benner, S.G., Blowes, D.W., and Ptacek, C.J. (1997). A full-scale porous reactive wall

for prevention of acid mine drainage. *Ground Water Monitoring and Remediation*, 17(4): 99-107.

Benner, S.G., Blowes, D.W., Gould, W.D., Herbert, R.B. and C. J. Ptacek (1999). Geochemistry of a permeable reactive barrier for metals and acid mine drainage. *Environmental Science and Technology*, 33(16): 2793-2799.

Bilbrey, L.C., and Shafer, J.M. (2001). Funnel-and-gate performance in a moderately heterogeneous flow domain. *Ground Water Monitoring and Remediation*, 21(3): 144-151.

Blowes, D.W., Ptacek, C.J., Benner, S.G., McRae, C.W.T., Bennett, T.A. and R. W. Puls (2000). Treatment of inorganic contaminants using permeable reactive barriers, *Journal of Contaminant Hydrology*, 45: 123-137.

Boudreau, B.P., and Westrich, J.T. (1984). The dependence of bacterial sulfate reduction on sulfate concentration in marine environments. *Geochimica et Cosmochimica Acta*, 48(12): 2503-2516.

Brierley, C.L. and Brierley, J.A. (1997). Microbiology for the metal mining industry. In *Manual of Environmental Microbiology, American Society for Microbiology*, Editors: Hurst, C.J., Kinudsen, G.R., McInerney, M.J., Stetzenbach, L.D., and Walter, M.V., 830-841.

Chang, I.S., Shin, P.K., and Kim, B.H. (2000). Biological treatment of acid mine drainage under sulphate-reducing conditions with solid waste materials as substrates. *Water Research*, 34(4): 1269-1277.

Chapra, S.C., and Canale, R.P. (2002). Numerical Methods for Engineers, 4th Edition, McGraw-Hill, New York, NY.

Chynoweth, D.P., and Pullammanappallil, P. (1996). Anaerobic digestion of municipal solid waste. Microbiology of Solid Waste, A. Palmasano and M.A. Barlaz, eds.,CRC Press, Boca Raton, FL, 77-113.

Clement, T.P. (1997). A Modular Computer Code for Simulating Reactive Multi-species Transport in 3-Dimensional Groundwater Systems RT3D version 1.0. U.S. Department of Energy and Pacific Northwest National Laboratory. PNNL-11720-1997.

Clement, T.P. (2003). RT3D v.2.5 Update Document, What is New in RT3D version 2.5. Electronic document: http://bioprocess.pnl.gov/rt3d.htm.

Deutsch, C.V., and Journel, A.G. (1998). GSLIB: Geostatistical Software Library and User's Guide, Oxford University Press, New York, NY.

Drever, J.I. (1997). The Geochemistry of Natural Waters – Surface and Groundwater Environments. 3rd Edition, Prentice-Hall, Upper Saddle River, NJ.

Drury, J.W. (2000). Modeling of sulfate reduction in anaerobic solid substrate bioreactors for mine drainage treatment. *Mine Water and the Environment*, 19(1):18-28.

Dvorak, D.H., Hedin, R.S., Edenborn, H.M., and McIntire, P.E. (1992). Treatment of metal-contaminated water using bacterial sulfate reduction: results from pilot-scale reactors. *Biotechnology and Bioengineering*, 40(5):609-616.

Elder, C.R. (2000). Evaluation and Design of Permeable Reactive Barriers Amidst Heterogeneity. Ph.D. Dissertation presented at the University of Wisconsin at Madison.

Elder, C.R., Benson, C.H., and Eykholt, G.R. (2002). Effects of heterogeneity on influent and effluent concentrations from horizontal permeable reactive barriers. *Water Resources Research*, 38(8): 27-1:27-19.

Eykholt, G.R. (1997). Uncertainty-based scaling of iron reactive barriers. *In Situ Remediation of the Geoenvironment*, J. Evans, ed., American Society of Civil Engineers, New York, NY, 41-45.

Eykholt, G.R., Elder, C.R., and Benson, C.H. (1999). Effects of aquifer heterogeneity and reaction mechanism uncertainty on a reactive barrier. *Journal of Hazardous Materials,* 68(1-2): 73-96.

Furukawa, Y., and Barnes, H.L. (1995). Reactions forming pyrite from precipitated amorphous ferrous sulfide. In *Geochemical Transformations of Sedimentary Sulfur, American Chemical Society Symposium Series no. 612* – Editors: Vairavamurthy, M.A., and Shoonen, M.A. Chapter 10, 194-205.

Gavaskar, A.R., Gupta, N., Sass, B.M., Janosy, R.J., and O'Sullivan. D. (1998). Permeable Barriers for Groundwater Remediation: Design, Construction, and Monitoring, Battelle Press, Columbus, OH.

Gazea, B., Adam, K., and Kontopoulos, A. (1996). A review of passive systems for the treatment of acid mine drainage. *Minerals Engineering*, 9(1): 23-42.

Gibert, O., de Pablo, J., Cortina, J.L., and Ayora, C. (2003). Evaluation of municipal compost/limestone/iron mixtures as filling material for permeable reactive barriers for in-situ acid mine drainage treatment. *Journal of Chemical Technology and Biotechnology*, 78(5): 489-496.

Gibert, O., de Pablo, J., Cortina, J.L., and Ayora, C. (2004). Chemical characterization of

natural organic substrates for biological mitigation of acid mine drainage. *Water Research*, 38(19): 4186-4196.

Groudev, S., Nicolova, M., Spasova, I., and Schutte, R. (2003). Treatment of waters from a copper mine by means of a permeable reactive barrier. Fifty Years of the University of Mining and Geology "St. Ivan Rilski", University of Mining and Geology, Sofia (Bulgaria), Volume 46, Part II, Section Mining and Mineral Processing, 229-231.

Groudev, S.N., Bratcova, S., and Komnitsas, K. (1999). Treatment of waters polluted with radioactive elements and heavy metals by means of a laboratory passive system. *Minerals Engineering*, 12(3): 261-270.

Gujer, W., and Zehnder, A.J. (1983). Conversion processes in anaerobic digestion. *Water Science and Technology*, 15(8-9): 127-167.

Hammack, R.W., and Edenborn, H.M. (1992). The removal of nickel from mine waters using bacterial sulfate reduction. *Applied Microbiology and Biotechnology*, 37(5): 674-678.

Harbaugh, A.W., Banta, E.R., Hill, M.C., and McDonald, M.G. (2000). MODFLOW-2000, the U.S. Geological Survey Modular Ground-Water Model – User Guide to Modularization Concepts and the Ground-Water Flow Process, USGS Open-File Report 00-92, Reston, VA.

Harris, M.A., and Ragusa, S. (2000). Bacterial mitigation of pollutants in acid drainage using decomposable plant material and sludge. *Environmental Geology*, 40(1-2):195-214.

Hulshof, A.H., Blowes, D.W., Ptacek, C.J., and Gould, W.D. (2003). Microbial and nutrient investigations into the use of in situ layers for treatment of tailings effluent.

Environmental Science and Technology, 37(21): 5027-5033.

Janssen, B.H. (1984). A simple method for calculating decomposition and accumulation of young soil organic matter. *Plant and Soil*, 76(1-3):297-304.

Langmuir, D. (1997). Aqueous Environmental Geochemistry. Prentice-Hall, Upper Saddle River, NJ.

Logan, M., Ahamann, D., and Figueroa, L. (2003). Assessment of microbial activity in anaerobic columns treating synthetic mine drainage. Proceedings of the 2003 Annual Meeting of the American Society for Mining and Reclamation, 3-6 June, Billings, MT, American Society for Mining and Reclamation, Lexington, KY, 658-678.

Ludwig, R.D., McGregor, R.G., Blowes, D.W., Benner, S.G. and K. Mountjoy (2002). A permeable reactive barrier for treatment of heavy metals, *Ground Water*, 40(1): 59-66.

Luptakova, A., and Kusnierova, M. (2005). Bioremediation of acid mine drainage contaminated by SRB. *Hydrometallurgy*, 77(1-2): 97-102.

Mayer, K.U., Frind, E.O, and Blowes, D.W. (2002). Multicomponent reactive transport modeling in variably saturated porous media using a generalized formulation for kinetically controlled reactions. *Water Resources Research*, 38(9):13-1 to 13-21.

McGregor, R., Blowes, D., Ludwig, R., Pringle, E., and Pomery, M. (1999). Remediation of a heavy metal plume using a reactive wall. Bioremediation of Metals and Inorganic Compounds, A. Leeson and B. Alleman, B, eds., 5th International In Situ and On-Site Bioremediation Symposium, San Diego, CA, Battelle Press, Columbus, OH, 19-24.

Mechemer, S.D., and Wildeman, T.R. (1992). Adsorption compared with sulfide precipitation as metal removal processes from acid mine drainage in a constructed

wetland. *Journal of Contaminant Hydrology*, 9(2): 115-131.

Middelburg, J.J. (1989). A simple rate model for organic matter decomposition in marine sediments. *Geochimica et Cosmochimica Acta*, 53(7):1577-1581.

Monod, J. (1949). The growth of bacterial cultures. *Annual Review of Microbiology*, 3:371-394.

Moreno, L., and Tsang, C.F. (1994). Flow channeling in strongly heterogeneous porous media: a numerical study. *Water Resources Research*, 30(3): 1421-1430.

MSE Technology Applications (2002). Final Report-Sulfate Reducing Bacteria Reactive Wall Demonstration. Mine Waste Technology Program, Activity III, Project 12, U.S. Environmental Protection Agency and U.S. Department of Energy, MWTP-206.

Nagpal, S., Chuichulcherm, S., Livingston, A., and Peeva, L. (2000). Ethanol utilization by sulfate-reducing bacteria: an experimental and modeling study. *Biotechnology and Bioengineering*, 70(5):533-543.

O'Hannesin, S.F., and Gillham, R.W. (1998). Long-term performance of an in situ "iron wall" for remediation of VOCs. *Ground Water*, 36(1): 164-170.

Pfleiderer, S., and Moltyaner, G.L. (1993). The use of velocity and conductivity data for the quantification of heterogeneity: a comparison. *Water Resources Research*, 29(12): 4151-4156.

Poeter, E., and Gaylord, D.R.(1990). Influence of aquifer heterogeneity on contaminant transport at the Hanford site. *Ground Water*, 28(6): 900-909.

Pollock, D.W. (1994). User's Guide for MODPATH/MODPATH-PLOT, Version 3: A Particle Tracking Post-Processing Package for MODFLOW, the U.S. Geological Survey Finite-Difference Ground-Water Flow Model, U.S. Geological Survey, Open-

File Report 94-464, Reston, VA.

Postgate, J.R. (1984). The Sulphate-Reducing Bacteria. 2nd Edition. Cambridge University Press, Cambridge, UK.

Pough, F.H. (1996). Rocks and Minerals. 5th Edition, Houghton Mifflin Company, New York, NY.

Prasad, D., Wai, M., Berube, P., and Henry, J.G. (1999). Evaluating substrates in the biological treatment of acid mine drainage. *Environmental Technology*, 20(5): 449-458.

Prommer, H., Barry, D.A., Chiang, W.H., and Zheng, C. (2001). PHT3D – a MODFLOW/MT3DMS-based reactive multi-component transport model. MODFLOW 2001 and Other Modeling Odysseys, H. Seo, E. Poeter, and C. Zheng, eds., International Ground-Water Modeling Center, Colorado School of Mines, Golden, CO, 477-483.

Roane, T.M., and Kellogg, S.T. (1996). Characterization of bacterial communities in heavy metal contaminated soils. *Canadian Journal of* Microbiology, 42 (6):593-603.

Robertson, W.D., Blowes, D.W., Ptacek, C.J. and Cherry, J.A. (2000). Long-term performance of in situ reactive barriers for nitrate remediation, *Ground Water*, 38 (5): 689-695.

Schafer, D., Schafer, W., and Kinzelbach, W. (1998a). Simulation of reactive processes related to biodegradation in aquifers. 1-structure of the three-dimensional reactive transport model. *Journal of Contaminant Hydrology*, 31(1-2): 167-186.

Schafer, D., Schafer, W., and Kinzelbach, W. (1998b). Simulation of reactive processes related to biodegradation in aquifers. 2-model application to a column study on

organic carbon degradation. *Journal of Contaminant Hydrology*, 31(1-2): 187-209.

Singer, P., and Stumm, W. (1970). Acid mine drainage: the rate-determining step, *Science*, 167: 1121-1123.

Sposito, G. (1989). The Chemistry of Soils. Oxford University Press, Oxford, UK.

Thomas, K. (2001). Remediation of Acid Mine Drainage under Sulfate Reducing Conditions. Undergraduate Thesis in Environmental Engineering, University of Western Australia, Crawley, Australia.

Thombre, M.S., Thomson, B.M., and Barton, L.L. (1997). Use of a permeable biological reaction barrier for groundwater remediation at a uranium mill tailings remedial action site, International Containment Technology Conference, 9-12 February, St. Petersburg, FL, U.S. Department of Energy and Florida State University Institute for International Cooperative Environmental Research, Tallahassee, FL, 744-750.

Tompson, A.F., Ababou, R., and Gelhar, L.W. (1989). Implementation of the three-dimensional turning bands random field generator. *Water Resources Research*, 25(10): 2227-2243.

Tuttle, J.H., Dugan, P.R., and Randles, C.I. (1969). Microbial sulfate reduction and its potential utility as an acid mine water pollution abatement procedure. *Applied Microbiology*, 17(2): 297-302.

US EPA (1998). Permeable Reactive Barrier Technologies for Containment Remediation. EPA/600/R-98/125. Washington DC.

US EPA (2002). Field Applications of In Situ Remediation Technologies: Permeable Reactive Barriers, Office of Solid Waste and Emergency Response, Washington DC.

Wakao, N., Takahashi, T., Sakurai, Y., and Shiota, H. (1979). A treatment of acid mine

water using sulfate-reducing bacteria. *Journal of Fermentation Technology*, 57(5): 445-452.

Waybrant, K.R., Blowes, D.W., and Ptacek, C.J. (1998). Selection of reactive mixtures for use in permeable reactive walls for treatment of mine drainage. *Environmental Science and Technology*, 32(13):1972-1979.

Waybrant, K.R., Ptacek, C.J., and Blowes, D.W. (2002). Treatment of mine drainage using permeable reactive barriers: column experiments. *Environmental Science and Technology*, 36(6): 1349-1356.

Webb, J.S., McGinness, S., and Lappin-Scott, H.M. (1998). Metal removal by sulphate-reducing bacteria from natural and constructed wetlands. *Journal of Applied Microbiology*, 84(2): 240-248.

Westrich, J.T., and Berner, R.A. (1984). The role of sedimentary organic matter in bacterial sulfate reduction: the G model tested. *Journal of Limnology and Oceanography*, 29(2): 236-249.

Whitehead, P.G., and Prior, H (2005). Bioremediation of acid mine drainage: an introduction to the Wheal Jane wetlands project. *Science of the Total Environment*, 338(1-2): 15-21.

Zheng, C., and Bennett, G.D. (2002). Applied Contaminant Transport Modeling, 2nd Edition, John Wiley and Sons, New York, NY.

Zheng, C., and Jiao, J.J. (1998). Numerical simulation of tracer tests in heterogeneous aquifers. *Journal of Environmental Engineering*, 124(6): 510-516.

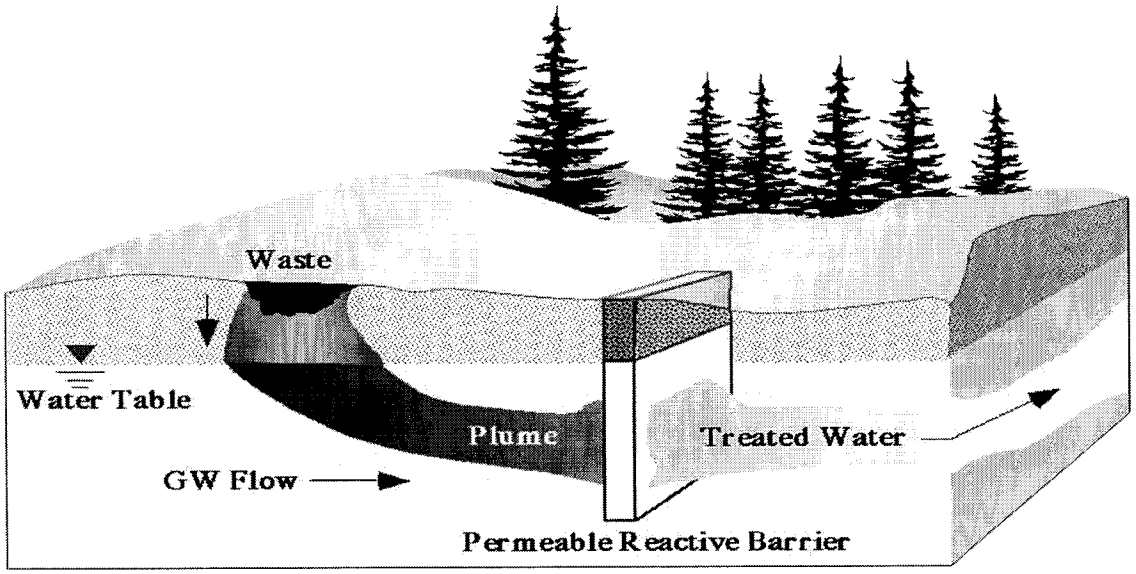

Figure 1.1 - General scenario for permeable reactive barriers (PRBs) (US EPA 1998).

CHAPTER 2

MATHEMATICAL MODEL OF SULFATE REDUCTION AND METALS PRECIPITATION BASED ON DECOMPOSING ORGANIC SOLIDS

ABSTRACT: The formulation of a new mathematical model for sulfate (SO_4^{2-}) reduction and metals precipitation with SO_4^{2-} reduction kinetics coupled to, and limited by, the decomposition of solid, particulate organic materials is presented. The model can be coupled to groundwater flow and contaminant transport, and is applicable, for example, for simulating the remediation of acid mine drainage (AMD) in sulfate-reducing (SR) systems. The organic solids consist of plant residues (detritus) rich in decomposable polysaccharides (cellulose/hemicellulose), such as leaf mulch compost, sawdust, wood chips, and alfalfa. The primary biochemical processes included in the model are (i) anaerobic decomposition of polysaccharides in solid, particulate organic materials, (ii) SO_4^{2-} reduction based on the incomplete oxidation of lactate, (iii) instantaneous or kinetically controlled precipitation of insoluble metal sulfides, (iv) partial volatilization of hydrogen sulfide (H_2S) to the gas phase, and (v) reversible kinetically controlled dissolution-precipitation of carbonate minerals, such as calcite ($CaCO_{3(s)}$) and siderite ($FeCO_{3(s)}$). Selected secondary processes included in the model are (i) SO_4^{2-} reductions based on the complete oxidation of lactate and on acetate, and (ii) methanogenesis. Finally, the simulation of a hypothetical SR column test with SO_4^{2-} reduction limited by cellulose decomposition and resulting in the precipitation of influent ferrous iron (Fe^{2+})

and zinc (Zn^{2+}) is presented as an illustrative example.

Key Words: Acid mine drainage, Bioremediation, Cellulose decomposition, Decomposition kinetics, Mathematical modeling, Polysaccharide decomposition, Solid organic materials, Siderite precipitation, Sulfate reduction.

2.1 INTRODUCTION

Several studies of field applications of sulfate reducing (SR) systems consisting of bioreactors, wetlands, and permeable reactive barriers (PRBs) based on solid (particulate) decomposable organic materials for the precipitation of heavy metals in waste solutions, such as acid mine drainage (AMD), have been reported (e.g., Thombre et al. 1997, US EPA 1998, Benner et al. 1999, McGregor et al. 1999, Benner et al. 2000, Gobla 2002, Ludwig et al. 2002, MSE 2002, Groudev et al. 2003). Examples of the solid, decomposable organic materials that have been evaluated include sawdust (e.g., Tuttle et al. 1969, Wakao et al. 1979), spent mushroom compost (e.g., Dvorak et al. 1992, Hammack and Edenborn 1992), fresh alfalfa (e.g., Bechard et al. 1994), and leaf compost/wood chips (e.g., Waybrant et al. 1998, Waybrant et al. 2002, Hulshof et al. 2003).

For example, Westrich and Berner (1984) and Bourdeau and Westrich (1984) considered the aerobic degradation of seawater plankton as precursor to sulfate (SO_4^{2-}) reduction in marine environments. In their model, the rate of SO_4^{2-} reduction was assumed equal to conversion factors multiplied by the rate of plankton decomposition (first-order kinetics with respect to carbon), with a hyperbolic term to account for SO_4^{2-} limitation. Drury (2000) considered anaerobic solid-substrate SR bioreactors in which the rate of SO_4^{2-} reduction was assumed equal to conversion factors multiplied by the rate of decomposition of the biodegradable solid waste materials, including a fist-order dependency on SO_4^{2-}. The solid degradation was modeled using first-order kinetics with a declining rate coefficient, based on an empirical declining rate function (Janssen 1984,

Middelburg 1989). However, both of the aforementioned models do not handle bacterial populations, i.e., decomposer bacteria and SR bacteria, or SRB, or the effects of bacterial growth and decay. Also, these models do not include dissolved organic substrates existing as decomposition products (e.g., Gujer and Zehnder 1983, Chynoweth and Pullammanappallil 1996).

Schafer et al. (1998a,b) developed a bioremediation model that includes aerobic reactions, fermentation, nitrate-, manganese-, iron-, and SO_4^{2-} reduction, and Prommer et al. (2001) describe the conceptual framework of a reactive transport model that includes geochemical equilibrium and kinetically controlled bioremediation. In both of these cases, Monod kinetics (Monod 1949) was used for modeling the growth of SRB. However, in both cases, bioremediation in the models is assumed to be sustained by the injection of dissolved organic substrates (e.g., lactate-propionate, ethanol, sucrose) instead of considering decomposing solid organic materials.

Mayer et al. (2002) describe the conceptual framework for a reactive transport model including AMD genesis, transport (impacted by equilibrium with a number of alumino-silicates, carbonates, and gypsum), and bioremediation partly based on kinetically controlled SO_4^{2-} reduction. However, the model described by Mayer et al. (2002) does not address bacterial populations (e.g., decomposers and SRB) or the effects of bacterial growth and decay, and also does not include solid decomposing organic materials. Additionally, the actual kinetic expressions for modeling SO_4^{2-} reduction and the assumptions with respect to dissolved organic substrates required for SO_4^{2-} reduction are not given.

Benner et al. (2002) and Amos et al. (2004) describe a model based on SO_4^{2-}

reduction for AMD remediation in which the rate of SO_4^{2-} reduction is assumed equal to a constant value multiplied by a hyperbolic term accounting for SO_4^{2-} limitation. The constant rate of SO_4^{2-} reduction in this model is determined by fitting SO_4^{2-} experimental data, for example from a previous column test. Bacterial populations and the effects of bacterial growth and decay, as well as the existence of solid or dissolved organic substrates that may limit the extent of SO_4^{2-} reduction, are not considered by the model. As a result, the model potentially oversimplifies SR systems in which the rate of SO_4^{2-} reduction is critically limited by the presence of a dissolved organic substrate generated from decomposition of solids and critically linked to bacterial growth and decay (e.g., Boudreau and Westrich 1984, Westrich and Berner 1984, Dvorak et al. 1992, Bechard et al. 1994, Drury 2000, Chang et al. 2000, Logan et al. 2003).

As noted above, none of the existing models for SO_4^{2-} reduction and metals precipitation include both the effects of decomposing solid (particulate) organic materials and biological growth and decay on the rates of SO_4^{2-} reduction for metals precipitation. As a result, the objective of this chapter is to present the formulation of a new mathematical model for SO_4^{2-} reduction and metals precipitation in which SO_4^{2-} reduction kinetics is coupled to, and limited by, the decomposition of solid organic materials, and the growth and decay of decomposer bacteria and SRB are also included.

The new biochemical-reactivity model can be inserted as a new user-defined reactivity subroutine into the multi-species contaminant transport program RT3D version 2.5 (Clement 2003), which is based on a groundwater flow solution from MODFLOW-2000 version 1.7 (Harbaugh et al. 2000). Also, when simulating no-flow scenarios, such as batch equilibrium experiments, the mathematical model can be numerically integrated

as a stand-alone system of equations with time as the only independent variable, i.e., not coupled to flow and transport.

2.2 CONCEPTUAL BASIS, AND BICHEMICAL AND KINETIC EQUATIONS FOR THE MODEL

A flowchart including primary and secondary biochemical processes incorporated in the mathematical model is shown in Fig. 2.1. The primary processes in the model (i.e., dark boxes and arrows in Fig. 2.1) include (i) decomposition of polysaccharides in solid, particulate organic materials, producing lactate with hydrolysis as the rate limiting step, (ii) sulfate reduction based on the incomplete oxidation of lactate (i.e., designated sulfate reduction 1), (iii) instantaneous or kinetically controlled precipitation of insoluble metal mono-sulfides, (iv) partial volatilization of hydrogen sulfide (H_2S) to the gas phase, and (v) reversible kinetically controlled dissolution-precipitation of carbonate minerals, such as calcite ($CaCO_{3(s)}$) and siderite ($FeCO_{3(s)}$). The selected secondary processes include (i) sulfate reductions based on the complete oxidation of lactate and on acetate, and (ii) methanogenesis. Besides the aforementioned biochemical reactivity, the model can coupled reactivity to groundwater flow and contaminant transport, i.e., the biochemical-reactivity model is inserted as a new user-defined reactivity subroutine into the multi-species contaminant transport program RT3D version 2.5 (Clement 2003, 1997). The processes in the biochemical-reactivity model are described in detail in the following sub-sections.

2.2.1 Primary Biochemical Reactivity Processes

Model Variables:

[CE_i]: decomposable polysaccharide concentration (i=1..n). n: total number of polysaccharide materials.

[$X_{d,i}$]: biomass concentration of decomposer bacteria (i=1..n).

[LA]: concentration of lactate.

[X_{SRB1}]: biomass concentration of sulfate-reducing bacteria 1.

[SO]: concentration of sulfate.

[H_2S]: concentration of hydrogen sulfide in solution.

[$H_2S]_g$: concentration of hydrogen sulfide in the gas phase.

[M_k]: concentration of metal (k=1..m).

[MS_k]: concentration of metal sulfide (k=1..m).

[M_kCO_3]: concentration of metal carbonate (k=1..m).

[A]: concentration of acetate.

[Ca]: concentration of calcium.

[HCO_3]: concentration of bicarbonate.

[H]: hydrogen proton concentration (assumed ~ constant).

t: time.

Parameters:

$k_{f,i}$: First-order rate coefficient for decomposition of polysaccharide 'i'.

$k_{c,i}$: Contois rate coefficient for decomposition of polysaccharide 'i'.

$K_{c,i}$: Contois half saturation coefficient for decomposition of polysaccharide 'i'.

$d_{d,i}$: First-order rate coefficient for decay of decomposer bacteria 'i'.

μ_{SRB1}: Monod maximum specific growth rate of SRB_1.

K_{V1}: Monod half-saturation coefficient for lactate in sulfate reduction 1.

K_{SO1}: Monod half-saturation coefficient for sulfate in sulfate reduction 1.

d_1: First-order rate coefficient for decay of SRB_1.

k_k: First-order precipitation rate coefficient for the solid MS_k.

$r_{d,c}$: dissolution rate for calcite.

$r_{d,kc}$: dissolution rate for M_kCO_3.

$K_{sp,c}$: solubility product for calcite.

$K_{sp,kc}$: solubility product for M_kCO_3.

k_v: First-order volatilization rate coefficient for $H_2S \rightarrow H_2S_{(g)}$.

K: Dimensionless Henry's law coefficient for $H_2S \rightarrow H_2S_{(g)}$.

Mass yield coefficients:

$Y_{Xd/CE}$: mass yield coefficient for decomposer bacteria / polysaccharide, = 0.1827 g/g.

$Y_{LA/CE}$: mass yield coefficient for lactate / polysaccharide, = 0.8588 g/g.

$Y_{SO/SRB1}$: mass yield coefficient for sulfate / SRB_1, = 11.097 g/g.

$Y_{HS/SRB1}$: mass yield coefficient for H_2S / SRB_1, = 3.9350 g/g.

$Y_{LA/SRB1}$: mass yield coefficient for lactate / SRB_1, = 21.880 g/g.

$Y_{A/SRB1}$: mass yield coefficient for acetate / SRB_1, = 13.632 g/g.

$Y_{HCO3/SRB1}$: mass yield coefficient for HCO_3 / SRB_1, = 14.089 g/g.

$Y_{MSk/HS}$ (e.g., $Y_{FES/HS}$): mass yield coefficient for MS_k (FeS) to H_2S in precipitation (e.g., = 2.5811 g/g).

$Y_{Mk/HS}$ (e.g., $Y_{FE/HS}$): mass yield coefficient for M_k (e.g., ferrous iron) to H_2S in precipitation, (e.g., = 1.6397 g/g).

$Y_{Ca/CaCO3}$: mass yield coefficient for calcium with respect to calcite.

$Y_{HCO3/CaCO3}$: mass yield coefficient for bicarbonate with respect to calcite.
$Y_{Mk/MkCO3}$: mass yield coefficient for M_k with respect to M_kCO_3.
$Y_{HCO3/MkCO3}$: mass yield coefficient for bicarbonate with respect to M_kCO_3.

2.2.1.1 Polysaccharide Hydrolysis

Decomposition of solid organic materials has been observed to be the rate-limiting step in bacterial sulfate reduction (Tuttle et al. 1969, Lovley and Klug 1986, Westrich and Berner 1988, Bechard et al. 1994, Drury 2000, Chang et al. 2000, Logan et al. 2003). Polysaccharides (cellulose and hemicellulose) occur in large amounts (e.g., ~ 60 - 70 % by dry weight) in plant residues of woods, straw, and leaves, and are susceptible to anaerobic decomposition (Stephens and Heichel 1975, Fan et al. 1987, Jain et al. 1992, Owens and Chynoweth 1993, Chynoweth and Pullammanappallil 1996, Micales and Skog 1997, Sylvia et al. 1998).

Cellulose (Fig. 2.2) and hemicellulose are large polymers that are insoluble in water and initially decompose via a hydrolytic step (heterogeneous reaction). Hydrolysis in the anaerobic environment is exclusively bacterial, since anaerobic fungi are restricted to the bovine rumen (Lynd et al. 2002). Lignin undergoes negligible decomposition in anaerobic environments and, therefore, is neglected in the model (Micales and Skog 1997). However, polysaccharide association with lignin contributes to a more recalcitrant behavior of the polysaccharide components (Micales and Skog 1997, Lynd et al. 2002). Hydrolysis is promoted by the activity of a consortium of microorganisms, facilitated by extracellular enzymes, and generally observed to be the rate-limiting step in the anaerobic decomposition of organic solids, including plant residues, decomposing municipal solid waste, and wastewater solids (Jain et al. 1992, Chynoweth and Pullammanappallil 1996, Vavilin et al. 1996, Lai and Pullammanappallil 1998, Lai et al. 2001, Lynd et al. 2002,

Logan et al. 2003, Vavilin et al. 2004). Therefore, the homogenous reactions occurring after hydrolysis (cellobiose→glucose→fatty acids) are assumed not to be kinetically limiting, and the rate of lactate production is assumed as directly proportional to the rate of polysaccharide hydrolysis.

In contrast with complex, more mechanistic hydrolysis models (e.g., Humphrey 1979, Negri et al. 1992, Lai and Pullammanappallil 1998, Batstone et al. 2000), the relatively simple first-order and the Contois kinetic (Contois 1959) models are frequently used in the simulation of anaerobic digestion of organic matter (e.g., Vasiliev et al. 1993, Gujer et al. 1995, Vavilin et al. 1996, Bagley and Brodkorb 1999, Rittmann and McCarty 2001, Vavilin et al. 2001, Batstone et al. 2002, Vavilin 2003, Vavilin et al. 2004). These less mechanistic, simpler models often are preferred because these models can provide an average yet relatively accurate representation of decomposition over time without the requirement for detailed and extensive input parameter values (Vavilin et al. 1996, Vavilin et al. 2001, Batstone et al. 2002), and consist of simple kinetic expressions that incorporate cumulative effects of different processes (Vavilin et al. 2001, Vavilin et al. 2004).

Based on the first-order model, the rate of polysaccharide decomposition is given as follows:

$$\frac{d[CE_i]}{dt} = -k_{f,i}\,[CE_i]\frac{1}{1+\left([LA_u]/K_i\right)^{m_i}} \qquad (2.1)$$

where $[CE_i]$ is the concentration of decomposable polysaccharide 'i' in terms of dry mass

of decomposable polysaccharide per volume of solution, $[LA_u]$ is the concentration of undissociated lactic acid, $k_{f,i}$ is a rate coefficient (1/T), and K_i and m_i are the inhibition constant and degree index, respectively. Based on the assumption that undissociated organic acids will be negligible for systems opperating within the pH range for the model, the resulting first-order expression can be written as follows:

$$\frac{d[CE_i]}{dt} = -k_{f,i}\,[CE_i] \tag{2.2}$$

In terms of Contois kinetics (Contois 1959), the rate of polysaccharide decomposition is proportional to the concentration of decomposer bacteria associated with the decomposable material, and regulated by the ratio between the concentrations of decomposable polysaccharide and bacteria, as follows:

$$\frac{d[CE_i]}{dt} = -k_{c,i}\,[X_{d,i}]\,\frac{\left([CE_i]/[X_{d,i}]\right)}{K_{c,i} + \left([CE_i]/[X_{d,i}]\right)} \tag{2.3}$$

where $[X_{d,i}]$ is the biomass concentration of decomposer bacteria 'i' associated with material 'i', $k_{c,i}$ is a Contois rate coefficient (1/T), and $K_{c,i}$ is a Contois affinity constant. This expression transitions between the two limiting cases of first-order kinetics with respect to $[CE_i]$ at low $[CE_i]/[X_{d,i}]$ ratios, and first-order kinetics with respect to $[X_{d,i}]$ at high $[CE_i]/[X_{d,i}]$ ratios (i.e., exponential $X_{d,i}$ growth). A rate coefficient such as $k_{c,i}$

lumps the effects of intrinsic material degradability and particle gradation (i.e., surface area) that would be included in more mechanistic approaches (e.g., Negri et al. 1992).

Equation 2.2 or 2.3 represents the slowest step in polysaccharide decomposition to generate lactate and, therefore, the rates of lactate production in solution and $X_{d,i}$ growth are taken simply as proportional to $d[CE_i]/dt$, as follows:

$$\frac{d[LA]}{dt} = Y_{LA/CE} \sum_{i=1}^{n} \left(-\frac{d[CE_i]}{dt} \right) \tag{2.4}$$

and

$$\frac{d[X_{d,i}]}{dt} = Y_{Xd/CE} \left(-\frac{d[CE_i]}{dt} \right) - d_{d,i}[X_{d,i}] \tag{2.5}$$

where [LA] is the concentration of lactate, $Y_{LA/CE}$ is the mass-yield coefficient for LA (mass of LA produced per gram of polysaccharide decomposed), n is the total number of decomposable materials incorporated in the system, $Y_{Xd/CE}$ is the mass-yield coefficient for $X_{d,i}$ (mass of $X_{d,i}$ produced per gram of polysaccharide decomposed), and $d_{d,i}$ is the first-order bacterial decay rate (1/T). Decomposer bacteria gain energy and grow from the transformation of glucose into fatty acids (Humphrey 1979). However, since this step is not limiting, the growth rate ultimately depends on the rate of the heterogeneous reaction, and a Monod expression representing the growth of $X_{d,i}$ based on glucose is not required (Fig. 2.1).

As presented, mass-yield coefficients for LA and $X_{d,i}$ are assumed invariable with

CE_i (i.e., are assumed the same for different decomposable polysaccharide residues). The values of $Y_{LA/CE}$ and $Y_{Xd/CE}$ are obtained from sequential stoichiometries as follows:

$$n\underbrace{(C_6H_{10}O_5)}_{\text{cellulose}} + H_2O \rightarrow (n-2)(C_6H_{10}O_5) + \underbrace{C_{12}H_{22}O_{11}}_{\text{cellobiose}} \tag{2.6}$$

$$\left.\begin{aligned} &\underbrace{C_{12}H_{22}O_{11}}_{\text{cellobiose}} + H_2O \rightarrow 2\underbrace{C_6H_{12}O_6}_{\text{glucose}} \\ &2\underbrace{C_6H_{12}O_6}_{\text{glucose}} + 0.524NH_4^+ \rightarrow 3.126\underbrace{C_3H_5O_3^-}_{\text{lactate}} + 3.652H^+ + 1.573H_2O + \\ &0.524\underbrace{C_5H_7O_2N}_{\text{biomass}} \end{aligned}\right\} \tag{2.7}$$

resulting in $Y_{LA/CE}$ = 0.8588 g/g, and $Y_{Xd/CE}$ = 0.1827 g/g. The formula for cellulose is assumed as representative of the bulk of the decomposable polysaccharides, and the formula for biomass is a simplified form of possible more complete formulas including, for example, S and P, such as $C_5H_7O_2NS_{0.1}P_{0.06}$ (e.g., Speece 1987).

2.2.1.2 Sulfate Reduction Based on Lactate

The rate of sulfate reduction is limited by the availability of dissolved (i.e., utilizable) organic substrates for the growth of SRB, which are released in solution from decomposition of solid organic materials. The volatile fatty acids are produced upon solid decomposition and are the major SRB substrates (Schonheit et al. 1982, Ingvorsen et al. 1984). The major and most abundant genera of SRB are incomplete oxidizers of lactate and propionate (i.e., lumped in the model as lactate) (Widdel 1988, Langmuir 1997,

Schaufer et al. 1998b, Chang et al. 2000, Jong and Parry 2003, Logan et al. 2003), examples of which include *Desulfovibrio*, *Desulfotomaculum*, and *Desulfomonas* (Postgate 1984, Widdel 1988). This SRB category is heretofore designated as SRB_1 (Fig. 2.1).

The growth of SRB_1 is modeled using Monod kinetics (Monod 1949), as previously adopted for sulfate reduction on limiting dissolved substrates (e.g., Middleton and Lawrence 1977, Ingvorsen et al. 1984, Okabe et al. 1995, Konishi et al. 1996). Dual-substrate Monod expressions representing SRB growth limited by lactate and SO_4^{2-}, and including a first-order bacterial decay term, are written as follows:

$$\frac{d[X_{SRB_1}]}{dt} = \mu_{SRB_1}[X_{SRB_1}]\left(\frac{[LA]}{K_{V1}+[LA]}\right)\left(\frac{[SO]}{K_{SO1}+[SO]}\right) - d_1[X_{SRB_1}] \qquad (2.8)$$

where $[X_{SRB1}]$ is the biomass concentration of SRB_1 (mg/L), [SO] is the concentration of SO_4^{2-}, [LA] is the concentration of lactate, μ_{SRB1} is the maximum specific growth rate for SRB_1 on LA (1/T), K_{V1} is the half-saturation coefficient for LA, and K_{SO1} is the half-saturation coefficient for SO_4^{2-}. The first-order rate coefficient, d_1, corresponds to SRB_1 decay (1/T). The kinetic expression for lactate (LA) combines solid decomposition and sulfate reduction 1. The term accounting for LA consumption is directly linked to SRB_1 growth using a mass yield coefficient, and the resulting expression is written as follows:

$$\left.\begin{aligned}\frac{d[LA]}{dt} = Y_{LA/CE}\sum_{i=1}^{n}\left(\frac{d[CE_i]}{dt}\right)\\ -Y_{LA/SRB1}\,\mu_{SRB_1}[X_{SRB_1}]\left(\frac{[LA]}{K_{V1}+[LA]}\right)\left(\frac{[SO]}{K_{SO1}+[SO]}\right)\end{aligned}\right\} \quad (2.9)$$

where $Y_{LA/SRB1}$ is the mass-yield coefficient for LA with respect to growth of SRB_1.

The kinetic expressions for SO_4^{2-}, H_2S, HCO_3^-, and acetate consumed/produced in sulfate reduction 1 also are linked to SRB_1 growth as follows:

$$\frac{d[C]}{dt} = Y_{c/SRB1}\,\mu_{SRB_1}[X_{SRB_1}]\left(\frac{[LA]}{K_{V1}+[LA]}\right)\left(\frac{[SO]}{K_{SO1}+[SO]}\right) \quad (2.10)$$

where [C] represents the concentration of either SO_4^{2-}, H_2S, HCO_3^-, or acetate, and $Y_{c/SRB1}$ is the mass yield coefficient corresponding to species c. For SO_4^{2-}, $Y_{C/SRB1} = -Y_{SO/SRB1}$, and for H_2S, HCO_3^-, and acetate, $Y_{C/SRB1} = +Y_{HS/SRB1}$, $+Y_{HCO3/SRB1}$, $+Y_{A/SRB1}$, respectively. Mass-yield coefficients are obtained assuming the following sulfate reduction stoichiometry (Kim et al. 1999):

$$SRB_1: \left\{\begin{aligned}&2.128\underbrace{C_3H_5O_3^-}_{\text{lactate}} + SO_4^{2-} + 0.0766NH_4^+ \rightarrow 2HCO_3^- + 0.234H_2O +\\ &H_2S + 2\underbrace{C_2H_3O_2^-}_{\text{acetate}} + 0.0766\underbrace{C_5H_7O_2N}_{\text{biomass}}\end{aligned}\right\} \quad (2.11)$$

which leads to $Y_{LA/SRB1}$ = 21.880 g/g, $Y_{SO/SRB1}$ = 11.097 g/g, $Y_{HS/SRB1}$ = 3.935 g/g, $Y_{HCO3/SRB1}$ = 14.089 g/g, and $Y_{A/SRB1}$ = 13.632 g/g.

2.2.1.3 Precipitation of Metal Sulfides

The model considers metal mono sulfides (i.e., 1:1 metal to S^{2-} on an atomic mole basis) as the stoichiometric form of the sulfide precipitate, which is, in the case of iron, in agreement with the observed formation of amorphous $FeS_{(s)}$ and an approximation for mackinawite, i.e., $FeS_{0.9(s)}$ (e.g., Benner et al. 1999, Waybrant et al. 1998, Waybrant et al. 2002, Hulshof et al. 2003). The model is capable of handling multiple heavy metals of concern, such as Fe^{2+}, Cd^{2+}, Cu^{2+}, Pb^{2+}, and Zn^{2+}, commonly associated with contaminated aquifers impacted by AMD in the western U.S.A. (www.epa.gov/region08). The equilibrium reaction for the precipitation/dissolution of a generic metal mono-sulfide (MS_k) can be written as follows:

$$M_k^{2+} + H_2S \underset{k_{d,k}}{\overset{k_{p,k}}{\rightleftharpoons}} MS_{k(s)} + 2H^+ \tag{2.12}$$

where M_k^{2+} is any divalent generic heavy metal, and $k_{d,k}$ and $k_{p,k}$ are the dissolution and precipitation rate coefficients for MS_k, respectively.

The net rate of precipitation of MS_k (i.e., $r_{p,k}^{net}$) is obtained by subtracting the rate of dissolution (i.e., $r_{d,k}$) from the rate of precipitation (i.e., $r_{p,k}$) as follows (Morel and Hering 1993):

$$r_{p,k}^{net} = \underbrace{k_{p,k}[M_k][H_2S]}_{r_{p,k}} - \underbrace{k_{d,k}[H^+]^2}_{r_{d,k}} \tag{2.13}$$

where $k_{p,k}$ and $k_{d,k}$ are the precipitation and dissolution rate coefficients, respectively. Additionally, the solubility product for MS_k can be written as follows:

$$K_{sp,k} = \frac{k_{d,k}}{k_{p,k}} = \frac{r_{d,k} / [H^+]^2}{r_{p,k} / [M_k][H_2S]} \tag{2.14}$$

The rate coefficient $k_{d,k}$ can be eliminated from Eq. 2.13 by combining with Eq. 2.14, or:

$$r_{p,k}^{net} = k_{p,k} K_{sp,k} [H^+]^2 \left\{ \frac{[M_k][H_2S] / [H^+]^2}{K_{sp,k}} - 1 \right\} \tag{2.15}$$

where the net rate of precipitation is expressed as a function of the super saturation of the solution with respect to M_k and H_2S. At equilibrium, the net rate of precipitation is zero. However, the SR system is assumed not to be at equilibrium with the solid phase (i.e., for each time step, a new aliquot of H_2S is release by sulfate reduction, and a new aliquot of MS_k is formed). Also, the dissolution of MS_k during the operational life of the SR system is neglected, resulting in the following simplified equation for the precipitation of MS_k:

$$r_{p,k}^{net} = k_{p,k} [M_k][H_2S] \tag{2.16}$$

Finally, the rate coefficient for precipitation can be defined in terms of the concentration (mg/L) of H_2S consumed, and the kinetics can be written as follows:

$$\frac{d[H_2S]}{dt} = -\sum_{k=1}^{m} k_k [M_k][H_2S] \tag{2.17}$$

$$\frac{d[M_k]}{dt} = -Y_{M_k/HS}\, k_k [M_k][H_2S] \tag{2.18}$$

$$\frac{d[MS_k]}{dt} = Y_{MS_k/HS}\, k_k [M_k][H_2S] \tag{2.19}$$

where k_k is the rate coefficient for precipitation in terms of H_2S, and = $k_{p,k}/Y_{MSk/HS}$, $Y_{Mk/HS}$ and $Y_{MSk/HS}$ are mass-yield coefficients for M_k and MS_k with respect to H_2S, and m is the total number of precipitating metals in the system. The kinetics of H_2S including production (sulfate reduction) and precipitation are as follows:

$$\left.\begin{aligned}\frac{d[H_2S]}{dt} = {} & Y_{HS/SRB1}\, \mu_{SRB_1} [X_{SRB_1}] \left(\frac{[LA]}{K_{V1} + [LA]}\right)\left(\frac{[SO]}{K_{SO1} + [SO]}\right) \\ & -\sum_{k=1}^{m} k_k [M_k][H_2S]\end{aligned}\right\} \tag{2.20}$$

As the value of the precipitation rate coefficient (k_k) increases, precipitation approaches the limiting case of an instantaneous process. Apart from kinetically-controlled precipitation, an alternative consideration in the model is the use of an instantaneous

equilibrium based precipitation algorithm, with the basic algorithm consisting of the calculations that follow:

$$
\begin{aligned}
&\bullet \quad \text{if } [H_2S]^t < [M]^t, \text{ then} \\
&\left.\begin{aligned}
[M]^{t+1} &= [M]^t - [H_2S]^t\, Y_{M/HS} \\
[MS]^{t+1} &= [MS]^t + [H_2S]^t\, Y_{MS/HS} \\
[H_2S]^{t+1} &= 0
\end{aligned}\right\} \\
&\bullet \quad \text{if } [M]^t < [H_2S]^t, \text{ then} \\
&\left.\begin{aligned}
[H_2S]^{t+1} &= [H_2S]^t - [M]^t / Y_{M/HS} \\
[MS]^{t+1} &= [MS]^t + [M]^t [\,(Y_{MS/HS})/(Y_{M/HS})] \\
[M]^{t+1} &= 0
\end{aligned}\right\}
\end{aligned}
\tag{2.21}
$$

where the variables and mass yield coefficients have been defined before, but subscript "k" is omitted in Eq. 2.21 in order to simplify the presentation (i.e., generic metal and metal sulfide are M and MS, respectively). The superscripts 't' and 't+1' denote present and future integration time steps, respectively. The first condition, i.e., H_2S in solution being limiting to precipitation, is generally the case in the SR system.

2.2.1.4 Partial Volatilization of Hydrogen Sulfide

The partial volatilization of H_2S to the gas phase requires the presence of liquid-gas interfaces (i.e., open system) within the SR system. In this case, the equilibrium reaction for the mass transfer can be written as follows:

$$
H_2S^o_{(l)} \underset{k_s}{\overset{k_v}{\rightleftharpoons}} H_2S_{(g)} \tag{2.22}
$$

where k_v and k_s are the rate coefficients of volatilization and gas solubilization, respectively.

The net rate of H_2S volatilization to the gas phase can be obtained by subtracting the rate of gas solubilization from the rate of volatilization as follows:

$$r_v^{net} = k_v[H_2S] - k_s[H_2S]_{(g)} \tag{2.23}$$

where the net rate r_v^{net} corresponds to the net rate of H_2S loss from solution (i.e., $= -d[H_2S]/dt$). If the concentrations in the two phases are at equilibrium, then $r_v^{net} = 0$, and the dimensionless Henry's law coefficient, K, equal to k_v/k_s, is defined. However, for concentrations in the two phases that are not at equilibrium, the kinetic rates of mass transfer are given as follows (e.g., Chynoweth and Pullammanappallil 1996, Valsaraj 2000, Batstone et al. 2002):

$$\frac{d[H_2S]}{dt} = -k_v\left\{[H_2S] - \frac{[H_2S]_{(g)}}{K}\right\} \tag{2.24}$$

and

$$\frac{d[H_2S]_{(g)}}{dt} = -\frac{V_l}{V_g}\left(\frac{\partial[H_2S]}{\partial t}\right) \tag{2.25}$$

where $[H_2S]_{(g)}/K$ represents the liquid-phase concentration $[H_2S]$ that would be at equilibrium with the gas phase concentration $[H_2S]_{(g)}$, and V_l/V_g is the volume ratio

(liquid phase/gas phase). If the gas phase is assumed to be vented to the atmosphere, then $V_g \rightarrow$: ($V_l/V_g \rightarrow 0$), $[H_2S]_g$ remains equal to zero at all times, and the rate of mass loss from the liquid phase is a maximum, as given by the following expression:

$$\frac{d[H_2S]}{dt} = -k_v[H_2S] \tag{2.26}$$

Apart from kinetically-controlled H_2S volatilization, an alternative consideration in the model is the use of an instantaneous equilibrium based volatilization algorithm, requiring the input of a venting frequency, and with the basic algorithm consisting of the calculations that follow:

$$\begin{cases} [H_2S]^{t+1} = [H_2S]^t + \dfrac{[H_2S]^t_{(g)}}{\left(\dfrac{V_l}{V_g} + K\right)} - \dfrac{\dfrac{V_g}{V_l}K}{\left(1 + \dfrac{V_g}{V_l}K\right)}[H_2S]^t \\ [H_2S]^{t+1}_{(g)} = [H_2S]^t_{(g)} + \dfrac{[H_2S]^t}{\left(\dfrac{V_g}{V_l} + \dfrac{1}{K}\right)} - \dfrac{\dfrac{V_l}{V_g}\dfrac{1}{K}}{\left(1 + \dfrac{V_l}{Vg}\dfrac{1}{K}\right)}[H_2S]^t_{(g)} \end{cases} \tag{2.27}$$

where all variables have been defined before, and the superscripts 't' and 't+1' denote present and future integration time steps, respectively. The lines of command containing the calculations above would be invoked in the source code every certain time interval, i.e., every venting event.

2.2.1.5 Reversible Dissolution-Precipitation of Carbonates

The reversible dissolution-precipitation of calcite ($CaCO_{3(s)}$) and metal carbonates (i.e., $M_kCO_{3(s)}$), such as siderite or $FeCO_{3(s)}$, can represent an alternative mechanism for metal removal in the SR systems provided that metal carbonates precipitate as $CaCO_{3(s)}$ dissolves releasing HCO_3^- in solution. For example, Amos et al. (2004) noted that siderite ($FeCO_{3(s)}$) was a significant Fe^{2+} sink, along with FeS precipitation, in the column experiments previously performed by Waybrant et al. (2002). However, other studies based on SR column and batch experiments have not arrived at the same conclusion (Bechard et al. 1994, Chang et al. 2000, Hulshof et al. 2003) and, in some cases, mixed results have been shown such as an initial tendency to precipitate $FeCO_{3(s)}$, followed by a tendency to dissolve $FeCO_{3(s)}$ and precipitate $CaCO_{3(s)}$ (Waybrant et al. 1998).

The equilibrium reactions for the dissolution-precipitation of $CaCO_{3(s)}$ and M_kCO_3 can be written as follows (e.g., Drever 1997):

$$CaCO_{3(s)} + H^+ \underset{k_{p,c}}{\overset{k_{d,c}}{\rightleftharpoons}} Ca^{2+} + HCO_3^- \tag{2.28}$$

$$M_kCO_{3(s)} + H^+ \underset{k_{p,kc}}{\overset{k_{d,kc}}{\rightleftharpoons}} M_k^{2+} + HCO_3^- \tag{2.29}$$

where k_d and k_p are, respectively, the dissolution and precipitation rate coefficients for the solids (subscript 'c' denotes Ca^{2+}-carbonate, and subscript 'kc' denotes M_k-carbonate). The 25-°C values for the logarithms of the equilibrium constants for Eqs. 2.28 and 2.29 are = 1.85 and – 0.56 (if $M_k = Fe^{2+}$ in Eq. 2.29), respectively (Drever 1997).

The net rates of precipitation of $CaCO_{3(s)}$ and $M_kCO_{3(s)}$, i.e., r_p^{net}, can be written by subtracting the rates of dissolution (i.e., r_d) from the rates of precipitation (i.e., r_p), as follows:

$$r_{p,c}^{net} = r_{p,c} - r_{d,c} = k_{p,c}[Ca^{2+}][HCO_3^-] - k_{d,c}[H^+] \tag{2.30}$$

$$r_{p,kc}^{net} = r_{p,kc} - r_{d,kc} = k_{p,kc}[M_k^{2+}][HCO_3^-] - k_{d,kc}[H^+] \tag{2.31}$$

Additionally, solubility products can be written as follows:

$$K_{sp,c} = \frac{k_{d,c}}{k_{p,c}} = \frac{r_{d,c} / [H^+]}{r_{p,c} / [Ca^{2+}][HCO_3^-]} \tag{2.32}$$

$$K_{sp,kc} = \frac{k_{d,kc}}{k_{p,kc}} = \frac{r_{d,kc} / [H^+]}{r_{p,kc} / [M_k^{2+}][HCO_3^-]} \tag{2.33}$$

where $K_{sp,c}$ and $K_{sp,kc}$ are the solubility products for $CaCO_{3(s)}$ and $M_kCO_{3(s)}$, respectively.

Since the rates of mineral precipitation and dissolution are related by Eqs. 2.32 and 2.33, the net rates of precipitation (r_p^{net}) can be expressed as a function of only one

type of rates (i.e., either mineral precipitation or dissolution). Since values for the rates of mineral dissolution were obtained from the literature (Schafer et al. 1998b, Amos et al. 2004), r_p^{net} for the minerals was written in terms of the rates of dissolution.

In order to do so, the rates of mineral precipitation were written as a function of the rates of mineral dissolution, by combining equations. The expressions for r_p^{net}, which also are equal to $d[CaCO_3]/dt$ or $d[M_kCO_3]/dt$ (i.e., similarly to the previously shown for $FeS_{(s)}$) result as follows:

$$\frac{d[CaCO_3]}{dt} = r_{d,c}\left\{\frac{[Ca^{2+}][HCO_3^-]/[H^+]}{K_{sp,c}}\right\} - r_{d,c} \tag{2.34}$$

$$\frac{d[M_kCO_3]}{dt} = r_{d,kc}\left\{\frac{[M_k^{2+}][HCO_3^-]/[H^+]}{K_{sp,kc}}\right\} - r_{d,kc} \tag{2.35}$$

where the net rates of precipitation are expressed as a function of the super saturation of the solution with respect to the ions (e.g., Yabusaki et al. 2001, Li et al. 2005). At equilibrium, the term between brackets goes to 1.0, and the net rate of precipitation goes to zero. However, the system is assumed not to be at equilibrium (e.g., the expected behavior is that for each time step, a new aliquot of $CaCO_{3(s)}$ will dissolve, and a new aliquot of $M_kCO_{3(s)}$ will be formed, until calcite is depleted).

The rates of dissolution are assumed to be constant while the solid phases are

present (i.e., model pH is assumed to remain approximately constant). Hyperbolic terms in the form $[CaCO_3]/(K+[CaCO_3])$ and $[M_kCO_3]/(K+[M_kCO_3])$ are included as factors multiplying "r_d" on the right-hand side of Eqs. 2.34 and 2.35 to ensure in the model that the rates of mineral dissolution go to zero as the amounts of solid materials (i.e., $CaCO_{3(s)}$ and $M_kCO_{3(s)}$) go to zero during dissolution. The adopted value for the half-saturation constant (i.e., K), = 1 mg/L, was assumed sufficiently low to have a negligible impact on the calculated rates of dissolution/precipitation.

The solution concentrations of Ca^{2+}, M_k, and HCO_3^- are affected by precipitation/dissolution of $CaCO_{3(s)}$ and $M_kCO_{3(s)}$, and kinetic expressions for these species are directly linked to Eqs. 2.34 and 2.35 including the corresponding mass yield coefficients (i.e., $Y_{Ca/CaCO3} = 0.400$ g/g, $Y_{HCO3/CaCO3} = 0.609$ g/g, and, for example, if $M_k = Fe^{2+}$, $Y_{Fe/FeCO3} = 0.482$ g/g, and$Y_{HCO3/FeCO3} = 0.526$ g/g).

2.2.2 Secondary Biochemical Reactivity Processes

Variables:
$[X_{SRB2}]$: biomass concentration of sulfate-reducing bacteria 2.
$[X_{SRB3}]$: biomass concentration of sulfate-reducing bacteria 3.
$[X_M]$: biomass concentration of methanogens.

Parameters:
μ_{SRB2}: Monod maximum specific growth rate of SRB_2.
K_{V2}: lactate half-saturation coefficient in sulfate reduction 2.
K_{SO2}: sulfate half-saturation coefficient in sulfate reduction 2.
d_{SRB2}: decay first-order rate coefficient, SRB_2.
μ_{SRB3}: Monod maximum specific growth rate of SRB_3.
K_A: acetate half-saturation coefficient in sulfate reduction 3.
K_{SO3}: sulfate half-saturation coefficient in sulfate reduction 3.
d_{SRB3}: decay first-order rate coefficient, SRB_3.
μ_M: Monod maximum specific growth rate of methanogens.
K_{AM}: acetate half-saturation coefficient in methanogenesis.
d_M: decay first-order rate coefficient, methanogens.

Mass yield coefficients:

$Y_{SO/SRB2}$: mass yield coefficient for sulfate with respect to SRB in sulfate reduction 2.
$Y_{HS/SRB2}$: mass yield coefficient for H_2S with respect to SRB in sulfate reduction 2.
$Y_{HCO3/SRB2}$: mass yield coefficient for bicarbonate with respect to SRB in sulfate reduction 2.
$Y_{LA/SRB2}$: mass yield coefficient for lactate with respect to SRB in sulfate reduction 2.
$Y_{SO/SRB3}$: mass yield coefficient for sulfate with respect to SRB in sulfate reduction 3.
$Y_{HS/SRB3}$: mass yield coefficient for H_2S with respect to SRB in sulfate reduction 3.
$Y_{HCO3/SRB3}$: mass yield coefficient for bicarbonate with respect to SRB in sulfate reduction 3.
$Y_{A/SRB3}$: mass yield coefficient for acetate with respect to SRB in sulfate reduction 3.
$Y_{HCO3/M}$: mass yield coefficient for bicarbonate in methanogenesis.
$Y_{A/M}$: mass yield coefficient for acetate in methanogenesis.

2.2.2.1 Secondary Sulfate Reductions

Complete oxidizers of lactate (denoted SRB_2) are reported to be less abundant in the environment than SRB_1 (Widdel 1988). Acetoclastic SRB (denoted SRB_3) generally have slower rates of growth, are significantly less abundant than SRB_1, and are better suited for saline environments (Widdel 1988). Accordingly, Schafer et al. (1998b) modeled sulfate reduction considering only the incomplete oxidation of propionate, which is similar to lactate, and neglected the possibility of sulfate reduction on acetate. Chang et al. (2000) and Logan et al. (2003) verified experimentally that the amount of sulfate reduction on acetate was minor compared to that based on lactate. As a result, SRB_2 and SRB_3 are assumed to be secondary populations in the model formulation.

The growths of SRB_2 and SRB_3 are modeled using dual-substrate Monod kinetics, including a first-order bacterial decay term, as follows:

$$\frac{d[X_{SRB_2}]}{dt} = \mu_{SRB_2}[X_{SRB_2}]\left(\frac{[LA]}{K_{V2}+[LA]}\right)\left(\frac{[SO]}{K_{SO2}+[SO]}\right) - d_2[X_{SRB_2}] \qquad (2.36)$$

$$\frac{d[X_{SRB_3}]}{dt} = \mu_{SRB_3}[X_{SRB_3}]\left(\frac{[A]}{K_A + [A]}\right)\left(\frac{[SO]}{K_{SO3} + [SO]}\right) - d_3[X_{SRB_3}] \qquad (2.37)$$

where $[X_{SRB}]$ denotes the biomass concentrations for SRB_2 and SRB_3 (mg/L), μ_{SRB} are maximum specific growth rates (1/T), K_{V2} and K_A are the half-saturation coefficients for the electron donors (lactate or acetate), K_{SO} are the half-saturation coefficients for SO_4^{2-}, and d are the first-order decay rate coefficients (1/T). The kinetics of SO_4^{2-}, H_2S, HCO_3^-, lactate, and acetate are impacted by sulfate reductions 2 and 3 similarly to what was previously shown for SRB_1. If the secondary sulfate reductions are included in the model, mass yield coefficients for SO_4^{2-}, H_2S, HCO_3^-, lactate, and acetate with respect to sulfate reductions 2 and 3 are obtained based on the following stoichiometries (Kim et al. 1999):

$$SRB_2: \left\{ \begin{array}{l} 0.749\underbrace{C_3H_5O_3^-}_{\text{lactate}} + SO_4^{2-} + 0.0497NH_4^+ + 0.6817H^+ \rightarrow 2HCO_3^- + \\ 0.1496H_2O + H_2S + 0.0497\underbrace{C_5H_7O_2N}_{\text{biomass}} \end{array} \right\} \qquad (2.38)$$

$$SRB_3: \left\{ \begin{array}{l} 1.087\underbrace{C_2H_3O_2^-}_{\text{acetate}} + SO_4^{2-} + 0.035NH_4^+ + 1.052H^+ \rightarrow 2HCO_3^- + \\ 0.104H_2O + H_2S + 0.035\underbrace{C_5H_7O_2N}_{\text{biomass}} \end{array} \right\} \qquad (2.39)$$

2.2.2.2 Methanogenesis

Evidence of methane gas production in the SR systems along with sulfate reduction suggests that acetate produced by sulfate reduction 1 likely is consumed in

methanogenesis (e.g., Hammack et al. 1994, Logan et al. 2003). However, methanogenesis will only affect the rate of sulfate reduction if sulfate reduction 3 is present and, therefore, methanogenesis does not have a practical impact when considering only the primary processes. However, if required, a Monod kinetic expression for methanogenic growth on acetate can be included. In this case, the stoichiometric basis for relating the amount of bacterial growth to the amount of acetate consumed can be obtained using the following reaction:

$$X_m : \left\{ \begin{array}{l} \underbrace{C_2H_3O_2^-}_{\text{acetate}} + 0.894H_2O + 0.02NH_4^+ \rightarrow 0.952HCO_3^- + 0.952\underbrace{CH_{4(g)}}_{\text{methane}} + \\ 0.02\underbrace{C_5H_7O_2N}_{\text{biomass}} \end{array} \right\} \quad (2.40)$$

2.2.3 Model Assumptions and Limitations

The model assumes a temperature range from approximately 5 to 35 °C, but the effect of temperature must be introduced in the model by previously adjusting the parameter values. The model pertains to SR systems with near-neutral pH ranging from 6.0 to 8.0, i.e., the acidity of the solution is assumed significantly neutralized by previous processes of mineral dissolution/precipitation occurring before sulfate reduction. For the pH range assumed in the model, the volatile fatty acids are deprotonated, to lactate ($C_3H_5O_3^-$, pKa = 3.86) and acetate ($C_2H_3O_2^-$, pK_a at 25 °C = 4.74), reduced-nitrogen species are in the form of ammonium (NH_4^+, pK_a = 9.2), and sulfuric species are in the form of SO_4^{2-} (first pK_a = 1.99). Carbonate species are partitioned between bicarbonate (HCO_3^-) and carbonic acid ($H_2CO_3^o$), with pK_a at 25 °C = 6.35, and, pKa at 5 °C = 6.52

(Langmuir 1997), and the bicarbonate form (HCO_3^-) is adopted as the model carbonate species for the purpose of stoichiometries. Also, hydrogen sulfide (H_2S) species are partitioned between HS^- and H_2S^o, with pKa at 25 °C = 6.99, and, pKa at 5 °C = 7.28 (Langmuir 1997), and the H_2S^o form is considered more appropriate for the model considering the pH range.

2.3 MASS BALANCES

Species mass balances can be written considering either fixed-volume transient (i) batch (no-flow) reactors, or (ii) advective-dispersive (AD) reactors. The batch reactor is assumed perfectly mixed and with no input/output fluxes. The AD reactor is assumed to contain no recycle. In AD reactors, the temporal rate of mass accumulation/removal for any species in the system is equal to a combination of (i) the rate of mass utilization, i.e., production/consumption within the reactor, and (ii) the balance between the rates of mass input/output, such that mass balance can be written as follows:

$$\frac{dM_i}{dt} = Vn\frac{d[C_i]}{dt} = -V\left(\vec{\nabla}\bullet\vec{J}_i\right) + Vn\,r_{ut,i} \tag{2.41}$$

where M_i and $[C_i]$ are the mass and concentration of a generic species, respectively, V and n are the volume and porosity of the control volume, t is time, $-\vec{\nabla}\bullet\vec{J}_i$ is the temporal net rate of mass input/output, and $r_{ut,i}$ is the temporal net rate of mass utilization (biochemical processes). The mass flux vector $\mathbf{J_i}$ (input/output due to contaminant transport) can be calculated as follows (e.g., Shackelford 1995):

$$\vec{J}_i = \{q_x[C_i] + nD_{xx}\frac{\partial[C_i]}{\partial x}\}\vec{x} + \{q_y[C_i] + nD_{yy}\frac{\partial[C_i]}{\partial y}\}\vec{y} + \{q_z[C_i] + nD_{zz}\frac{\partial[C_i]}{\partial z}\}\vec{z} \quad (2.42)$$

where **x**, **y**, and **z** are the space coordinated directions, q_x, q_y, and q_z are Darcy's velocities parallel to x, y, and z, respectively, and based on Darcy's law, and D_{xx}, D_{yy}, and D_{zz} are components of the hydrodynamic dispersion tensor under the assumption of principal directions.

In batch (no-flow) systems, or when considering the immobile species in AD systems, Eq. 2.41 simplifies to:

$$\frac{dM_i}{dt} = Vn\frac{d[C_i]}{dt} = Vn\, r_{ut,i} \quad (2.43)$$

since $\mathbf{J_i}$ is equal to zero.

2.4 MATHEMATICAL BASIS AND SOLUTION FOR THE MODEL

The model solution requires simultaneous integration in time of the system of interdependent mass balance equations. The system comprises a non-steady state non-linear partial differential equation (NLPDE) for each mobile species in the reactor, and a non-steady state non-linear ordinary differential equation (ODE) for each immobile species in the reactor. Considering 'p' mobile and 'q-p' immobile species, the generic system can be written as follows:

$$\left.\begin{aligned}
&\frac{\partial[C_1]}{\partial t} = f_1(t,[C_1],[C_2],...,[C_q]) - \frac{1}{n}\{\vec{\nabla} \bullet \vec{J}_1\} \\
&\vdots \\
&\frac{\partial[C_p]}{\partial t} = f_p(t,[C_1],[C_2],...,[C_q]) - \frac{1}{n}\{\vec{\nabla} \bullet \vec{J}_p\} \\
&\frac{\partial[C_{p+1}]}{\partial t} = f_{p+1}(t,[C_1],[C_2],...,[C_q]) \\
&\vdots \\
&\frac{\partial[C_q]}{\partial t} = f_q(t,[C_1],[C_2],...,[C_q])
\end{aligned}\right\} \qquad (2.44)$$

where $[C_1]$ to $[C_p]$ are the mobile-, and $[C_{p+1}]$ to $[C_q]$ are the immobile-species concentrations. The functions f_1 to f_q are non-linear algebraic expressions representing biochemical reactivity, i.e., the superposition of all biochemical processes in the model that may affect the fate of the species. Mass yield coefficients relating biochemical processes to any given species may be positive, representing a source (production of the species due to the process), negative, representing a sink (consumption of the species due to the process), or null, representing no effect. In Eq. 2.44, sorption is neglected, i.e., the retardation factor R_d for linear, instantaneous, and reversible sorption is implicitly assumed equal to 1.0 (Shackelford 1995).

Multi-species reactive contaminant transport was solved using the program RT3D version 2.5 (U.S. Department of Energy, February 2003) described in Clement (2003, 1997), which is based on groundwater flow solutions obtained with MODFLOW-2000 version 1.7 (U.S. Geological Survey, December 2001) described in Harbaugh et al. (2000) and McDonald and Harbaugh (1988). Advection, hydrodynamic dispersion, and sink/source mixing can be solved in RT3D, identically to MT3DMS (Zheng and Wang

1999), using, among others, the Total Variation Diminishing method based on higher-order finite differences (Zheng 1990, Zheng and Wang 1999). Additionally, RT3D includes the advantage of accepting user defined reactivity subroutines, such as the biochemical-reactivity subroutine developed in this research.

The biochemical-reactivity subroutine encoded for this research (Compaq Visual Fortran 6.0) was linked to the RT3D source-code files and an edited RT3D executable was built. Reaction operator splitting was used in RT3D as the numerical strategy for coupling in time and solving transport and reactivity simultaneously (e.g., Wheeler et al. 1987, Rifai and Bedient 1990, Odencrantz et al. 1990, Zheng 1990, Valocchi and Malmstead 1992, Morshed and Kaluarachchi 1995, Clement 1997).

The strategy in reaction operator splitting consists of (i) splitting the original system of equations in two parts, a system of linear PDEs that can be solved with finite differences, and a system of non-linear ODEs that can be solved with a numerical integrator such as the Runge-Kutta-Fehlberg (RKF) algorithm (Chapra and Canale 2002) and (ii) merging in time the PDE and ODE results for each time step.

Concentrations at the previous time level ('t-1') are updated by advancing the finite difference method (contaminant transport) by one transport time step. Subsequently, these updated conservative-transport concentrations (time level 't') are input as initial conditions for advancing the RKF algorithm from 't-1' to 't'. At the end of this process, reactive-transport concentrations at time level 't' are obtained, and the process is re-started for the next transport time step. The required size of transport time steps is automatically defined by RT3D based on requirements for advection, dispersion, and sink/source mixing (e.g., Zheng 1990). Reaction or RKF integration time steps are significantly

smaller than transport time steps, i.e., RT3D supports a up to a maximum of 3000 RKF integration time steps within each transport time step. Also, the size of RKF integration time steps in RT3D is adaptive, and automatically adjusted to minimize integration errors.

With respect to boundary conditions for flow and transport, column-test simulations frequently include specified-flux and constant concentration boundary conditions located at the column influent, and free-draining and zero-dispersive mass flux conditions at the column effluent. With respect to initial conditions, the input of an initial concentration for species at all cells in the domain is required, i.e., $C(x,y,z,t=0)=C_i(x,y,z)$), such that $C_i \neq 0$ for species initially present in the domain, and = 0 for daughter (product) species.

For batch (no-flow) systems, a system of mass balance equations similar to Eq. 2.43 is integrated alone in time, starting from initial conditions. Point wise numerical evaluations of functional values $[C_i]$ at future time levels ('t + Δt') for each $[C_i]$ in the system were accomplished with a stand-alone RKF algorithm encoded in this research (Compaq Visual Fortran 6.0). Two independent numerical integrations are performed at each time step, i.e., one of fifth order and one of fourth order, using coefficients developed by Cash and Karp in 1990 (Chapra and Canale 2002). Relative local truncation errors (E_i) affecting newly calculated $[C_i](t + \Delta t)$ values are calculated as follows:

$$E_i(t+\Delta t)=\frac{\left|[C_i^{rk5}](t+\Delta t)-[C_i^{rk4}](t+\Delta t)\right|}{[C_i^{rk5}](t+\Delta t)} \tag{2.45}$$

where superscripts 'rk5' and 'rk4' imply the fifth- and fourth-order RKF evaluations. The

error E_i must be $\leq 5 \times 10^{-6}$ mg/L per 1.0 mg/L for all species in order for the simulation to be valid.

When instantaneous precipitation and/or volatilization are considered, the equations for the species involved in the processes are modified by omitting the process kinetic term, which is replaced by code lines corresponding to the instantaneous processes, added within the main time loop of the RKF algorithm, after the evaluation of $[C_i^{rk5}](t + \Delta t)$ and $[C_i^{rk4}](t + \Delta t)$, and therefore modifying the concentration values of species involved in the processes.

Graphical visualizations of flow-and-transport results are obtained with the three-dimensional U.S. Geological Survey software ModelViewer version 1.0 (March 2002), described in Hsieh and Winston (2002).

2.5 INITIAL CONCENTRATIONS OF BIOLOGICAL SPECIES

2.5.1 Decomposable Polysaccharides

The distinction between the amounts of total organic solids and anaerobically decomposable polysaccharides is an important consideration prior to the application of a decomposition model. The total solid materials in a SR system comprise inorganic (e.g., sand, gravel, limestone) and organic materials. The decomposable polysaccharides (cellulose/hemicellulose) are only a fraction of the organics. Lignin is usually reported to have negligible decomposition (e.g., Micales and Skog 1997) and should be discounted from the pool of decomposable materials. Lignin contents range from approximately 25 to 35 % (dry mass) in woods (Fan et al. 1987, Stephens and Heichel 1975, Rowell 1997), 10 to 15 % in leaf tissues (Rowell 1997), 17 to 20 % in grass fibers (Rowell 1997), and 6

to 13 % in corn and wheat residues (Sylvia et al. 1998). Also, soluble organic constituents, such as sugars and proteins, are easily washed and lost from the system, and should be discounted from the pool of decomposable materials. Soluble organics may amount to approximately 5 % (dry mass) in woods (Fan et al. 1987), 13 to 24 % in leaf tissues (Rowell 1997), and 20 to 30 % in corn and wheat residues (Sylvia et al. 1998).

The combined amounts of lignin and soluble organics may reach approximately 25 to 40 % (dry mass) in wood and leaf tissues and, as a result, the contents of cellulose/hemicellulose may be on the order of 60 to 75 % (dry mass) of the total dry mass of woods and leaf tissues (e.g., ~ 70 % in woods, Fan et al. 1987, and 55 % in corn and wheat residues, Sylvia et al. 1998, or, for cellulose alone, 45 % in woods, Stephens and Heichel 1975, 47 to 62 % in leaf tissues, Rowell 1997, and 50 % in wheat straw, Stephens and Heichel 1975). Additionally, the cellulose/hemicellulose pool contains hardly decomposable, protected tissues in close association with lignin that also should be discounted from the pool of decomposable materials (Micales and Skog 1997, Humphrey 1979, Chynoweth and Pullammanappallil 1996), and Micales and Skog (1997) cite references supporting the estimate of at least 18 % (dry mass) recalcitrant polysaccharides in plant refuse.

Despite variability and uncertainty, the combination of representative percentages described above suggests that the percentage of decomposable polysaccharides with respect to the total dry mass of wood and leaf materials (e.g., wood chips, sawdust, leaf mulch compost, alfalfa) can be assumed on the order of 50 % (dry mass). For a material such as municipal sewage sludge, the content of decomposable polysaccharides is expected to be significantly lower since the carbon content of the material is low

compared to that of wood chips, sawdust, and leaf mulch (i.e., 0.093 g/g vs. 0.35 to 0.47 g/g, Waybrant et al. 1998).

The concentrations $[CE_i]$ are used in the model to express the dry mass of decomposable polysaccharide 'i' per unitary volume of the liquid phase (pore liquid). A polysaccharide mass fraction, $mf_{c,i}$, (on a unitary-volume basis) can be correlated to $[CE_i]$ as follows:

$$[CE_i] = \underbrace{\left(\frac{f_{om,i}\, f_{do,i}}{(1+w)} \right)}_{mf_{c,i}} \frac{\rho_{bulk}}{n} \tag{2.46}$$

where $f_{om,i}$ is the fraction of organic material in the total mixture (dry mass), $f_{do,i}$ is the fraction of decomposable polysaccharides in the organic material (dry mass), and w, n, and ρ_{bulk} are the gravimetric moisture content, porosity, density of the mixture.

2.5.2 Bacterial Populations

2.5.2.1 Decomposer Bacteria

When multiple decomposable organic solids are present in an SR system, multiple populations of decomposer bacteria are assumed in the model, each population colonizing one of the decomposing solids. The equivalent biomass concentration by dry mass of polysaccharide decomposer bacteria colonizing each decomposable polysaccharide ranges from 0.1 to 10 mg biomass/g of dry polysaccharide, based on cell coverage ranging from approximately 10^9 to 10^{10} cells/g of dry detritus, and considering

from 10^{-10} to 10^{-9} mg per cell on a dry mass basis (e.g., Fenchel and Harrison 1976). A cell coverage ranging from 2 to 15 cells/100 μm^2 of fiber of decomposable detritus is obtained assuming fibers with a 2-mm diameter, 5-mm length, and ~ 3 mg/fiber (Fenchel and Harrison 1976, Henriksen and Breland 2002). Intermediate equivalent concentrations corresponding to concentration ratios by dry mass of decomposer bacteria to decomposable polysaccharide, $[X_d]/[CE]$, ranging from 2.75 x 10^{-3} to 1 x 10^{-2} generally were used for the simulations.

2.5.2.2 Sulfate Reducing Bacteria

The equivalent biomass concentration by dry mass for SRB that are incomplete oxidizers of lactate (e.g., *Desulfovibrio vulgaris*) was estimated to range from 1 to 1000 mg biomass/L of pore liquid when SO_4^{2-} reduction is active. This range is based on the converted abundance ranging from 10^7 to 10^9 cells/mL of pore liquid (e.g., Benner et al. 2002), considering 10^{-10} to 10^{-9} mg/cell by dry mass corresponding to cylindrical cells with a height of 2.35 μm and a diameter of 0.75 μm (Postage 1984). An intermediate value of 50 mg biomass/L of pore liquid generally was used for the simulations, and is equivalent to approximately 10^7 to 10^8 cells/mL of pore liquid, which is consistent with the most probable number (MPN) for SRB of 10^7 cells/g of solid material (i.e., 5 x 10^7 cells/mL of pore liquid) reported by Hulshof et al. (2003). Moreover, the MPN reported by Hulshof et al. (2002) was measured after the termination of the experiment such that presumably higher SRB values may have occurred during active SO_4^{2-} reduction.

2.6 PARAMETER VALUES

Some indicative parameter values can be found in the literature, and provide a basis for model parameter values to be subsequently adjusted using experimental data.

2.6.1 Polysaccharide Decomposition

Indicative values for the first-order rate coefficient (k_f) for decomposition of organic solids can be found in the literature. For example, at 25 – 35 °C, k_f = 0.04 to 0.07 d^{-1} for composted vegetation in waste (Chynoweth and Pullammanappallil 1996, Ritmann and McCarty 2001), 0.085 d^{-1} for leaves, 0.14 d^{-1} for newspaper (Owens and Chynoweth 1993, Chynoweth and Pullammanappallil 1996), 0.04 to 0.10 d^{-1} for cellulose (Gujer and Zehnder 1983, Vavilin et al. 1996), and 0.25 d^{-1} for activated sludge/swine waste (Vavilin et al. 1996). Contois decomposition parameter values are more difficult to find in the literature. The Contois rate coefficient, k_c, for cellulose decomposition at 35 °C is reported to be equal to 1.25 d^{-1}, with half-saturation constant, K_c, equal to 7.5 g/g. For sewage sludge decomposition at 25 °C, k_c is reported to range from 4.0 to 8.0 d^{-1}, with K_c equal to 40 g/g (Vavilin et al. 1996). The first-order bacterial decay rate coefficient was assumed equal to 10 % of the decomposition rate coefficient.

2.6.2 Sulfate Reduction 1

Monod parameter values for sulfate reduction 1 (e.g., *Desulfovibrio desulfuricans*) can be found in the literature. For growth at pH equal to 7.0 and 25 °C, the maximum specific growth rate, μ_{SRB1}, and the half-saturation coefficient with respect to lactate, K_{V1}, are reported as 9.0 d^{-1}, and 1.4 to 10 mg/L, respectively (Okabe and Characklis 1992).

Also for pH equal to 7.0, μ_{SRB1} = 1.4 d^{-1} and K_{V1} = 3.7 mg/L for 12 °C (Okabe and

Characklis 1992), $\mu_{SRB1} = 9.0\ d^{-1}$, $K_{VI} = 2.2$ mg/L, and the half-saturation coefficient with respect to sulfate, K_{SO}, ranges from 1.0 to 2.0 mg/L for 35 °C (Okabe at al. 1992, Konishi et al. 1996). The SRB first-order decay rate coefficient can range from 1.0 and 10 % of μ_{SRB1} (e.g., Omil et al. 1998).

2.6.3 Sulfide Precipitation

The first-order rate coefficients for metal-sulfide precipitation were considered variable in the model, and adjusted with experimental data. For example, for FeS (i.e., k_{Fe}), the value of 0.1 d^{-1} was found to be sufficiently high to approximate instantaneous precipitation under batch conditions.

2.6.4 Hydrogen Sulfide Volatilization

The dimensionless Henry's law coefficient for volatilization of H_2S at 25 °C is found to range from 0.42 (Valsaraj 2000) to 0.53 (Rittmann and McCarty 2001). The first-order rate coefficient for H_2S volatilization was consdiered variable in the model, and adjsuted using experimental data. For example, values ranging from 1.0 d^{-1} to 100 d^{-1} were used.

2.6.5 Calcite and Siderite

First-order dissolution rate coefficients for $CaCO_{3(s)}$ and $FeCO_{3(s)}$ were adopted in the model as 300 mg/L-d and 200 mg/L-d, respectively (e.g., Schafer et al. 1998b, Yabusaki et al. 2001, Amos et al. 2004). Solubility products for $CaCO_{3(s)}$ of $10^{1.85}$ and for $FeCO_{3(s)}$ of $10^{-0.56}$ were adopted from Drever (1997).

2.6.6 Sulfate Reductions 2 and 3

Monod parameter values for sulfate reduction 2 were assumed equal to those for sulfate reduction 1. However, Monod parameter values for sulfate reduction 3 were found to be significantly different. At pH equal to 7.0 and 30 °C, the maximum specific growth rate, μ_{SRB3}, and half-saturation coefficients with respect to acetate and sulfate, K_A and K_{SO3}, were found to be equal to 0.61 d^{-1}, 25 mg/L and 25 mg/L, respectively (Kalyuzhnyi et al. 1998). For 25 °C, μ_{SRB3} is reported as 0.46 d^{-1}, and K_A as 92 mg/L (Middleton and Lawrence 1977). Also, at 30 °C, μ_{SRB3} has been reported as 0.72 d^{-1}, with K_A equal to 5.0 mg/L and K_{SO3} equal to 20 mg/L (Ingvorsen et al. 1982), or μ_{SRB3} equal to 0.12 d^{-1}, with K_A equal to 55 mg/L and K_{SO3} equal to 33 mg/L (Omil et al. 1998).

2.6.7 Methanogenesis

Monod parameter values for methanogenic bacteria at pH equal to 7.0 and 30 °C have been reported as maximum specific growth rate, μ_M, equal to 0.23 d^{-1}, with half-saturation coefficients with respect to acetate, K_{AM}, on the order of 100 mg/L (Kalyuzhnyi et al. 1998), or μ_M equal to 0.26 d^{-1}, with K_{AM} on the order of 300 mg/L (Lawrence and McCarty 1969), or also μ_M equal to 0.67 d^{-1}, with K_{AM} on the order of 180 mg/L (Schonheit et al. 1982).

2.7 ILLUSTRATIVE EXAMPLE

The simulation of a reactive column test including decomposable cellulose, X_d, lactate, acetate, SO_4^{2-}, SRB_1, H_2S, Fe^{2+}, Zn^{2+}, $FeS_{(s)}$, and $ZnS_{(s)}$ is shown as an illustrate

model application. The column is 400-mm long, and the solution residence time within the column is equal to 14.5 d (i.e., = one column pore volume of flow, PVF, =vt/L, where v is the seepage velocity, t is time, and L is the column length).

The column influent solution contains 2000 mg/L of SO_4^{2-}, 500 mg/L of Fe^{2+}, and 250 mg/L of Zn^{2+}. The first 50 mm near the column inlet and the last 15 mm near the column outlet are assumed as non-reactive layers of sand. Approximately 15,000 mg of dry decomposable cellulose, along with a population of cellulose decomposers equivalent to $[X_d]/[CE]$ of 5.0×10^{-2}, and a population of SRB_1 equivalent to 50 mg/L are initially uniformly distributed through the reactive portion of the column. Cellulose decomposition producing lactate is simulated using Contois kinetics with the parameter values directly obtained from Vavilin et al. (1996) considering 35 °C, i.e., rate coefficient $k_c = 1.25\ d^{-1}$ and half-saturation coefficient $K_c = 7.5$ g/g. Sulfate reduction based on the incomplete oxidation of lactate is simulated using Monod kinetics with the following parameter values: $\mu_{SRB1} = 4.0\ d^{-1}$, $K_{VI} = 5.0$ mg/L, and $K_{SO} = 2.0$ mg/L. The precipitation of Fe^{2+} and Zn^{2+} mono sulfides is simulated using first-order kinetics for kinetically controlled precipitation, with rate coefficients of $1.0\ d^{-1}$ for $FeS_{(s)}$, and $5.0\ d^{-1}$ for $ZnS_{(s)}$. Liquid-gas interfaces within the column are neglected, and, consequently, the volatilization of H_2S to the gas phase also is neglected. The secondary model processes are not considered, and the possibility of sorption of Fe^{2+} and Zn^{2+} to the organic materials is neglected. The effects of space and time variability in flow and reactivity, as well as the effects of non-uniform initial distributions of substrates and bacterial populations are also not considered.

As shown in Fig. 2.3, the decomposition of labile cellulose within the column

occurs rapidly, i.e., in approximately 60 d (4.0 PVF). The rate of cellulose decomposition initially increased with time, from 0 to 1.0 PVF, and subsequently declined with time after approximately 3.0 PVF.

The removal of influent SO_4^{2-}, Fe^{2+} and Zn^{2+} can be observed by comparing Figs. 2.4a, b, c, and d. Figure 2.4a illustrates the conservative (non-reactive) transport of SO_4^{2-}, Fe^{2+} or Zn^{2+}, whereas Figs. 2.4b, c, and d show SO_4^{2-}, Fe^{2+} and Zn^{2+} concentrations along the column length for reactive transport, respectively. After 4.0 PVF, only a relatively small SO_4^{2-} breakthrough is observed (C/C_o of approximately 0.2), and Fe^{2+} and Zn^{2+} are absent from the effluent solution. Fig. 2.5 shows a comparison between effluent concentrations expected on the basis of non-reactive transport and those for SO_4^{2-}, Fe^{2+} or Zn^{2+} obtained on the basis of reactive transport. For non-reactive transport, breakthrough occurs at approximately one PVF, whereas more than 4.0 PVF are required for breakthrough when considering reactive transport.

Bacterial populations of cellulose decomposers and sulfate reducers (SRB_1) occurring in the column concomitantly with the remediation of the influent solution are shown in Figs. 2.6a and b, respectively. A uniform growth of decomposer bacteria is expected, as shown in Fig. 2.6a, resulting from the simulation assumptions. On the other hand, SRB_1 growth is non-uniform and expected to vary with the temporal and spatial variability of available substrates (lactate and SO_4^{2-}). As shown in Fig. 2.6b, after 4.0 PVF, the SRB population has grown by a factor of 10 compared to the initial population, and growth was predominantly concentrated within the half column near the influent side. The populations of decomposers and SRB undergo net decay after approximately 4.0 PVF, due to the depletion of decomposable cellulose.

The concentrations for the precipitates of $FeS_{(s)}$ and $ZnS_{(s)}$ along the column length are shown in Figs. 2.7 a and b, respectively. Precipitation is as asymmetrical, with the majority of the precipitates forming within the half column near the influent side (e.g., Yabusaki et al. 2001). Finally, in Figs. 2.8a to d, the concentrations of lactate and H_2S along the column length are compared versus time in different simulations. For the hypothetical case of cellulose decomposition with no sulfate reduction, lactate concentrations are shown in Fig. 2.8a. However, when sulfate reduction occurs, lactate concentrations remain at lower levels, as shown in Fig. 2.8b. Moreover, Fig. 2.8b suggests that lactate is a limiting factor for sulfate reduction, since lactate concentrations approach zero. Also, in the hypothetical case of decomposition and sulfate reduction with no metal precipitation, H_2S concentrations are shown in Fig. 2.8c. However, when metal precipitation occurs, H_2S concentrations remain at lower levels, as shown in Fig. 2.8d. The results in Fig. 2.8d suggest that solution H_2S is a limiting factor for metal precipitation in the column.

2.8 CONCLUSIONS

A mathematical model for the biochemical reactivity of sulfate-reducing systems for metals precipitation with sulfate reduction kinetics coupled to, and limited by, the decomposition of solid organic materials was presented considering a combination of meaningful biochemical processes not combined in any of the reviewed models. The model was coupled to groundwater flow and contaminant transport using the public domain, and widely accepted, computer models MODFLOW and RT3D. The primary processes in the biochemical-reactivity model are expected to account for the major

trends observed in SR systems limited by solid substrates, such as, for example, organic bioreactors, wetlands, and permeable reactive barriers for acid mine drainage remediation. The example application provides insight into the types of expected model results, as well as, more specifically, into trends observed in SR flow-through (column) systems, such as the significant capacity of the column to remove influent heavy metals, and the expected accumulation of SRB biomass and solid precipitates near the influent end of the column.

2.9 ACKNOWLEDGEMENTS

This research was funded by the U. S. EPA Science to Achieve Results (STAR) Program under Grant No. R-82951501-0 as part of the U. S. EPA's *Rocky Mountain Regional Hazardous Substance Research Center*.

2.10 REFERENCES

Amos, R.T., Mayer, K.U., Blowes, D.W., and Ptacek, C.J. (2004). Reactive transport modeling of column experiments for remediation of acid mine drainage. *Environmental Science and Technology*, 38(11): 3131-3138.

Bagley, D.M., and Brodkorb, T.S. (1999). Modeling microbial kinetics in an anaerobic sequencing batch reactor-model development and experimental validation. *Water Environment Research*, 71(7): 1320-1332.

Batstone, D.J., Keller, J., Angelidaki, I., Kalyuzhnyi, S., Pavlostathis, S., Rozzi, A., Sanders, W., Siegrist, H., and Vavilin, V.A. (2002). The IWA anaerobic digestion model No. 1 (ADM1). *Water Science and Technology*, 45(10): 65-73.

Batstone, D.J., Keller, J., Newell, R., and Newland, M. (2000). Modeling anaerobic degradation of complex wastewater: I model development. *Bioresource Technology*, 75(1): 67-74.

Bechard, G., Yamazaki, H., Gould, W.D., and Bedard, P. (1994). Use of cellulosic substrates for the microbial treatment of acid mine drainage. *Journal of Environmental Quality*, 23(1): 111-116.

Benner, S.G, Blowes, D.W., Ptacek, C.J., and Mayer, K.U. (2002). Rates of sulfate reduction and metal sulfide precipitation in a permeable reactive barrier. *Applied Geochemistry*, 17(1): 301-320.

Benner, S.G., Blowes, D.W., Gould, W.D., Herbert, R.B. and C. J. Ptacek (1999). Geochemistry of a permeable reactive barrier for metals and acid mine drainage, *Environmental Science and Technology*, 33(16): 2793-2799.

Benner, S.G., Gould, W.D. and D.W. Blowes (2000). Microbial populations associated with the generations and treatment of acid mine drainage, *Chemical Geology*, 169(3-4): 435-448.

Boudreau, B.P., and Westrich, J.T. (1984). The dependence of bacterial sulfate reduction on sulfate concentration in marine environments. *Geochimica et Cosmochimica Acta*, 48(12): 2503-2516.

Chang, I.S., Shin, P.K., and Kim, B.H. (2000). Biological treatment of acid mine drainage under sulphate-reducing conditions with solid waste materials as substrates. *Water Research*, 34(4):1269-1277.

Chapra, S.C., and Canale, R.P. (2002). Numerical Methods for Engineers, 4th Edition, McGraw-Hill, New York, NY.

Chynoweth, D.P., and Pullammanappallil, P. (1996). Anaerobic digestion of municipal solid waste. *Microbiology of Solid Waste*, A. Palmasano and M.A. Barlaz, eds.,CRC Press, Boca Raton, FL, 77-113.

Chynoweth, D.P., and Pullammanappallil, P. (1996). Anaerobic digestion of municipal solid waste. *Microbiology of Solid Waste*, A. Palmasano and M.A. Barlaz, eds.,CRC Press, Boca Raton, FL, 77-113.

Cleary, R.W., and Adrian, D.D. (1973). Analytical solution of the convective-dispersive equation for cation adsorption in soils. *Soil Science Society of America Journal*, 37(2): 197-199.

Clement, T.P. (1997). A Modular Computer Code for Simulating Reactive Multi-species Transport in 3-Dimensional Groundwater Systems RT3D version 1.0. U.S. Department of Energy and Pacific Northwest National Laboratory. PNNL-11720-1997.

Clement, T.P. (2003). RT3D v.2.5 Update Document, What is New in RT3D version 2.5. Electronic document: http://bioprocess.pnl.gov/rt3d.htm.

Contois, D.E. (1959). Kinetics of bacterial growth, relationship between population density and specific growth rate of continuous cultures. *Journal of General Microbiology*, 21(1): 40-50.

Drury, J.W. (2000). Modeling of sulfate reduction in anaerobic solid substrate bioreactors for mine drainage treatment. *Mine Water and the Environment*, 19(1):18-28.

Dvorak, D.H., Hedin, R.S., Edenborn, H.M., and McIntire, P.E. (1992). Treatment of metal-contaminated water using bacterial sulfate reduction: results from pilot-scale reactors. *Biotechnology and Bioengineering*, 40(5):609-616.

Fan, L.T., Gharpuray, M.M, and Lee, Y.H. (1987). Cellulose Hydrolysis. Springer-Verlag, Berlin, Germany.

Fenchel, T., and Harrison, P. (1976). The significance of bacterial grazing and mineral cycling for the decomposition of particulate detritus. *The Role of Terrestrial and Aquatic Organisms in Decomposition Processes*, J.M. Anderson and A. Macfadyen, eds., Blackwell Scientific Publications, Oxford, UK, 285-299.

Gobla, M.J. (2002). A rapid response to cleanup – Gilt Edge Superfund site, South Dakota. *Proceedings of the 9th International Conference on Tailings and Mine Waste*, 27-30 January, Fort Collins, CO, A. A. Balkema, Lisse, The Netherlands, 421-425.

Groudev, S., Nicolova, M., Spasova, I., and Schutte, R. (2003). Treatment of waters from a copper mine by means of a permeable reactive barrier. *Fifty Years of the University of Mining and Geology "St. Ivan Rilski"*, University of Mining and Geology, Sofia (Bulgaria), Volume 46, Part II, Section Mining and Mineral Processing, 229-231.

Gujer, W., and Zehnder, A.J. (1983). Conversion processes in anaerobic digestion. *Water Science and Technology*, 15(8-9): 127-167.

Gujer, W., Henze, M., Mino, T., Matsuo, T., Wentzel, M., and Maraist, G. (1995). The activated sludge model No. 2: biological phosphorous removal. *Water Science and Technology*, 31(2): 1-11.

Hammack, R.W., and Edenborn, H.M. (1992). The removal of nickel from mine waters using bacterial sulfate reduction. *Applied Microbiology and Biotechnology*, 37(5): 674-678.

Hammack, R.W., Edenborn, H.M., and Dvorak, D.H. (1994). Treatment of water from an open pit copper mine using biogenic sulfide and limestone: a feasibility study. *Water*

Resources, 28(11): 2321-2329.

Harbaugh, A.W., Banta, E.R., Hill, M.C., and McDonald, M.G. (2000). *MODFLOW-2000, the U.S. Geological Survey Modular Ground-Water Model – User Guide to Modularization Concepts and the Ground-Water Flow Process*, USGS Open-File Report 00-92, Reston (VA).

Henriksen, T.M., and Breland, T.A. (2002). Carbon mineralization, fungal and bacterial growth, and enzyme activities as affected by contact between crop residues and soil. *Biology and Fertilization of Soils*, 35(1): 41-48.

Hsieh, P.A., and Winston, R.B. (2002). User's Guide to Model Viewer, a Program for Three-Dimensional Visualization of Ground-Water Model Results. U.S. Geological Survey. Open-File Report 02-106, Menlo Park (CA).

Hulshof, A.H., Blowes, D.W., Ptacek, C.J., and Gould, W.D. (2003). Microbial and nutrient investigations into the use of in situ layers for treatment of tailings effluent. *Environmental Science and Technology*, 37(21): 5027-5033.

Humphrey, A. E. (1979). The Hydrolysis of Cellulosic Materials to Useful Products. *Hydrolysis of Cellulose: Mechanisms of Enzymatic and Acid Catalysis*, Chapter 2, Advances in Chemistry Series, No. 181, American Chemical Society, Washington D.C., 25-53.

Ingvorsen, K., Zehnder, A. J., and Jorgensen, B. (1984). Kinetics of sulfate uptake by *Desulfobacter postgatei*. *Applied and Environmental Microbiology*, 47(2):403-408.

Jain, S., Lala, A., Bhatia, S., and Kudchadker, A. (1992). Modeling of hydrolysis controlled anaerobic digestion. *Journal of Chemical Technology and Biotechnology*, 53(4) 337-344.

Janssen, B.H. (1984). A simple method for calculating decomposition and accumulation of young soil organic matter. *Plant and Soil*, 76(1-3):297-304.

Jong, T., and Parry, D.L. (2003). Removal of sulfate and heavy metals by sulfate reducing bacteria in short-term bench scale upflow anaerobic packed bed reactor runs. *Water Research*, 37(14): 3379-3389.

Kalyuzhnyi, S., Fedorovish, V, Lens, P., Hulshoff Pol, L., and Lettinga, G. (1998). Mathematical modeling as a tool to study population dynamics between sulfate reducing and methanogenic bacteria. *Biodegradation*, 9:187-199.

Kim, S.D., Kilbane, J.J., and Cha, D.K. (1999). Prevention of acid mine drainage by sulfate reducing bacteria: organic substrate addition to mine waste piles. *Environmental Engineering Science*, 16(2):139-145.

Konishi, Y., Yoshida, N., and Asai, S. (1996). Desorption of hydrogen sulfide during batch growth of the sulfate-reducing bacterium *Desulfovibrio desulfuricans*. *Biotechnology Progress*, 12(3):322-330.

Lai, T.E., and Pullammanappallil, P. (1998). A mathematical model for hydrolysis of cellulosic substrate. *Second Asia-Pacific Conference on Sustainable Energy and Environmental Technologies*, G.Q. Lu, V. Rudolph, and P.F. Greenfield, eds., University of Queensland Press, Brisbane, Australia, 175-182.

Lai, T.E., Nopharatana, A., Pullammanappallil, P., Clarke, W. (2001). Cellulolytic activity in leachate during leach-bed anaerobic digestion of municipal solid waste. *Bioresource Technology*, 80(3) 205-210.

Langmuir, D. (1997). Aqueous Environmental Geochemistry. Prentice-Hall, Upper Saddle River, NJ.

Lawrence, A.W., and McCarty, P.L. (1969). Kinetics of methane fermentation in anaerobic treatment. *Journal of Water Pollution Control Federation*, 41(2): 1-17.

Li, L., Benson, C.H., and Lawson, E.M. (2005). Impact of mineral fouling on hydraulic behavior of permeable reactive barriers. *Ground Water*, 43(4): 582-596.

Logan, M., Ahamann, D., and Figueroa, L. (2003). Assessment of microbial activity in anaerobic columns treating synthetic mine drainage. *Proceedings of the 2003 Annual Meeting of the American Society for Mining and Reclamation,* 3-6 June, Billings, MT, American Society for Mining and Reclamation, Lexington, KY, 658-678.

Lovley, D.R., and Klug, M.J. (1986). Model for the distribution of sulfate reduction and methanogenesis in freshwater sediments. *Geochimica et Cosmochimica Acta*, 50(1):11-18.

Ludwig, R.D., McGregor, R.G., Blowes, D.W., Benner, S.G. and K. Mountjoy (2002). A permeable reactive barrier for treatment of heavy metals, *Ground Water*, 40(1): 59-66.

Lynd, L., Weimer, P., van Zyl, W., and Pretorius, I. (2002). Microbial cellulose utilization: fundamentals and biotechnology. *Microbiology and Molecular Biology Reviews*, 66(3): 506-577.

Mayer, K.U., Frind, E.O, and Blowes, D.W. (2002). Multicomponent reactive transport modeling in variably saturated porous media using a generalized formulation for kinetically controlled reactions. *Water Resources Research*, 38(9):13-1 to 13-21.

McDonald, M.G., and Harbaugh, A.W. (1988). A Modular Three-Dimensional Finite-Difference Ground-Water Flow Model. U.S. Geological Survey Techniques of Water-Resources Investigations, Book 6 (Modeling Techniques), Chapter A1.

McGregor, R., Blowes, D., Ludwig, R., Pringle, E., and Pomery, M. (1999). Remediation

of a heavy metal plume using a reactive wall. *Bioremediation of Metals and Inorganic Compounds,* A. Leeson and B. Alleman, B, eds., *5th International In Situ and On-Site Bioremediation Symposium,* San Diego, CA, Battelle Press, Columbus, OH, 19-24.

Micales, J.A., and Skog, K.E. (1997). The decomposition of forest products in landfills. *Intermational Biodeterioration and Biodegradation*, 39(2-3): 145-158.

Middelburg, J.J. (1989). A simple rate model for organic matter decomposition in marine sediments. *Geochimica et Cosmochimica Acta*, 53(7):1577-1581.

Middleton, A.C., and Lawrence, A.W. (1977). Kinetics of microbial sulfate reduction. *Journal of Water Pollution Control Federation*, 49(7):1659-1670.

Monod, J. (1949). The growth of bacterial cultures. *Annual Review of Microbiology*, 3:371-394.

Morel, F.M.M., and Hering, J.G. (1993). Principles and Applications of Aquatic Chemistry. John Wiley and Sons, New York, NY.

Morshed, J., and Kaluarachchi, J. J. (1995). Critical assessment of the operator-splitting technique in solving the advection-dispersion-reaction equation: Monod kinetics and coupled transport. *Advances in Water Research*, 18(2): 101-110.

MSE Technology Applications (2002). *Final Report-Sulfate Reducing Bacteria Reactive Wall Demonstration.* Mine Waste Technology Program, Activity III, Project 12, U.S. Environmental Protection Agency and U.S. Department of Energy, MWTP-206.

Negri, E.D., Mata-Alvarez, J., Sans, C., and Cecchi, F. (1992). A mathematical model of volatile fatty acids production in a plug flow reactor treating the organic fraction of municipal solid waste. *Proceedings of the International Symposium on Anaerobic Digestion of Solid Waste, Venice*, 14-17 April, Stamperia de Venezia, Venice (Italy),

256-268.

Odencrantz, J.E., Valocchi, A.J., and Rittmann, B.E. (1990). Modeling two-dimensional solute transport with different biodegradation kinetics. Proceedings of Petroleum Hydrocarbons and Organic Chemicals in Ground Water. October 31st to November 2nd 1990, Houston (TX).

Ogata, A., and Banks, R.B. (1961). A solution of the differential equation of longitudinal dispersion in porous media. *U.S. Geological Survey Prof. Paper 411-A*, U.S. Geological Survey, Washington, D.C.

Okabe, S., and Characklis, W.G. (1992). Effects of temperature and phosphorous concentration on microbial sulfate reduction by *Desulfovibrio desulfuricans*. *Biotechnology and Bioengineering*, 39(10):1031-1042.

Okabe, S., Nielsen, P.H., and Characklis, W.G. (1992). Factors affecting microbial sulfate reduction by *Desulfovibrio desulfuricans* in continuous culture: limiting nutrients and sulfide concentration. *Biotechnology and Bioengineering*, 40(6):725-734.

Okane, S., Nielsen, P.H., Jones, W.L., and Characklis, W.G. (1995). Rate and stoichiometry of microbial sulfate reduction by *Desulfovibrio desulfuricans* in biofilms. *Biofouling*, 9(1):63-83.

Omil, F., Lens, P., Visser, A., Hulshoff Pol, L.W., and Lettinga, G. (1998). Long-term competition between sulfate reducing and methanogenic bacteria in UASB reactors treating volatile fatty acids. *Biotechnology and Bioengineering*, 57(6):676-685.

Owens, J.M., and Chynoweth, D.P. (1993). Biochemical methane potential of municipal solid waste (MSW) components. *Water Science and Technology*, 27(2): 1-14.

Postgate, J.R. (1984). *The Sulphate-Reducing Bacteria.* 2nd Edition. Cambridge

University Press, Cambridge (UK).

Prasad, D., Wai, M., Berube, P., and Henry, J.G. (1999). Evaluating substrates in the biological treatment of acid mine drainage. *Environmental Technology*, 20(5): 449-458.

Prommer, H., Barry, D.A., Chiang, W.H., and Zheng, C. (2001). PHT3D – a MODFLOW/MT3DMS-based reactive multi-component transport model. *MODFLOW 2001 and Other Modeling Odysseys*, H. Seo, E. Poeter, and C. Zheng, eds., International Ground-Water Modeling Center, Colorado School of Mines, Golden, CO, 477-483.

Rifai, H.S., and Bedient, P.B. (1990). Comparison of biodegradation kinetics with an instantaneous reaction model for groundwater. *Water Resources Research*, 26(4): 637-645.

Rittman, B.E., and McCarty, P.L. (2001). *Environmental Biotechnology: Principles and Applications*. McGraw-Hill, NewYork, NY.

Rowell, R.M. (1997). Composites from agri-based resources. *The Use of Recycled Wood and Paper in Building Applications*, Forest Products Society, Proceedings No. 7286, Madison, WI, 217-222.

Schafer, D., Schafer, W., and Kinzelbach, W. (1998a). Simulation of reactive processes related to biodegradation in aquifers. 1-structure of the three-dimensional reactive transport model. *Journal of Contaminant Hydrology*, 31(1-2): 167-186.

Schafer, D., Schafer, W., and Kinzelbach, W. (1998b). Simulation of reactive processes related to biodegradation in aquifers. 2-model application to a column study on organic carbon degradation. *Journal of Contaminant Hydrology*, 31(1-2): 187-209.

Schönheit, P., Krisjansson, J. K., and Thauer, R. K. (1982). Kinetic mechanism for the ability of sulfate reducers to out-compete methanogens for acetate. *Archives of Microbiology*, 132(3):285-288.

Shackelford, C. D. (1995). Analytical models for cumulative mass column testing, *Geoenvironment 2000.* ASCE Geotechnical Special Publication No. 46, Y. B. Acar and D. E. Daniel, eds., ASCE, Reston, VA, 355-372.

Speece, R.E. (1996). Anaerobic Biotechnology for Industrial Wastewaters. Archae Press, Nashville (TN).

Stephens, G.R., and Heichel, G.H. (1975). Agricultural and forest products as sources of cellulose. *Cellulose as a Chemical and Energy Resource*, C.R. Wilke, ed., *Cellulose Conference*, Berkeley, CA, John Wiley and Sons, New York, NY, 27-42.

Sylvia, D.M., Fuhmann, J.J., Hartel, P.G., and Zuberer, D.A. (1998). Principles and Applications of Soil Microbiology. Prentice Hall. Upper Saddle River, New Jersey (NJ).

Thombre, M.S., Thomson, B.M., and Barton, L.L. (1997). Use of a permeable biological reaction barrier for groundwater remediation at a uranium mill tailings remedial action site, *International Containment Technology Conference,* 9-12 February, St. Petersburg, FL, U.S. Department of Energy and Florida State University Institute for International Cooperative Environmental Research, Tallahassee, FL, 744-750.

Tuttle, J.H., Dugan, P.R., and Randles, C.I. (1969). Microbial sulfate reduction and its potential utility as an acid mine water pollution abatement procedure. *Applied Microbiology*, 17(2):297-302.

US EPA (1998). *Permeable Reactive Barrier Technologies for Containment*

Remediation. EPA/600/R-98/125. Washington DD. September 1998.

Valocchi, A., and Malmstead, M. (1992). Accuracy of operator splitting for advection-dispersion-reaction problems. *Water Resources Research*, 28(5): 1471-1476.

Valsaraj, K.T. (2000). Elements of Environmental Engineering – Thermodynamics and Kinetics. 2nd Edition, Lewis Publishers, Boca Raton, FL.

Vasiliev, V.B., Vavilin, V.A., Rytov, S.V., and Ponomarev, A.V. (1993). Simulation model of anaerobic digestion of organic matter by a microorganism consortium: basic equations. *Water Resources*, 20(6): 714-725.

Vavilin, V.A., Lokshima, L., Jokela, J., and Rintala, J. (2004). Modeling solid waste decomposition. *Bioresource Technology*, 94(1): 69-81.

Vavilin, V.A., Rytov, S., Lokshima, L., Pavlostathis, S., and Barlaz, M. (2003). Distributed model of solid waste anaerobic digestion-effects of leachate recirculation and pH adjustment. *Biotechnology and Bioengineering*, 81(1): 66-73.

Vavilin, V.A., Rytov, S., Lokshina, L., Rintala, J., and Lyberatos, G. (2001). Simplified hydrolysis models for the optimal design of two-stage anaerobic digestion. *Water Research*, 35(17): 4247-4251.

Vavilin, V.A., Rytov, S.V., and Lokshina, L. (1996). A description of hydrolysis kinetics in anaerobic degradation of particulate organic matter. *Bioresource Technology*, 56(1): 229-237.

Wakao, N., Takahashi, T., Sakurai, Y., and Shiota, H. (1979). A treatment of acid mine water using sulfate-reducing bacteria. *Journal of Fermentation Technology*, 57(5): 445-452.

Waybrant, K.R., Blowes, D.W., and Ptacek, C.J. (1998). Selection of reactive mixtures

for use in permeable reactive walls for treatment of mine drainage. *Environmental Science and Technology*, 32(13):1972-1979.

Waybrant, K.R., Ptacek, C.J., and Blowes, D.W. (2002). Treatment of mine drainage using permeable reactive barriers: column experiments. *Environmental Science and Technology*, 36(6): 1349-1356.

Westrich, J.T., and Berner, R.A. (1984). The role of sedimentary organic matter in bacterial sulfate reduction: the G model tested. *Journal of Limnology and Oceanography*, 29(2): 236-249.

Wheeler, M.F., Dawson, C.N., Bedient, P.B., Chiang, C.Y., Borden, R.C., and Rifai, H.S. (1987). Numerical simulation of microbial biodegradation of hydrocarbons in ground water. *Conference on Solving Groundwater Problems with Models*, February 1987, Denver (CO).

Widdel, F. (1988). Microbiology and ecology of sulfate reducing bacteria., *Biology of Anaerobic Microorganisms*. Chapter 10, A. J. B. Zehnder, ed. Wiley Interscience, New York, NY, 469-585.

Zheng, C. (1990). MT3D: *A Modular Three-Dimensional Transport Model for Simulation of Advection, Dispersion and Chemical Reaction of Contaminants in Groundwater Systems*. U.S. Environmental Protection Agency and Robert S. Kerr Environmental Research Laboratory, Ada (OK).

Zheng, C., and Wang, P.P. (1999). MT3DMS: *A Modular Three-Dimensional Multispecies Model for Simulation of Advection, Dispersion, and Chemical Reactions of Contaminants in Groundwater Systems; Documentation and User's Guide*. U.S. Army Corps of Engineers. Contract Report SERDP-99-1, December 1999.

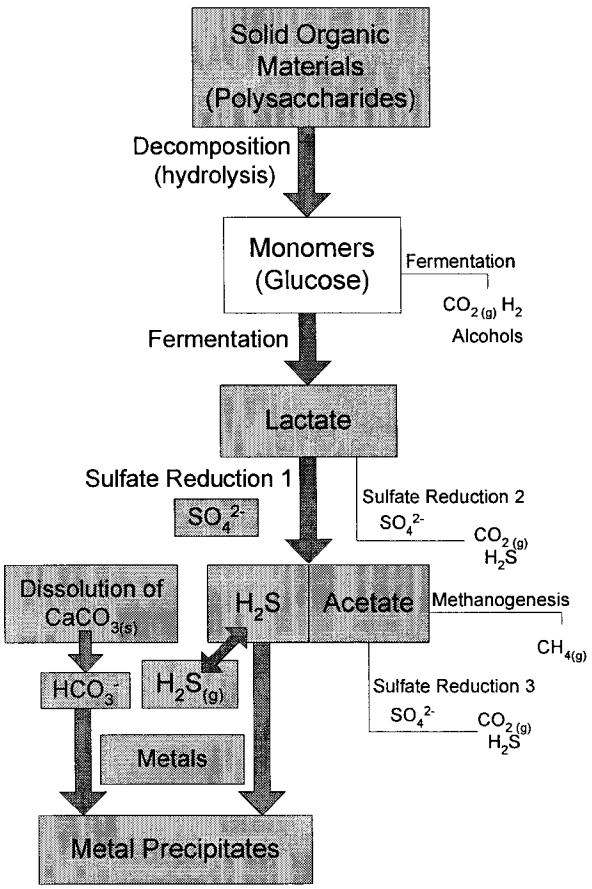

Figure 2.1 – Flowchart of primary and secondary biochemical processes in the mathematical model.

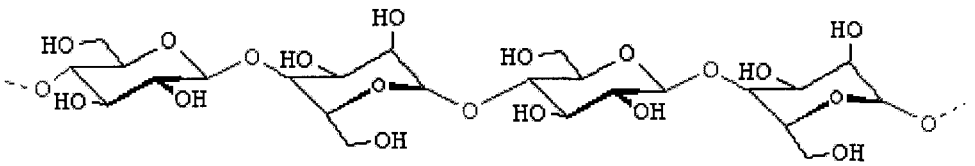

Figure 2.2 – Structure of cellulose fibril (Note: an atom of carbon is located at each intersection of lines) (Fan et al. 1987).

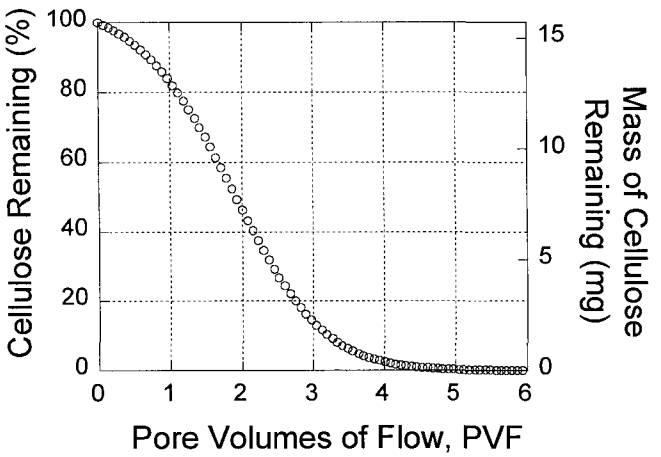

Figure 2.3 – Simulated percentage of initial cellulose, and cellulose mass, remaining in the column versus pore volumes of flow.

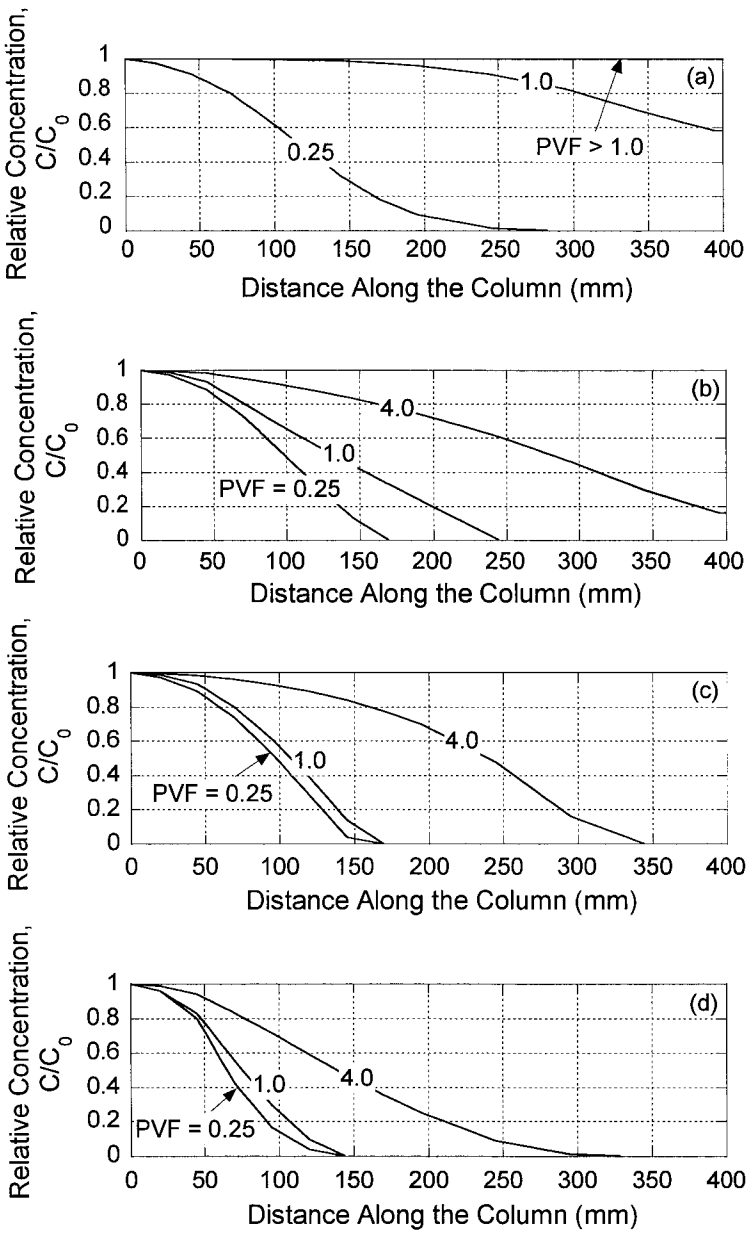

Figure 2.4 – Simulated concentrations along the column length for (a) non reactive transport, and for the reactive transport of (b) sulfate, (c) ferrous iron, and (d) zinc (PVF = pore volumes of flow).

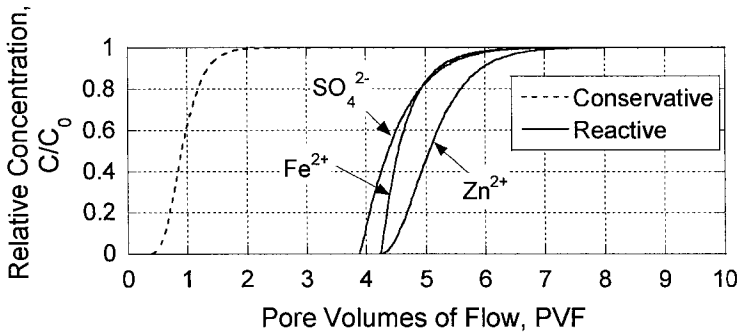

Figure 2.5 – Simulated effluent concentrations versus pore volumes of flow.

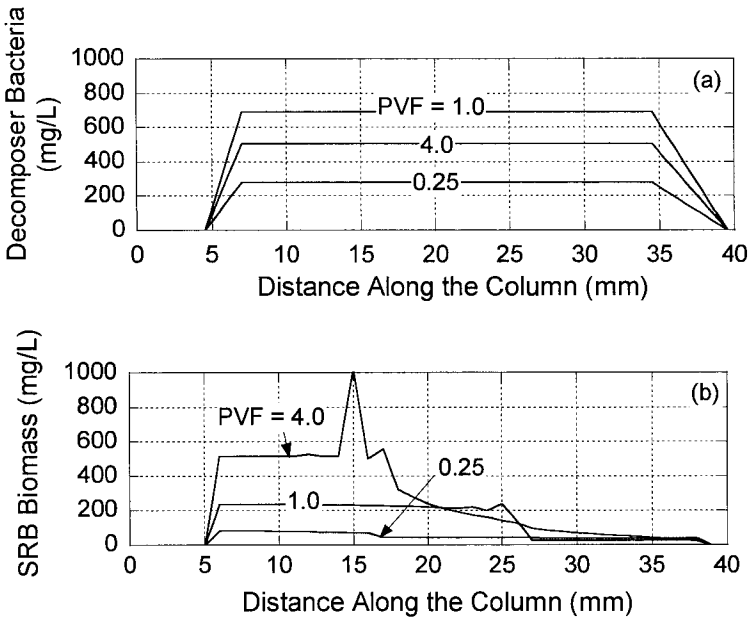

Figure 2.6 – Simulated equivalent biomass concentrations along the column length, (a) cellulose decomposer bacteria, and (b) sulfate reducing bacteria (PVF = pore volumes of flow).

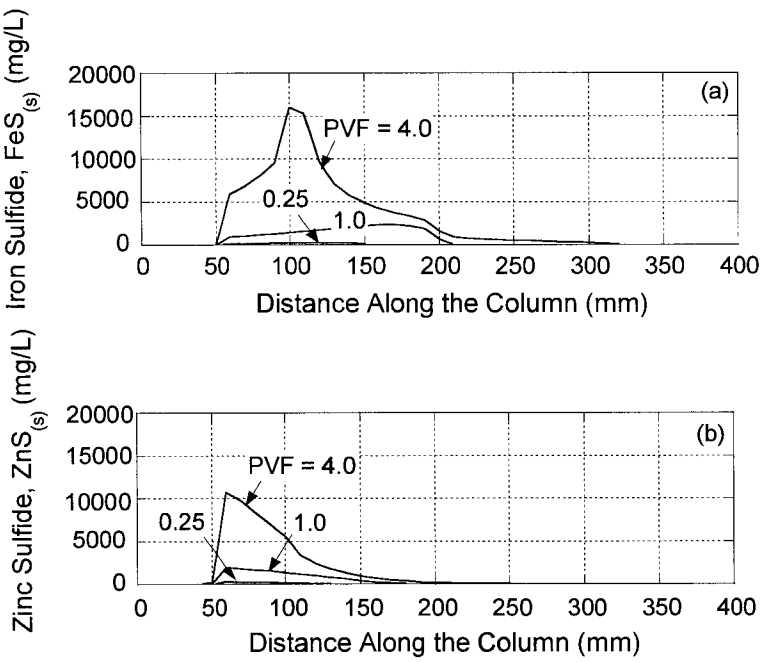

Figure 2.7 – Simulated precipitate concentrations along the column length, (a) $FeS_{(s)}$, and (b) $ZnS_{(s)}$ (PVF = column pore volumes of flow).

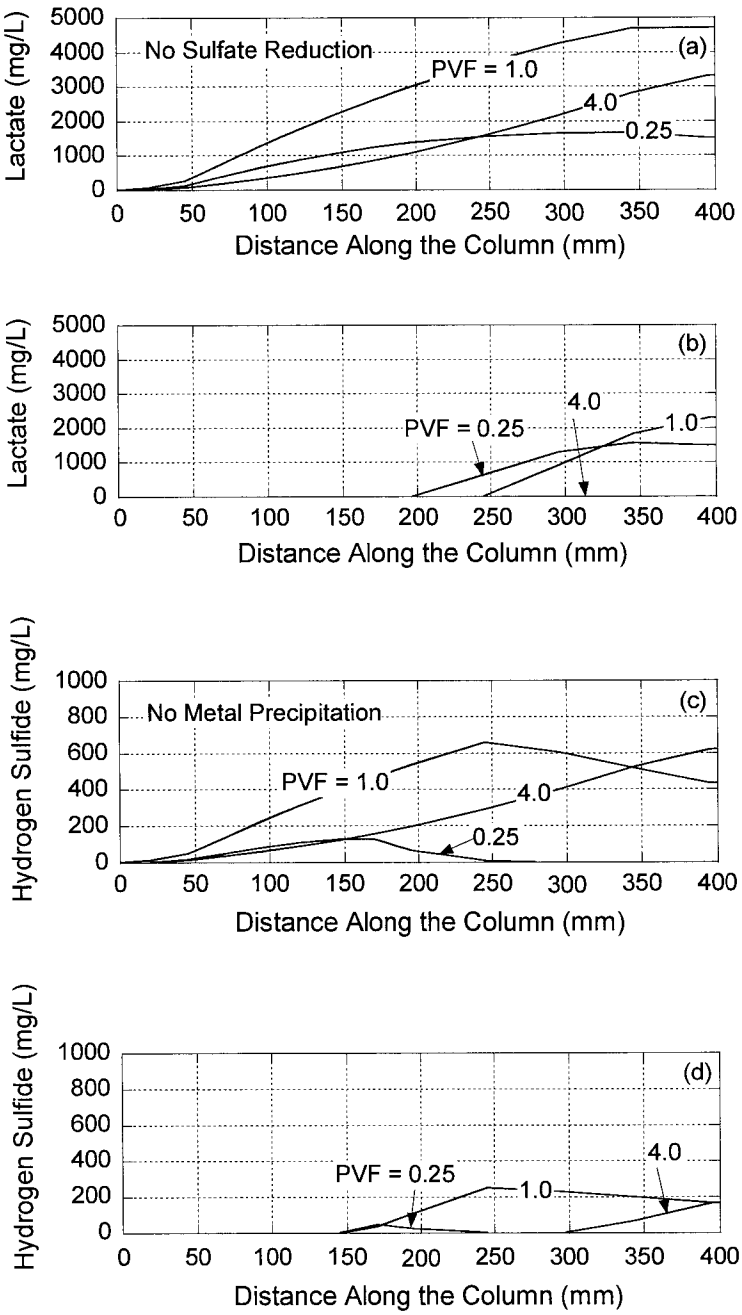

Figure 2.8 – Simulated concentrations along the column length, (a) lactate with no sulfate reduction, (b) lactate, (c) hydrogen sulfide with no metal precipitation, and (d) hydrogen sulfide (PVF = pore volumes of flow).

CHAPTER 3

MODELING THE INFLUENCE OF DECOMPOSING ORGANIC SOLIDS ON SULFATE REDUCTION RATES FOR IRON PRECIPITATION

ABSTRACT: The influence of decomposing organic solids on sulfate (SO_4^{2-}) reduction rates for metals precipitation in sulfate-reducing systems, such as in bioreactors and permeable reactive barriers for treatment of acid mine drainage, is modeled. The results are evaluated by comparing the model simulations with published experimental data for two single-substrate and two multiple-substrate batch equilibrium experiments. The comparisons are based on the temporal trends in SO_4^{2-}, ferrous iron (Fe^{2+}), and hydrogen sulfide (H_2S) concentrations, as well as on rates of sulfate reduction. The temporal behaviors of organic solid materials, dissolved organic substrates, and different bacterial populations also are simulated. The simulated results using Contois kinetics for polysaccharide decomposition, Monod kinetics for lactate-based sulfate reduction, instantaneous or kinetically controlled precipitation of ferrous iron mono-sulfide ($FeS_{(s)}$), and partial volatilization of H_2S to the gas phase compare favorably with the experimental data. When Contois kinetics of polysaccharide decomposition is replaced by first-order kinetics to simulate one of the single-substrate batch experiments, a comparatively poorer approximation of the rates of sulfate reduction is obtained. The effect of sewage sludge in boosting the short-term rate of sulfate reduction in one of the multiple-substrate experiments also is approximated reasonably well. The results illustrate the importance of the type of kinetics used to describe the decomposition of

organic solids on metals precipitation in sulfate-reducing systems, as well as the potential application of the model as a predictive tool for assisting in the design of similar biochemical systems.

Key Words: Cellulose decomposition, Decomposition kinetics, Metals precipitation, Polysaccharide decomposition, Solid organic materials, Sulfate reduction.

3.1 INTRODUCTION

A number of laboratory experiments have demonstrated remediation of acid mine drainage (AMD) based on sulfate (SO_4^{2-}) reduction and metal-sulfide precipitation. Examples of the solid, decomposable organic materials that have been evaluated for this purpose include sawdust (e.g., Tuttle et al. 1969, Wakao et al. 1979), spent mushroom compost (e.g., Dvorak et al. 1992, Hammack and Edenborn 1992), fresh alfalfa (e.g., Bechard et al. 1994), whey/cow manure (e.g., Christensen et al. 1996), alfalfa hay/sawdust/cellulose (Thombre et al. 1997), alfalfa/sawdust/manure (e.g., Gilbert et al. 1999), leaf compost/sewage sludge (e.g., Prasad et al. 1999), spent mushroom compost/oak chips/wastepaper sludge (e.g., Chang et al. 2000), leaf compost/sawdust/wood chips/sewage sludge (e.g., Waybrant et al. 1998, Waybrant et al. 2002), leaf compost/wood chips/poultry manure (e.g., Cocos et al. 2002), wood chips/pulp and paper waste (Hulshof et al. 2003), walnut wood shavings/cattle manure/alfalfa (e.g., Logan et al. 2003), and wheat straw (Frommichen et al. 2003), among others. In some cases, organic solid materials have been amended with dissolved organic substrates such as ethanol or sucrose (e.g., Bechard et al. 1994, Thombre et al. 1997, Frommichen et al. 2003).

Several studies involving field applications of sulfate reducing (SR) systems for AMD remediation in the form of permeable reactive barriers (PRBs) and bioreactors also have been reported (Hammack et al. 1994, Benner et al. 1999, Benner et al. 2000, Blowes et al. 2000, Steed et al. 2000, Ludwig et al. 2002, Groudev et al. 2003). For example, an SR-PRB containing 50 % gravel, 20 % municipal compost, 20 % leaf mulch, 9 % wood chips, and 1 % limestone, all by volume, was constructed in 1995 at the Nickel Rim mine

in Ontario, Canada (Benner et al. 1999, Benner et al. 2000), and, after three years of operation, SO_4^{2-} removal declined by ~ 30% and Fe^{2+} removal declined by ~ 50%. Also, an SR-PRB containing leaf detritus, spent mushroom compost, cow manure, and sawdust was constructed in 1997 in central Bulgaria, intercepting the discharge from a former copper mine, and removing high concentrations of copper, cadmium, iron, and arsenic from the AMD effluents (Groudev et al. 2003).

With respect to mathematical modeling of the rate of SO_4^{2-} reduction in SR systems, Bourdeau and Westrich (1984) and Westrich and Berner (1984) considered aerobic degradation of seawater plankton as a precursor to SO_4^{2-} reduction in marine environments, suggesting first-order kinetics with respect to carbon as a model for the rates of plankton degradation and SO_4^{2-} reduction, the latter also including a hyperbolic term to account for SO_4^{2-} limitation. Drury (2000) developed a model that assumes the rate of SO_4^{2-} reduction in anaerobic solid-substrate bioreactors to be proportional to the rate of decomposition of biodegradable solid waste materials (e.g., manure, compost, wood chips) initially added to the bioreactor (without replenishment of organic carbon). Drury (2000), modeled the degradation of solid organic materials using first-order kinetics with a declining rate coefficient (Janssen 1984, Middelburg 1989) and empirically equated the rate of SO_4^{2-} reduction to conversion factors multiplied by the rate of solids decomposition and by the concentration of SO_4^{2-}. However, neither Bourdeau and Westrich (1984) nor Drury (2000) considered the possibility of Monod kinetics (Monod 1959) for SO_4^{2-} reduction, the dynamics of bacterial populations (i.e., decomposers and SR bacteria, SRB), or the effects of bacterial growth and decay. Dissolved organic electron donors existing as the products of hydrolysis/fermentation

reactions and utilizable as SRB substrates (Gujer and Zehnder 1983, Chynoweth and Pullammanappallil 1996) also were not considered.

Mayer et al. (2002) describe the conceptual framework of a reactive transport model that includes kinetically controlled pyrrhotite oxidation by O_2 and Fe^{3+}, transport of AMD species impacted by equilibrium with a number of aluminosilicate and carbonate minerals, as well as the sulfate mineral gypsum, and remediation based in part on kinetically-controlled SO_4^{2-} reduction, although the kinetic equations for SO_4^{2-} reduction and substrate consumption were not provided. However, the model proposed by Mayer et al. (2002) does not handle bacterial populations (e.g., decomposers and SRB) or the effects of bacterial growth and decay. The model also does not consider kinetic expressions for decomposition of solid organic materials or the kinetics of dissolved organic substrates required for SO_4^{2-} reduction.

Prommer et al. (2001) describe a reactive transport model based on MODFLOW (Harbaugh et al. 2000), MT3DMS (Zheng and Wang 1999), and the equilibrium geochemical model PHREEQC-2 (Parkhurst and Appelo 1999) that can handle both equilibrium and kinetically controlled reactions. An application of the model involving treatment of AMD containing SO_4^{2-} and Zn^{2+} is described, whereby the rate of SO_4^{2-} reduction is modeled considering Monod kinetics and including bacterial growth and decay, although the actual kinetic expressions are not given. However, the model does not consider solid decomposable organic materials, and the application is based on an injected treatment zone created by injection wells in which a dissolved organic substance (ethanol) is introduced in the subsurface to promote the growth of SRB, H_2S production, and precipitation of $ZnS_{(s)}$.

Benner et al. (2002) and Amos et al. (2004) describe a simplified model for the rate of SO_4^{2-} reduction for AMD remediation in which a constant rate of SO_4^{2-} reduction is multiplied by a hyperbolic term that accounts for SO_4^{2-} limitation (Boudreau and Westrich 1984). This model does not consider the bacterial population (i.e., neglects the effects of bacterial growth and decay), and the SO_4^{2-} reduction rate in the model is assumed to be constant with a reduction rate that is based on *a priori* fitting to measured sulfate data, e.g., from the effluent of a column test (Amos et al. 2004). This proposed approach is empirical and potentially oversimplifies SO_4^{2-} reduction, since the rate of SO_4^{2-} reduction typically is limited by the concentration of dissolved organic electron donors/SRB substrates associated with solid decomposition and also is linked to the growth of the SRB population (e.g., Boudreau and Westrich 1984, Westrich and Berner 1984, Dvorak et al. 1992, Bechard et al. 1994, Drury 2000, Chang et al. 2000, Logan et al. 2003).

The objective of this study is to model the influence of decomposing organic solids on SO_4^{2-} reduction rates for the purpose of describing the precipitation of iron in SR systems. The simulated results are obtained using a new mathematical model in which SO_4^{2-} reduction kinetics are coupled to, and limited by, the decomposition of solid organic materials, and simultaneously combining meaningful biochemical processes not combined in any of the aforementioned models (Chapter 2). Experimental results taken from the literature are used as the basis for calibrating parameter values (initially taken from the literature) used in the simulations, and subsequently validating the ability of the model to describe the influence of decomposing organic solids on SO_4^{2-} reduction rates for ferrous iron (Fe^{2+}) precipitation.

3.2 SYSTEM ANALYSES

Simulated results for SO_4^{2-}, Fe^{2+}, and H_2S in solution are compared with experimental results for the same species based on four batch-test experiments reported by Waybrant et al. (1998) performed at room temperature, which is assumed as 25 °C. The experimental results are derived from two single-substrate (i.e., one containing delignified waste cellulose, and one containing composted leaf mulch compost) and two multiple-substrate (i.e., one containing leaf mulch/sawdust, and one containing leaf mulch/sawdust/wood chips/sewage sludge) batch tests (Fig. 3.1). Simulations of solid decomposable organic materials, dissolved organic substrates, and different populations of bacteria also are included but are not compared with experimental results since no such results were reported. The solid phases consisting of the decomposable polysaccharide and the bacterial populations are assumed uniformly dispersed in the liquid phase (i.e., batch experiments are continuously mixed).

Although Zn^{2+} was present in some of the batch tests at initial concentrations of approximately 0.8 mg/L (i.e., ~ 0.1 %, mg/L basis, of those for Fe^{2+}), Zn^{2+} precipitation with H_2S was assumed to be negligible relative to that for Fe^{2+}. Also, although Ni^{2+} was present in some batch tests at initial concentrations of approximately 1.1 mg/L (i.e., ~ 0.1 %, mg/L basis, of those for Fe^{2+}), and $Cd^{2+}$and Pb^{2+} were spiked in some batch tests, the simulations of these metals are not considered because (i) no quantitative monitored data are provided for these elements, (ii) the reported initial concentrations are low relative to those for Fe^{2+}, and (iii) the life spans of these metals in the systems are only ~ 10 % of the total testing time. Finally, although Na^+, K^+, and Mg^{2+} were monitored in the

experiments, the temporal behaviors of these metals were not simulated because these metals are not included within the scope of the model used to perform the simulations.

Significant, abrupt declines in the concentrations for SO_4^{2-} and Fe^{2+} are reported in Waybrant et al. (1998), particularly in the case of Fe^{2+}, apparently at time equal to zero (i.e., immediately after the mixing of solids/batch solution). These abrupt declines in the concentrations for SO_4^{2-} and Fe^{2+} may be attributed to either (i) instantaneous SO_4^{2-} reduction based on a dissolved available substrate, and/or (ii) sorption to the solid organic materials. If lactate is taken as representative of the dissolved substrates, then different stoichiometric amounts of lactate would be required at time zero in order to justify the declines in both Fe^{2+} and SO_4^{2-} per batch test, suggesting that the presence of lactate at time zero cannot be used to explain both declines. For example, for the leaf mulch/sawdust batch test, the decline in Fe^{2+} is 507 mg/L, which would require 1720 mg/L lactate, whereas the decline in SO_4^{2-} is 400 mg/L, which would require 790 mg/L lactate. As a result, the simulations in this study focus on the longer-term behavior of SR systems based on the decomposition of solid substrates, and SO_4^{2-} reduction based on dissolved substrates possibly present at time zero is neglected.

With respect to sorption, Fe^{2+} is more likely than SO_4^{2-} to undergo instantaneous (and reversible) sorption to the negatively charged surfaces of organic materials (Sposito 1989). However, sorption was not evaluated by Waybrant et al. (1998) and similarly is not considered in this study. Thus, declines in Fe^{2+}concentrations that are presumably not related to SO_4^{2-} reduction and metal-sulfide precipitation are not considered in this study.

The initial pH of each batch mixture was reported in Waybrant et al. (1998) to range from 5.5 to 6.5, and the pH was maintained consistently within the range from 6.5

to 7.5 after the start of SO_4^{2-} reduction, which is compatible with the pH range of 6.0 to 8.0 assumed for speciation in the model. The SO_4^{2-} concentrations in the system are affected by gypsum ($CaSO_4 \cdot 2H_2O$) dissolution, since gypsum was added to the creek sediment in the tests. However, this process was not considered in the evaluation of SO_4^{2-} reduction rates in Waybrant et al. (1998) because the contribution of gypsum to the measured SO_4^{2-} concentrations could not be isolated. Therefore, this process also is not considered in the simulations performed in this study.

With respect to precipitation of Fe^{2+}, SO_4^{2-} reduction and precipitation of $FeS_{(s)}$ and $FeS_{0.9(s)}$ (mackinawite) was reported in Waybrant et al. (1998) to have controlled Fe^{2+} removal from the time when SO_4^{2-} reduction became active (~ 20 d) until Fe^{2+} depletion (~ 80 d). Geochemical modeling based on measured concentrations of Ca^{2+}, Fe^{2+}, HCO_3^-, and SO_4^{2-} reported in Waybrant et al. (1998) indicated a tendency for the solution to be under saturated with respect to calcite and over saturated with respect to gypsum and siderite ($FeCO_{3(s)}$) at earlier times (< 20 d). After ~ 20 d, this tendency reverts, and gypsum and siderite tend to dissolve and calcite ($CaCO_{3(s)}$) tends to precipitate. Before sulfate reduction was active (< ~ 20 d), an unknown amount of Fe^{2+} may have precipitated as $FeCO_{3(s)}$, but the geochemical modeling also suggests that Fe^{2+} would have returned to solution upon $FeCO_{3(s)}$ dissolution after ~ 20 d. The present simulations assume only $FeS_{(s)}$ as the sink for Fe^{2+}, and the validity of this assumption will be addressed by comparing simulated and experimental Fe^{2+} trends.

3.3 MODEL DESCRIPTION

The simulations are based on a conceptual model that includes (i) anaerobic decomposition of polysaccharides in solid organic materials due to the activity of decomposer bacteria and producing lactate, (ii) sulfate reduction based on the incomplete oxidation of lactate, (iii) instantaneous or kinetically controlled precipitation of heavy-metal mono-sulfides, and (iv) partial volatilization of H_2S to the gas phase. Verifications of mass balances and levels of numerical accuracy are provided at the end of this study. The explanation of the conceptual basis for the model, description of biochemical processes, kinetic and mass balance equations can be found in Chapter 2.

3.3.1. Initial Conditions and Parameter Values

The volume of batch solution, total dry mass of solids (inorganic and organic), equivalent concentration of solids (i.e., dry mass of solid material per liter of batch solution), percentage and composition of organic solids with respect to the total mass of solids (by dry mass), and estimated initial amounts of decomposable polysaccharides (by dry mass) are shown for each batch test in Table 3.1. The distinction between the amounts of total organic solids and anaerobically decomposable polysaccharides is important. The estimated initial amounts of decomposable polysaccharides in each batch test of 50 % (by dry mass) with respect to the total dry mass of leaf mulch, sawdust, and wood chips were based on representative percentages reported in the literature (Chapter 2). For delignified waste cellulose, the decomposable-cellulose content is expected to be closer to unity (e.g., 85 %). Waybrant et al. (1998) indicate that municipal sewage sludge has a carbon content that is significantly lower than the carbon content in cellulose, leaf mulch, sawdust, and wood chips (i.e., 0.093 g/g, by dry mass, vs. values ranging from

0.35 to 0.47 g/g). Thus, the content of decomposable organic solids of generic formula CH_2O in municipal sewage sludge can be assumed to be proportionally lower. The content of decomposable solids in municipal sewage sludge was estimated as 12 % on a dry mass basis.

The initial concentrations assumed for SO_4^{2-}, Fe^{2+}, H_2S, lactate ($C_3H_5O_3^-$) and acetate ($C_2H_3O_2^-$) for each batch test are shown in Table 3.2. Approximately 40 to 60 % (by dry mass), or < 15 % by volume, of anaerobic creek sediment was mixed with the solid materials in each batch experiment to serve as bacterial source or inoculating material (Waybrant et al. 1998).

The SRB that are incomplete oxidizers of lactate, such as *Desulfovibrio vulgaris,* are significantly more abundant than SRB that oxidize acetate or that are complete oxidizers of lactate (Widdel 1988, Chang et al. 2000). The equivalent biomass concentration (by dry mass) of SRB that are incomplete oxidizers of lactate when SO_4^{2-} reduction is active is estimated to range from 1 to 1000 mg biomass/L. This range is based on the abundance range of 10^7 to 10^9 cells/mL (Hulshof et al. 2003, Benner et al. 2002), considering 10^{-10} to 10^{-9} mg/cell by dry mass, i.e., cylindrical cells with approximately 2.35 μm of height and 0.75 μm of diameter (Postgate 1984). The intermediate value of 50 mg biomass/L generally was used in simulations, corresponding to an abundance range from 5×10^7 to 5×10^8 cells/mL.

The estimated range for the equivalent biomass concentration (by dry mass) of cellulolytic/hemicellulolytic decomposing bacteria colonizing the decomposable polysaccharides ranges from 0.1 to 10 mg biomass/g of dry polysaccharide, based on the cell coverage range of approximately 10^9 to 10^{10} cells/g of dry detritus, and considering

10^{-10} to 10^{-9} mg/cell by dry mass (e.g., Fenchel and Harrison 1976) report 5 x 10^{-10} mg/cell). The cell coverage is obtained from 2 to 15 cells/100 μm^2 of fiber of decomposable detritus (Fenchel and Harrison 1976, Henriksen and Breland 2002), assuming fibers of approximately 2 mm of diameter, 5 mm of length, and 3.0 mg/fiber. Values for the decomposer biomass concentration divided by the concentration of decomposable polysaccharide by dry mass, or $[X_d]/[CE]$, ranging from 2.75 x 10^{-3} to 1 x 10^{-2} were used for the simulations.

The parameter values used in different simulation cases for each batch test are shown in Table 3.3. In batch test 1, the first case (Case 1a, Table 3.3) corresponds to parameter values from Vavilin et al. (1996) for cellulose decomposition at 35 °C. Subsequent Cases 1b and 1c reflect the adjustment of these parameters to 25 °C. In the case of leaf mulch, sawdust, and wood chips, decomposition parameter values were adjusted and compared, and once the parameter values for a given material were adjusted in a batch test, the same parameter values were kept for that material in the other batch test simulations. For sewage sludge, decomposition parameter values from Vavilin et al. (1996) for 25 °C were used.

Parameter values for SO_4^{2-} reduction via Monod kinetics based on lactate were obtained from the literature (Chapter 2, and Okabe and Characklis 1992, Okabe et al. 1992, Konishi et al. 1996), and were maintained constant in the simulations in the present methodology, since the major emphasis in this study is placed on the effects of organic matter decomposition in SR systems. These parameter values included a maximum specific SRB growth rate, μ_{SRB}, of 4.0 d^{-1}, and half-saturation coefficients for lactate (K_V) and sulfate (K_{SO}) of 5.0 and 1.5 mg/L, respectively.

3.4 RESULTS AND DISCUSSION

3.4.1. Batch Test 1

The simulated results of batch test 1 (batch mixture 8 in Waybrant et al. 1998) containing decomposable, delignified waste cellulose at an estimated initial concentration of 18,600 mg/L are compared to the experimental results in Figs. 3.2 to 3.6. Simulated concentrations for SO_4^{2-}, Fe^{2+}, and H_2S versus batch reaction time are obtained considering Contois (Contois 1959) or first-order kinetic models for the decomposition of cellulose, Monod kinetics for lactate-based sulfate reduction, and instantaneous precipitation of $FeS_{(s)}$. In some cases, partial volatilization of H_2S to a periodically vented gas phase is considered.

3.4.1.1 Sulfate, Ferrous Iron, and Hydrogen Sulfide

Simulated SO_4^{2-} concentrations with time are compared to experimental results in Fig. 3.2. As shown in Fig. 3.2a, when parameter values from Vavilin et al. (1996) for cellulose decomposition at 35°C (Case 1a, Table 3.3) are used, SO_4^{2-} reduction is significantly over predicted. As a result, cellulose decomposition kinetics was adjusted to 25 °C by decreasing the decomposition rate constant by 50 % for the 10-°C drop, and increasing the half-saturation coefficient, K_c (Middleton and Lawrence 1977, Rittman and McCarty 2001). The temperature adjusted parameter values (Cases 1b and 1c, Table 3.3) result in much more favorable approximations of the experimental data (Figs. 3.2b and 3.2c), with the results using K_c = 37.5 g/g and $[X_d]/[CE]$ = 0.00275 (Case 1b, Fig. 3.2b) providing the best, observed fit to the experimental data. Accordingly, the simulated Fe^{2+} and H_2S concentrations were compared to the experimental Fe^{2+} and H_2S

concentrations, respectively, using the parameter values for Case 1b. As shown in Fig. 3.3a, the simulated Fe^{2+} concentrations compare favorably with the experimental data for the case where K_c = 37.5 g/g and $[X_d]/[CE]$ = 0.00275 (Case 1b, Table 3.3), i.e., Case 1b provides favorable SO_4^{2-} and Fe^{2+} approximations. Since the instantaneous-precipitation algorithm resulted in good approximations of Fe^{2+} concentrations versus time, the kinetically-controlled (first-order kinetics) model for precipitation was not used for this case.

However, the cumulative concentrations of H_2S in solution with no volatilization shown in Fig. 3.3b far exceed the experimental results after depletion of Fe^{2+}, but are in agreement with the sulfur mass balance for the system. For example, up to 124 d (SO_4^{2-} depletion), ~ 1418 mg of H_2S has been released by SO_4^{2-} reduction and ~ 671 mg H_2S has been precipitated as $FeS_{(s)}$, thus requiring ~ 747 mg H_2S to remain in solution if no volatilization of H_2S is considered (Fig. 3.3b). The head-space gas phase of the reaction flask was vented periodically to allow excess gas to escape, which is presumably a requirement for closing the sulfur mass balance for the results reported in Waybrant et al. (1998). As a result, three simulations were performed assuming different values for the unknown frequency of head-space venting (i.e., once every one, two, or three days) and a dimensionless Henry's law coefficient for H_2S of 0.53 (Rittman and McCarty 2001), as shown in Fig. 3.3b. The simulations including volatilization show that the measured H_2S concentrations may be realistic assuming that volatilization was allowed periodically.

3.4.1.2 Rates of Sulfate Reduction and Precipitation

Simulated rates of SO_4^{2-} reduction with time are compared in Fig. 3.4 to rates calculated from the SO_4^{2-} data in Waybrant et al. (1998) considering either Contois

decomposition kinetics (Cases 1a, 1b and 1c, Table 3.3) as shown in Fig. 3.4a, or first-order decomposition kinetics (Cases 1d, 1e, and 1f) as shown in Fig. 3.4b. Simulated rates of sulfate reduction for Contois kinetics using a rate coefficient, k_c, of 1.25 d^{-1} and a half-saturation coefficient, K_c, of 7.5 g/g (Case 1a) are significantly higher than the experimental data, whereas those using half the value for k_c (i.e., 0.625/d) and K_c of either 37.5 g/g (Case 1b) of 30.0 g/g (Case 1c) provide good approximations of the experimental data, except for the period between approximately 60 and 70 d, where an abrupt decline in the experimental rate of SO_4^{2-} reduction occurs. Such abrupt discontinuities in the experimental data generally cannot be simulated using the current model, which is based on continuous functions that predict smooth trends in data (i.e., without changing initial conditions).

The simulated results based on first-order decomposition kinetics (Cases 1d, 1e, and 1f, Fig. 3.4b) predict the rate of SO_4^{2-} reduction to be at the maximum value at time zero and decline monotonically with time. However, this behavior contradicts the experimental behavior in which the rate of sulfate reduction reaches a maximum value only several days after the beginning of the experiment. Therefore, Contois kinetics appears to be a preferable model for the decomposition of organic solids in this SR system, with the Contois parameter values corresponding to Case 1b (i.e., k_c = 0.625/d, K_c = 37.5 g/g, and $[X_d]/[CE]$ = 0.00275) resulting in the best comparisons with the experimental data.

Accordingly, the simulated rates of cellulose decomposition, SO_4^{2-} reduction, and Fe^{2+} precipitation for the Contois parameter values associated with Case 1b are shown in Fig. 3.5. The results in Figs. 3.5a and b show that SO_4^{2-} reduction rates increase with

increasing rates of cellulose decomposition before SO_4^{2-} becomes limiting to sulfate reduction. Between 73 to 124 d, the rates of SO_4^{2-} reduction decline, first as a result of the declining rate of cellulose decomposition and finally due to the depletion of SO_4^{2-}. The simulated rates of Fe^{2+} precipitation follow an analogous relationship (i.e., increase with increasing rates of cellulose decomposition) until 66 d when Fe^{2+} is depleted from the system and the rates of Fe^{2+} precipitation decline abruptly and independently from the rate of cellulose decomposition.

3.4.1.3 Cellulose, Decomposer Bacteria, and Sulfate Reducing Bacteria

The simulated results for the percentage of the initial decomposable cellulose remaining and concentrations of decomposer bacteria for the Contois kinetics Case 1b are shown in Fig. 3.6a, and the corresponding concentrations of SRB are shown in Fig. 3.6b. The time scales in Figs. 3.6a and 3.6b are extended to 240 d to better illustrate the trends. As shown in Fig. 3.6a, the percentage of initial cellulose remaining at 124 d (i.e., SO_4^{2-} depletion) ranges from 40 – 60 %, depending on the value for $[X_d]/[CE]$. The simulations shown in Fig. 3.6b illustrate the succession of different phases in the dynamics of the SRB population, which is expected based on bacterial growth on limiting substrates (Monod 1959). The early lag-growth stage agrees with the initial lag in the growth of cellulose decomposers, and low initial rates of cellulose decomposition and SO_4^{2-} reduction. The brief stationary phase in SRB dynamics corresponds to equilibrium between Monod growth based on SO_4^{2-} and lactate ($C_3H_5O_3^-$) and first-order decay. As SO_4^{2-} approaches depletion near 124 d, the rate of growth decreases until a point when the population undergoes purely exponential decay. The stationary phase would be expected to be longer in scenarios with replenishment of SO_4^{2-}, such as general field

applications of SR systems for AMD remediation, or replenished flow-through experiments. In those cases, the decay phase probably would be more gradual and caused by increasing $C_3H_5O_3^-$ scarcity in the system rather than SO_4^{2-} depletion.

3.4.2. Batch Test 2

The simulated results of batch test 2 (batch mixture 3 in Waybrant et al. 1998) containing decomposable, composted leaf mulch at an estimated initial concentration of 22,300 mg/L are compared to the experimental results as shown in Figs. 3.7 to 3.9. Simulated concentrations for SO_4^{2-} and Fe^{2+} versus batch reaction time are obtained considering the Contois model for the decomposition of polysaccharides, Monod kinetics for lactate-based SO_4^{2-} reduction, and instantaneous precipitation of $FeS_{(s)}$. Results for H_2S are not given in Waybrant et al. (1998) for this batch test.

3.4.2.1 Sulfate and Ferrous Iron

Simulated SO_4^{2-} and Fe^{2+} concentrations based on Contois kinetics for a range of values for $[X_d]/[CE]$ are compared to experimental results in Fig. 3.7. The best comparisons for the SO_4^{2-} concentrations are obtained with $[X_d]/[CE] = 0.01$ (Case 2a) or with $[X_d]/[CE] = 0.005$ (Case 2b). However, with respect to the approximation of Fe^{2+}, instantaneous precipitation with the same $[X_d]/[CE]$ ratios used for SO_4^{2-} results in simulated Fe^{2+} concentrations that decline faster than occur for the experimental data. Therefore, $FeS_{(s)}$ precipitation appears to follow slower kinetics than instantaneous precipitation. In this case, kinetically-controlled precipitation of $FeS_{(s)}$, rather than instantaneous precipitation, may be more appropriate to approximate the observed Fe^{2+} data. For this reason, kinetically-controlled precipitation of iron-sulfide will be used

subsequently to model the data from batch tests 3 and 4. The results also suggest that the consideration of any additional sink for Fe^{2+}, such as $FeCO_{3(s)}$ precipitation, would cause the simulated behavior of Fe^{2+} to deviate even more from the experimental data.

Based on the decomposition parameter values for the leaf mulch of batch test 2, the leaf mulch is more degradable than the cellulose in batch test 1. This consideration is in agreement with the earlier depletion of SO_4^{2-} in batch test 2 (i.e., at 65 d, as opposed to 124 d in batch test 1), and can be explained by the difference in the nitrogen content of the two materials. The leaf mulch is reported to have a carbon-to-nitrogen (C/N) ratio of 21 (Waybrant et al. 1998), which is within the range of values associated with more easily degradable materials (Chynoweth and Pullammanappallil 1996). The cellulose in batch test 1 is reported to lack in nitrogen (Waybrant et al. 1998), a condition that makes decomposer colonization and activity more difficult.

3.4.2.2 Rates of Sulfate Reduction

Simulated rates of SO_4^{2-} reduction with time are compared in Fig. 3.8 to values calculated from the SO_4^{2-} data given in Waybrant et al. (1998) considering Contois decomposition kinetics (Cases 2a and 2b). In this case, the maximum rate of SO_4^{2-} reduction occurs several days after the beginning of the experiment, which compares reasonably well with the experimental data. In contrast, the use of first-order decomposition kinetics would result in the maximum rate of sulfate reduction occurring at time zero, as previously shown and discussed for batch test 1.

3.4.2.3 Polysaccharide, Decomposer Bacteria, and Sulfate Reducing Bacteria

Based on the parameter values for Contois decomposition kinetics (Cases 2a and 2b, Table 3.3), the simulated percentages of the initial decomposable polysaccharide remaining and concentrations of decomposer bacteria, as well as the simulated concentrations of SRB are shown in Fig. 3.9, with time scales extended to 240 d to better illustrate the trends. The percentage of initial polysaccharide remaining at 65 d (i.e., SO_4^{2-} depletion) ranges from 55 – 75 % (Case 2a), and 50 – 60 % (Case 2b), depending on the value for $[X_d]/[CE]$. The SRB concentrations in this experiment are higher than those in batch test 1, which is in agreement with faster leaf mulch degradation kinetics, but earlier depletion of SO_4^{2-} (i.e., at 65 d, instead of 124 d) causes the SRB stationary phase to be negligible; i.e., the population enters an exponential decay due to SO_4^{2-} depletion before the time that would be required for the stationary phase to be achieved.

3.4.3. Batch Test 3

The simulated results of batch test 3 (batch mixture 6 in Waybrant et al. 1998) containing decomposable, composted leaf mulch and maple sawdust at estimated initial concentrations of 13,300 and 8,900 mg/L, respectively, are compared to the experimental results in Figs. 3.10 and 3.11. Simulated concentrations for SO_4^{2-} and Fe^{2+} versus batch reaction time are obtained considering a Contois kinetic model for the decomposition of polysaccharides, Monod kinetics for lactate-based SO_4^{2-} reduction, and both instantaneous and kinetically-controlled precipitation of $FeS_{(s)}$. Two decomposer populations are assumed, each population directly associated with a decomposing material, and the amounts of lactate produced in solution over time include contributions from the two decompositions. The concentrations of H_2S, polysaccharides and bacterial

populations are not shown because simulated results are similar to those shown for batch tests 1 and 2.

3.4.3.1 Sulfate and Rates of Sulfate Reduction

Simulated SO_4^{2-} concentrations and rates of SO_4^{2-} reduction are compared to experimental results in Fig. 3.10. Leaf mulch decomposition kinetics is assumed to be equal to that in batch test 2, and the parameter values for sawdust decomposition are adjusted. As shown in Fig. 3.10, the simulated SO_4^{2-} concentrations and rates of SO_4^{2-} reduction with time compare well with the experimental data, i.e., when sawdust decomposition is assumed equal to that of leaf mulch (see Table 3.3). Although wood usually is expected to be more recalcitrant than leaf detritus, the sawdust is characterized by fine gradation and high specific surface area, factors that enhance degradability (Humphrey 1979), and may assist in the decomposition of the sawdust.

3.4.3.2 Ferrous Iron and Rates of Precipitation

Simulated Fe^{2+} concentrations and rates of Fe^{2+} precipitation with time are compared to experimental results in Fig. 3.11 based on both instantaneous precipitation of $FeS_{(s)}$, and kinetically controlled precipitation with rate constants, k, of 0.1 d^{-1} and 0.0005 d^{-1}. As shown in Fig. 3.11 both instantaneous precipitation of $FeS_{(s)}$ and kinetically controlled precipitation with k = 0.1 d^{-1} are equivalent in terms of Fe^{2+} concentrations and rates of Fe^{2+} precipitation, indicating that the rate constant of 0.1 d^{-1} is essentially equivalent to instantaneous precipitation in this system. However, the best approximation of Fe^{2+} concentrations and rates of Fe^{2+} precipitation is obtained when the precipitation of FeS is more kinetically limited with k = 0.0005 d^{-1}. This kinetic

limitation to $FeS_{(s)}$ precipitation also was previously observed for the comparisons based on batch test 2.

As shown in Fig. 3.11, the initial rate of Fe^{2+} precipitation with k = 0.1 d^{-1} is significantly higher than that associated with k = 0.0005 d^{-1} (i.e., 20 mg/L-day vs.1 mg/L-day), but the maximum rate of Fe^{2+} precipitation with k = 0.1 d^{-1} is only approximately 30 % higher than the maximum rate associated with k = 0.0005 d^{-1} (i.e., 36 mg/L-day vs. 25 mg/L-day). The results show that the rates of Fe^{2+} precipitation with time are not directly proportional to the precipitation rate constant. The lack in proportionality is caused by the differences in H_2S concentrations in solution. For example, H_2S concentrations at 7 d are in the order of 40 mg/L for the case with k = 0.0005 d^{-1}, but only 0.3 mg/L for the case with k = 0.1 d^{-1}. Higher levels of H_2S in solution increase the rate of Fe^{2+} precipitation and, therefore, cause the rates of Fe^{2+} precipitation to increase for the case with k = 0.0005 d^{-1}.

3.4.4 Batch Test 4

The simulated results of batch test 4 (batch mixture 7 in Waybrant et al. 1998) containing decomposable leaf mulch, sawdust, wood chips, and sewage sludge at estimated initial concentrations of 19,100, 3,200, 4,800, and 1,100 mg/L, respectively, are compared to the experimental results as shown in Fig. 3.12. Simulated concentrations for SO_4^{2-} versus batch reaction time are obtained considering a Contois kinetic model for the decomposition of polysaccharides, and Monod kinetics for lactate-based SO_4^{2-} reduction. In this test, experimental Fe^{2+} results are neglected due to the decline of more than 90 % of the initial concentration of Fe^{2+} occurring at time zero, which is assumed not to be related to the biochemistry of SR systems based on decomposable solid materials. The

concentrations of H_2S, polysaccharides and bacterial populations are not shown because simulated results are similar to those shown for batch tests 1 and 2. Leaf mulch and sawdust are grouped as a single decomposable material and, therefore, three different decomposable materials are considered (i.e., leaf mulch/sawdust, wood chips, and sewage sludge). Accordingly, three populations of decomposer bacteria are assumed, each population associated to one of the substrates (Chapter 2).

3.4.4.1 Sulfate and Rates of Sulfate Reduction

Both simulated SO_4^{2-} concentrations and rates of SO_4^{2-} reduction are compared to experimental results in Figs. 3.12a and b, where the experimental SO_4^{2-} reduction rates were calculated from the SO_4^{2-} data given in Waybrant et al. (1998), for the range of parameter values shown. Leaf mulch and sawdust decomposition kinetics were assumed to be the same as for batch tests 2 and 3, and the parameter values for wood chips were adjusted. As shown in Fig. 3.12a, the simulated SO_4^{2-} concentrations with time compare well with the experimental data for both cases shown (Cases 4a and 4b).

The results for Cases 4c and 4d shown in Fig. 3.12b were obtained by isolating the contribution of the sewage sludge to the rate of SO_4^{2-} reduction. Accordingly, the rates of sulfate reduction associated with Cases 4b, 4c, and 4d are compared in Fig. 3.12b. Case 4b provides a good approximation to the experimental rates of SO_4^{2-} reduction, whereas Cases 4c (including all organic substrates except for sewage sludge) and 4d (only including sewage sludge) provide poorer approximations. A comparison of the simulated rates obtained in Cases 4b, 4c and 4d illustrates the role of the easily degradable material in boosting the initial rates of SO_4^{2-} reduction. However, the results for Case 4d indicate that SO_4^{2-} reduction based on sewage sludge alone would decline

quickly (i.e., the rate declines by more than 2 mg/L-d every day after 5 d) and, therefore, the SR system requires materials that degrade more slowly in order to sustain sulfate reduction.

3.5. LOCAL TRUNCATION ERRORS AND ELEMENTAL MASS CONSERVATION

Relative local truncation errors (Chapter 2) are evaluated over time for each species in each batch test based on the Runge Kutta predictors utilized in the numerical algorithm. For batch test 1 (Case 1b, Table 3.3), the truncation errors versus time for cellulose, decomposer bacteria, SRB, and lactate are shown in Fig. 3.13a, and the errors for SO_4^{2-}, H_2S, Fe^{2+}, and precipitate are shown in Fig. 3.13b. For batch test 3 (Case 3a), the truncation errors for the two polysaccharide materials, the two decomposer bacteria, SRB, and lactate are shown in Fig. 3.14a, and the errors for SO_4^{2-}, H_2S, Fe^{2+}, and precipitate and shown in Fig. 3.14b. Plots of the errors in batch tests 2 and 4 are not shown to avoid repetition.

The range of errors for polysaccharides, decomposer bacteria, SRB, lactate, H_2S, and precipitate are equal to, or limited by, the value of 1×10^{-6} mg/L per 1.0 mg/L, except for a maximum value of approximately 5×10^{-6} mg/L per 1.0 mg/L observed for polysaccharides and SRB in Fig. 3.14a. These ranges are considered acceptable in this study. In the case of SO_4^{2-} and Fe^{2+}, the truncation errors are observed to increase as the species approach the point of depletion from the batch system, which corresponds to the denominator of the truncation error equation approaching zero. As the concentrations of SO_4^{2-} and Fe^{2+} decline from 100 % to < 0.5 % of the initial values, the relative errors

increase from approximately 1 x 10^{-8} mg/L per 1.0 mg/L to 1 x 10^{-4} mg/L per 1.0 mg/L. Since the higher level of errors is associated with very low percentages of the initial concentrations (i.e., depletion of the species from the system), this range of errors also is assumed acceptable in this study.

Verifications of elemental mass conservation within the batch systems over time were performed after all simulations. Given the biochemical transformations occurring in the systems, and the fact that the systems are not replenished, elemental mass conservations for total iron, sulfur, and carbon (i.e., with respect to the initial elemental mass added at the beginning of the simulation) must be respected at all times. Figure 3.15 illustrates the mass conservation of iron, sulfur, and carbon in the simulation of batch test 1 (Case 1b). The plots show the elemental mass distribution into different species over time on the primary y-axis (i.e., left-hand side y-axis) and the mass balance ratio on the secondary y-axis over time. For example, the sulfur mass distribution includes the species SO_4^{2-}, H_2S, and $FeS_{(s)}$ at all times (Fig. 3.15b). The mass balance ratio is the ratio between the total elemental mass (of iron, sulfur, or carbon) accounted in the system at any time, with respect to the total mass initially added. As shown in Figs. 3.15a and b, elemental mass balances for iron and sulfur were near unity. As observable in Fig. 3.15c, the elemental carbon mass balance ranged from 1.0 to 0.91, which was assumed as acceptable. In all other batch simulations, the levels of carbon mass balance were similar to those in batch test 1.

3.6. CONCLUSIONS

Simulation results from a model for SO_4^{2-} reduction and metal precipitation in SR systems with kinetics of SO_4^{2-} reduction coupled to, and limited by, the decomposition of organic solid materials were compared to experimental results from two single-substrate and two multiple-substrate batch equilibrium experiments reported in the literature. Rates of SO_4^{2-} reduction varying from 15 - 50 mg SO_4^{2-}/L-d (batch test 1), 40 - 80 mg SO_4^{2-}/L-d (batch tests 2 and 3) and 80 - 100 mg SO_4^{2-}/L-d (batch test 4), when SO_4^{2-} reduction was active, were satisfactorily simulated using adjusted parameters for Contois kinetics for polysaccharide decomposition and Monod kinetics for lactate-based SO_4^{2-} reduction. When Contois kinetics of polysaccharide decomposition was replaced by first-order kinetics, comparatively poorer approximations of SO_4^{2-} reduction rates were obtained. For the same conditions used in SO_4^{2-} approximations, instantaneous precipitation of $FeS_{(s)}$ provided a good approximation to Fe^{2+} concentrations in batch test 1, but some degree of kinetic limitation to $FeS_{(s)}$ precipitation was required to better approximate batch tests 2 and 3. The simulated results for Fe^{2+} suggest that the inclusion of any additional sink for Fe^{2+}, such as $FeCO_{3(s)}$ precipitation, would not enhance Fe^{2+} approximations. The adjusted parameters for polysaccharide decomposition in cellulose, leaf mulch, sawdust, wood chips, and sewage sludge can be used as starting points for the simulation of other SR systems based on similar organic materials (e.g., batch and column experiments, field bioreactor or PRB) in which the rates of SO_4^{2-} reduction can be modeled on the basis of organic matter decomposition following the serial application of Contois and Monod models employed in this study.

3.7. ACKOWLEDGMENTS

This research was funded by the U. S. EPA Science to Achieve Results (STAR) Program under Grant No. R-82951501-0 as part of the U. S. EPA's *Rocky Mountain Regional Hazardous Substance Research Center*.

3.8. REFERENCES

Amos, R.T., Mayer, K.U., Blowes, D.W., and Ptacek, C.J. (2004). Reactive transport modeling of column experiments for remediation of acid mine drainage. *Environmental Science and Technology*, 38(11): 3131-3138.

Bechard, G., Yamazaki, H., Gould, W.D., and Bedard, P. (1994). Use of cellulosic substrates for the microbial treatment of acid mine drainage. *Journal of Environmental Quality*, 23(1): 111-116.

Benner, S.G, Blowes, D.W., Ptacek, C.J., and Mayer, K.U. (2002). Rates of sulfate reduction and metal sulfide precipitation in a permeable reactive barrier. *Applied Geochemistry*, 17(1): 301-320.

Benner, S.G., Blowes, D.W., Gould, W.D., Herbert, R.B., and Ptacek, C. J. (1999). Geochemistry of a permeable reactive barrier for metals and acid mine drainage, *Environmental Science and Technology*, 33(16): 2793-2799.

Benner, S.G., Gould, W.D., and Blowes, D.W. (2000). Microbial populations associated with the generations and treatment of acid mine drainage, *Chemical Geology*, 169 (3-4): 435-448.

Boudreau, B.P., and Westrich, J.T. (1984). The dependence of bacterial sulfate reduction on sulfate concentration in marine environments. *Geochimica et Cosmochimica Acta*, 48(12): 2503-2516.

Chang, I.S., Shin, P.K., and Kim, B.H. (2000). Biological treatment of acid mine drainage under sulphate-reducing conditions with solid waste materials as substrates. *Water Research*, 34(4): 1269-1277.

Christensen, B., Laake, M., and Lien, T. (1996). Treatment of acid mine water by sulfate-reducing bacteria; results from a bench scale experiment. *Water Research*, 30(7): 1617-1624.

Chynoweth, D.P., and Pullammanappallil, P. (1996). Anaerobic digestion of municipal solid waste. *Microbiology of Solid Waste*, A. Palmasano and M.A. Barlaz, eds.,CRC Press, Boca Raton, FL, 77-113.

Cocos, I.A., Zagury, G.J., Clement, B., and Samson, R. (2002). Multiple factor design for reactive mixture selection for use in reactive walls in mine drainage treatment. *Water Research*, 36(1): 167-177.

Contois, D.E. (1959). Kinetics of bacterial growth, relationship between population density and specific growth rate of continuous cultures. *Journal of General Microbiology*, 21(1): 40-50.

Drury, J.W. (2000). Modeling of sulfate reduction in anaerobic solid substrate bioreactors for mine drainage treatment. *Mine Water and the Environment*, 19(1): 18-28.

Dvorak, D.H., Hedin, R.S., Edenborn, H.M., and McIntire, P.E. (1992). Treatment of metal-contaminated water using bacterial sulfate reduction: results from pilot-scale reactors. *Biotechnology and Bioengineering*, 40(5): 609-616.

Fenchel, T., and Harrison, P. (1976). The significance of bacterial grazing and mineral cycling for the decomposition of particulate detritus. In *The Role of Terrestrial and*

Aquatic Organisms in Decomposition Processes, J.M. Anderson and A. Macfadyen, Eds., Blackwell Scientific Publications: Oxford, UK.

Figueroa, L., Ahmann, D., Blowes, D., Carlson, K., Shackelford, C., Woods, S., DuTeau, N., Reardon, K., and Wilderman, T. (2002). Metal removal capabilities of passive bioreactor systems: effects of organic matter and microbial population dynamics. *Proceedings of the 9th International Conference on Tailings and Mine Waste*, 27-30 January, Fort Collins, CO, A. A. Balkema, Lisse, The Netherlands, 21-22.

Frommichen, R., Kellner, S., and Friese, K. (2003). Sediment conditioning with organic and/or inorganic carbon sources as a first step in alkalinity generation of acid mine pit lake water (pH 2-3). *Environmental Science and Technology*, 37(7): 1414-1421.

Gilbert, J.S., Wildeman, T.R., and Ford, K.L. (1999). Laboratory experiments designed to test the remediation properties of materials. *Proceedings of the 16th Annual Meeting of the American Society for Surface Mining and Reclamation*, 13-19 August, Scottsdale, AZ, American Society for Surface Mining and Reclamation, Blacksburg, VA, 592-598.

Groudev, S., Nicolova, M., Spasova, I., and Schutte, R. (2003). Treatment of waters from a copper mine by means of a permeable reactive barrier. *Fifty Years of the University of Mining and Geology "St. Ivan Rilski"*, University of Mining and Geology, Sofia (Bulgaria), Volume 46, Part II, Section Mining and Mineral Processing, 229-231.

Gujer, W.,and Zehnder, A.J. (1983). Conversion processes in anaerobic digestion. *Water Science and Technology*, 15(8-9), 127-167.

Hammack, R.W., and Edenborn, H.M. (1992). Treatment of water from an open pit copper mine using biogenic sulfide and limestone: a feasibility study. *Applied Microbiology and Biotechnology*, 37(5): 674-678.

Hammack, R.W., Edenborn, H.M., and Dvorak, D.H. (1994). Treatment of water from an open pit copper mine using biogenic sulfide and limestone: a feasibility study. *Water Resources*, 28(11): 2321-2329.

Harbaugh, A.W., Banta, E.R., Hill, M.C., and McDonald, M.G. (2000). *MODFLOW-2000, the U.S. Geological Survey Modular Ground-Water Model – User Guide to Modularization Concepts and the Ground-Water Flow Process*, USGS Open-File Report 00-92.

Henriksen, T.M., and Breland, T.A. (2002). Carbon mineralization, fungal and bacterial growth, and enzyme activities as affected by contact between crop residues and soil. *Biology and Fertilization of Soils*, 35(1), 41-48.

Hulshof, A.H., Blowes, D.W., Ptacek, C.J., and Gould, W.D. (2003). Microbial and nutrient investigations into the use of in situ layers for treatment of tailings effluent. *Environmental Science and Technology*, 37(21): 5027-5033.

Humphrey, A. E. (1979). The Hydrolysis of Cellulosic Materials to Useful Products. *Hydrolysis of Cellulose: Mechanisms of Enzymatic and Acid Catalysis*, Chapter 2, Advances in Chemistry Series, No. 181, American Chemical Society, Washington D.C., 25-53.

Janssen, B.H. (1984). A simple method for calculating decomposition and accumulation of young soil organic matter. *Plant and Soil*, 76(1-3), 297-304.

Konishi, Y., Yoshida, N., and Asai, S. (1996). Desorption of hydrogen sulfide during batch growth of the sulfate-reducing bacterium *Desulfovibrio desulfuricans. Biotechnology Progress*, 12(3), 322-330.

Logan, M., Ahamann, D., and Figueroa, L. (2003). Assessment of microbial activity in anaerobic columns treating synthetic mine drainage. *Proceedings of the 2003 Annual Meeting of the American Society for Mining and Reclamation,* 3-6 June, Billings, MT, American Society for Mining and Reclamation, Lexington, KY, 658-678.

Ludwig, R.D., McGregor, R.G., Blowes, D.W., Benner, S.G., Mountjoy, K. (2002). A permeable reactive barrier for treatment of heavy metals. *Ground Water*, 40(1), 59-66.

Mayer, K.U., Frind, E.O, and Blowes, D.W. (2002). Multicomponent reactive transport modeling in variably saturated porous media using a generalized formulation for kinetically controlled reactions. *Water Resources Research*, 38(9): 13-1 to 13-21.

Middelburg, J.J. (1989). A simple rate model for organic matter decomposition in marine sediments. *Geochimica et Cosmochimica Acta*, 53(7), 1577-1581.

Middleton, A.C., and Lawrence, A.W. (1977). Kinetics of microbial sulfate reduction. *Journal of Water Pollution Control Federation*, 49(7): 1659-1670.

Monod, J. (1949). The growth of bacterial cultures. *Annual Review of Microbiology*, 3: 371-394.

Negri, E.D., Mata-Alvarez, J., Sans, C., and Cecchi, F. (1992). A mathematical model of volatile fatty acids production in a plug flow reactor treating the organic fraction of municipal solid waste. *Proceedings of the International Symposium on Anaerobic*

Digestion of Solid Waste, Venice, 14-17 April, Stamperia de Venezia, Venice (Italy), 256-268.

Okabe, S., and Characklis, W.G. (1992). Effects of temperature and phosphorous concentration on microbial sulfate reduction by *Desulfovibrio desulfuricans*. *Biotechnology and Bioengineering*, 39(10), 1031-1042.

Okabe, S., Nielsen, P.H., and Characklis, W.G. (1992). Factors affecting microbial sulfate reduction by *Desulfovibrio desulfuricans* in continuous culture: limiting nutrients and sulfide concentration. *Biotechnology and Bioengineering*, 40(6), 725-734.

Parkhurst, D.L., and Appelo, C.A. (1999). *User's Guide to PHREEQC – A Computer Program for Speciation, Batch Reaction, One Dimensional Transport, and Inverse Geochemical Calculations*, Technical Report 4227, US Geological Survey.

Postgate, J.R. (1984). *The Sulphate-Reducing Bacteria,* 2nd Edition; Cambridge University Press: Cambridge, UK.

Prasad, D., Wai, M., Berube, P., and Henry, J.G. (1999). Evaluating substrates in the biological treatment of acid mine drainage. *Environmental Technology*, 20(5): 449-458.

Prommer, H., Barry, D.A., Chiang, W.H., and Zheng, C. (2001). PHT3D – a MODFLOW/MT3DMS-based reactive multi-component transport model. *MODFLOW 2001 and Other Modeling Odysseys*, H. Seo, E. Poeter, and C. Zheng, eds., International Ground-Water Modeling Center, Colorado School of Mines, Golden, CO, 477-483.

Rittman, B.E., and McCarty, P.L. (2001). *Environmental Biotechnology: Principles and Applications*. McGraw-Hill, NewYork, NY.

Schafer, D., Schafer, W., and Kinzelbach, W. (1998a). Simulation of reactive processes related to biodegradation in aquifers. 1-structure of the three-dimensional reactive transport model. *Journal of Contaminant Hydrology*, 31(1-2): 167-186.

Schafer, D., Schafer, W., and Kinzelbach, W. (1998b). Simulation of reactive processes related to biodegradation in aquifers. 2-model application to a column study on organic carbon degradation. *Journal of Contaminant Hydrology*, 31(1-2): 187-209.

Sposito, G. (1989). *The Chemistry of Soils*. Oxford University Press, Oxford, UK.

Steed, V., Suidan, M., Gupta, M., Miyahara, T., Acheson, C., Sayles, G. (2000). Development of a sulfate-reducing biological process to remove heavy metals from acid mine drainage. *Water Environment Research*, 72(5), 530-535.

Thombre, M.S., Thomson, B.M., and Barton, L.L. (1997). Use of a permeable biological reaction barrier for groundwater remediation at a uranium mill tailings remedial action site, *International Containment Technology Conference,* 9-12 February, St. Petersburg, FL, U.S. Department of Energy and Florida State University Institute for International Cooperative Environmental Research, Tallahassee, FL, 744-750.

Tuttle, J.H., Dugan, P.R., and Randles, C.I. (1969). Microbial sulfate reduction and its potential utility as an acid mine water pollution abatement procedure. *Applied Microbiology*, 17(2): 297-302.

Vavilin, V.A., Rytov, S.V., and Lokshina, L. (1996). A description of hydrolysis kinetics in anaerobic degradation of particulate organic matter. *Bioresource Technology*, 56(1): 229-237.

Zheng, C., and Wang, P.P. (1999). *MT3DMS: A Modular Three-Dimensional Multispecies Model for Simulation of Advection, Dispersion, and Chemical Reactions of Contaminants in Groundwater Systems; Documentation and User's Guide*, U.S. Army Corps of Engineers, Contract Report SERDP-99-1.

Wakao, N., Takahashi, T., Sakurai, Y., and Shiota, H. (1979). A treatment of acid mine water using sulfate-reducing bacteria. *Journal of Fermentation Technology*, 57(5): 445-452.

Waybrant, K.R., Blowes, D.W., and Ptacek, C.J. (1998). Selection of reactive mixtures for use in permeable reactive walls for treatment of mine drainage. *Environmental Science and Technology*, 32(13): 1972-1979.

Waybrant, K.R., Ptacek, C.J., and Blowes, D.W. (2002). Treatment of mine drainage using permeable reactive barriers: column experiments. *Environmental Science and Technology*, 36(6): 1349-1356.

Westrich, J.T., and Berner, R.A. (1984). The role of sedimentary organic matter in bacterial sulfate reduction: the G model tested. *Journal of Limnology and Oceanography*, 29(2): 236-249.

Widdel, F. (1988). Microbiology and ecology of sulfate reducing bacteria., *Biology of Anaerobic Microorganisms*. Chapter 10, A. J. B. Zehnder, ed. Wiley Interscience, New York, NY, 469-585.

Table 3.1– Solids and decomposable organic fraction composition for four batch experiments reported in Waybrant et al. (1998).

Batch test	Batch volume (mL)	Solids (dry mass basis)				Decomposable organic fraction (dry mass basis)					
		Total		Organic fraction		Total (g/L)	Composition				
		(g)	(g/L)	(%)	(mg/L)		Cellulose (mg/L)	Leaf mulch (mg/L)	Sawdust (mg/L)	Wood chips (mg/L)	Sewage sludge (mg/L)
1	959	117	122	19	23,200	18.6	18,600 (100%)	-	-	-	-
2	466	77	165	27	44,500	22.3	-	22,300 (100%)	-	-	-
3	897	128	143	31	44,300	22.2	-	13,300 (60%)	8,900 (40%)	-	-
4	857	114	133	48	63,800	28.2	-	19,100 (60%)	3,200 (10%)	4,800 (15%)	1,100 (15%)

Table 3.2 – Assumed initial concentrations of sulfate, ferrous iron, hydrogen sulfide, lactate, and acetate for four batch experiments performed by Waybrant et al. (1998).

Batch test	Materials	Initial concentrations (mg/L)				
		SO_4^{2-}	Fe^{2+}	H_2S	Lactate	Acetate
1	Cellulose	4000	1110	0	0	0
2	Leaf mulch	3480	510	0	0	0
3	Leaf mulch/sawdust	4400	744	0	0	0
4	Leaf mulch/sawdust/wood chips/sewage sludge	3300	200	0	0	0

Table 3.3 – Parameter values used for simulation cases of the results of the four batch experiments reported in Waybrant et al. (1998).

Batch test	Case	Decomposition					Precipitation	
		Materials	Contois kinetics			First-order	Instan-taneous	First-order
			k_c (d^{-1})	K_c (mg/mg)	$[X_d]_i/[CE]_i$	k_f (d^{-1})		k (d^{-1})
1	1a	Cellulose	1.25	7.5	0.0005,0.00275,0.005	-	yes	-
	1b		0.625	37.5	0.0005,0.00275,0.005	-	yes	-
	1c		0.625	30	0.0005,0.00275,0.005	-	yes	-
	1d		-	-	-	0.02	yes	-
	1e		-	-	-	0.01	yes	-
	1f		-	-	-	0.005	yes	-
2	2a	Leaf mulch	0.625	30	0.00275,0.005,0.01	-	yes	-
	2b		0.8	30	0.00275,0.005	-	yes	-
3	3a	Leaf mulch + sawdust	0.625	30	0.01	-	yes	-
	3b		0.8	30	0.005	-	yes	-
	3c		0.8	30	0.005	-	-	0.1
	3d		0.8	30	0.005	-	-	0.0005
4	4a	Leaf mulch + sawdust	0.625	30	0.01	-	yes	-
		Wood chips	0.4	30	0.005			
		Sewage sludge	8.0	30	0.01			
	4b	Leaf mulch + sawdust	0.8	30	0.005	-	yes	-
		Wood chips	0.4	30	0.005			
		Sewage sludge	8.0	30	0.01			
	4c	Leaf mulch + sawdust	0.8	30	0.005	-	yes	-
		Wood chips	0.4	30	0.005			
		Sewage sludge	0.0	-	-			
	4d	Leaf mulch + sawdust	0.0	-	-	-	yes	-
		Wood chips	0.0	-	-			
		Sewage sludge	8.0	30	0.01			

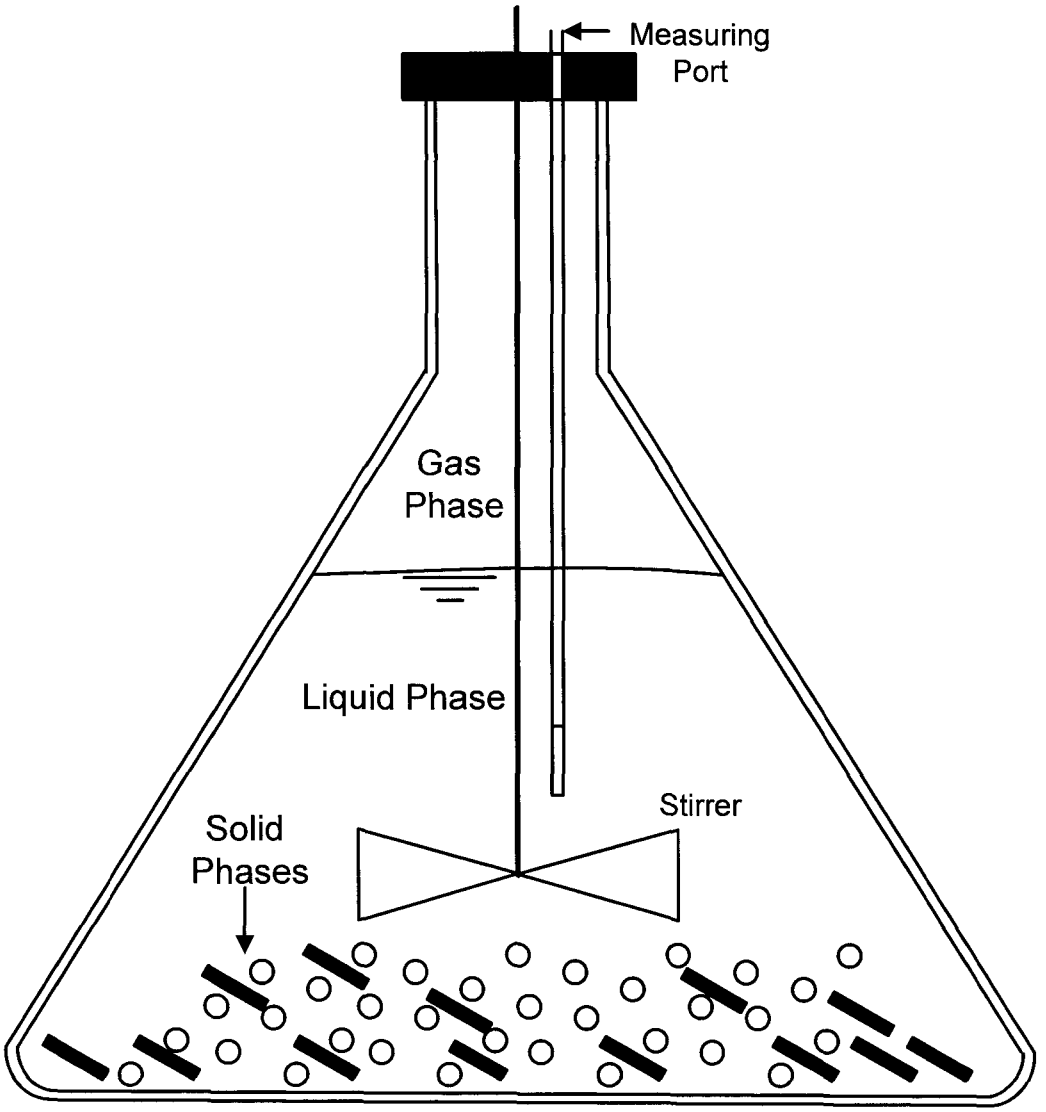

Figure 3.1 – Illustration of batch-equilibrium experiment, including the solid, liquid, and gas phases.

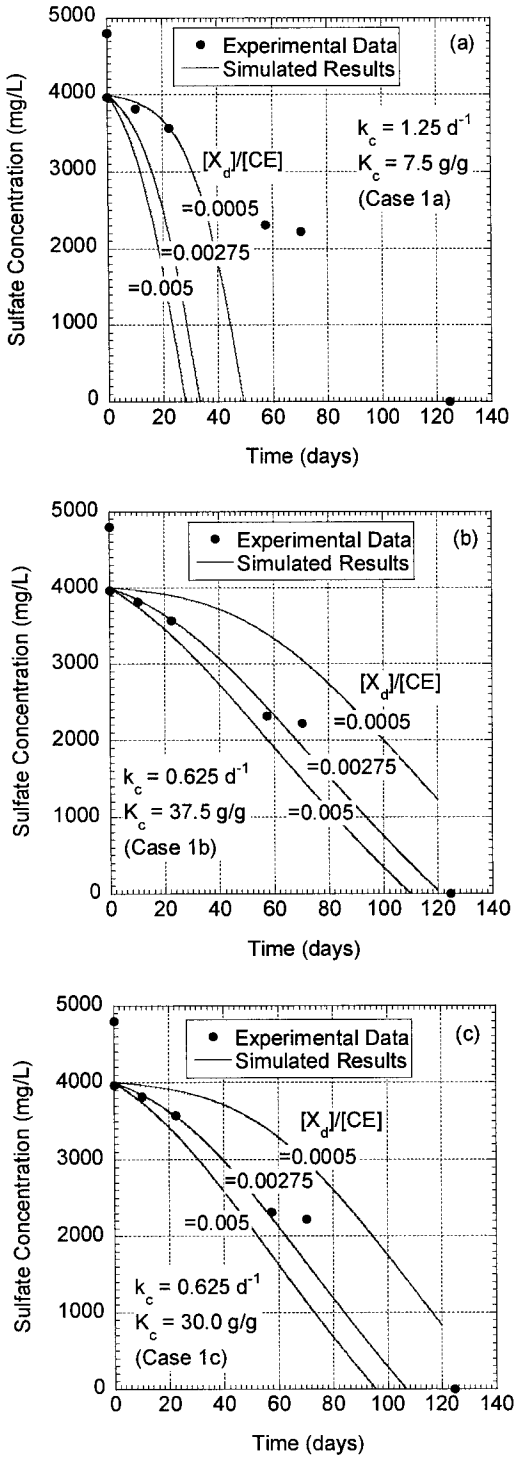

Figure 3.2 – Comparison of experimental and simulated sulfate concentrations based on Contois decomposition kinetics for batch test 1 (k_c = decomposition rate coefficient; K_c = half-saturation coefficient; $[X_d]/[CE]$ = initial concentration ratio of decomposer bacteria to polysaccharide).

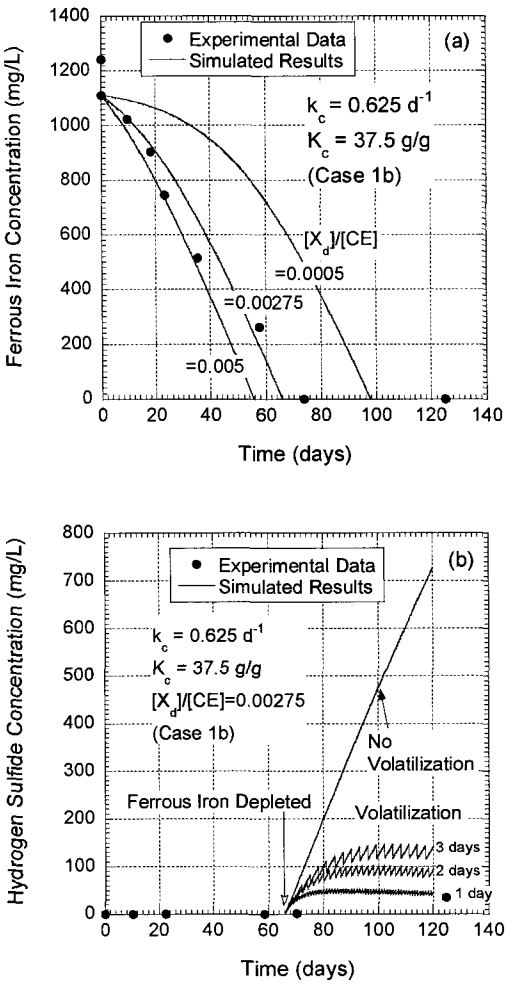

Figure 3.3 – Comparison of experimental and simulated concentrations based on Contois decomposition kinetics for batch test 1: (a) ferrous iron, and (b) hydrogen sulfide concentrations versus time (k_c = decomposition rate coefficient; K_c = half-saturation coefficient; $[X_d]/[CE]$ = initial concentration ratio of decomposer bacteria to polysaccharide).

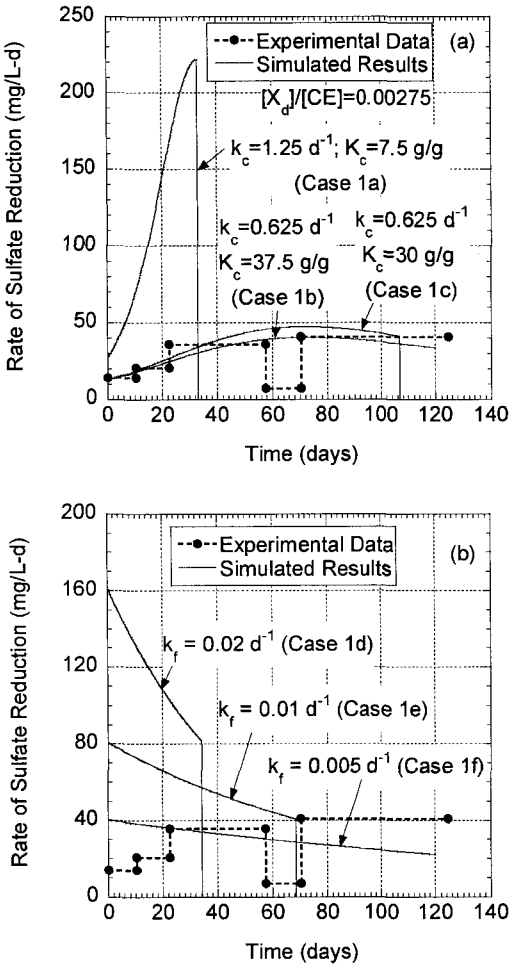

Figure 3.4 – Comparison of experimental and simulated rates of sulfate reduction versus time for batch test 1: (a) Contois decomposition kinetics, and (b) first-order decomposition kinetics (k_c = decomposition rate coefficient; K_c = half-saturation coefficient; $[X_d]/[CE]$ = initial concentration ratio of decomposer bacteria to polysaccharide; k_f = first-order decomposition rate coefficient).

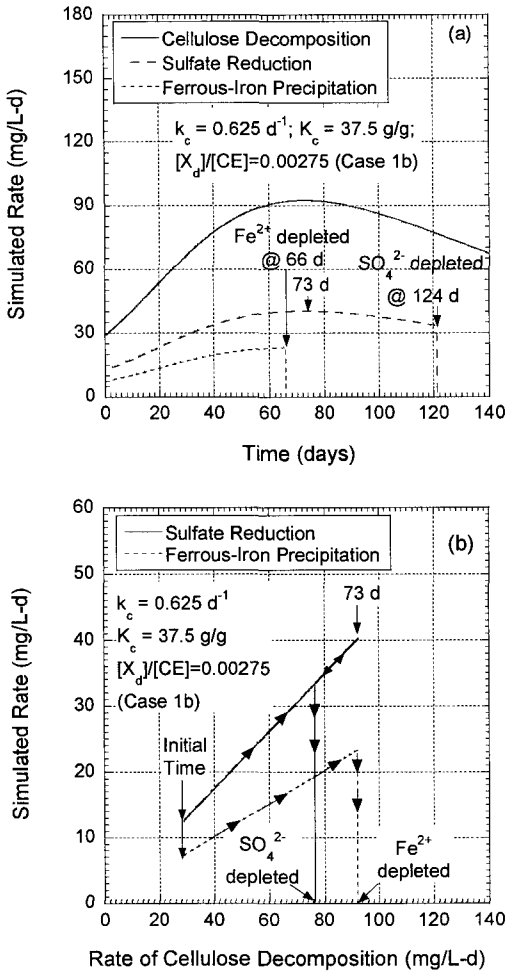

Figure 3.5 – Simulated results for batch test 1, (a) rates of cellulose decomposition, sulfate reduction and ferrous iron precipitation versus time, and (b) rates of sulfate reduction and ferrous iron precipitation versus cellulose decomposition (k_c = decomposition rate coefficient; K_c = half-saturation coefficient; $[X_d]/[CE]$ = initial concentration ratio of decomposer bacteria to polysaccharide).

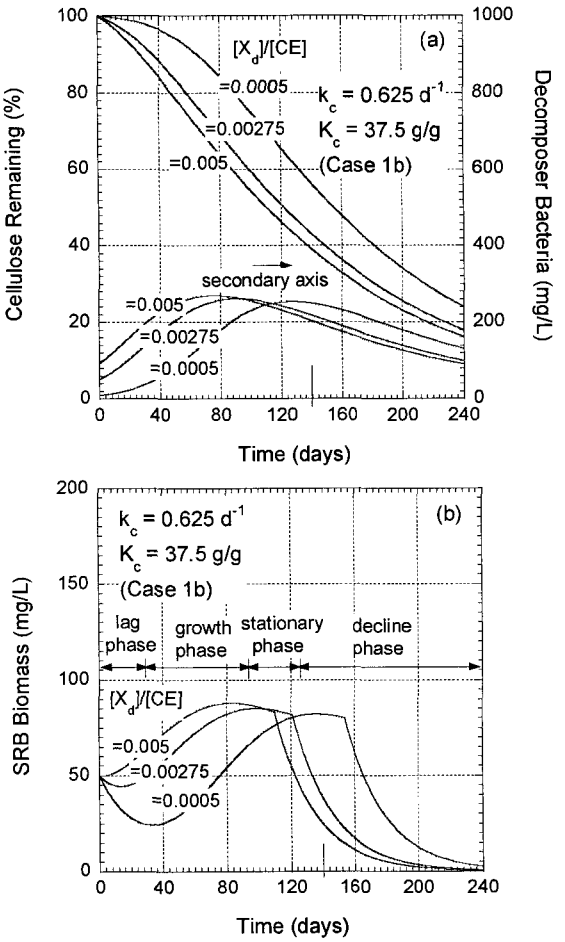

Figure 3.6 – Simulated results for batch test 1: (a) percentage of initial cellulose and decomposer bacteria concentrations, and (b) concentrations of SRB (k_c = decomposition rate coefficient; K_c = half-saturation coefficient; $[X_d]/[CE]$ = initial concentration ratio of decomposer bacteria to polysaccharide).

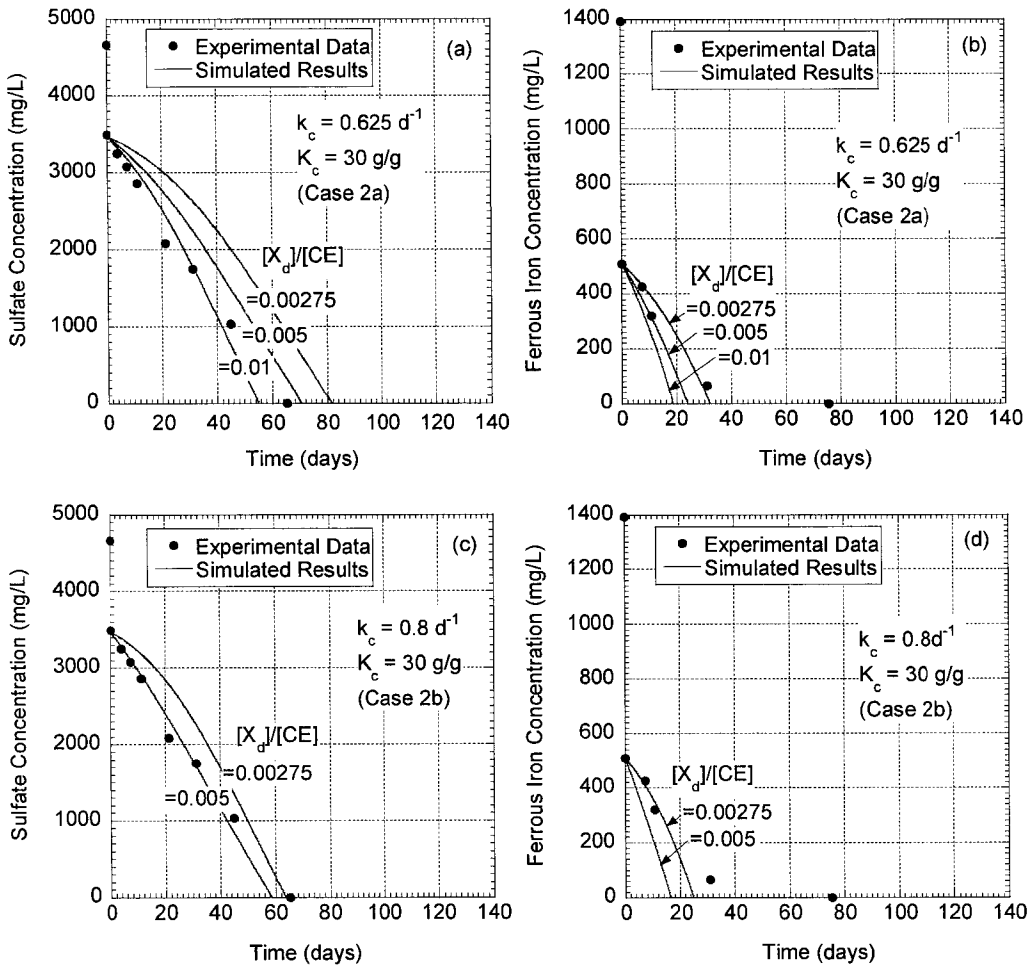

Figure 3.7 – Comparison of experimental and simulated sulfate and ferrous iron concentrations for batch test 2 based on different Contois decomposition kinetics (k_c = decomposition rate coefficient; K_c = half-saturation coefficient; $[X_d]/[CE]$ = initial concentration ratio of decomposer bacteria to polysaccharide).

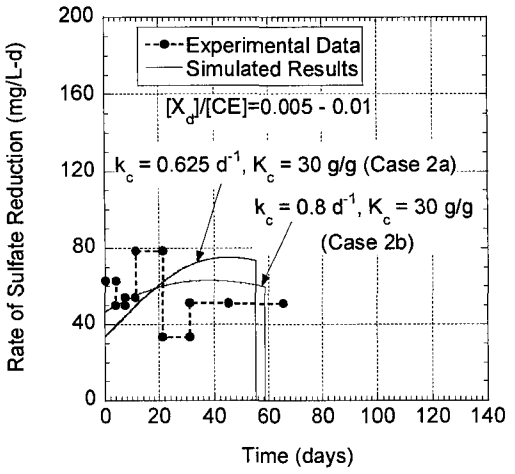

Figure 3.8 – Comparison of simulated and experimental rates of sulfate reduction for batch test 2, with different Contois decomposition kinetics (k_c = decomposition rate coefficient; K_c = half-saturation coefficient; $[X_d]/[CE]$ = initial concentration ratio of decomposer bacteria to polysaccharide).

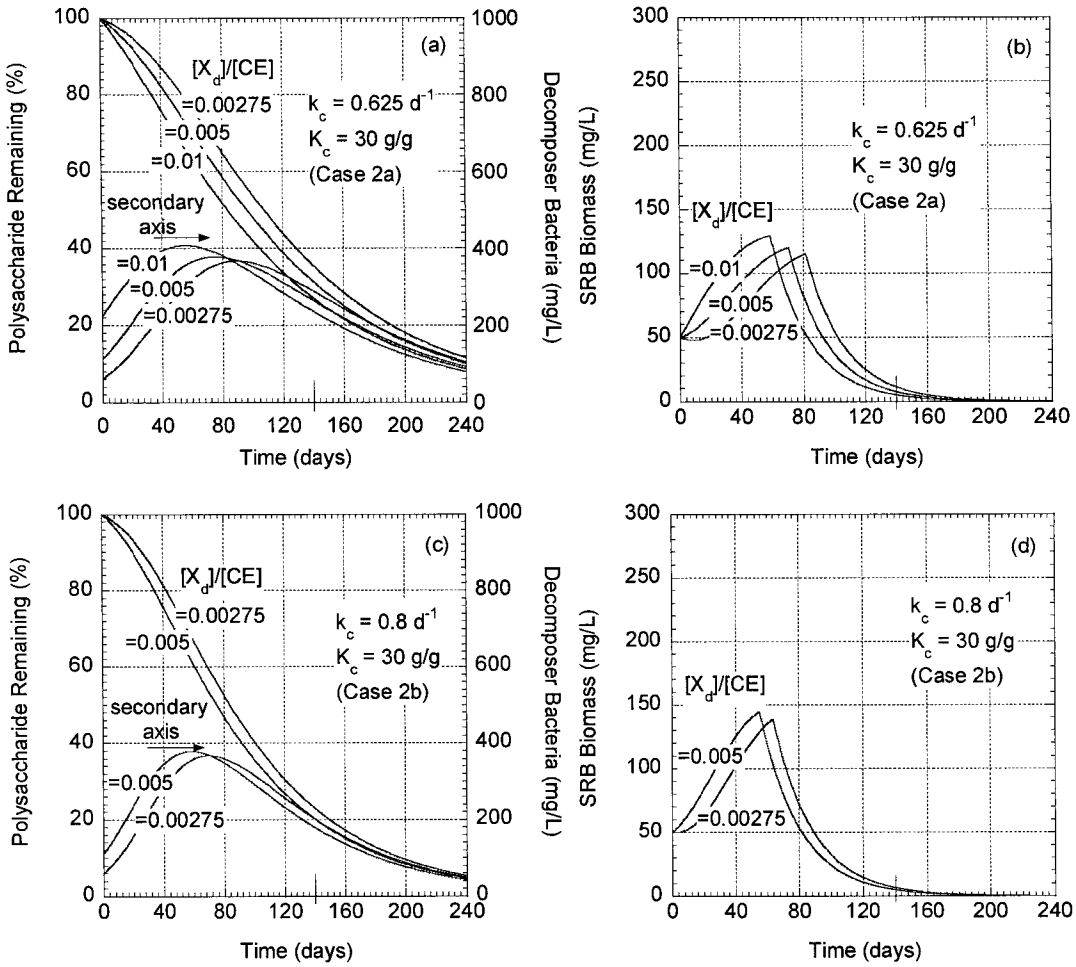

Figure 3.9 – Simulated percentages of initial polysaccharide, and decomposer and sulfate-reducing bacteria concentrations for batch test 2 based on different Contois decomposition kinetics (k_c = decomposition rate coefficient; K_c = half-saturation coefficient; $[X_d]/[CE]$ = initial concentration ratio of decomposer bacteria to polysaccharide).

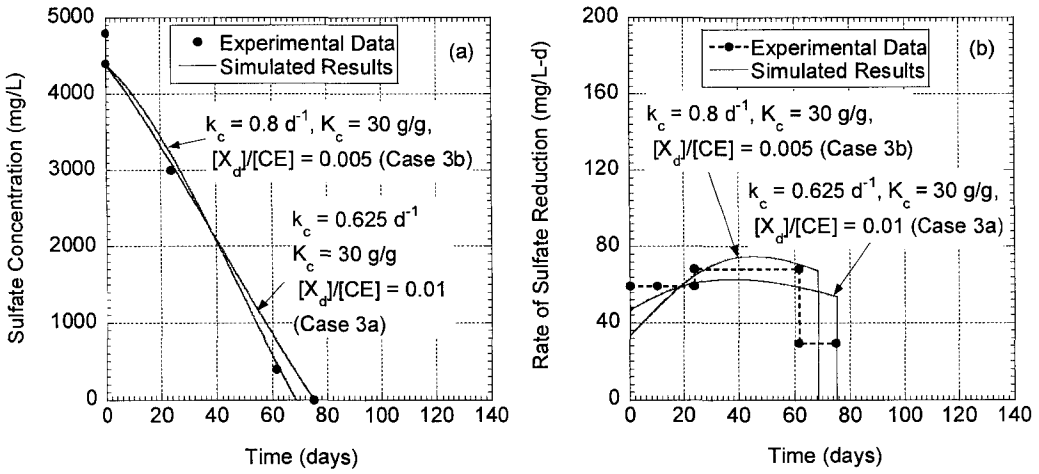

Figure 3.10 – Comparison of experimental data and simulated results for batch test 3 based on different Contois decomposition kinetics (k_c = decomposition rate coefficient; K_c = half-saturation coefficient; $[X_d]/[CE]$ = initial concentration ratio of decomposer bacteria to polysaccharide).

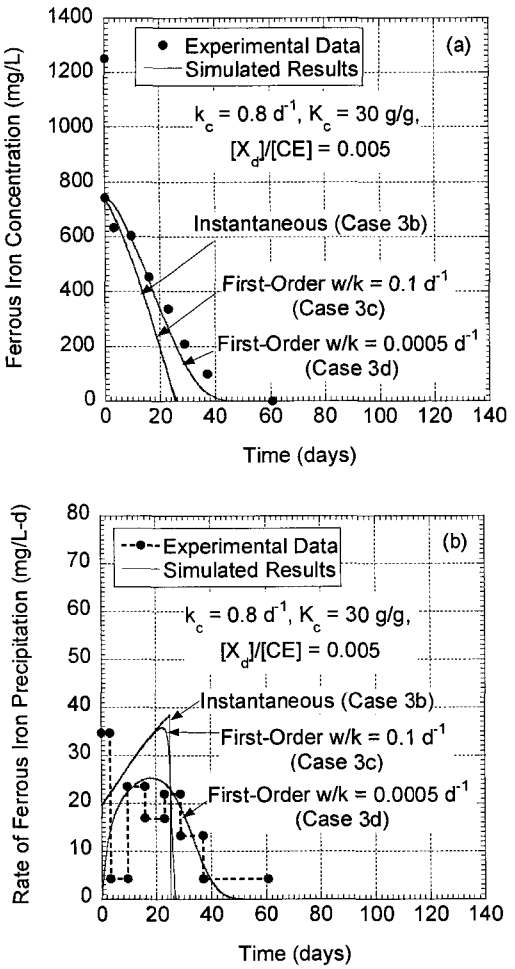

Figure 3.11 – Comparison of experimental data and simulated results for batch test 3 based on different Contois decomposition kinetics and assuming instantaneous or first-order precipitation (k_c = decomposition rate coefficient; K_c = half-saturation coefficient; $[X_d]/[CE]$ = initial concentration ratio of decomposer bacteria to polysaccharide; k = first-order precipitation rate coefficient).

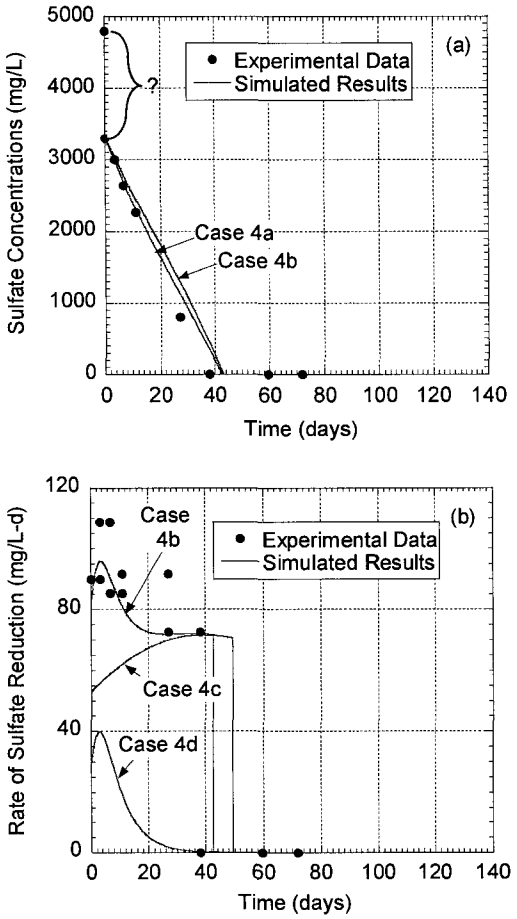

Figure 3.12 – Comparison of experimental and simulated sulfate concentrations and rates of sulfate reduction for batch test 4 (refer to Table 3 for parameter values for Cases 4a – 4d).

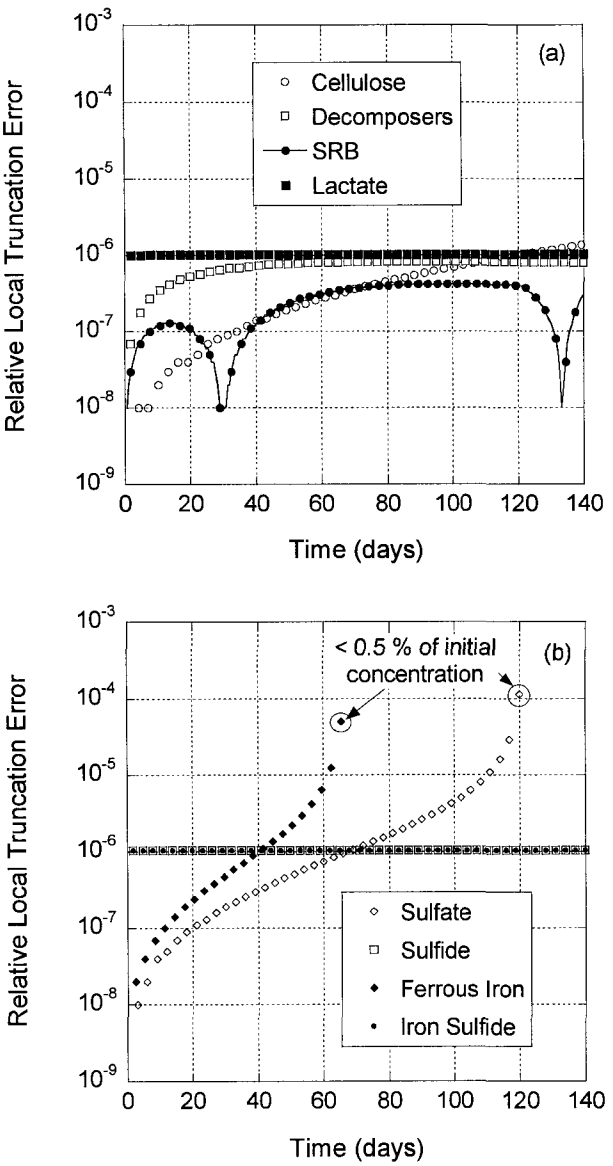

Figure 3.13 – Relative local truncation error in batch test 1 (Case 1b) for: (a) cellulose, decomposer bacteria, SRB, and lactate, and (b) sulfate, hydrogen sulfide, ferrous iron, and iron sulfide.

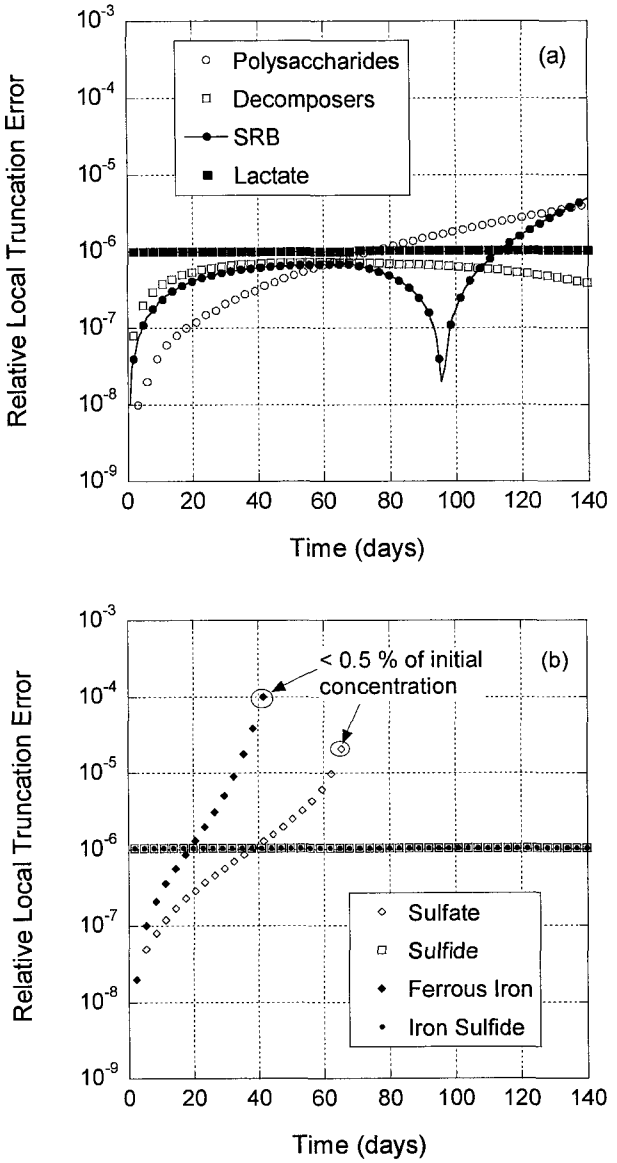

Figure 3.14 – Relative local truncation error in batch test 3 (Case 3a) for: (a) polysaccharides, decomposer bacteria, SRB, and lactate, and (b) sulfate, hydrogen sulfide, ferrous iron, and ferrous iron sulfide.

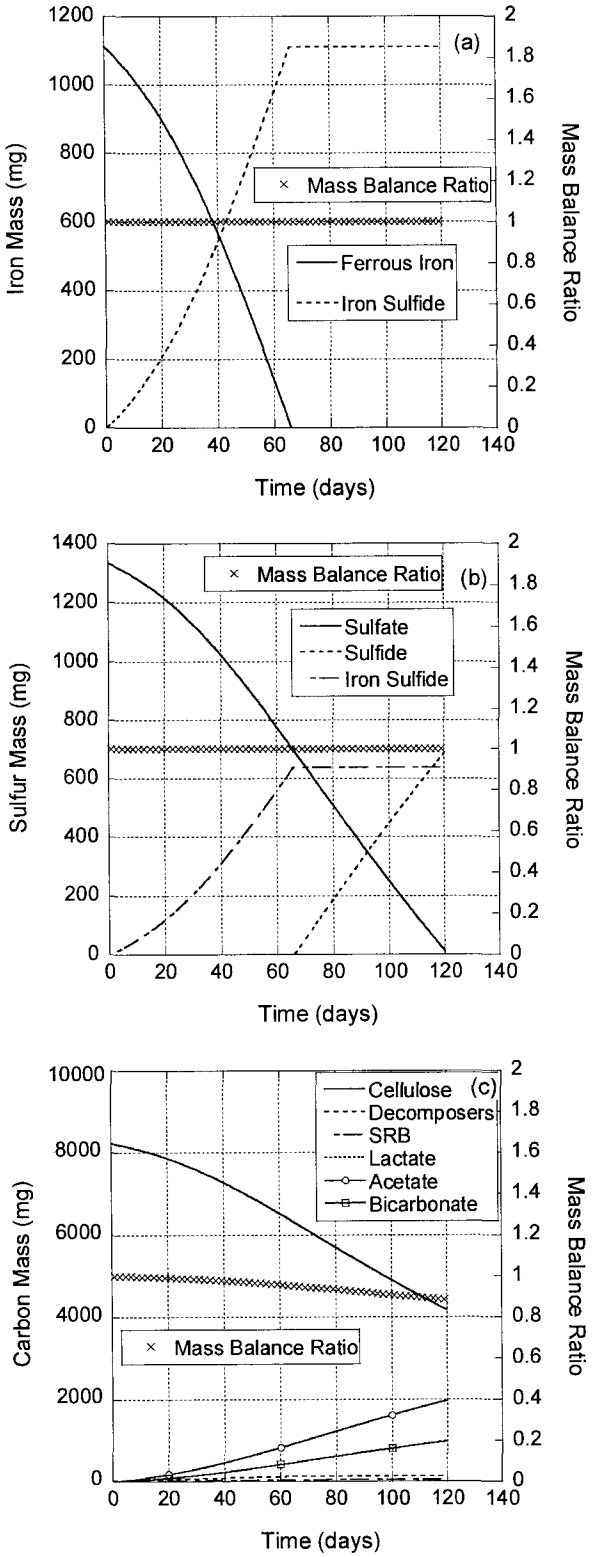

Figure 3.15 – Examples of elemental mass conservation verifications in batch test 1 (Case 1b) (a) iron, (b) sulfur, and (c) carbon.

CHAPTER 4

MODELING COLUMN EXPERIMENTS FOR METALS PRECIPITATION BASED ON SULFATE REDUCTION AND DECOMPOSITION OF ORGANIC SOLIDS

ABSTRACT: Simulated effluent concentrations are compared to previously reported measured concentrations from two column tests. For one column, the comparison is based on ferrous iron (Fe^{2+}), sulfate (SO_4^{2-}), hydrogen sulfide (H_2S), and calcium (Ca^{2+}), whereas Fe^{2+}, SO_4^{2-}, and zinc (Zn^{2+}) are compared for the other column. The concentrations of decomposable polysaccharides, bacterial populations, dissolved organic substrates, and precipitates of iron sulfide ($FeS_{(s)}$), zinc sulfide ($ZnS_{(s)}$), calcite ($CaCO_{3(s)}$), and siderite ($FeCO_{3(s)}$) along the column length also are simulated. Good temporal approximations of the measured concentrations were simulated when using Contois kinetics for decomposition of polysaccharides, Monod kinetics for lactate-based sulfate reduction, kinetically controlled precipitation of metal sulfides and, for one column, the concomitant kinetically controlled reversible dissolution-precipitation of $CaCO_{3(s)}$ and $FeCO_{3(s)}$. For one column, Fe^{2+} removal occurs both as $FeS_{(s)}$ based on SO_4^{2-} reduction coupled to, and limited by, polysaccharide decomposition, and as $FeCO_{3(s)}$ limited by $CaCO_{3(s)}$ dissolution, with the long-term removal capacity attributable to sustained SO_4^{2-} reduction. For the other column, competitive precipitation between Fe^{2+} and Zn^{2+} with H_2S results in stratification of these precipitates along the column length. The mathematical model coupled to flow and contaminant transport was

capable of approximating experimental trends in data as well as providing insight into the behavior of other species (e.g., bacterial populations) in both column tests. Adjusted parameter values, and insight gained with the simulations, are useful for future modeling of other column tests or field-scale systems based on similar biochemistry.

Key Words: Acid mine drainage, Bioremediation, Calcite dissolution, Cellulose decomposition, Column tests, Decomposition kinetics, Mathematical modeling, Polysaccharide decomposition, Siderite Precipitation, Solid organic materials, Sulfate reduction.

4.1 INTRODUCTION

The results of several studies involving sulfate-reducing (SR) flow-through experiments for metals precipitation based on decomposable organic solids, such as column and bioreactor tests, have demonstrated the potential use of sulfate (SO_4^{2-}) reduction and metal-sulfide precipitation for remediation of acid mine drainage (AMD) (e.g., Tuttle at al. 1969, Wakao et al. 1979, Dvorak et al. 1992, Hammack and Edenborn 1992, Bechard et al. 1994, Chang et al. 2000, Waybrant et al. 2002, Gibert et al. 2003, Hulshof et al. 2003, Amos et al. 2004, Gibert et al. 2004, Luptakova and Kusnierova 2005, Whitehead et al. 2005). Examples of the solid, decomposable organic materials that have been evaluated for this purpose include sawdust (e.g., Tuttle et al. 1969, Wakao et al. 1979), spent mushroom compost (e.g., Dvorak et al. 1992, Hammack and Edenborn 1992), fresh alfalfa (e.g., Bechard et al. 1994), and wood chips (e.g., Chang et al. 2000, Waybrant et al. 2002, Hulshof et al. 2003).

Studies involving field applications of SR systems for AMD remediation in permeable reactive barriers (PRBs) and large-scale bioreactors also have been reported. Examples of field applications include the SR-PRB constructed at the Nickel Rim mine in Ontario, Canada (Benner et al. 1999) and the SR-PRB constructed at a former copper mine in central Bulgaria (Groudev et al. 2003).

In terms of modeling the rate of SO_4^{2-} reduction in these systems, growth of SR bacteria (i.e., SRB) based on Monod kinetics (Monod 1949) has been included in some models, but the precursor decomposition of solid organic materials has not been included (e.g., Schafer et al. 1998a,b, Prommer et al. 2001). In other models, the rate of SO_4^{2-}

reduction has been linked to a modeled rate of organic-material decomposition, but the associated bacterial populations and growth have not been included (e.g., Bourdeau and Westrich 1984, Westrich and Berner 1984, Drury 2000).

Mayer et al. (2002) describe a reactive transport model including AMD remediation based on SO_4^{2-} reduction, but this model apparently does not include bacterial populations and solid organic substrates. Also, Benner et al. (2002) and Amos et al. (2004) describe a simple model where the rate of SO_4^{2-} reduction is assumed equal to a constant value multiplied by a hyperbolic term that accounts for SO_4^{2-} limitation, with the constant value based on *a priori* fitting to measured SO_4^{2-} data, for example, from a previous column test.

The objective of this study is to extend the previous evaluation of a new biochemical model in Chapter 3 (Hemsi et al. 2005) based on batch equilibrium (no-flow tests) to systems involving solution flow that are more characteristic of field applications. The biochemical model applied in this study includes SO_4^{2-} reduction and metals precipitation coupled to, and limited by, the decomposition of polysaccharides in solid organic materials, as well as iron precipitation as a carbonate solid phase limited by dissolution of calcite ($CaCO_{3(s)}$) for one of the columns, and also includes the dynamics of the bacterial populations. The objective is achieved by comparing the results of simulations using the biochemical model coupled with flow and contaminant transport to experimental data from two SR column tests in the literature. The columns evaluated in this study are assumed to be representative of saturated flow-through systems (e.g., permeable reactive barriers) that are at sufficient depth below the ground surface so as to represent closed systems (i.e., no interchange between the atmosphere and the permeable

reactive medium).

4.2 BASIS FOR EVALUATION

Simulated results for SO_4^{2-}, Fe^{2+}, H_2S, and Ca^{2+} (Column 1) and SO_4^{2-}, Fe^{2+} and Zn^{2+} (Column 2) versus time are compared to column experimental data from Waybrant et al. (2002) and Hulshof et al. (2003), respectively. The experiments were performed at room temperature, which is assumed equal to 25 °C (e.g., Amos et al. 2004). Measured influent and effluent pH for the columns ranged from approximately 6.5 to 7.5, which is consistent with the range in pH assumed in the model. All simulations are based on saturated, steady-state flow in a homogeneous system.

For Column 1 (Waybrant et al. 2002), the comparisons include simulated results previously obtained by Amos et al. (2004). The simulated behaviors of polysaccharides, dissolved organic substrates, resident bacterial populations (i.e., decomposers and SRB), and solid precipitates (i.e., $FeS_{(s)}$, calcite, and siderite for Column 1, and $FeS_{(s)}$ and $ZnS_{(s)}$ for Column 2), which are not shown in the aforementioned references, also are presented in this study. For Column 2 (Hulshof et al. 2003), H_2S data is not reported and, therefore, is not shown in this study. The possibility of H_2S volatilization was neglected by Waybrant et al. (2002) and Amos et al. (2004) on the basis that H_2S generated by SO_4^{2-} reduction was readily removed through metal precipitation. Thus, although partial volatilization of H_2S to the gas phase is included in the model, this process was neglected in the simulations, which is consistent with the assumption of saturated conditions and negligible liquid-gas interfaces (i.e., a closed system). The possibility of sorption of Fe^{2+} and Zn^{2+} to the surfaces of the organic materials, which were likely to be negatively

charged for the range of pH in the columns (e.g., Sposito 1989), also was neglected by Waybrant et al. (2002), Hulshof et al. (2003), and Amos et al. (2004), and similarly is not evaluated in this study. Although $Zn^{2+}$and Ni^{2+} (Column 1) and Ni^{2+}, Cd^{2+}, and Cu^{2+} (Column 2) were present in the influent solutions at low concentrations (i.e., ~ 1 to 5 % of the concentration for Fe^{2+} on a mg/L basis), the precipitation of these metals with H_2S was neglected, assuming this precipitation to be negligible relative to that for Fe^{2+}, which is consistent with the assumption by Amos et al. (2004).

Only the longer term column reactivity and SRB growth couple to, and limited by, the decomposition of solid organic materials is simulated in this study. Dissolved organic substrates (e.g., lactate or $C_3H_5O_3^-$) are assumed to be absent from both the influent solution and the initial pore-space solution in the columns. The SRB acclimatization period prior to the onset of the experiments is not simulated in this study. During this period, the columns were flushed with a $CaSO_4$/Na-lactate solution, and significant growth of the resident SRB population was observed (e.g., in Column 2, the SRB most probable numbers increased by approximately three orders of magnitude). The initial equivalent SRB biomass concentrations adopted in this study are assumed to incorporate the effect of the acclimatization period. Also, uniform initial distributions of organic decomposable materials and bacterial populations within the reactive portions of the columns are assumed. A schematic profile for both Columns 1 and 2 is provided in Fig. 4.1. The composition of the influent solutions for Columns 1 and 2 used for the simulations are given in Table 4.1.

4.2.1 Column 1

Column 1 is an experiment based on sewage sludge, leaf mulch, sawdust, and wood chips (Waybrant et al. 2002). The specific discharge, solution residence time, and measured longitudinal dispersivity (α_L) for this column were approximately 13.9 mm/d, 15.4 d, and 20 mm, respectively.

The total and pore volumes for the reactive portion of the column were approximately 658 cm^3 and 352 cm^3 (i.e, a porosity of 0.535), respectively. The column was filled with 52 % inorganic materials and 48 % organic materials, with the organic materials comprised of approximately 40.5 % leaf mulch, 22 % sawdust, 21 % sewage sludge, and 16.5 % wood chips, all by dry mass. For the simulations, the initial dry masses of organic materials in the reactive portion were estimated at 21,800 mg leaf mulch, 11,800 mg sawdust, 11,300 mg sewage sludge, and 8,900 mg wood chips.

The inorganic materials in the column included gypsum ($CaSO_4.2H_2O_{(s)}$) and were soaked in a solution saturated with respect to calcite ($CaCO_{3(s)}$). As a result, SO_4^{2-} concentrations may have been impacted by (i) the dissolution of $CaSO_4{\cdot}2H_2O_{(s)}$, (ii) the oxidation of crushed pyrite in an inorganic layer located near the column inlet, and (iii) the $CaSO_4$/Na-lactate solution permeated through the column prior to the onset of the experiment (Waybrant et al. 2002). However, these processes were not considered in Waybrant et al. (2002) and Amos et al. (2004), and similarly are neglected in this study.

Effluent calcium (Ca^{2+}) concentrations significantly higher than those in the influent solution were measured for approximately 250 d. After 250 d, Ca^{2+} effluent concentrations equaled the influent concentrations. Based on a geochemical analysis using the chemical composition of the effluent solution, Waybrant et al. (2002) concluded

that, for the initial 250 d, the solution was under saturated with respect to $CaSO_4{\cdot}2H_2O_{(s)}$ and $FeCO_{3(s)}$ and over saturated with respect to $CaCO_{3(s)}$. However, after 250 d, the analysis indicated under saturation with respect to $CaCO_{3(s)}$ and over saturation with respect to $FeCO_{3(s)}$. In contrast, Amos et al. (2004) interpreted that the solution was under saturated with respect to $CaCO_{3(s)}$ and over saturated with respect to $FeCO_{3(s)}$ for the period ranging from approximately 100 to 300 d.

Since the interpretation by Amos et al. (2004) is more consistent with the behavior indicated by the Ca^{2+} effluent concentrations, this interpretation also is adopted herein. In this regard, the mutual enhancement of $CaCO_{3(s)}$ dissolution and $FeCO_{3(s)}$ precipitation between about 100 and 300 d constituted a major mechanism for Fe^{2+} removal in the column (Amos et al. 2004), and the initial amount of $CaCO_{3(s)}$ present in the column was adjusted such that $CaCO_{3(s)}$ was depleted after about 300 d (Amos et al. 2004). As a result, the main mechanisms for Fe^{2+} removal considered for this column are Fe^{2+} precipitation as Fe^{2+} mono-sulfide (i.e., an approximation to mackinawite, $FeS_{0.9(s)}$, and/or amorphous $FeS_{(s)}$), and Fe^{2+} precipitation as siderite ($FeCO_{3(s)}$), limited by $CaCO_{3(s)}$ dissolution. The pH buffering capacity of the sulfate-reducing column requires HCO_3^- that is produced by SO_4^{2-} reduction to remain in solution to partially neutralize the acidity of the influent solution. Based on this rationale, HCO_3^- released by SO_4^{2-} reduction was assumed unavailable for $FeCO_{3(s)}$ precipitation, similar to what was assumed by Amos et al. (2004).

Finally, although the column influent solution contained $Zn^{2+}$and Ni^{2+} at concentrations generally < 1 mg/L and < 3.3 mg/L, respectively, with a spike for Ni^{2+} of 12 mg/L, precipitation of these metals with H_2S likely was negligible relative to that for

Fe^{2+}, because the $Zn^{2+}$and Ni^{2+} concentrations were on the order of only 1 % (mg/L basis) of that for Fe^{2+}. Thus, the fate and mobility of both $Zn^{2+}$and Ni^{2+} are not considered in this study, which is consistent with the assumption in Amos et al. (2004). Although the influent solution contained Na^{+}, K^{+}, and Mg^{2+}, these elements were assumed by Amos et al. (2004) to be non-reactive, and similarly are not considered in this study. Finally, although Mn^{2+} also was present in the influent solution, no experimental data for Mn^{2+} is shown in Waybrant et al. (2002), and Amos et al. (2004) reported that Mn^{2+} should have a negligible impact on the system. As a result, Mn^{2+} is not considered in this study.

4.2.2 Column 2

Column 2 is the experiment using wood chips reported by Hulshof et al. (2003). The specific discharge and solution residence time for this column were approximately 14.5 mm/d and 14.1 d, respectively. The value of α_L was not measured, so a value of 20 mm is assumed for the simulations. This assumption is evaluated subsequently with additional simulations using α_L of 10 mm and 40 mm.

The total and pore volumes of the reactive portion of the column were approximately 628 cm^3 and 305 cm^3 (i.e., porosity of 0.485), respectively. The column was filled with 80 % inorganic materials and 20 % wood chips, by volume. These volume-based percentages correspond to dry-mass percentages of approximately 97 % for inorganic materials and 3 % for wood chips. The initial dry mass of wood chips in the reactive portion of this column is estimated at approximately 13,000 mg.

The tailings material added to the reactive mixture in the column as part of the non-sulfide minerals contained < 1 % (dry mass) $CaCO_{3(s)}$, approximately four times this

amount in dolomite ($CaMg(CO_3)_{2(s)}$), and approximately 0.3 to 0.5 % (dry mass) $CaSO_4 \cdot 2H_2O_{(s)}$ in a natrojarosite residue (Hulshof et al. 2003). Dolomite is assumed to have a relatively minor impact in this study due to relatively slow dissolution kinetics (e.g., Drever 1997). The geochemical analysis performed by Hulshof et al. (2003) based on the chemical compositions of the influent and effluent solutions indicated that the influent solution tended to be under saturated, whereas the effluent solution was super saturated with respect to $CaCO_{3(s)}$ and $CaSO_4 \cdot 2H_2O_{(s)}$. Thus, this analysis indicated the tendency to dissolve $CaCO_{3(s)}$ and $CaSO_4 \cdot 2H_2O_{(s)}$ near the influent side of the column, and to precipitate these minerals near the effluent side. Measured Ca^{2+} concentrations in the effluent solution that were approximately 40 % higher than those in the influent solution suggest the existence of sources of Ca^{2+} in the column. These sources may have been due to $CaCO_{3(s)}$ and $CaSO_4 \cdot 2H_2O_{(s)}$ dissolution overcoming precipitation, as well as the $CaSO_4$/Na-lactate solution used as the initial permeant liquid in the column experiment.

However, the existence of a net source for Ca^{2+} in the column does not necessarily imply the existence of a comparable net source for SO_4^{2-}, since SO_4^{2-} concentrations are unaffected by the presence of calcite and dolomite. In addition, SO_4^{2-} is practically unaffected by the $CaSO_4$/Na-lactate solution, since SRB growth and SO_4^{2-} reduction consumed SO_4^{2-} during acclimatization. More specifically, the longer term (i.e., > 100 d) measured SO_4^{2-} effluent concentrations ranging from about 4,000 to 4,500 mg/L are essentially equal to the input concentration, indicating that the effect of net sources for SO_4^{2-} in the column was negligible.

The possible precipitation of Fe^{2+} and Zn^{2+} as $FeCO_{3(s)}$ and smithsonite ($ZnCO_{3(s)}$)

also appear to have relatively little effect compared to the precipitation of Fe^{2+} and Zn^{2+} as mono-sulfides (Hulshof et al. 2003). For Zn^{2+}, the geochemical analysis performed by Hulshof et al. (2003) suggested the possibility of over saturation with respect to $ZnCO_{3(s)}$, and although an unknown fraction of Zn^{2+} may have precipitated as $ZnCO_{3(s)}$, the process was not quantified such that $ZnS_{(s)}$ remains the only sink for Zn^{2+} considered in this study.

Finally, although the column influent solution contained Cd^{2+}, Cu^{2+}, and Ni^{2+}, the precipitation of these metals with H_2S likely was negligible relative to that for Fe^{2+} and Zn^{2+}, since the concentrations of Cd^{2+} (< 5 mg/L), Cu^{2+} (< 2 mg/L), and Ni^{2+} (< 3 mg/L) were only ~ 5 % (mg/L basis) of the combined concentrations of $Fe^{2+}$and Zn^{2+}. Thus, Cd^{2+}, Cu^{2+}, and Ni^{2+} are not considered in this study.

4.3 MODEL DESCRIPTION AND SOLUTION

The mathematical model in this study includes (Chapter 2): (i) anaerobic decomposition of polysaccharides in solid organic materials due to the activity of decomposer bacteria in accordance with the Contois kinetic model (Contois 1959), (ii) SO_4^{2-} reduction based on the incomplete oxidation of lactate, including SRB growth in accordance with the Monod kinetic model (Monod 1949), (iii) kinetically controlled precipitation of metal mono-sulfides, and (iv) reversible kinetically controlled dissolution or precipitation of carbonate minerals. Although available in the model, the partial volatilization of H_2S to the gas phase (Hemsi et al. 2005), and secondary biochemical processes such as SO_4^{2-} reduction based on acetate and methanogenesis were not included in the simulations.

Steady-state flow and multi-species reactive contaminant transport were modeled using MODFLOW 2000 version 1.7 (Harbaugh et al. 2000) and RT3D version 2.5 (Clement 1997, 2003), with transport coupled in time with the user-defined subroutine containing the biochemical reactions which consisted of a system of ordinary differential equations (Chapter 2) that can be step-wise integrated in time using a numerical Runge-Kutta-Fehlberg (RKF) method (Chapra and Canale 2002). Advection, dispersion, and sink/source mixing were solved in RT3D using the Total Variation Diminishing method (Zheng and Wang 1999). Reaction operator splitting then is used to couple contaminant transport and reactivity (Clement 1997). Transport time steps were selected on the basis of the requirements for advection, dispersion, and sink/source mixing (e.g., Zheng 1990) automatically set in RT3D, and were on the order of 0.015 d. Multiple reaction time steps for RKF integration are allowed within each transport time step, and RT3D stops if more than 3000 RKF time steps are required within each transport time step (Clement 1997). The columns were modeled as discretized domains with uniform grid discretization of 5 mm. At the column inlet, specified flux and constant-concentration boundary conditions were applied for flow and transport, and freely draining and zero dispersive mass flux (i.e., $\partial C/\partial x = 0$) boundary conditions were applied at the column outlet.

Non-reactive (i.e., advective-dispersive) transport in the columns was verified (Fig. 4.2) prior to coupling biochemical reactivity to transport. As shown in Fig. 4.2a, breakthrough curves for non-reactive transport in Column 1 were modeled and compared to those based on one-dimensional analytical solutions by Ogata and Banks (1961) and Cleary and Adrian (1973) as implemented in Microsoft® Excel and Mathsoft® Mathcad, respectively. For α_L = 20 mm, modeled results compared more favorably with the

Cleary-Adrian solution than with the Ogata-Banks solution, due to the fact that the effluent boundary condition in the model ($\partial C/\partial x = 0$ at $x = L$, where L is the column length) coincides with that in the Cleary-Adrian solution (e.g., Shackelford 1995a). Also, as shown in Fig. 4.2a, for $\alpha_L = 0$ (i.e., purely advective transport), the level of numerical dispersion for the modeled breakthrough curve is negligible. For Column 2, breakthrough curves for non-reactive transport considering $\alpha_L = 10$, 20, and 40 mm are shown in Fig. 4.2b, with modeled results again comparing favorably with those based on the Cleary-Adrian solution.

4.4 INITIAL CONCENTRATIONS AND PARAMETER VALUES

Initial concentrations and parameter values used in this study for all simulation cases are summarized in Table 4.2 for Column 1 and Table 4.3 for Column 2. Further details regarding the bacterial populations, polysaccharide decomposition, sulfate reduction, sulfide precipitation, and dissolution and precipitation of calcite and siderite follow.

4.4.1 Bacterial Populations

Bacterial populations were inoculated into the columns using sediments from the anaerobic zone of a local creek for Columns 1 and 2 as well as from a mine tailings concentrator for Column 2. The equivalent biomass concentration by dry mass of polysaccharide decomposer bacteria colonizing each decomposable polysaccharide ranges from 0.1 to 10 mg biomass/g of dry polysaccharide, based on cell coverage ranging from approximately 10^9 to 10^{10} cells/g of dry detritus, and considering from 10^{-10}

to 10^{-9} mg per cell on a dry mass basis (e.g., Fenchel and Harrison 1976). A cell coverage ranging from 2 to 15 cells/100 μm^2 of fiber of decomposable detritus is obtained assuming fibers with a 2-mm diameter, 5-mm length, and ~ 3 mg/fiber (Fenchel and Harrison 1976, Henriksen and Breland 2002). Intermediate equivalent concentrations corresponding to concentration ratios by dry mass of decomposer bacteria to decomposable polysaccharide, $[X_d]/[CE]$, ranging from 2.75×10^{-3} to 1×10^{-2} generally were used for the simulations.

The equivalent biomass concentration by dry mass for SRB that are incomplete oxidizers of lactate (e.g., *Desulfovibrio vulgaris*) was estimated to range from 1 to 1000 mg biomass/L of pore liquid when SO_4^{2-} reduction is active. This range is based on the converted abundance ranging from 10^7 to 10^9 cells/mL of pore liquid (e.g., Benner et al. 2002), considering 10^{-10} to 10^{-9} mg/cell by dry mass corresponding to cylindrical cells with a height of 2.35 μm and a diameter of 0.75 μm (Postage 1984). An intermediate value of 50 mg biomass/L of pore liquid generally was used for the simulations, and is equivalent to approximately 10^7 to 10^8 cells/mL of pore liquid, which is consistent with the most probable number (MPN) for SRB of 10^7 cells/g of solid material (i.e., 5×10^7 cells/mL of pore liquid) reported by Hulshof et al. (2003). Moreover, the MPN reported by Hulshof et al. (2002) was measured after the termination of the experiment such that presumably higher SRB values may have occurred during active SO_4^{2-} reduction.

4.4.2 Polysaccharide Decomposition

Consideration of the amounts of anaerobically decomposable polysaccharides within the total organic materials is important prior to the use of the model. Based on a

combination of representative percentages, the initial content of decomposable polysaccharides was estimated to be 50 % of the total dry mass of leaf mulch, sawdust, and wood chips, and 12 % in the case of sewage sludge (Chapter 2). Thus, the initial amounts of decomposable polysaccharides were estimated as 4,000 mg/L sewage sludge, 31,000 mg/L leaf mulch, 17,000 mg/L sawdust, and 13,000 mg/L wood chips (Column 1), and 21,200 mg/L wood chips (Column 2). For Column 2, from 0 to ~ 19 % by dry mass of the polysaccharides in the wood chips was assumed to be more favorably decomposable.

Contois kinetic parameters for polysaccharide decomposition in Column 1 were initially taken on the basis of literature values (Vavilin et al. 1996), and values obtained from the simulation of batch-equilibrium (no-flow) experiments using similar materials (Chapter 3 and Hemsi et al. 2005), and were subsequently adjusted to approximate the experimental results. For sewage sludge, leaf mulch, sawdust, and wood chips, the adjusted Contois decomposition rate coefficients (k_c) were 6.0, 0.5, 0.5, and 0.3 d^{-1}, respectively, and the half-saturation constant (K_c) was 30 mg/mg. For Column 2, more than 81 % (dry mass) of the wood chips was simulated using k_c = 0.3 d^{-1}, whereas the more easily decomposable fraction was simulated using k_c = 2.5 d^{-1}. The adjusted decomposition rate coefficients are from 25 to 35 % lower than those used in Chapter 3 (see Hemsi et al. 2005) for the same materials under batch conditions, whereas the adjusted half-saturation constant is equal to that used in Chapter 3.

4.4.3 Sulfate Reduction

Monod parameters for SRB growth on lactate are the same as those used in

Chapter 3 (also Hemsi et al. 2005), which were based on values taken from the literature. The maximum specific SRB growth rate (μ_{SRB}) was 4.0 d^{-1}, and the half-saturation constants for lactate (K_V) and sulfate (K_{SO}) were 5.0 and 2.0 mg/L, respectively.

4.4.4 Sulfide Precipitation

Kinetically controlled precipitation of Fe^{2+} and Zn^{2+} mono-sulfides was modeled using first-order kinetics (Chapter 2, Hemsi et al. 2005). The first-order rate coefficient for precipitation of $FeS_{(s)}$ (i.e., k_{Fe}) was 1.0 d^{-1}, which is sufficiently high to approximate instantaneous precipitation, based on previous batch-test simulation results (Chapter 3). Despite the fact that Zn^{2+} and Fe^{2+} influent concentrations are similar, effluent Zn^{2+} concentrations (Column 2) are significantly lower than those for Fe^{2+}, suggesting more favorable precipitation kinetics for $ZnS_{(s)}$ as compared to $FeS_{(s)}$. For this reason, a first-order rate coefficient for precipitation of $ZnS_{(s)}$ (i.e., k_{Zn}) of 5.0 d^{-1} was used.

4.4.5 Calcite and Siderite

Reversible dissolution of $CaCO_{3(s)}$ and precipitation of $FeCO_{3(s)}$ were modeled using modified first-order kinetics (Chapter 2). The initial dry mass of $CaCO_{3(s)}$ was assumed as 4,200 mg, or 12,000 mg $CaCO_{3(s)}$/L, which generally agrees with the initial volume fraction of 0.0031 assumed by Amos et al. (2004), considering the mixture porosity of 0.535, and assuming a density of $CaCO_{3(s)}$ in crushed limestone of approximately 2,000 g/L. Dissolution rate coefficients for $CaCO_{3(s)}$ and $FeCO_{3(s)}$ were 300 mg/L-d and 200 mg/L-d, respectively (e.g., Schafer et al. 1998b, Yabusaki et al. 2001, Amos et al. 2004), and precipitation rate coefficients were expressed in terms of

the dissolution rate coefficients. Solubility products for $CaCO_{3(s)}$ of $10^{1.85}$ and for $FeCO_{3(s)}$ of $10^{-0.56}$ were adopted from Drever (1997).

4.5 RESULTS AND DISCUSSION

4.5.1 Reactive Transport for Column 1

4.5.1.1 Concentrations

Simulated SO_4^{2-}, Fe^{2+}, and H_2S effluent concentrations based on Cases 1a and 1b (see Table 4.2) are compared to effluent experimental data. In Fig. 4.3a, SO_4^{2-} experimental data are reasonably approximated by simulated results after adjusting parameter values (i.e., Case 1b). However, as shown in Figs. 4.3b and 4.3c, simulation Case 1b does not provide reasonable approximations to the Fe^{2+} and H_2S experimental data, with significant discrepancies between simulated and experimental Fe^{2+} and H_2S effluent concentrations. Consistent with the assumption in Amos et al. (2004), SO_4^{2-} reduction alone appears to be insufficient to justify the extent of Fe^{2+} removal in Fig. 4.3b, as an additional ~ 1,900 mg of Fe^{2+} would have to be removed in order for the simulated results for Case 1b to approximate the experimental data.

Simulated effluent concentrations for SO_4^{2-}, Fe^{2+}, H_2S, and Ca^{2+} based on Cases 1c and 1d (see Table 4.2) are compared to effluent experimental data. The simulated effluent concentrations for SO_4^{2-} shown in Fig. 4.4a are the same as those based on Case 1b (Fig. 4.3a), since the inclusion of $FeCO_{3(s)}$ precipitation for Cases 1c and 1d does not affect SO_4^{2-}. The simulated effluent concentrations for Fe^{2+} based on Cases 1c and 1d are compared in Fig. 4.4b to effluent experimental data and simulated results by Amos et al. (2004). The simulated results compare favorably with the experimental data for times >

250 d, but show a peak in Fe^{2+} at approximately 240 d that is not evident in the experimental data. Although the effect of influent HCO_3^- appears to be minor, the peak Fe^{2+} concentration at approximately 240 d is reduced by about 40 % based on Case 1d relative to that for Case 1c. Simulated effluent concentrations for Fe^{2+} slowly increase with time after 250 d, which is consistent with decreasing SO_4^{2-} reduction. However, the simulated results by Amos et al. (2004) indicate that effluent Fe^{2+} would decrease with time in the long-term (i.e., > 250 d) for an unspecified reason.

Simulated effluent concentrations for H_2S based on Cases 1c and 1d are compared to effluent experimental data and simulated results by Amos et al. (2004) in Fig. 4.4c. During the initial 75 d, Fe^{2+} is absent from the influent solution, and effluent concentrations of H_2S remain at approximately 360 mg/L, which is consistent with the stoichiometric amount of SO_4^{2-} reduced (Fig. 4.3a). After about 125 d, the simulated results compare favorably with the experimental data. Simulated effluent concentrations for Ca^{2+} based on Cases 1c and 1d, with effluent Ca^{2+} released by $CaCO_{3(s)}$ dissolution, are compared in Fig. 4.4d to experimental data and simulated results obtained by Amos et al. (2004). Simulated results are significantly lower than the experimental data, indicating that sources for Ca^{2+} other than those considered in the simulations (e.g., cation exchange in the organic material, gypsum dissolution) apparently had significant impacts on effluent Ca^{2+}.

Considering Case 1c, simulated equivalent concentrations for $FeS_{(s)}$, $CaCO_{3(s)}$, and $FeCO_{3(s)}$ are shown in Fig. 4.5 as a function of pore volumes of flow, PVF (= vt/L, where v is the seepage velocity, t is time, and L is the length of column). The precipitation of $FeS_{(s)}$ within the column (Fig. 4.5a) begins after 75 d (i.e., ~ 15 PVF),

and is asymmetrical, with greater amounts of $FeS_{(s)}$ precipitating near the column inlet (e.g., Yabusaki et al. 2001). The net dissolution of $CaCO_{3(s)}$ (Fig. 4.5b) is observed to propagate along the column following dissolution fronts that move from the column inlet towards the column outlet such that $CaCO_{3(s)}$ is depleted after about 230 d (15 PVF). The net precipitation of $FeCO_{3(s)}$ (Fig. 4.5c) begins to occur near the column influent side, following $CaCO_{3(s)}$ dissolution, and moving longitudinally towards the column outlet. As $CaCO_{3(s)}$ is depleted, $FeCO_{3(s)}$ precipitation ceases to occur in the column after 15 PVF.

Considering Case 1c, the simulated behavior of decomposable polysaccharides ($n(C_6H_{10}O_5)$) is shown in Fig. 4.6a. The percentages degraded for decomposable polysaccharides in sewage sludge, leaf mulch/sawdust, and wood chips after 425 d are 100, ~ 95, and ~ 83 %, respectively. These percentages indicate that approximately 20,000 mg (124 mmol) of decomposable $C_6H_{10}O_5$ have been degraded, capable of reducing the approximately 91 mmol of SO_4^{2-}, as reported in Amos et al. (2004). The resulting adjusted Contois decomposition rate coefficients are approximately 25 to 35 % lower than those in Chapter 3 (also Hemsi et al. 2005). Slower decomposition kinetics in column experiments relative to those for batch experiments may be due, in part, to the different solid-to-solution ratios and exposure of the organic materials to the liquid phase (i.e., greater exposure of solids in batch tests would tend to favor faster degradation of the solids).

The simulated equivalent concentrations for decomposer bacteria and SRB are shown in Figs. 4.6b and 4.6c, respectively. Wood-chip decomposers grow more steadily and sustain the population over a longer steady-state period than the other populations of decomposers in this system. The simulated SRB population undergoes asymmetrical net

growth during the first 8 PVF and thereafter enters a phase of net decay due to lactate ($C_3H_5O_3^-$) scarcity.

The simulated concentrations for $C_3H_5O_3^-$ and HCO_3^- based on Case 1c are shown in Figs. 4.7a and 4.7b, respectively. High effluent concentrations of $C_3H_5O_3^-$ (~ 2,000 mg/L) occur between 0.5 and 1 PVF and are caused by insufficient SO_4^{2-} reduction during this period. Once SO_4^{2-} reduction becomes active (i.e., SO_4^{2-} reaches the entire column), $C_3H_5O_3^-$ effluent concentrations are approximately zero. High concentrations for HCO_3^- on the order of approximately 160 mg/L, which is in equilibrium with $CaCO_{3(s)}$ with about 110 mg/L Ca^{2+} (Fig. 4.4d), are observed before 5 PVF during the period where $FeCO_{3(s)}$ precipitation is null (influent Fe^{2+} is zero). After about 5 PVF when $FeCO_{3(s)}$ precipitation becomes active, HCO_3^- concentrations drop significantly and approach zero after approximately 13 PVF.

4.5.1.2 Cumulative Mass

The experimental and simulated results also may be reported in terms of the cumulative masses of individual species based on the effluent solution and/or results (e.g., Shackelford 1994, 1995b,c Shackelford and Glade 1997, Navarro et al. 2004). The cumulative mass represents an intermediate step towards determining mass balance verifications.

For simulation Case 1c, SO_4^{2-} mass balances are shown in Figs. 4.8a,b, where the cumulative mass of SO_4^{2-} removed versus time (Fig. 4.8b) was calculated as follows:

$$M_{removed}(t) = An\{\underbrace{\int_0^t [vC_{in}(t) + D(\partial C_{in}/\partial x)]dt}_{M_{in}(t)} - \underbrace{\int_0^t [vC_{eff}(t)]dt}_{M_{out}(t)} - \underbrace{\int_0^L C(x,t)dx}_{M_{stored}(t)}\} \quad (4.1)$$

where $M_{removed}$ is the mass removed, A and L are the cross-sectional area and length of the column, respectively, n is the porosity of the porous medium in the column, D is the coefficient of hydrodynamic dispersion, and C_{in}, C_{eff}, and C are influent (based on Table 4.1), effluent (simulated), and resident (simulated) concentrations, respectively. As shown in Fig. 4.8c, the simulated cumulative mass of SO_4^{2-} reduced after 425 d is approximately 8,000 mg, and compares favorably with a cumulative mass of SO_4^{2-} reduced that can be calculated on the basis of the experimental effluent data using the following expression:

$$M^*_{removed}(t) = A\,n\,v\int_0^t [C_{in}(t) - C^*_{eff}(t)]\,dt \quad (4.2)$$

where $M^*_{removed}$ is the mass removed evaluated from the effluent concentration data, and C^*_{eff} is the measured effluent concentration. The integral is in fact a summation considering all time intervals between measured effluent concentrations, and the evaluation based on Eq. 4.2 neglects the effect of the mass stored.

The cumulative mass of Fe^{2+} precipitated versus time (Case 1c) can be calculated in two ways, i.e., either using mass balances (Fig. 4.9) based on Eq. 4.1, or using the simulated results for $FeS_{(s)}$ and $FeCO_{3(s)}$. Considering the second methodology, the cumulative precipitated masses of $FeS_{(s)}$ and $FeCO_{3(s)}$ were calculated by integration

based on the simulated precipitate concentrations ($C_{precipitate}$) along the column, as follows:

$$M_{precipitate}(t) = An\int_0^L C_{precipitate}(x,t)\,dx \tag{4.3}$$

where $M_{precipitate}$ and $C_{precipitate}$ are the simulated mass and concentration for the precipitate, respectively. As shown in Fig. 4.10a, the cumulative mass of $FeS_{(s)}$ after 425 d is approximately 4,100 mg (i.e., 2,700 mg as Fe^{2+}) and, as shown in Fig. 4.10b, the cumulative mass of $FeCO_{3(s)}$ after about 230 d (i.e., 15 PVF) is approximately 4,000 mg (i.e., 1,900 mg as Fe^{2+}). These masses for $FeS_{(s)}$ and $FeCO_{3(s)}$ can be used as the basis for calculating the mass of Fe^{2+} precipitated through the use of stoichiometric mass yield coefficients, Y, shown in Figs. 4.10a and 4.10b (e.g., the precipitation of one mol or 55.85 g of Fe^{2+} corresponds stoichiometrically to one mole or 87.91 g of $FeS_{(s)}$ resulting in Y = 0.635). As shown in Fig. 4.10c, the resulting cumulative mass of precipitated Fe^{2+} calculated from the precipitated masses of $FeS_{(s)}$ and $FeCO_{3(s)}$ compares favorably versus time with the cumulative mass removed that was evaluated on the basis of the measured effluent concentrations for Fe^{2+} and Eq. 4.2.

4.5.1.3 Mass Balance

Mass balance ratios [= $M_{in}/(M_{out} + M_{stored} + M_{removed})$] for sulfur (S), iron (Fe), and carbon (C) are shown in Fig. 4.11. Mass balance ratios for S and Fe range from unity to ~ 1.01 and ~ 1.03, respectively (Figs. 4.11a,b). For C, separate mass balance ratios

were evaluated for decomposition and SO_4^{2-} reduction based on each of the following respective reactions:

$$2\underbrace{C_6H_{10}O_5}_{\text{cellulose}} + 2H_2O + 0.524NH_4^+ \rightarrow 3.126\underbrace{C_3H_5O_3^-}_{\text{lactate}} + 3.652H^+ + 1.573H_2O + 0.524\underbrace{C_5H_7O_2N}_{\text{biomass, } X_d} \quad (4.4)$$

$$2.128\underbrace{C_3H_5O_3^-}_{\text{lactate}} + SO_4^{2-} + 0.0766NH_4^+ \rightarrow 2HCO_3^- + 0.234H_2O + H_2S + 2\underbrace{C_2H_3O_2^-}_{\text{acetate}} + 0.0766\underbrace{C_5H_7O_2N}_{\text{biomass, } X_{SRB}} \quad (4.5)$$

As shown in Fig. 4.11c, the mass balance ratios for C in decomposition range from unity to ~ 1.05, whereas the mass balance ratios for C in SO_4^{2-} reduction range from ~ 0.95 to unity. In addition, mass budget discrepancies for contaminant transport obtained from RT3D are plotted versus time in Fig. 4.12 for the mobile species. As shown in Fig. 4.12, mass budget discrepancies were $< 10^{-4}$ mg/mg for all species.

4.5.2 Reactive Transport for Column 2

4.5.2.1 Concentrations

Simulated effluent concentrations for SO_4^{2-} based on Cases 2a to 2d are compared to experimental effluent data in Fig. 4.13a. The simulation results based on Case 2d appear to provide the best approximation to the measured SO_4^{2-} concentrations since the simulated concentrations between approximately 20 and 70 d for Case 2d are the lowest among the four cases, whereas the simulated results for all cases are practically the same after about 70 d. However, after about 100 d, the measured effluent concentrations appear to approach the influent concentrations, whereas the simulated SO_4^{2-} concentrations for all cases remain slightly lower than the influent concentrations; i.e., experimental rates of

SO_4^{2-} reduction decline more abruptly towards the end of the experiment relative to the simulated results.

Simulated effluent concentrations for Fe^{2+} based on Cases 2a to 2d are compared to experimental effluent data in Fig. 4.13b. Similar to the simulations for SO_4^{2-}, the simulation results based on Case 2d appear to provide a better approximation to the measured Fe^{2+} concentrations, i.e., with simulated concentrations of approximately zero during the first 45 d and ranging from approximately 30 to 100 mg/L thereafter. The simulated results indicate that the shapes for the temporal distributions in effluent and influent Fe^{2+} are similar, which is expected based on contaminant transport but not readily apparent when considering only the experimental data.

Simulated effluent concentrations for Zn^{2+} are compared to measured Zn^{2+} concentrations in Fig. 4.13c. Similar to the results for Fe^{2+}, the simulated effluent concentrations for Zn^{2+} based on Case 2d also appear to provide a better approximation to the measured Zn^{2+}concentrations. Although influent concentrations for Fe^{2+} and Zn^{2+} are on the same order of magnitude, effluent concentrations for Zn^{2+} are essentially zero, and significantly lower than those for Fe^{2+}.

The effects of changing (i) the initial values for the populations of decomposer bacteria, $[X_d]/[CE]$, from 0.005 for Cases 2a to 2d to 0.00275 and 0.01 for Cases 2e and 2f, respectively, and (ii) α_L from 20 mm for Cases 2a to 2d to 10 and 40 mm for Cases 2g and 2h, respectively, on the simulated effluent concentrations for Fe^{2+} are shown in Figs. 4.14a and 4.14b, respectively. As shown in Fig. 4.14a, increasing the initial population of decomposer bacteria accelerates decomposition and SO_4^{2-} reduction, resulting in lower SO_4^{2-} effluent concentrations versus time, as expected. As shown in Fig. 4.14b,

increasing α_L from 10 to 40 mm has a negligible impact on simulated SO_4^{2-} effluent concentrations such that the use of 20 mm for α_L for the majority of the simulation cases for Column 2 is not expected to constrain the validity of the simulated results.

Considering Case 2d, simulated concentrations $FeS_{(s)}$ and $ZnS_{(s)}$ are shown versus PVF in Fig. 4.15a and 4.15b, respectively. In view of the competitive precipitation between Fe^{2+} and Zn^{2+} with H_2S, Zn^{2+} is initially favored, due to the fact that the precipitation first-order rate coefficient for $Zn^{2+}$is higher than that for Fe^{2+}. In comparing the results in Figs. 4.15a and 4.15b, concentrations of $ZnS_{(s)}$ precipitate are significantly higher than those for $FeS_{(s)}$ towards the influent side of the column, such that the majority of Zn^{2+} precipitate is within this portion of the column. However, towards the effluent side of the column, the Zn^{2+} concentrations are sufficiently low as to allow $FeS_{(s)}$ precipitation to increase and dominate relative to $ZnS_{(s)}$ precipitation. Snapshots of $FeS_{(s)}$ and $ZnS_{(s)}$ contours at 15, 75, and 130 d are shown in Fig. 4.15c to help visualize the stratification of $ZnS_{(s)}$ and $FeS_{(s)}$ precipitates in the column.

The simulated behavior of decomposable polysaccharides in wood chips is shown in Fig. 4.16a. Only about 29 % of the bulk wood chips decomposed after 130 d, whereas 100 % of the easily-decomposable fraction decomposed during this same time frame. The simulated equivalent concentrations for decomposer bacteria and SRB are shown in Figs. 4.16b and 4.16c. Given that only 29 % of the bulk wood chips decomposed after 130 d of operation, the continued net growth in the population of decomposers associated with this material subsequent to this time frame is consistent. The simulated SRB population in this column undergoes net growth only up to about the first 3 PVF, followed by net decay thereafter. Growth appears to occur more evenly distributed along the column length in

this column in comparison to Column 1, presumably due to the relatively slower kinetics of decomposition in Column 2.

4.5.2.2 Cumulative Mass

The cumulative mass of SO_4^{2-} removed versus time for the simulation based on Case 2d is calculated using SO_4^{2-} mass balance (e.g., Figs. 4.17a,b), considering reactive transport (Fig. 4.17b) and Eq. 4.1. As shown in Fig. 4.17c, this cumulative mass of reduced SO_4^{2-} compares well with the cumulative mass of reduced SO_4^{2-} determined using Eq. 4.2 and the experimental effluent concentrations for SO_4^{2-}. By the end of the experiment, corresponding to 130 d, from 1,000 to 1,200 mg SO_4^{2-} have been reduced.

Hulshof et al. (2003) estimated rates of SO_4^{2-} reduction by comparing the experimental effluent data for SO_4^{2-} to influent SO_4^{2-} concentrations (C_{in}), with an underlying assumption that a fixed amount of SO_4^{2-} of 400 mg/L must be added to C_{in} to account for gypsum dissolution. Integrating these rates of SO_4^{2-} reduction with respect to time, the trend shown as open circles in Fig. 4.17c is obtained. Additionally, adding 400 mg/L to C_{in}, and considering the simulated results based on Case 2d, the trend shown as the dashed line in Fig. 4.17c is obtained. However, the consideration of a fixed amount of SO_4^{2-} of 400 mg/L to account for gypsum dissolution appears to be exaggerated relative to both the experimental data and the simulated results based on Case 2d, also due to the fact that the 400 mg/L were estimated by Hulshof et al. (2003) on the basis of the total excess of Ca^{2+} in the effluent solution compared to the influent solution.

The cumulative mass of Fe^{2+} precipitated versus time for Case 2d was calculated using Fe^{2+} mass balance (Figs. 4.18a,b) considering reactive transport (Fig. 4.18b) and

Eq. 4.1. As shown in Fig. 4.18c, approximately 275 mg of Fe^{2+} precipitated within the column during the test, which compares favorably with the cumulative mass of Fe^{2+} removed based on Eq. 4.2 and the experimental concentrations for Fe^{2+}. Similarly, the cumulative mass of Zn^{2+} precipitated was calculated using Eq. 4.1 and Zn^{2+} mass balance (Figs. 4.19a,b), for reactive transport of Zn^{2+} (i.e., Fig. 4.19b). As shown in Fig. 4.19c, approximately 350 mg of Zn^{2+} precipitated during the test, which compares favorably with the cumulative mass of Zn^{2+} removed based on Eq. 4.2 and the experimental concentrations for Zn^{2+}.

4.5.2.3 Mass Balance

Mass balance ratios for sulfur (S), iron (Fe), zinc (Zn), and carbon (C) are shown in Fig. 4.20. Mass balance ratios for S, Fe, and Zn range from unity to ~ 1.01, ~ 1.02, and ~ 1.04, respectively. Carbon mass balance ratios based on decomposition (Eq. 4.4) and SO_4^{2-} reduction (Eq. 4.5) are closer to unity than for Column 1. Additionally, as shown in Fig. 4.21, transport mass budget discrepancies are $< 3 \times 10^{-5}$ mg/mg for all species and, therefore, were considered acceptable.

4.6 CONCLUSIONS

Simulations using a new mathematical model for biochemical reactions coupled to flow and contaminant transport were compared with measured effluent concentrations for two closed-system column tests reported in the literature. The biochemical model included Contois kinetics for decomposition of polysaccharides in solid organic materials, Monod kinetics for lactate-based SO_4^{2-} reduction, first-order kinetically

controlled precipitation of Fe^{2+} and Zn^{2+} mono sulfides and, for one of the columns, the concomitant kinetically controlled reversible dissolution-precipitation of $CaCO_{3(s)}$ and $FeCO_{3(s)}$. Although available in the model, the kinetically controlled partial volatilization of H_2S to the gas phase was neglected, assuming negligible contact between liquid and gas phases in the columns consistent with that for closed systems.

Effluent concentrations for SO_4^{2-}, Fe^{2+}, and H_2S from Column 1 were approximated using the model considering SO_4^{2-} reduction and $FeS_{(s)}$ precipitation with kinetics of SO_4^{2-} reduction coupled to, and limited by, the decomposition of polysaccharides in organic solids, and $FeCO_{3(s)}$ precipitation limited by $CaCO_{3(s)}$ dissolution in the column. Calcite was depleted from the column after approximately 230 d or 15 pore volumes of flow (PVF), and Fe^{2+} removal after approximately 250 d was due exclusively to $FeS_{(s)}$ precipitation, with effluent Fe^{2+} concentrations increasing with time as SO_4^{2-} reduction declined. A cumulative mass analyses indicated that approximately 8,000 mg of SO_4^{2-} were reduced in the column and 2,700 mg of Fe^{2+} were precipitated as $FeS_{(s)}$ throughout the duration of the test (i.e., 425 d), and that approximately 1,900 mg Fe^{2+} were precipitated as $FeCO_{3(s)}$ until 230 d.

Effluent concentrations for SO_4^{2-}, Fe^{2+}, and Zn^{2+} from Column 2 were approximated using the model with SO_4^{2-} reduction limited by wood chips decomposition, and competitive precipitation between Fe^{2+} and Zn^{2+} with H_2S. Zinc precipitation was initially favored, due to the fact that the precipitation first-order rate coefficient for $Zn^{2+}$was higher than that for Fe^{2+}. The majority of Zn^{2+} was precipitated within the half column near to the influent side. Towards the effluent side, Zn^{2+} concentrations were sufficiently low as to allow $FeS_{(s)}$ precipitation to increase and

dominate relative to $ZnS_{(s)}$ precipitation. A cumulative mass analyses indicated that, throughout the duration of the test (i.e., 130 d), from 1,000 to 1,200 mg SO_4^{2-} were reduced in the column, and approximately 275 mg Fe^{2+} and 350 mg Zn^{2+} were precipitated as $FeS_{(s)}$ and $ZnS_{(s)}$, respectively.

The mathematical model coupled to flow and contaminant transport was capable of approximating experimental trends in data as well as providing insight into the behavior of other species (e.g., bacterial populations) in both column tests. Adjusted parameter values, and insight gained with the simulations, are useful for future modeling of other column tests or field-scale systems based on similar biochemistry.

4.7 ACKNOWLEDGEMENTS

This research was funded by the U. S. EPA Science to Achieve Results (STAR) Program under Grant No. R-82951501-0 as part of the U. S. EPA's *Rocky Mountain Regional Hazardous Substance Research Center*. The author extends his thanks to Mr. Christian Johnson, Senior Development Engineer, Battelle-PNWD, Richland (WA), for excellent initial RT3D support.

4.8 REFERENCES

Amos, R.T., Mayer, K.U., Blowes, D.W., and Ptacek, C.J. (2004). Reactive transport modeling of column experiments for remediation of acid mine drainage. *Environmental Science and Technology*, 38(11): 3131-3138.

Bechard, G., Yamazaki, H., Gould, W.D., and Bedard, P. (1994). Use of cellulosic substrates for the microbial treatment of acid mine drainage. *Journal of*

Environmental Quality, 23(1): 111-116.

Benner, S.G, Blowes, D.W., Ptacek, C.J., and Mayer, K.U. (2002). Rates of sulfate reduction and metal sulfide precipitation in a permeable reactive barrier. *Applied Geochemistry*, 17(1): 301-320.

Benner, S.G., Blowes, D.W., Gould, W.D., Herbert, R.B. and C. J. Ptacek (1999). Geochemistry of a permeable reactive barrier for metals and acid mine drainage. *Environmental Science and Technology*, 33(16): 2793-2799.

Boudreau, B.P., and Westrich, J.T. (1984). The dependence of bacterial sulfate reduction on sulfate concentration in marine environments. *Geochimica et Cosmochimica Acta*, 48(12): 2503-2516.

Chang, I.S., Shin, P.K., and Kim, B.H. (2000). Biological treatment of acid mine drainage under sulphate-reducing conditions with solid waste materials as substrates. *Water Research*, 34(4): 1269-1277.

Chapra, S.C., and Canale, R.P. (2002). *Numerical Methods for Engineers*. 4th Edition, McGraw-Hill, New York, NY.

Cleary, R.W., and Adrian, D.D. (1973). Analytical solution of the convective-dispersive equation for cation adsorption in soils. *Soil Science Society of America Journal*, 37(2): 197-199.

Clement, T.P. (1997). A Modular Computer Code for Simulating Reactive Multi-species Transport in 3-Dimensional Groundwater Systems RT3D version 1.0. U.S. Department of Energy and Pacific Northwest National Laboratory. PNNL-11720-1997.

Clement, T.P. (2003). RT3D v.2.5 Update Document, What is New in RT3D version 2.5.

Electronic document: http://bioprocess.pnl.gov/rt3d.htm.

Contois, D.E. (1959). Kinetics of bacterial growth, relationship between population density and specific growth rate of continuous cultures. *Journal of General Microbiology*, 21(1): 40-50.

Drever, J.I. (1997). *The Geochemistry of Natural Waters – Surface and Groundwater Environments*. 3rd Edition, Prentice-Hall, Upper Saddle River, NJ.

Drury, J.W. (2000). Modeling of sulfate reduction in anaerobic solid substrate bioreactors for mine drainage treatment. *Mine Water and the Environment*, 19(1): 18-28.

Dvorak, D.H., Hedin, R.S., Edenborn, H.M., and McIntire, P.E. (1992). Treatment of metal-contaminated water using bacterial sulfate reduction: Results from pilot-scale reactors. *Biotechnology and Bioengineering*, 40(5): 609-616.

Fenchel, T., and Harrison, P. (1976). The significance of bacterial grazing and mineral cycling for the decomposition of particulate detritus. *The Role of Terrestrial and Aquatic Organisms in Decomposition Processes*, J.M. Anderson and A. Macfadyen, eds., Blackwell Scientific Publications, Oxford, UK, 285-299.

Gibert, O., de Pablo, J., Cortina, J.L., and Ayora, C. (2003). Evaluation of municipal compost/limestone/iron mixtures as filling material for permeable reactive barriers for in-situ acid mine drainage treatment. *Journal of Chemical Technology and Biotechnology*, 78(5): 489-496.

Gibert, O., de Pablo, J., Cortina, J.L., and Ayora, C. (2004). Chemical characterization of natural organic substrates for biological mitigation of acid mine drainage. *Water Research*, 38(19): 4186-4196.

Groudev, S., Nicolova, M., Spasova, I., and Schutte, R. (2003). Treatment of waters from

a copper mine by means of a permeable reactive barrier. *Fifty Years of the University of Mining and Geology "St. Ivan Rilski"*, University of Mining and Geology, Sofia (Bulgaria), Volume 46, Part II, Section Mining and Mineral Processing, 229-231.

Hammack, R.W., and Edenborn, H.M. (1992). The removal of nickel from mine waters using bacterial sulfate reduction. *Applied Microbiology and Biotechnology*, 37(5): 674-678.

Harbaugh, A.W., Banta, E.R., Hill, M.C., and McDonald, M.G. (2000). *MODFLOW-2000, the U.S. Geological Survey Modular Ground-Water Model – User Guide to Modularization Concepts and the Ground-Water Flow Process*, USGS Open-File Report 00-92, Reston, VA.

Hemsi, P.S., Shackelford, C.D., and Figueroa, L.A. (2005). Modeling the influence of decomposing organic solids on sulfate reduction rates for iron precipitation. *Environmental Science and Technology*, 39(9): 3215-3225.

Henriksen, T.M., and Breland, T.A. (2002). Carbon mineralization, fungal and bacterial growth, and enzyme activities as affected by contact between crop residues and soil. *Biology and Fertilization of Soils*, 35(1): 41-48.

Hulshof, A.H., Blowes, D.W., Ptacek, C.J., and Gould, W.D. (2003). Microbial and nutrient investigations into the use of in situ layers for treatment of tailings effluent. *Environmental Science and Technology*, 37(21): 5027-5033.

Luptakova, A., and Kusnierova, M. (2005). Bioremediation of acid mine drainage contaminated by SRB. *Hydrometallurgy*, 77(1-2): 97-102.

Mayer, K.U., Frind, E.O, and Blowes, D.W. (2002). Multicomponent reactive transport modeling in variably saturated porous media using a generalized formulation for

kinetically controlled reactions. *Water Resources Research*, 38(9): 13-1 to 13-21.

Monod, J. (1949). The growth of bacterial cultures. *Annual Review of Microbiology*, 3: 371-394.

Navarro, A., Collado, D., Carbonell, M., and Sanchez, J. (2004). Impact of mining activities on soils in a semi-arid environment: Sierra Almagrera district, SE Spain. *Environmental Geochemistry and Health*, 26(4): 383-393.

Ogata, A., and Banks, R.B. (1961). A solution of the differential equation of longitudinal dispersion in porous media. *U.S. Geological Survey Prof. Paper 411-A*, U.S. Geological Survey, Washington, D.C.

Postgate, J.R. (1984). *The Sulphate-Reducing Bacteria*. 2nd Edition. Cambridge University Press, Cambridge, UK.

Prommer, H., Barry, D.A., Chiang, W.H., and Zheng, C. (2001). PHT3D – a MODFLOW/MT3DMS-based reactive multi-component transport model. *MODFLOW 2001 and Other Modeling Odysseys*, H. Seo, E. Poeter, and C. Zheng, eds., International Ground-Water Modeling Center, Colorado School of Mines, Golden, CO, 477-483.

Schafer, D., Schafer, W., and Kinzelbach, W. (1998a). Simulation of reactive processes related to biodegradation in aquifers. 1-Structure of the three-dimensional reactive transport model. *Journal of Contaminant Hydrology*, 31(1-2): 167-186.

Schafer, D., Schafer, W., and Kinzelbach, W. (1998b). Simulation of reactive processes related to biodegradation in aquifers. 2-Model application to a column study on organic carbon degradation. *Journal of Contaminant Hydrology*, 31(1-2): 187-209.

Shackelford, C. D. (1994). Critical concepts for column testing. *Journal of Geotechnical*

Engineering, 120(10): 1804-1828.

Shackelford, C. D. (1995a). Analytical models for cumulative mass column testing. *ASCE Specialty Conference Geoenvironment 2000*, ASCE Geotechnical Special Publication No. 46, Y. B. Acar and D. E. Daniel, eds., New York, NY, 355-372.

Shackelford, C. D. (1995b). Cumulative mass approach for column testing. *Journal of Geotechnical Engineering*, 121(10): 696-703.

Shackelford, C. D. (1995c). Column testing for geoenvironmental applications. *Geo-Environmental Issues Facing the Americas*, E. J. Macari, J. David Frost, and L. F. Pumarada, eds., ASCE, Reston, VA, 117-125.

Shackelford, C. D. and Glade, M.J. (1997). Analytical mass leaching model for contaminated soil and soil stabilized waste. *Ground Water*, 35(2): 233-242.

Sposito, G. (1989). *The Chemistry of Soils*. Oxford University Press, Oxford, UK.

Tuttle, J.H., Dugan, P.R., and Randles, C.I. (1969). Microbial sulfate reduction and its potential utility as an acid mine water pollution abatement procedure. *Applied Microbiology*, 17(2): 297-302.

Vavilin, V.A., Rytov, S.V., and Lokshina, L. (1996). A description of hydrolysis kinetics in anaerobic degradation of particulate organic matter. *Bioresource Technology*, 56(1): 229-237.

Wakao, N., Takahashi, T., Sakurai, Y., and Shiota, H. (1979). A treatment of acid mine water using sulfate-reducing bacteria. *Journal of Fermentation Technology*, 57(5): 445-452.

Waybrant, K.R., Ptacek, C.J., and Blowes, D.W. (2002). Treatment of mine drainage using permeable reactive barriers: column experiments. *Environmental Science and*

Technology, 36(6): 1349-1356.

Westrich, J.T., and Berner, R.A. (1984). The role of sedimentary organic matter in bacterial sulfate reduction: The G model tested. *Journal of Limnology and Oceanography*, 29(2): 236-249.

Whitehead, P.G., Cosby, B.J., and Prior, H. (2005). The Wheal Jane wetlands model for bioremediation of acid mine drainage. *Science of the Total Environment*, 338(1-2): 125-135.

Zheng, C. (1990). MT3D: *A Modular Three-Dimensional Transport Model for Simulation of Advection, Dispersion and Chemical Reaction of Contaminants in Groundwater Systems*. U.S. Environmental Protection Agency and Robert S. Kerr Environmental Research Laboratory, Ada, OK.

Zheng, C., and Wang, P.P. (1999). MT3DMS: *A Modular Three-Dimensional Multispecies Model for Simulation of Advection, Dispersion, and Chemical Reactions of Contaminants in Groundwater Systems; Documentation and User's Guide*. U.S. Army Corps of Engineers. Contract Report SERDP-99-1, December 1999.

Yabusaki, S., Cantrell, K., Sass, B., and Steefel, C. (2001). Multicomponent reactive transport in an in situ zero-valent iron cell. *Environmental Science and Technology*, 35(7): 1493-1503.

Table 4.1 – Composition of the influent solutions for Columns 1 and 2 simulated in this study.

Column	Time (d)	Concentration (mg/L)				
		SO_4^{2-}	Fe^{2+}	Zn^{2+}	Ca^{2+}	HCO_3^{-} (*)
1	0-72.2	1,010	-	-	-	-
	72.2-113.7	3,210	694	-	506	89.7
	113.7-141.4	3,894	1,181	-	99	33.4
	141.4-184.4	3,455	876	-	92	27.4
	184.4-238.2	3,660	956	-	83	20.7
	238.2-282.8	2,000	444	-	205	15.8
	282.8-330.4	1,623	379	-	214	6.8
	330.4-382.7	1,353	334	-	220	16.9
	382.7-425.7	1,400	316	-	-	14.5
2	0-15	4,000	29.3	120	-	-
	15-50	4,350	126.7	120	-	-
	50-75	4,350	116.6	73	-	-
	75-87	4,350	116.6	83	-	-
	87-94.5	4,350	173.3	83	-	-
	94.5-102	4,350	200	83	-	-
	102-107.5	4,350	144	83	-	-
	107.5-120	4,350	116.6	83	-	-
	120-122	4,350	34.7	67.5	-	-
	122-130	4,350	10.7	67.5	-	-

*Estimated from the alkalinity (molar basis) of the influent solution.

Table 4.2 – Parameter values for different simulation cases for Column 1.

Case	Materials	Decomposition (Contois kinetics)			Sulfate Reduction (Monod kinetics)	Precipitation (first-order kinetics)				Dispersivity
						$FeCO_{3(s)}$			$FeS_{(s)}$	
		Initial [CE] (mg/L)	k_c (d^{-1})	Initial $[X_d]$/[CE]	$[X_{SRB}]$ (mg/L)	Initial $CaCO_{3(s)}$ (mg)		Influent HCO_3^-	k_{Fe} (d^{-1})	α_L (mm)
1a	SS	4,000	8.0	0.01	50	No	0.0	No	1.0	20
	LM/S	48,000	0.8	0.005						
	WC	13,000	0.4							
1b	SS	4,000	6.0	0.01	50	No	0.0	No	1.0	20
	LM/S	48,000	0.5	0.005						
	WC	13,000	0.3							
1c	SS	4,000	6.0	0.01	50	Yes	4200	No	1.0	20
	LM/S	48,000	0.5	0.005						
	WC	13,000	0.3							
1d	SS	4,000	6.0	0.01	50	Yes	4200	Yes	1.0	20
	LM/S	48,000	0.5	0.005						
	WC	13,000	0.3							

SS: sewage sludge; LM/S: leaf mulch/sawdust; WC: wood chips.

Table 4.3 – Parameter values for different simulation cases for Column 2.

Case	Materials	Decomposition (Contois kinetics)			Sulfate Reduction (Monod kinetics)	Precipitation (first-order kinetics)		Dispersivity
						$FeS_{(s)}$	$ZnS_{(s)}$	
		Initial [CE] (mg/L)	k_c (d^{-1})	Initial $[X_d]$/ [CE]	$[X_{SRB}]$ (mg/L)	k_{Fe} (d^{-1})	k_{Zn} (d^{-1})	α_L (mm)
2a	WC	21,200	0.3	0.005	50	1.0	5.0	20
2b	WC	19,200	0.3	0.005	50	1.0	5.0	20
	EDWC	2,000	2.5					
2c	WC	18,200	0.3	0.005	50	1.0	5.0	20
	EDWC	3,000	2.5					
2d	WC	17,200	0.3	0.005	50	1.0	5.0	20
	EDWC	4,000	2.5					
2e	WC	17,200	0.3	0.00275	50	1.0	5.0	20
	EDWC	4,000	2.5					
2f	WC	17,200	0.3	0.01	50	1.0	5.0	20
	EDWC	4,000	2.5					
2g	WC	17,200	0.3	0.005	50	1.0	5.0	10
	EDWC	4,000	2.5					
2h	WC	17,200	0.3	0.005	50	1.0	5.0	40
	EDWC	4,000	2.5					

WC: wood chips; EDWC: easily decomposable wood chips.

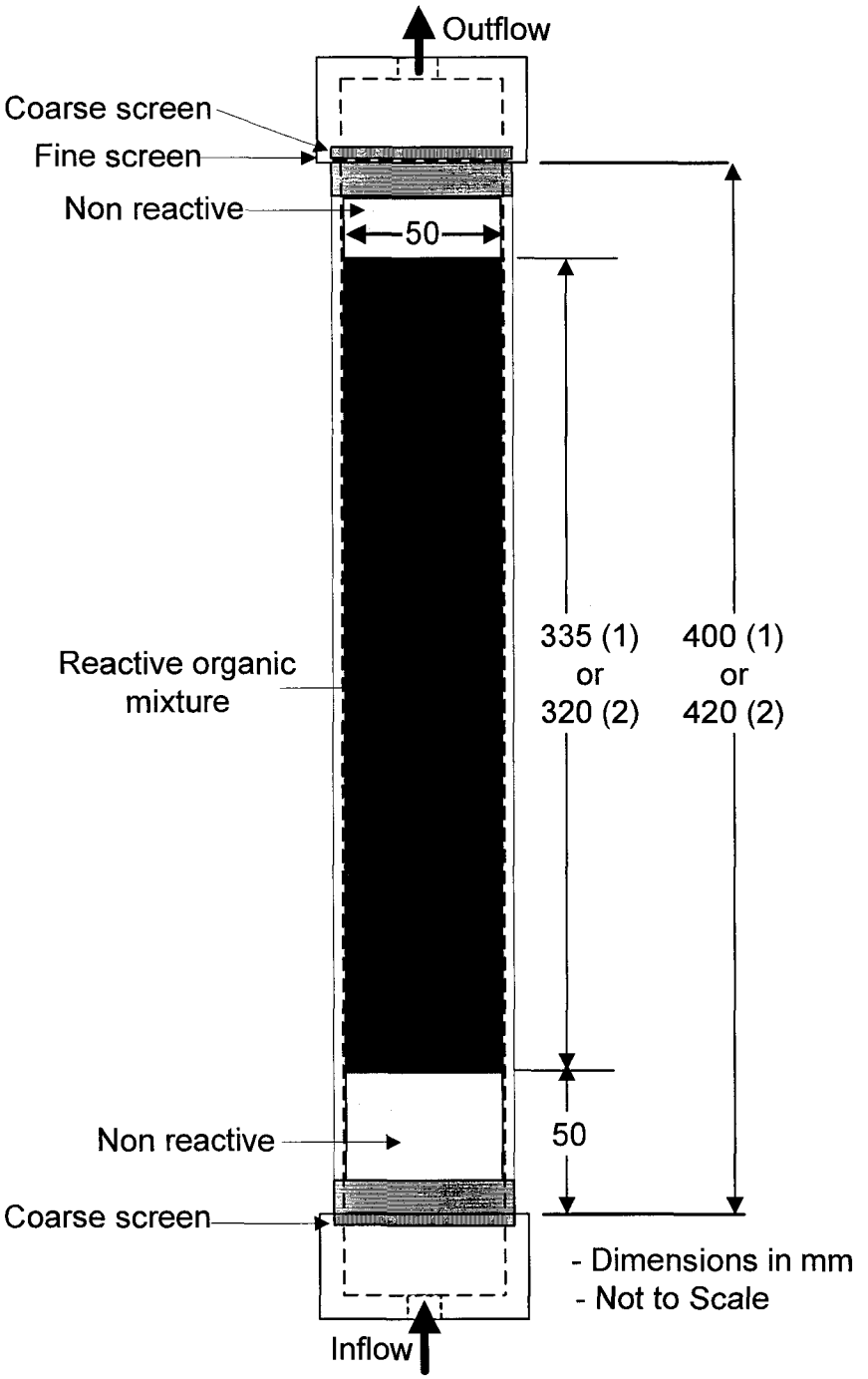

Figure 4.1 – Layout of Columns 1 and 2 (i.e., designated (1) and (2) above).

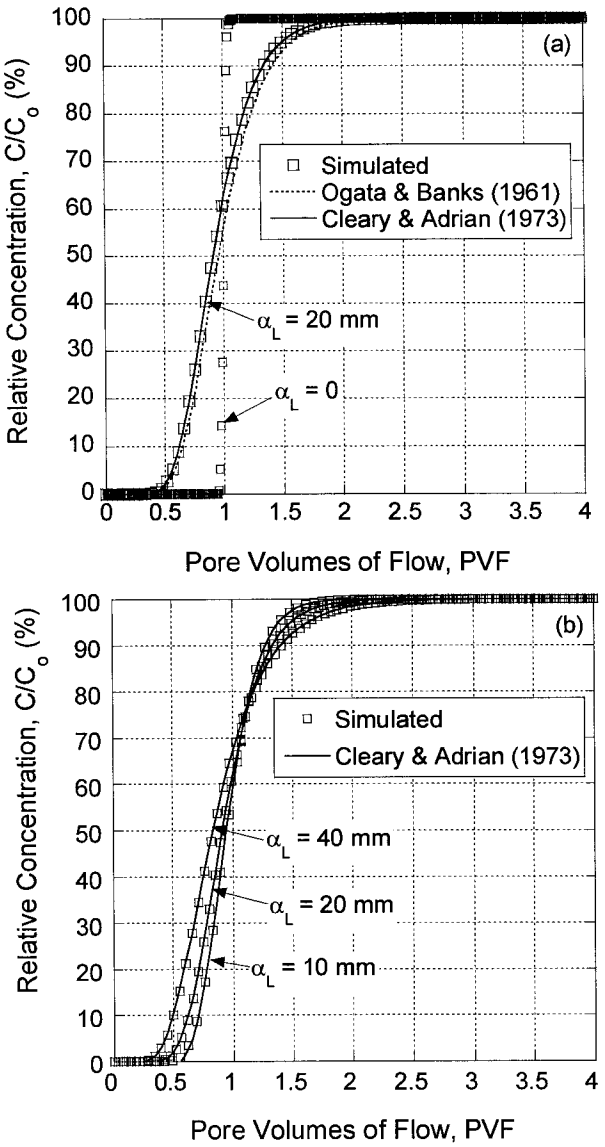

Figure 4.2 – Effluent breakthrough curves for non-reactive tracer compared to results from analytical solutions: (a) Column 1; (b) Column 2.

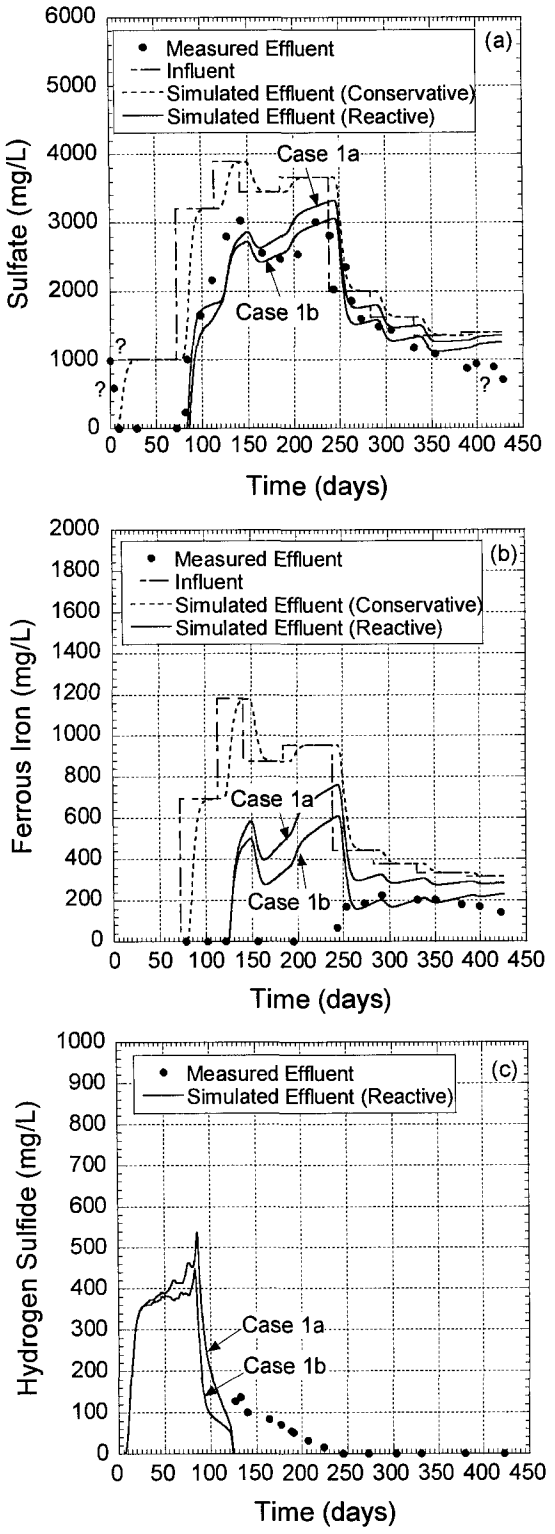

Figure 4.3 – Comparison of simulated and experimental effluent concentrations for Column 1 (Cases 1a and 1b): (a) sulfate, (b) ferrous iron, and (c) hydrogen sulfide.

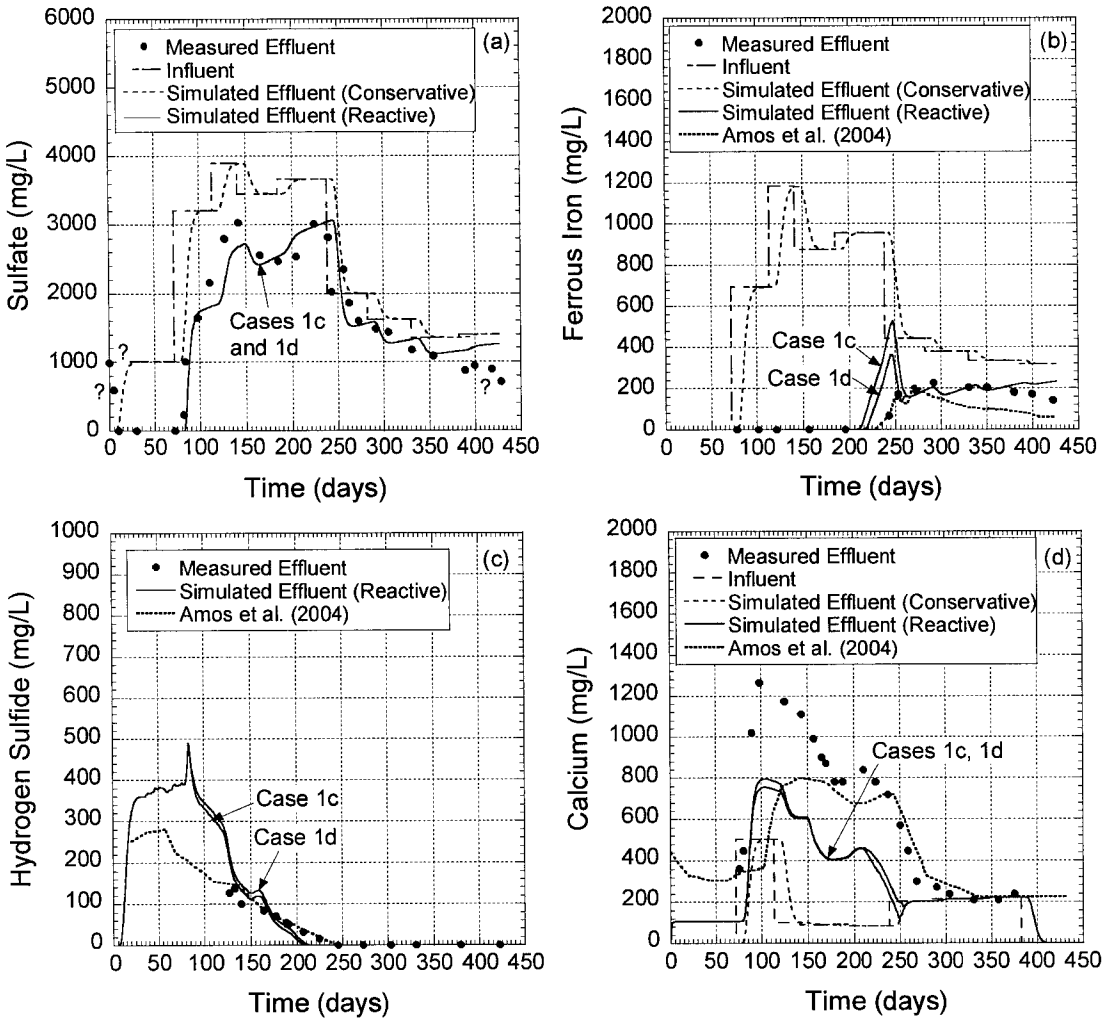

Figure 4.4 – Comparison of simulated and experimental effluent concentrations for Column 1 (Cases 1c and 1d): (a) ferrous iron, (b) hydrogen sulfide, and (c) calcium, including simulated results given by Amos et al. (2004).

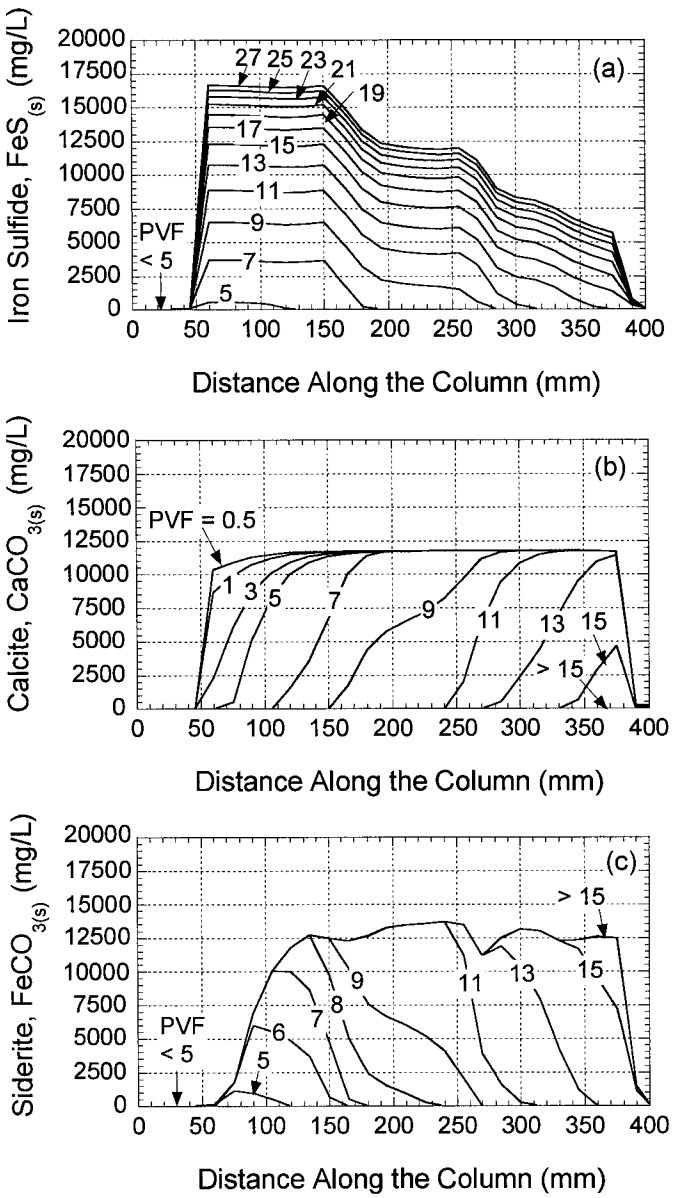

Figure 4.5 – Simulated equivalent precipitate concentrations along the column length for Column 1 (Case 1c): (a) iron sulfide, (b) calcite, and (c) siderite (PVF= pore volumes of flow).

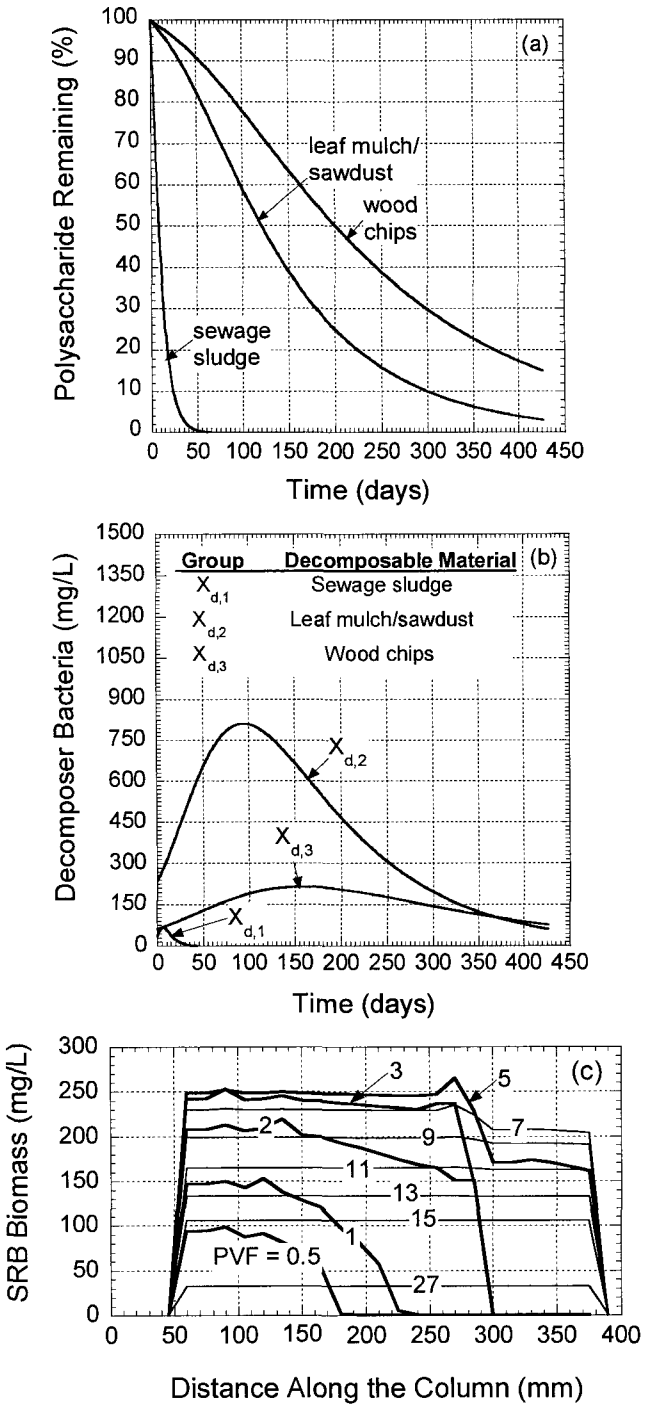

Figure 4.6 – Simulated results for Column 1 (Case 1c): (a) percentages of initial polysaccharides remaining, (b) equivalent decomposer-bacteria biomass concentration, and (c) equivalent SRB biomass concentration along the column length (PVF: column pore volumes of flow).

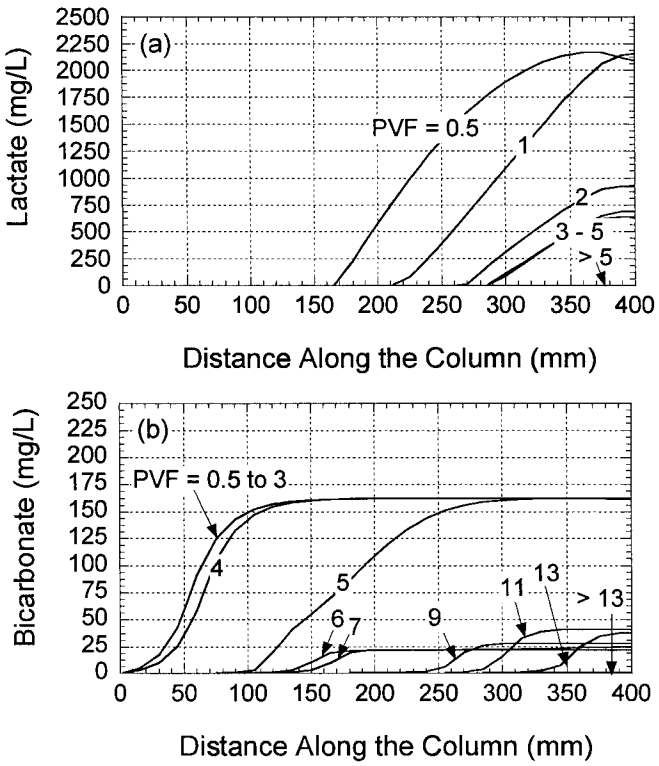

Figure 4.7 – Simulated concentrations along the column length for Column 1 (Case 1c): (a) lactate, and (b) HCO_3^- (PVF= pore volumes of flow).

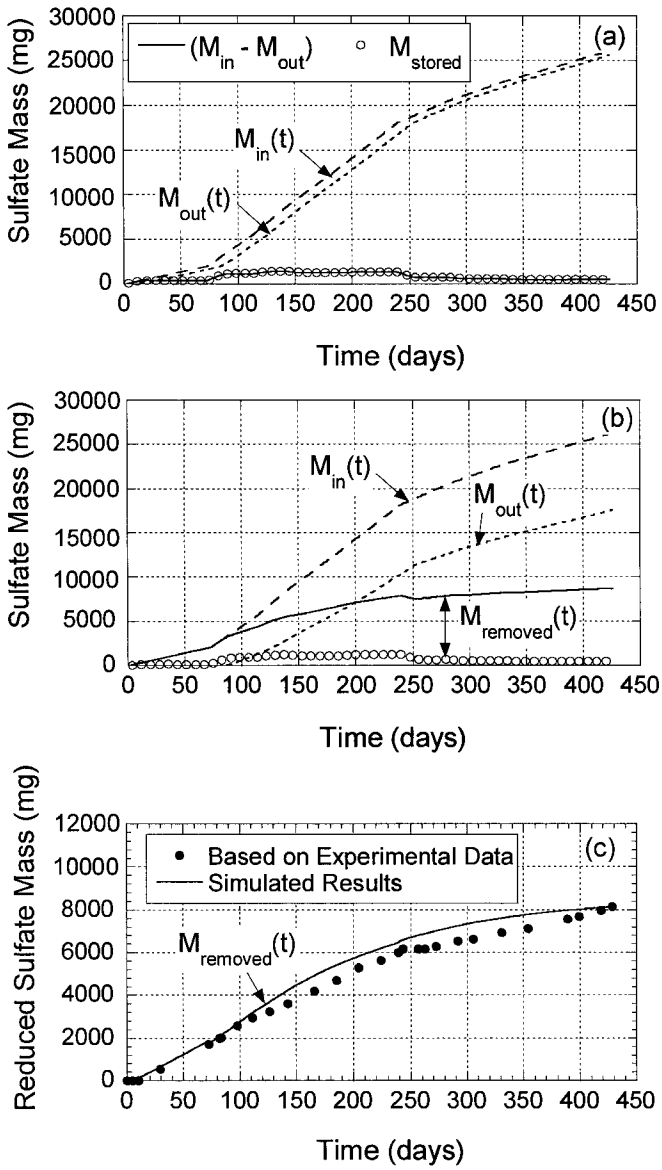

Figure 4.8 – Simulated cumulative masses input (M_{in}), output (M_{out}), stored (M_{stored}), and removed ($M_{removed}$) for sulfate: (a) conservative transport; (b) reactive transport (Case 1c); (c) comparison between simulated (Case 1c) and experimentally based results.

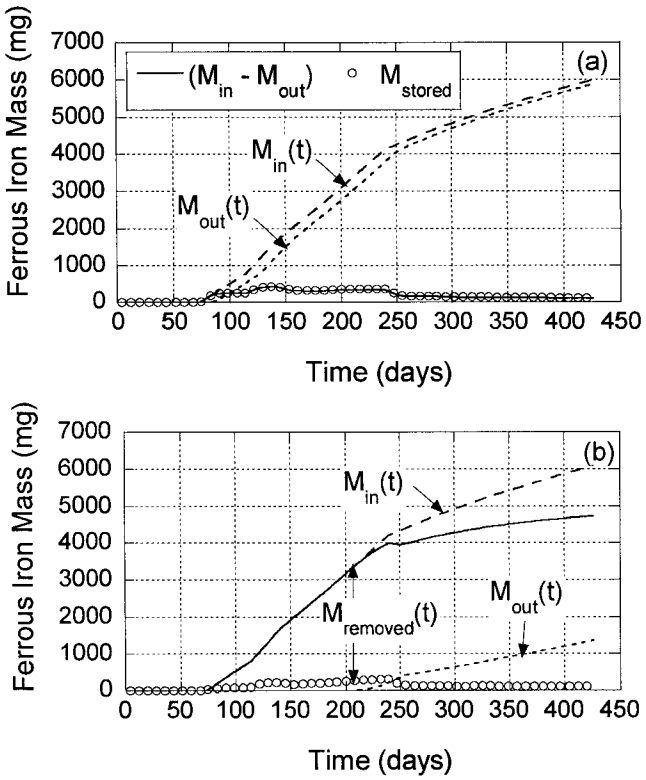

Figure 4.9 – Simulated cumulative masses input (M_{in}), output (M_{out}), stored (M_{stored}), and removed ($M_{removed}$) for ferrous iron: (a) conservative transport; (b) reactive transport (Case 1c).

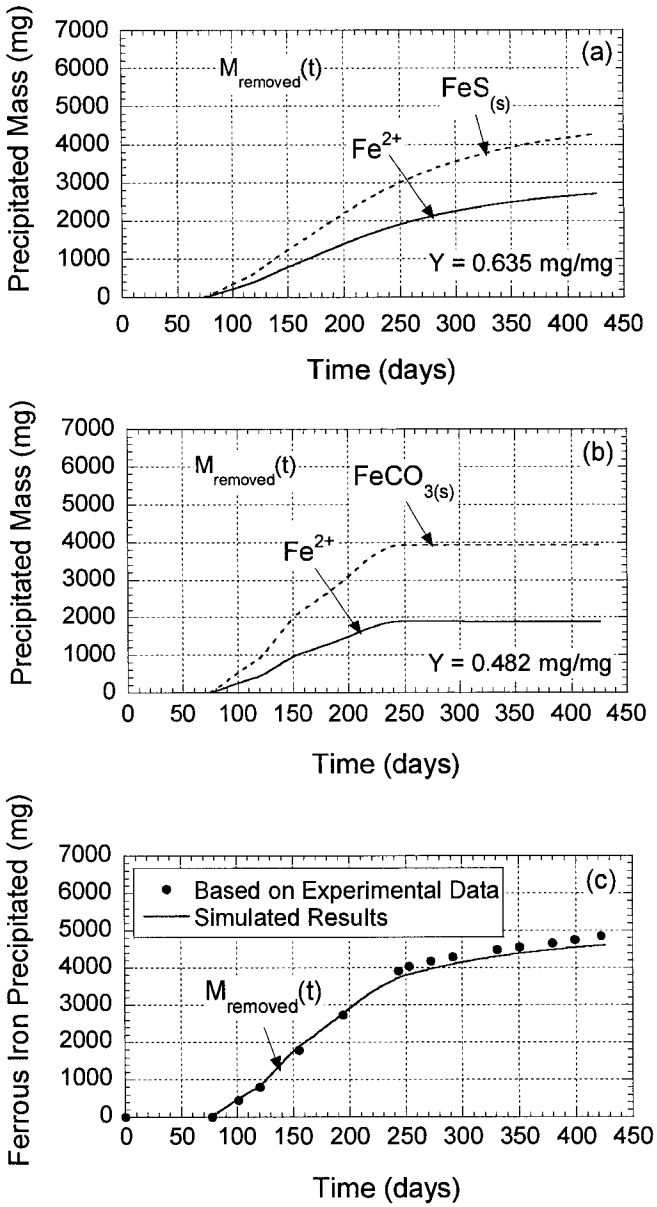

Figure 4.10 – Simulated cumulative masses of precipitated (a) FeS, and (b) $FeCO_{3(s)}$, Case 1c; (c) comparison between simulated (Case 1c) and experimentally based results.

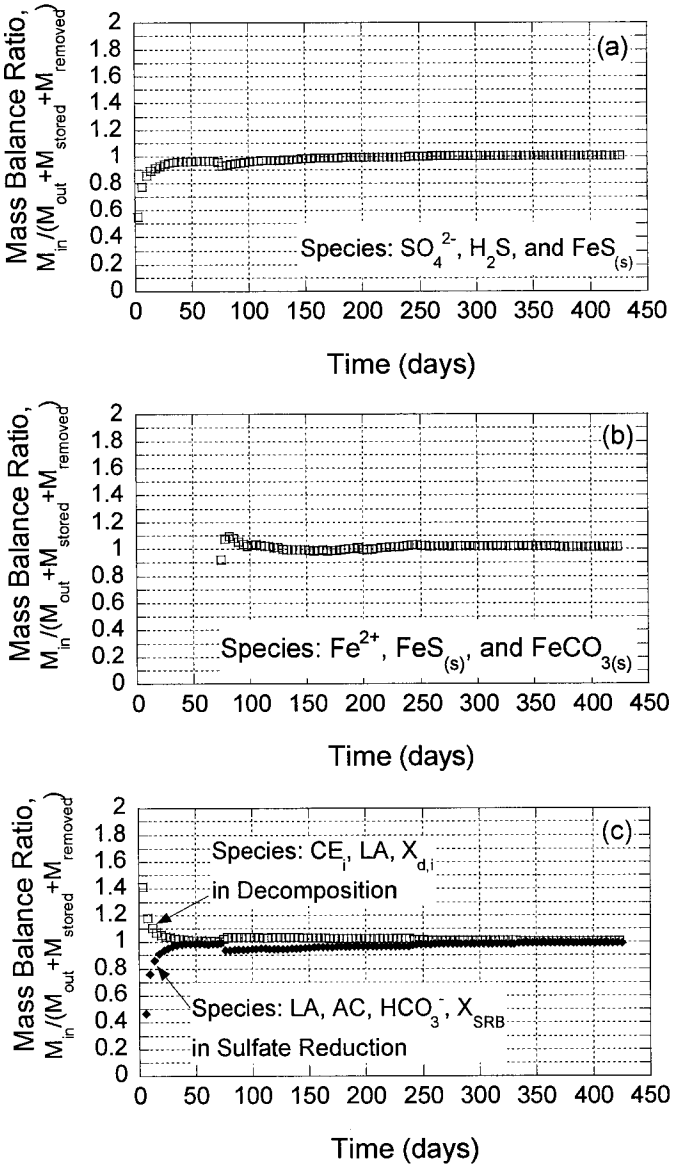

Figure 4.11 – Mass balance ratios for simulated results based on Case 1c: (a) sulfur, (b) iron, and (c) carbon.

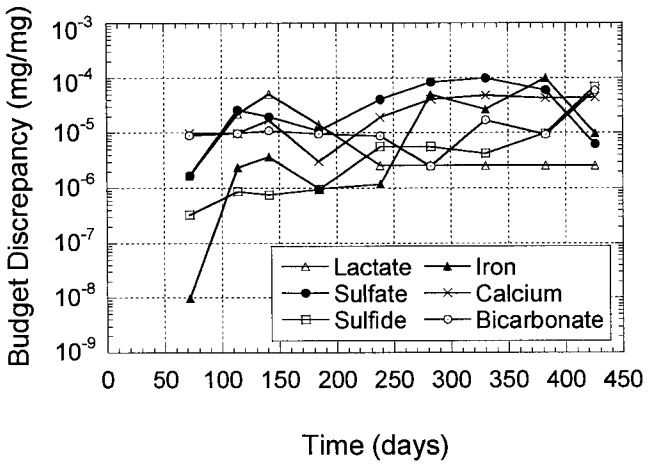

Figure 4.12 – Contaminant-transport cumulative mass budget discrepancy for Case 1c for mobile species.

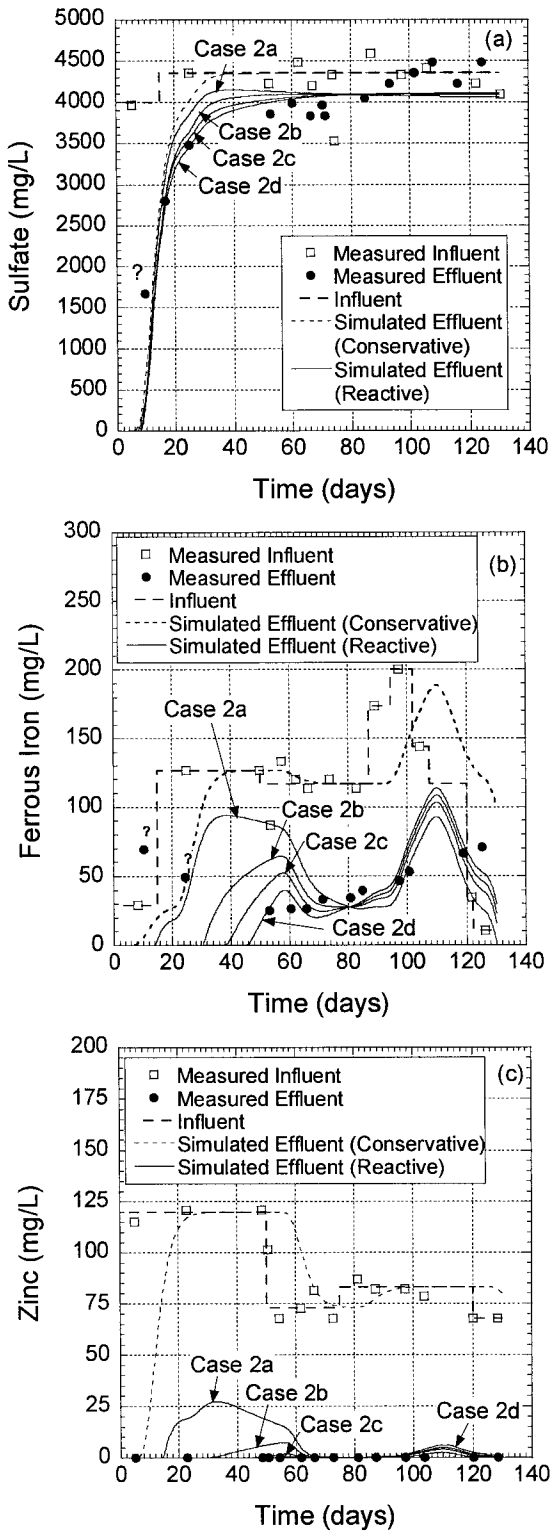

Figure 4.13 – Comparison of simulated and experimental effluent concentrations for Column 2 (Cases 2a, 2b, 2c, and 2d): (a) sulfate, (b) ferrous iron, and (c) zinc.

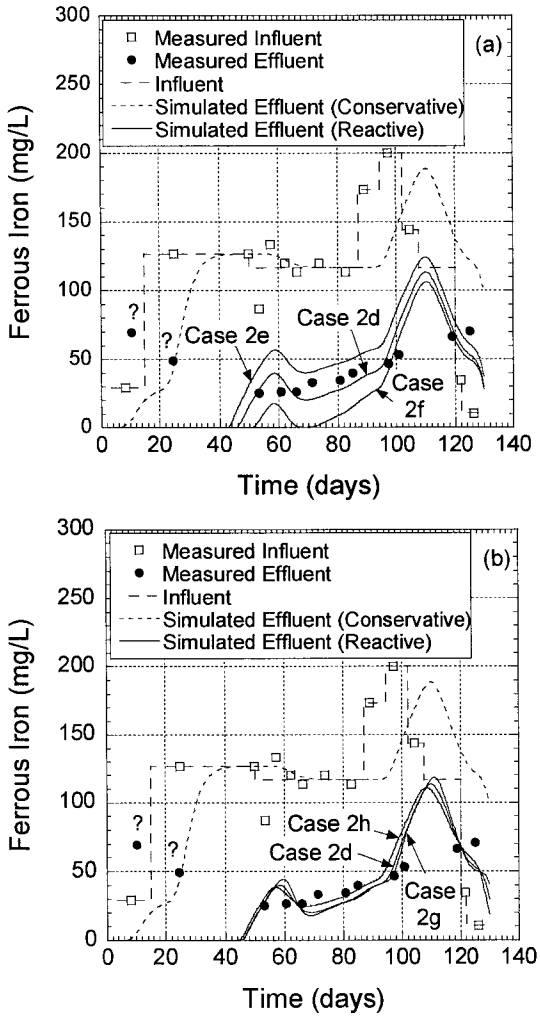

Figure 4.14 – Comparison of simulated and experimental ferrous-iron effluent concentrations for (a) Cases 2d, 2e, and 2f, and (b) Cases 2d, 2g, and 2h.

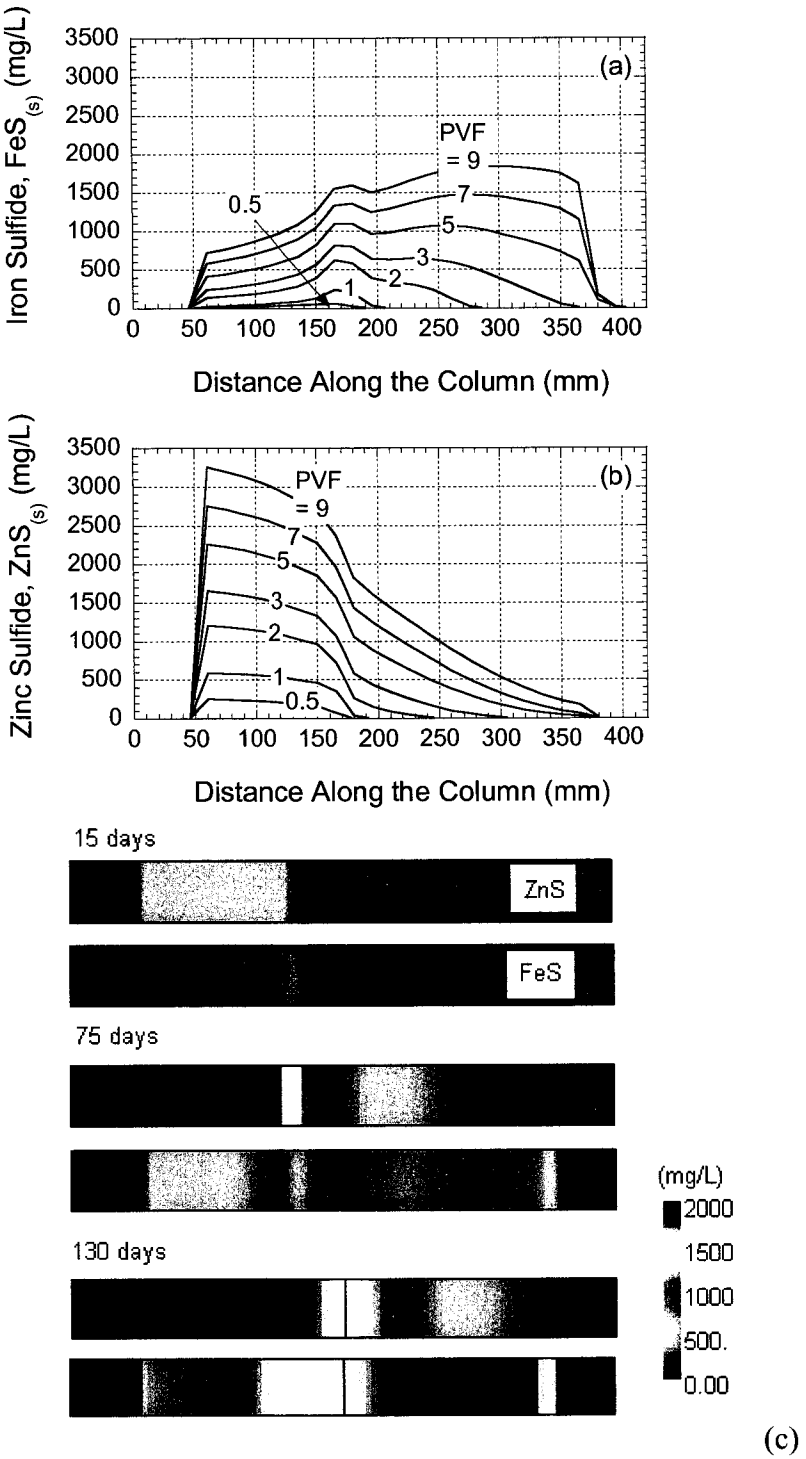

Figure 4.15 – Simulated equivalent precipitate concentrations along the column length for Column 2 (Case 2d): (a) FeS, (b) ZnS, and (c) illustrative profiles for FeS and ZnS (PVF= pore volumes of flow).

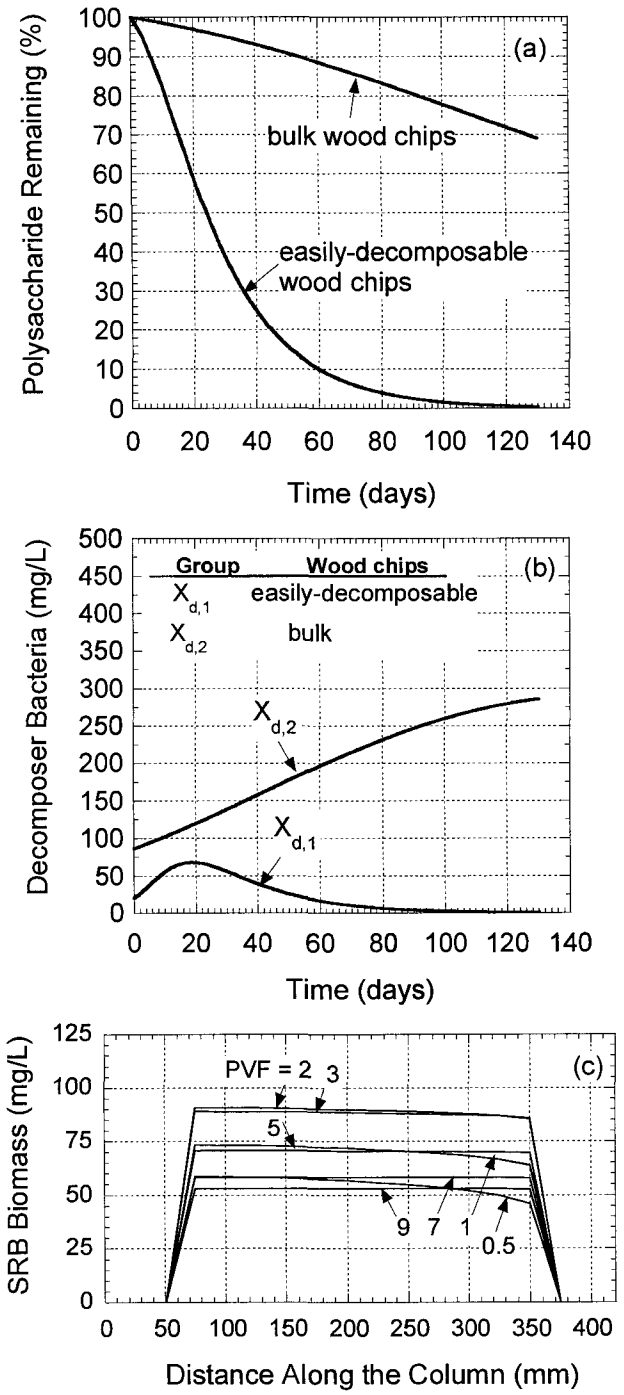

Figure 4.16 – Simulated results for Column 2 (Case 2d): (a) percentages of initial polysaccharides remaining, (b) equivalent decomposer-bacteria biomass concentration, and (c) equivalent SRB biomass concentration along the column length (PVF: pore volumes of flow).

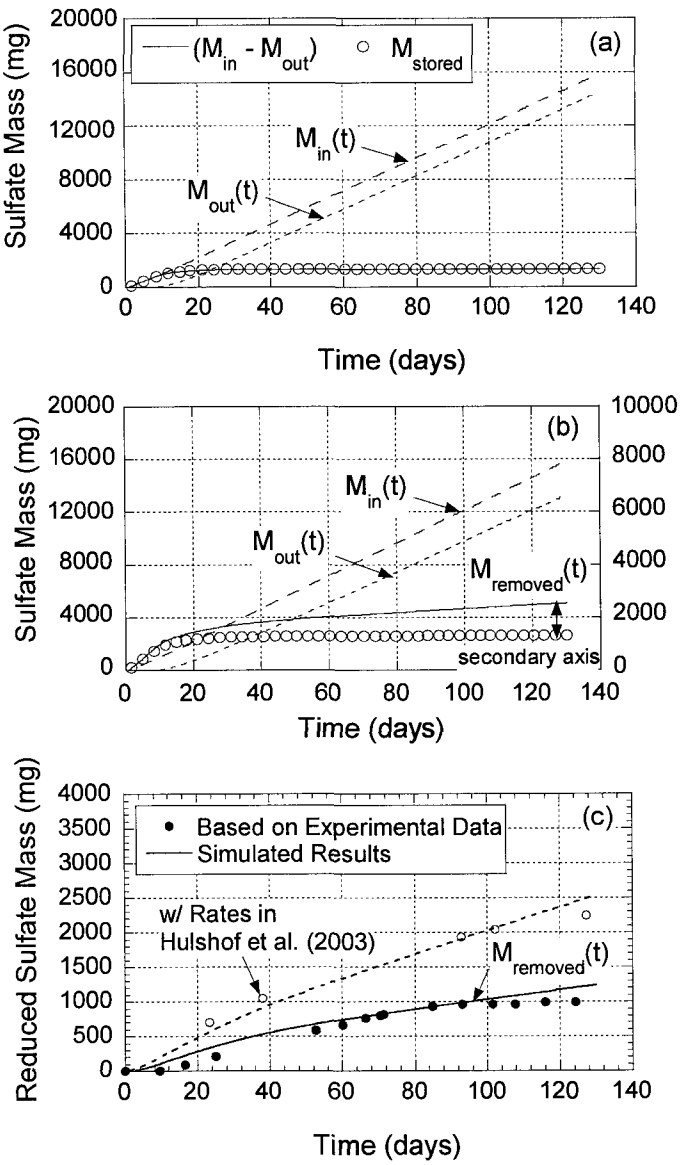

Figure 4.17 – Simulated cumulative masses input (M_{in}), output (M_{out}), stored (M_{stored}), and removed ($M_{removed}$) for sulfate: (a) conservative transport; (b) reactive transport (Case 2d); (c) comparison between simulated (Case 2d) and experimentally based results.

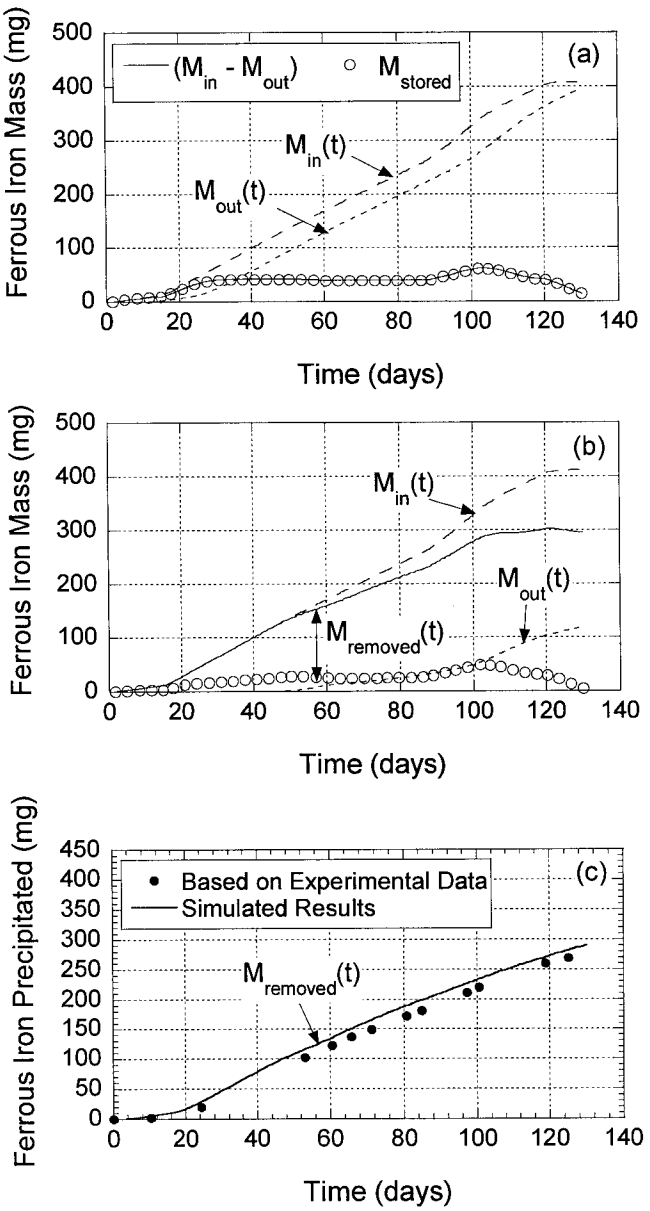

Figure 4.18 – Simulated cumulative masses input (M_{in}), output (M_{out}), stored (M_{stored}), and removed ($M_{removed}$) for ferrous iron: (a) conservative transport; (b) reactive transport (Case 2d); (c) comparison between simulated (Case 2d) and experimentally based results.

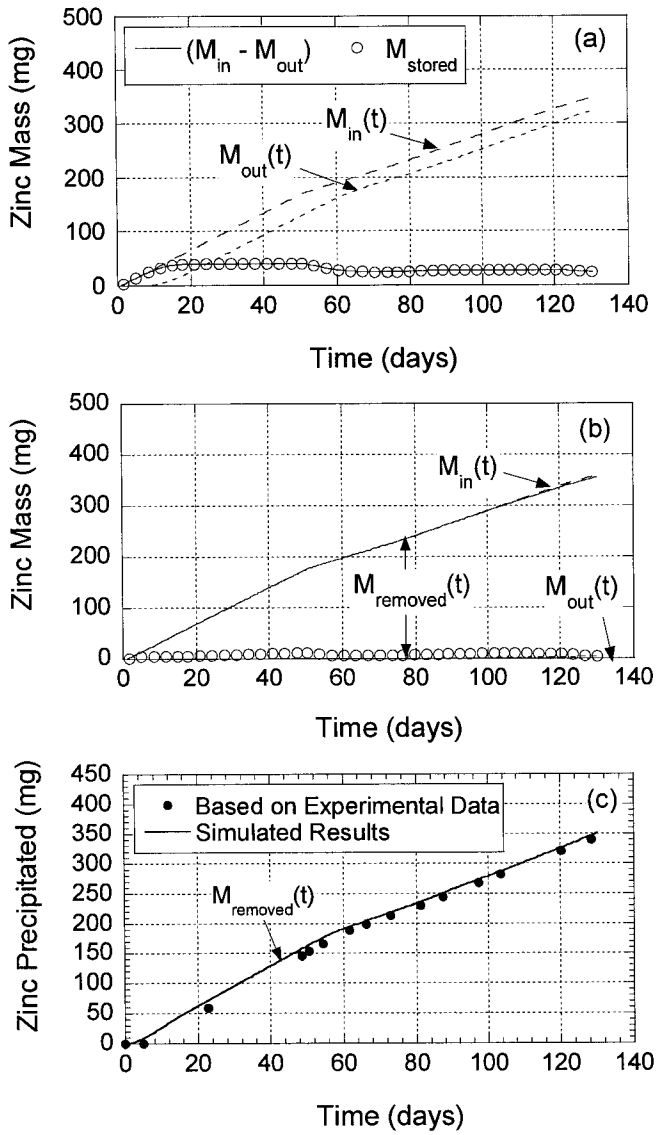

Figure 4.19 – Simulated cumulative masses input (M_{in}), output (M_{out}), stored (M_{stored}), and removed ($M_{removed}$) for zinc: (a) conservative transport; (b) reactive transport (Case 2d); (c) comparison between simulated (Case 2d) and experimentally based results.

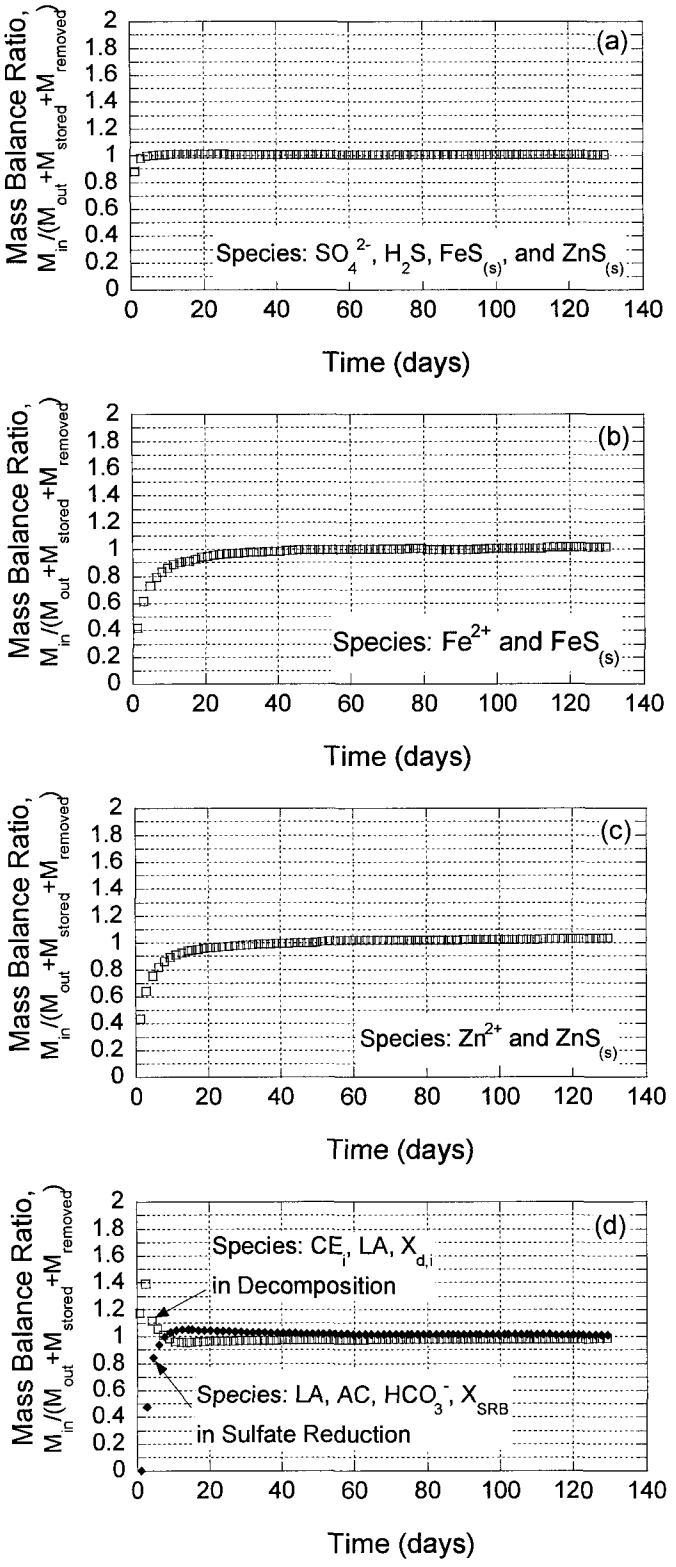

Figure 4.20 – Mass balance ratios for simulated results based on Case 2d, (a) sulfur, (b) iron, (c) zinc, and (d) carbon.

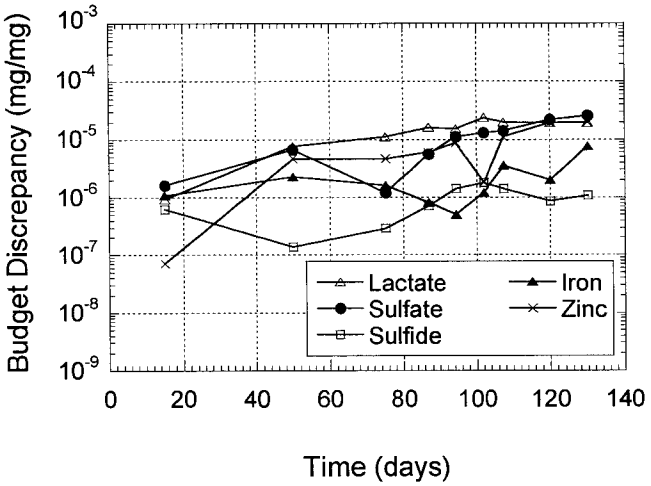

Figure 4.21 – Contaminant-transport cumulative mass budget discrepancy for Case 2d for mobile species.

Appendix

For Column 1, additional Cases 1e and 1f are not expected to approximate the experimental data, but to provide insight into Fe^{2+} removal due to $FeCO_{3(s)}$ precipitation alone, i.e., in the absence of SO_4^{2-} reduction. As shown in Fig. A.1, effluent Fe^{2+} concentrations remain at zero until approximately 160 d (11 PVF), i.e., during the period of active $FeCO_{3(s)}$ precipitation. Approaching 230 d, when $CaCO_{3(s)}$ is depleted, effluent Fe^{2+} concentrations increase, reaching the influent-solution concentrations. Due to $CaCO_{3(s)}$ dissolution, the long-term removal of Fe^{2+} in the column is necessarily dependent upon SO_4^{2-} reduction and $FeS_{(s)}$ precipitation, and not $FeCO_{3(s)}$ precipitation.

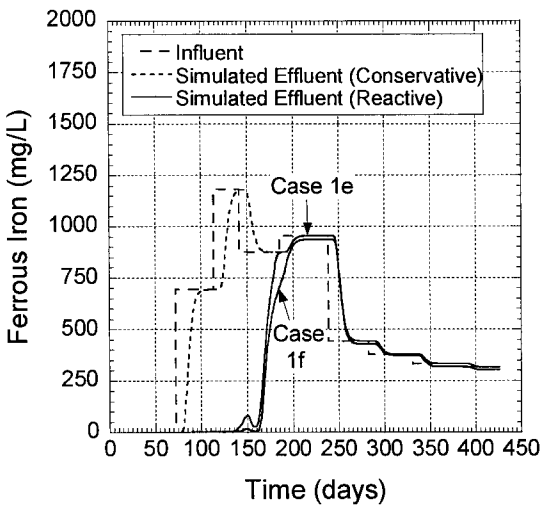

Figure A.1 – Simulated effluent ferrous iron concentrations in Column 1 for Cases 1e and 1f.

CHAPTER 5

MODELING BIOREACTOR EXPERIMENTS FOR IRON PRECIPITATION BASED ON SULFATE REDUCTION AND DECOMPOSITION OF ORGANIC SOLIDS

ABSTRACT: Simulated effluent concentrations for sulfate (SO_4^{2-}) and ferrous iron (Fe^{2+}) are compared to measured concentrations from three bioreactor experiments reported in the literature. The bioreactors are sulfate reducing (SR), aerobic-anaerobic systems open to the atmosphere and differ only in terms of the residence times. Decomposable polysaccharides in freshly cut alfalfa, bacterial populations, iron sulfide ($FeS_{(s)}$) precipitate, and lactate also are modeled. The biochemical model coupled to flow and contaminant transport includes Contois kinetics for polysaccharide decomposition, Monod kinetics for lactate-based SO_4^{2-} reduction, kinetically controlled precipitation of $FeS_{(s)}$ and volatilization of hydrogen sulfide (H_2S). The model is shown to be capable of approximating the primary experimental trends in the data, and to reproduce reasonably well the effect of residence time on effluent SO_4^{2-} and Fe^{2+} for two of the bioreactors, and on effluent Fe^{2+} alone for all three bioreactors. Adjusted parameter values (e.g., for freshly cut alfalfa decomposition), and insights gained from the simulations (e.g., rate coefficient for H_2S volatilization, and thickness of the non-SR zone) may be useful for modeling other open systems with similar biochemistry, such as wetlands for AMD remediation.

Key Words: Acid mine drainage, Bioreactor, Bioremediation, Cellulose decomposition, Decomposition kinetics, Ferrous Iron, Mathematical modeling, Polysaccharide decomposition, Solid organic materials, Sulfate reduction, Wetlands.

5.1 INTRODUCTION

The results of several bench-scale bioreactor experiments using solid organic materials have demonstrated the feasibility of treating acid mine drainage (AMD) based on sulfate (SO_4^{2-}) reduction with sulfate reducing bacteria (SRB) and metal-sulfide precipitation (e.g., Tuttle at al. 1969, Wakao et al. 1979, Dvorak et al. 1992, Hammack and Edenborn 1992, Bechard et al. 1994, Christensen et al. 1996, Gilbert et al. 1999, Groudev et al. 1999, Prasad et al. 1999, Luptakova and Kusnierova 2005). In particular, some wetland mesocosm experiments performed in the laboratory have included influent solutions, sediments, plants, and bacterial cultures identical to those occurring in operating wetlands (e.g., Wieder et al. 1990, Webb et al. 1998). Examples of the solid, decomposable organic materials that have been evaluated for this purpose include sawdust (e.g., Tuttle et al. 1969, Wakao et al. 1979), spent mushroom compost (e.g., Dvorak et al. 1992, Hammack and Edenborn 1992), and fresh alfalfa (e.g., Bechard et al. 1994), among others.

Several studies involving field applications of sulfate reducing (SR) systems for remediation of AMD in wetlands and large-scale bioreactors also have been reported. These studies include the SR wetlands constructed near the Big Five Tunnel in Idaho Springs, Colorado, USA (Mechemer and Wildeman 1992) and the Wheal Jane mine in Cornwall, UK (Webb et al. 1998, Whitehead and Prior 2005), and the passive SRB bioreactors filled with organic matter and limestone for AMD remediation constructed at an abandoned mine site (Calliope mine) near Butte, Montana (MSE, 2002). A review of AMD treatment in distinct types of wetlands is provided by Gazea et al. (1996).

Differences exist among models used to analyze or design bioreactor systems

based on SO_4^{2-} reduction. For example, some models consider the rate of SO_4^{2-} reduction to be linked to the rate of decomposition of organic solids, but do not include dissolved organic substrates, nor the bacterial populations of decomposers and SRB and the effects of bacterial growth and decay (e.g., Westrich and Berner 1984, Bourdeau and Westrich 1984, and Drury 2000). Other models include the SRB population, with Monod kinetics for growth (Monod 1949), but focus on injected dissolved organic substrates (e.g., lactate, ethanol) instead of solid decomposable organic materials (e.g., Schafer et al. 1998a,b, Prommer et al. 2001). In addition, other models do not include either bacterial populations (decomposers and SRB) or solid decomposable organic substrates (e.g., Mayer et al. 2002). Finally, some models consider the rate of SO_4^{2-} reduction to be represented by a constant value multiplied by a hyperbolic term that accounts for SO_4^{2-} limitation, with the constant value based on *a priori* fitting of column-test data (Benner et al. 2002, Amos et al. 2004). In essence, none of the aforementioned models considers the rate of SO_4^{2-} reduction to be linked to the rate of polysaccharide decomposition, and simultaneously models SO_4^{2-} reduction using Monod kinetics.

The objective of this chapter is to evaluate the use of a new biochemical model for the rate of SO_4^{2-} reduction for open, flow-through bioreactor systems. The evaluation will be based on comparisons of simulated results with experimental results from the literature for three bioreactor experiments. The evaluation reported herein differs from previous evaluations of the biochemical model in two ways: (i) unlike the evaluation reported in Chapter 3 (Hemsi et al. 2005a) based on the results of batch equilibrium experiments, solution flow and contaminant transport occur through the bioreactor systems considered herein; and (ii) unlike the evaluation reported in Chapter 4 (Hemsi et

al. 2005b) based on the results of column experiments, the bioreactor systems considered herein are open systems such that there is the possibility of exchange of hydrogen sulfide gas with the atmosphere and the top of the bioreactors are expected to be aerobic. The simulated results are obtained based on SO_4^{2-} reduction and $FeS_{(s)}$ precipitation kinetics coupled to, and limited by, the kinetics of decomposition of solid organic materials, and including growth and decay of decomposer bacteria and SRB and volatilization of hydrogen sulfide as previously described (Hemsi et al. 2005a). The evaluation reported herein is considered to be more applicable to open SR systems, such as passive wetlands used to treat AMD.

5.2 BASIS FOR EVALUATION

Simulated results for effluent SO_4^{2-} and Fe^{2+} concentrations versus time are compared to measured effluent concentrations for three bioreactor experiments reported in Bechard et al. (1994), operated with volumetric discharges of 720, 1,440, and 144 cm^3/d (i.e., residence times of 6.2, 3.1, and 31 d), and designated herein as Bioreactors 1, 2, and 3, respectively. The behaviors of decomposable polysaccharides, organic dissolved substrates (e.g., lactate or $C_3H_5O_3^-$), decomposer bacteria and SRB, and $FeS_{(s)}$ also are simulated. Finally, measured and simulated cumulative masses for SO_4^{2-} and Fe^{2+} also are compared.

The bioreactors were based on decomposable, freshly cut alfalfa (not amended with dissolved substrates, such as sucrose), providing nutrients for an anaerobic ecosystem involved in the remediation of an influent synthetic AMD solution through SO_4^{2-} reduction and precipitation of iron mono sulfide ($FeS_{(s)}$). Fresh alfalfa was selected

on the basis of (i) low content of lignin, (ii) relatively rapid decomposition, and (iii) presence of bacterial nutrients and proteins (Bechard et al. 1994).

The bioreactors consisted of mixed aerobic-anaerobic open systems (i.e., open to gas exchange with the atmosphere) representing small-scale wetlands for AMD remediation, as shown schematically in Fig. 5.1. Each bioreactor was a 410-mm long, 280-mm wide "Rubbermaid" plastic container, and was filled with a height of reactive material equal to 90 mm (Fig. 5.1), resulting in total and pore volumes of 10,332 and 5,042 cm^3, respectively, corresponding to a porosity of 0.487 (Bechard et al. 1994). The experiments are assumed to have been conducted at a room temperature of 25 ^{o}C, and the measured pH for the effluent solution ranged from 7.0 to 8.0 during active SO_4^{2-} reduction, which is consistent with the range in pH assumed in the model.

The material filling each bioreactor was sludge-like in consistency and included a total (wet) mass of 708 g of freshly cut alfalfa that was pre-mixed to a microbial inoculating material (water, a sulfide precipitate, and partially degraded straw obtained from an AMD treatment plant). Based on the sludge-like consistency, a gravimetric water content of 100 % was used for the mixture (i.e., assuming the mass of water in the mixture to be equal to the mass of the solids), resulting in a dry mass of approximately 354 g of freshly cut alfalfa for each bioreactor. Partially degraded straw in the inoculating material is not included in the pool of decomposing materials for the simulations because of a lack of quantitative information.

The presence of calcite ($CaCO_{3(s)}$) in the reactive mixtures used for the bioreactors was not reported in Bechard et al. (1994). Therefore, dissolution/precipitation of carbonate minerals (i.e., $CaCO_{3(s)}$, and siderite, or $FeCO_{3(s)}$) is not considered in the

simulations. Only the longer-term reactivity and SRB growth coupled to, and limited by, the decomposition of polysaccharides in alfalfa is simulated in this study. Dissolved organic substrates (e.g., lactate or $C_3H_5O_3^-$) are assumed to be absent from both the influent solution and the initial pore-space solution in the bioreactors. Also, the initial distributions of alfalfa and bacterial populations within the bioreactors are assumed to be uniform. Bechard et al. (1994) stated that the majority of the organic material was located under anaerobic conditions, which is consistent with the anaerobic polysaccharide decomposition assumed in the model simulations.

Since the bioreactors were open to the atmosphere (i.e., interface liquid-gas at the top of the reactive material) and air was continuously circulated in the gas phase, the possibility of partial volatilization of H_2S to the gas phase is included in the simulations, and the total thickness of saturated reactive material is assumed to be divided into a top non sulfate-reducing sub-layer (partly aerobic due to the inherent access to $O_{2(g)}$), and a bottom SR sub-layer (i.e., oxidation-reduction electrochemical potential in the range -200 or -250 mV for SO_4^{2-} reduction). Flooded sediments rich in labile organic matter and open to the atmosphere develop stratification of oxidation-reduction interfaces along the saturated thickness, and the depth separating the top aerobic sub-layer from the bottom sulfidic sub-layer may be on the order of a few centimeters (Ronen et al. 1987, Langmuir 1997). This depth is assumed to be variable in this study and to range from 10 to 40 mm for the simulations.

Although aerobic transformations such as Fe^{2+} oxidation to Fe^{3+} and subsequent hydrolysis and precipitation as $Fe(OH)_{3(s)}$ or $FeOOH_{(s)}$ could have occurred near the top aerobic sub-layer (Wieder et al. 1990, Webb et al. 1998), no discussion of such aerobic

transformations was provided in Bechard et al. (1994). As a result, such transformations are not considered in the model. Also, the possibility of sorption of Fe^{2+} to the negatively charged surfaces of organic materials (e.g., Sposito 1989) was not discussed in Bechard et al. (1994) and, similarly, is not evaluated in this study.

Although Al^{3+} was present in the influent solutions at ~ 16 to 25 mg/L (Bechard et al. 1994), this metal is disregarded in the simulations assuming that the removal of Al^{3+} was not predominantly related to SO_4^{2-} reduction and H_2S precipitation, but instead was related to precipitation of amorphous $Al(OH)_3$ and cation exchange or organic binding (Drever 1997, Langmuir 1997, Weider et al. 1990). Also, although microbial activity released considerable amounts of ammonium (NH_4^+) to the bioreactor effluents (Bechard et al. 1994), NH_4^+ is not included in this study due to the fact that the model herein does not include NH_4^+.

The simulations are based on saturated, steady-state flow in a homogeneous but anisotropic porous medium in terms of hydraulic conductivity (K), with the vertical K (i.e., K_v) being equal to one-tenth of the horizontal K (i.e., K_h), i.e., an anisotropy ratio, K_v/K_h, equal to 0.1. This anisotropy incorporates the predominance of horizontal flow versus vertical flow expected for wetlands. However, for the purpose of the model simulations, the porous medium is separated into nine adjacent, horizontal 10-mm-thick layers, and the MODFLOW vertical conductance between each pair of adjacent layers is calculated considering K_v equal to one-tenth of K_h. Flow channeling due to heterogeneity in K is not considered.

As shown in Fig. 5.1, the influent solution was injected into the bottom of each bioreactor at one end using a peristaltic pump, and the effluent solution was discharged

through plastic tubing toward the top of each bioreactor at the opposite end (Bechard et al. 1994). For the simulations performed herein, the influent solution is supplied using injection wells located at the first cell (left-hand side of the model) in layer '9' (bottom), and the effluent solution is discharged through drains located at the last cell (right-hand side) in layer '1' (top). As described in the following section, a cell is defined as a 5 x 10 x 10 mm^3 element of the finite-difference grid. The right-hand-side cells belonging to layers '2' to '9' are considered as no-flow cells, i.e., as horizontal flow barriers. The schematic of a lateral view of the bioreactors is provided in Fig. 5.1, and the composition of the influent solution used for the simulations herein is given in Table 5.1. Finally, each bioreactor experiment was performed in duplicate. The variability in measured SO_4^{2-} and Fe^{2+} effluent concentrations among each pair of duplicate tests is expressed using an error bar notation for several of the data points for each test.

5.3 MODEL DESCRIPTION AND SOLUTION

The biochemical model used for the simulations in this study includes (Chapter 2): (i) anaerobic decomposition of polysaccharides in freshly cut alfalfa due to the activity of decomposer bacteria and following the Contois kinetic model (Contois 1959), (ii) sulfate reduction based on the incomplete oxidation of lactate, including SRB growth and following the Monod kinetic model (Monod 1949), (iii) kinetically controlled precipitation of $FeS_{(s)}$, and (iv) partial volatilization of H_2S to the gas phase. The model also includes the possibility of reversible dissolution/precipitation of carbonate minerals and secondary processes (e.g., SO_4^{2-} reduction based on acetate) which are not considered for the simulations reported herein.

Steady-state flow and multi-species reactive contaminant transport are modeled using MODFLOW 2000 version 1.7 (Harbaugh et al. 2000) and RT3D version 2.5 (Clement 1997, 2003). The bioreactors are modeled as finite-differences three-dimensional domains containing 83 columns (i.e., parallel to the bioreactor width), 28 rows (i.e., parallel to the bioreactor length), and nine layers. The grid discretization consists of 5 and 10 mm along columns and rows, respectively, and 10 mm along the thickness. Specified flux and constant-concentration boundary conditions are considered at the location of the injection wells at the first cell in layer '9', and freely-draining and zero dispersive mass flux (i.e., $\partial C/\partial x = 0$) are considered at the location of the drains at the last cell in layer '1'. The last cells in layers '2' to '9' are horizontal flow barriers (Harbaugh et al. 2000).

Advection, dispersion, and sink/source mixing are solved in RT3D using the Total Variation Diminishing method (Zheng and Wang 1999). Contaminant transport is coupled in time with the user-defined subroutine containing the biochemical reactions using reaction operator splitting (Clement 1997). The biochemical reactions consist of a system of ordinary differential equations that is step-wise integrated in time using the Runge-Kutta-Fehlberg (RKF) method (Chapra and Canale 2002). Transport time steps are selected on the basis of the requirements for advection, dispersion, and sink/source mixing (Zheng 1990) that are automatically set in RT3D, and are on the order of 0.004 d. Multiple reaction time steps for RKF integration are allowed within each transport time step, and RT3D stops if more than 3000 RKF time steps are required within each transport time step (Clement 1997).

5.4 INITIAL CONCENTRATIONS AND PARAMETER VALUES

Initial concentrations and parameter values used for the simulation cases are summarized in Tables 5.2 and 5.3. Further details regarding the bacterial populations, polysaccharide decomposition, SO_4^{2-} reduction, $FeS_{(s)}$ precipitation, and H_2S volatilization follow.

5.4.1 Bacterial Populations

The influent solution contained potassium, K^+, magnesium, Mg^{2+}, and phosphate, PO_4^{2-}, which are not included in the model simulations, but expected to serve as bacterial nutrients for the populations of decomposers and SRB throughout the experiments. The equivalent biomass concentration by dry mass of polysaccharide decomposer bacteria colonizing each decomposable polysaccharide ranges from 0.1 to 10 mg biomass/g of dry polysaccharide, based on cell coverage ranging from ~ 10^9 to 10^{10} cells/g of dry detritus, and considering from 10^{-10} to 10^{-9} mg per cell on a dry mass basis (e.g., Fenchel and Harrison 1976). A cell coverage ranging from 2 to 15 cells/100 μm^2 of fiber of decomposable detritus is obtained for fibers with a 2-mm diameter and a 5-mm length, and a mass of 3 mg/fiber (Fenchel and Harrison 1976, Henriksen and Breland 2002). An intermediate equivalent concentration for the population of decomposer bacteria associated with fresh alfalfa corresponding to a concentration ratio by dry mass of decomposer bacteria to decomposable polysaccharide, $[X_d]/[CE]$, of 5 x 10^{-3} (Tables 5.2 and 5.3) is used for the simulations (Chapters 3 and 4).

The equivalent biomass concentration (dry mass) for SRB that are incomplete oxidizers of lactate (e.g., *Desulfovibrio vulgaris*) is estimated to range from 1 to 1000 mg

biomass/L of pore liquid when SO_4^{2-} reduction is active. This range is based on the converted abundance range of 10^7 to 10^9 cells/mL of pore liquid (e.g., Benner et al. 2002), considering 10^{-10} to 10^{-9} mg/cell by dry mass corresponding to cylindrical cells with a height of 2.35 μm and a diameter of 0.75 μm (Postage 1984). An intermediate value of 50 mg biomass/L of pore liquid (Tables 5.2 and 5.3) generally is used for the simulations, and is equivalent to from 10^7 to 10^8 cells/mL of pore liquid, which is consistent with an SRB most probable number of 10^7 cells/g of solid material or 5 x 10^7 cells/mL of pore liquid (Hulshof et al. 2003).

5.4.2 Polysaccharide Decomposition

Based on a combination of representative percentages reported in the literature (Chapter 2), the initial content of decomposable polysaccharides in freshly cut alfalfa is estimated as 50 % (dry mass basis). Thus, the initial dry mass of decomposable polysaccharides in each bioreactor is estimated as 177 g (35.2 g/L). Freshly cut alfalfa is simulated either as a single decomposable material or sub-divided into two pools of different reactivity. In the latter case, 20 % by dry mass of the initial amount of polysaccharides is assumed more readily decomposable (Chapter 4).

In spite of the open system, polysaccharide decomposition is assumed to be purely anaerobic, since the majority of the organic material was under anaerobic conditions (Bechard et al. 1994). Contois kinetic parameters for freshly cut alfalfa decomposition are adjusted in successive model simulations, since parameters for this material were not previously obtained. The Contois decomposition rate coefficient (k_c) and half-saturation constant (K_c) were initially selected on the basis of parameter values

for leaf mulch (Chapter 4), i.e., k_c of 0.5 d^{-1}, and K_c of 30 mg/mg. However, adjusting Contois rate coefficients for freshly cut alfalfa decomposition (i.e., using the same value of K_c = 30 mg/mg) resulted in values significantly higher than 0.5 d^{-1}, i.e., ranging from 0.75 to 1.50 d^{-1} for Bioreactor 1 to 1.5 to 2.25 d^{-1} for Bioreactor 2.

Decomposition rate coefficients for freshly cut alfalfa that are significantly higher than those previously adjusted for leaf mulch (Chapter 4) are consistent with the fact that the carbon-to-nitrogen (C/N) ratio for freshly cut alfalfa of 13 (Bechard et al. 1994) is lower than the ratio of 21 reported for the leaf mulch material previously used in Hemsi et al. (2005b) (Waybrant et al. 1998), and the lower the C/N ratio of a given solid organic material, the easier the decomposition of the material (Chynoweth and Pullammanappallil 1996). Also, freshly cut alfalfa was described as having a low content of lignin and containing bacterial nutrients and proteins (Bechard et al. 1994), factors that also enhance degradability. Finally, the actual temperatures occurring within the bioreactor materials are not reported in Bechard et al. (1994), and temperatures higher than 25 °C may have occurred. For example, for 35 °C, the Contois rate coefficient k_c for the decomposition of cellulose is reported to be 1.25 d^{-1} (Vavilin et al. 1996), which is in the range of values (0.75 – 1.50 d^{-1}) used in this study for freshly cut alfalfa in Bioreactor 1. For simulation Cases 1c, 1d, 2c, and 2d (Table 5.2 and 5.3), decomposition of more easily degradable fresh alfalfa is simulated with a Contois rate coefficient, k_c, equal to 4.0 d^{-1} (Tables 5.2 and 5.3).

5.4.3 Sulfate Reduction

Monod parameters for SRB growth on lactate are the same as those previously

used in Hemsi et al. (2005a,b). The maximum specific SRB growth rate (μ_{SRB}) is 4.0 d^{-1}, and the half-saturation constants for lactate (K_V) and sulfate (K_{SO}) are 5.0 and 2.0 mg/L, respectively.

5.4.4 Sulfide Precipitation

Kinetically controlled precipitation of Fe^{2+} mono-sulfide is modeled using first-order kinetics. The first-order rate coefficient for precipitation of $FeS_{(s)}$, or k_{Fe}, is 1.0 d^{-1}, which has been observed to be sufficiently high to approximate instantaneous precipitation under batch conditions (Hemsi et al. 2005a).

5.4.5 Hydrogen Sulfide Partial Volatilization

Kinetically controlled partial volatilization of H_2S to the gas phase is modeled using first-order kinetics (Hemsi et al. 2005a). The first-order rate coefficient for H_2S volatilization (i.e., k_v) is assumed equal to 10 d^{-1}, after verifying that the effect of volatilization on $FeS_{(s)}$ precipitation was negligible for k_v = 1.0 d^{-1} (data not shown). Although the rate of volatilization for k_v = 10 d^{-1} is expected to be greater than that for 1.0 d^{-1}, this rate also is dictated by H_2S concentrations in solution that decrease with increasing k_v and, therefore, is not directly proportional to the magnitude of k_v.

5.5 RESULTS AND DISCUSSION

5.5.1 Flow and Particle Tracking

Steady-state flow and particle tracking (MODPATH version 4.2, Pollock 1994) are used to determine patterns of flow and non-reactive advective transport in the

bioreactors. As shown in Fig. 5.2a (lateral view, see Fig. 5.1), the influent solution migrates along ascending pathlines through the material as the solution is injected into the first cell at the bottom layer (layer '9') and discharged at the opposite end in the top layer (layer '1'). As shown in Fig. 5.2b, the trajectory of product species (such as lactate and H_2S) toward the exit drain depends on the initial location, as expected. Flow boundary conditions imposed for simulation are observed to produce flow patterns (Fig. 5.2) that are consistent with the description of the imposed experimental conditions (Bechard et al. 1994). For transport simulations (RT3D), the first cell of layer '9' (i.e., injection cell) is assigned constant-concentration boundary condition with respect to SO_4^{2-} and Fe^{2+} (Table 5.1).

5.5.2 Reactive Transport for Bioreactor 1

5.5.2.1 Concentrations

Simulated SO_4^{2-} and Fe^{2+} effluent concentrations at the drain (i.e., at the last cell of layer '1') for Bioreactor 1 and based on Cases 1a – 1d (Table 5.2) are compared to effluent experimental concentrations in Fig. 5.3. As shown in Fig. 5.3a, simulated SO_4^{2-} concentrations based on Case 1a provide a reasonable approximations to the measured SO_4^{2-} concentrations earlier in the experiment (i.e., < 30 d), but appear to under estimate SO_4^{2-} concentrations towards the end of the experiment (e.g., > 110 d). In contrast, simulated SO_4^{2-} concentrations based on Case 1b do not follow the measured SO_4^{2-} concentrations near the beginning of the experiment (< 30 d), but provide a reasonable temporal approximation to the SO_4^{2-} data from 40 to 132 d.

As shown in Fig. 5.3b, the simulated Fe^{2+-} concentrations based on Case 1b also

better approximate the measured Fe^{2+} concentrations than do those based on Case 1a, with or without H_2S volatilization (i.e., with k_v equal to either 10 d^{-1} or zero), i.e., since the results based on Case 1a tend to over estimate effluent Fe^{2+} concentrations between 20 and 60 d. Based on a comparison of the results shown in Figs. 5.3c,d versus those in Figs. 5.3a,b, consideration of more easily degradable polysaccharides (Cases 1c and 1d) results in little effect on the simulated SO_4^{2-} and Fe^{2+} effluent concentrations, with any noticeable differences occurring primarily in the earlier period of the experiment (i.e., < 40 d). Thus, the results based on simulation Case 1b appear to provide the best approximation to the experimental data.

5.5.2.2 Cumulative Mass

The experimental and simulated results also may be presented and compared in terms of cumulative masses of SO_4^{2-} and Fe^{2+} based on the effluent solution and/or simulated results (Shackelford 1995). The cumulative mass represents an intermediate step towards determining mass balance verifications. Considering simulation Case 1b, SO_4^{2-} mass balance is shown in Fig. 5.4a, where the cumulative mass of SO_4^{2-} removed versus time is calculated as follows:

$$M_{removed}(t) = \underbrace{\int_0^t Q\{C_{in}(t) - C_{eff}(t)\}dt}_{M_{in}(t)-M_{out}(t)} - Wn \underbrace{\int_0^H \int_0^L C(x,z,t)\,dx\,dz}_{M_{stored}(t)} \qquad (5.1)$$

where $M_{removed}$ is the mass removed, Q is the volumetric discharge (cm^3/d) in the bioreactor, W, H, and L are the width, height, and length of bioreactor, respectively, n is

the porosity of the porous medium, and C_{in}, C_{eff}, and C are influent (Table 5.1), effluent (simulated), and resident (simulated) concentrations, respectively.

As shown in Fig. 5.4b, the simulated cumulative mass of SO_4^{2-} reduced after 132 d is approximately 44,000 mg, which compares favorably with the cumulative mass of SO_4^{2-} reduced of 41,000mg calculated on the basis of the experimental effluent data using the following expression:

$$M^*_{removed}(t) = \int_0^t Q \{C_{in}(t) - C^*_{eff}(t)\} dt \qquad (5.2)$$

where $M^*_{removed}$ is the mass removed evaluated from the effluent concentration data, and C^*_{eff} is the measured effluent concentration (data). The cumulative mass removed based on Eq. 5.2 represents a summation for all time intervals between measured effluent concentrations, and neglects the effect of the mass stored.

Based on Eqs. 5.1 and 5.2, Fe^{2+} mass balance and the cumulative mass of Fe^{2+} precipitated versus time (Case 1b) are shown in Figs. 5.5a and 5.5b, respectively. The simulated cumulative mass of Fe^{2+} precipitated (Eq. 5.1) after 132 d is approximately 16,000 mg, which compares favorably (see Fig. 5.5b) with the cumulative mass of 17,000 of Fe^{2+} precipitated evaluated on the basis of the measured effluent concentrations for Fe^{2+} (Eq. 5.2).

5.5.2.3 Other Simulated Species

The simulated behaviors of decomposable polysaccharides in freshly cut alfalfa

and decomposer bacteria (Case 1b) are shown in Fig. 5.6. For the relatively high decomposition rate coefficient, k_c, of 1.5 d^{-1}, approximately 95 % of the initial amount of decomposable polysaccharides is degraded after 132 d. With respect to decomposer bacteria (i.e., X_d), the population is observed to experience a three-fold growth, peak approximately one month after the onset of the experiment, and subsequently undergo net decay.

Snapshots of SRB biomass concentration contours along the bioreactor length and height (lateral view) versus time (Case 1b) are shown in Fig. 5.7a. The SRB population is observed to reach peak concentrations approximately two months after the onset of the experiments, and subsequently undergo net decay.

Snapshots of $FeS_{(s)}$ concentration contours along the bioreactor length and height versus time (Case 1b) are shown in Figs. 5.7b and 5.7c, considering the first-order rate coefficient for H_2S volatilization, k_v, equal to zero or 10 d^{-1}, respectively. The maximum precipitate concentration of ~ 30,000 mg/L is approximately equivalent to a volume fraction of $FeS_{(s)}$ of 0.0036, based on an $FeS_{(s)}$ density of 4 kg/L (e.g., mackinawite, $FeS_{0.9(s)}$). The precipitation of $FeS_{(s)}$ occurs over time and is located predominantly near the injection inlet of synthetic AMD solution (Fig. 5.7b,c), which is similar to the trends observed for previously modeled column tests (Hemsi et al. 2005b). An analogous behavior has been reported for the precipitation of Fe^{2+} oxides and carbonates within the iron cell of a pilot zero-valent iron (Fe^0) PRB (Yabusaki et al. 2001). The precipitation of $FeS_{(s)}$ near the bioreactor outlet (i.e., last cell of layer '1') shown in Fig. 5.7b results from the migration of some of the H_2S produced within the bioreactor through the upper layers (Fig. 5.2b) of the bioreactor such that H_2S eventually encounters Fe^{2+} near the vicinity of

bioreactor outlet (Fig. 5.2a). As a result of H_2S loss to the gas phase, $FeS_{(s)}$ precipitation near the top layers and in the vicinity of the bioreactor outlet becomes practically negligible (Fig. 5.7c).

Snapshots of H_2S concentration contours along the bioreactor length and height versus time (Case 1b) are shown in Figs. 5.7d and 5.7e for k_v equal to zero or to 10 d^{-1}, respectively. Based on a comparison of the results in Figs. 5.7d,e and 5.7b,c, H_2S concentrations remain approximately equal to zero in locations where $FeS_{(s)}$ precipitation is occurring, indicating that H_2S is a limiting factor to $FeS_{(s)}$ precipitation. Also, when including H_2S volatilization (Fig. 5.7e), resident H_2S concentrations after $FeS_{(s)}$ precipitation are only about 10 % of the resident H_2S concentrations occurring when volatilization is not included (Fig. 5.7d), i.e., indicating that volatilization with $k_v = 10\ d^{-1}$ has a significant effect on H_2S resident concentrations.

Snapshots of lactate (i.e., $C_3H_5O_3^-$) concentration contours along the bioreactor length and height versus time (Case 1b) are shown in Fig. 5.7f. Based on a comparison of the results in Figs. 5.7f and 5.7a, lactate concentrations are observed to remain approximately equal to zero (i.e., 0.05 mg/L) in locations where SRB growth (i.e., SO_4^{2-} reduction) is actively occurring in the bioreactor (e.g., compare contours for 5 to 60 d), indicating that lactate is a limiting factor to SO_4^{2-} reduction.

5.5.2.4 Elemental Mass Balances

Mass balance ratios [$= M_{in}/(M_{out} + M_{stored} + M_{removed})$] for sulfur (S), iron (Fe), and carbon (C) in Bioreactor 1 based on simulated results (Case 1b) are shown in Fig. 5.8. Mass balance ratios for S and Fe range remarkably close to unity (Figs. 5.8a,b). For

C, separate mass balance ratios for decomposition and SO_4^{2-} reduction are evaluated, based on each of the following respective reactions:

$$\underbrace{2C_6H_{10}O_5}_{\text{cellulose}} + 2H_2O + 0.524NH_4^+ \rightarrow 3.126\underbrace{C_3H_5O_3^-}_{\text{lactate}} + 3.652H^+ + 1.573H_2O + 0.524\underbrace{C_5H_7O_2N}_{\text{biomass, } X_d} \quad (5.3)$$

$$2.128\underbrace{C_3H_5O_3^-}_{\text{lactate}} + SO_4^{2-} + 0.0766NH_4^+ \rightarrow 2HCO_3^- + 0.234H_2O + H_2S + 2\underbrace{C_2H_3O_2^-}_{\text{acetate}} + 0.0766\underbrace{C_5H_7O_2N}_{\text{biomass, } X_{SRB}} \quad (5.4)$$

However, as shown in Fig. 5.8c, only the mass balance ratio for C in decomposition was evaluated, since acetate was not included in the model simulations. Mass balance ratios for C in decomposition ranging from unity to ~ 1.10 were considered acceptable.

5.5.2.5 Effects of Thickness of the Aerobic Zone and Dispersivity

The effect of varying the unknown thickness of the top, non-SR zone (i.e., T) on simulated effluent concentrations for SO_4^{2-} and Fe^{2+} is shown in Figs. 5.9a and 5.9b, respectively. As shown in Table 5.2, T is varied from the previous value of 30 mm (Case 1b) to 10 mm, 20 mm, and 40 mm (Cases 1e, 1f, and 1g, respectively). As shown in Fig. 5.9, effluent concentrations for SO_4^{2-} and Fe^{2+} versus time decrease as T decreases from 40 to 10 mm, as expected. Reasonable approximations of effluent SO_4^{2-} concentrations are obtained for T ranging from 20 to 40 mm (Fig. 5.9a) for the decomposition and SO_4^{2-} reduction parameter values considered in this study. Therefore, 30 mm assumed in Case 1b appears to be an acceptable value for the simulations in this study. In fact, T is likely to vary during the experiments, following the dynamics of decomposition and SO_4^{2-}

reduction in the systems.

The effect of varying the unknown longitudinal dispersivity (i.e., α_L) from zero (Case 1b) to 20 mm (Case 1h, Table 5.2) on simulated effluent concentrations for SO_4^{2-} and Fe^{2+} is shown in Figs. 5.10a and 5.10b, respectively. As expected due to the relatively short lengths of the bioreactors, changing α_L from zero to 20 mm had little effect (i.e., < 10 % on average) on the simulated effluent concentrations for SO_4^{2-}. In contrast, varying α_L from zero to 20 mm appeared to have a greater impact (> 85 d) on the simulated effluent concentrations for Fe^{2+}. However, for the ranges in parameters considered in this study, the effect of α_L is not significant enough to alter the interpretation of the experiment based on Case 1b.

5.5.3 Reactive Transport for Bioreactor 2

The only difference between Bioreactors 1 and 2 is that the volumetric discharge for Bioreactor 2 is twice as great relative to that for Bioreactor 1 (i.e., 1,440 cm^3/d for Bioreactor 2 versus 720 cm^3/d for Bioreactor 1). The increase in volumetric discharge represents a decrease in residence time from 6.2 d for Bioreactor 1 to 3.1 d for Bioreactor 2. Thus, simulation of Bioreactor 2 is performed to assess the ability of the model to approximate this difference in residence time.

5.5.3.1 Concentrations

Simulated SO_4^{2-} and Fe^{2+} effluent concentrations for Bioreactor 2 based on Cases 2a – 2d (Table 5.3) are compared to effluent experimental concentrations in Fig. 5.11. As shown in Fig. 5.11a, simulated SO_4^{2-} concentrations based on Cases 2a and 2b provide

reasonable approximations to measured SO_4^{2-} concentrations before ~ 40 d and after ~ 80 d. However, between 40 and 80 d, the simulated SO_4^{2-} concentrations are lower than measured concentrations by ~ 250 mg/L for Case 2a and by ~ 150 mg/L for Case 2b.

As shown in Fig. 5.11b, throughout the duration of the experiment, the simulated Fe^{2+} concentrations compare favorably with measured concentrations. In agreement with the experimental data, the simulated Fe^{2+} concentrations remain < 20 mg/L until 40 d, and thereafter increase and approach the influent concentration of ~ 215 mg/L at 130 d. As shown in Figs. 5.11c,d, considering part of the decomposable polysaccharides to be more easily degradable (Cases 2c and 2d in Table 5.3) slightly improves the approximation of the SO_4^{2-} effluent data relative to those based on Cases 1a and 1b, whereas essentially no improvement in the approximations of the Fe^{2+} concentrations occurs. The approximations of measured data based on simulation Cases 2b and 2d appear to be essentially equivalent. However, simulation Case 2b is simpler than simulation Case 2d because simulation Case 2b does not assume the decomposable polysaccharides as divided into two pools.

5.5.3.2 Cumulative Mass

The experimental and simulated results for Bioreactor 2 are presented and compared in terms of cumulative masses of SO_4^{2-} and Fe^{2+}. Considering simulation Case 2b, SO_4^{2-} mass balance is shown in Fig. 5.12a, where the simulated cumulative mass of SO_4^{2-} removed versus time is calculated using Eq. 5.1. As shown in Fig. 5.12b, the simulated cumulative mass of SO_4^{2-} reduced after 132 d is approximately 49,000 mg, whereas the cumulative mass of SO_4^{2-} reduced calculated based of the experimental

effluent data and Eq. 5.2 is approximately 32,000 mg. The simulated cumulative mass of SO_4^{2-} reduced is greater than the cumulative mass given by the experimental data because the simulated effluent concentrations for SO_4^{2-} (Case 2b) are lower than the measured concentrations, as previously discussed. Therefore, the simulated cumulative mass should be approximately 17,000 mg greater than the cumulative mass based on the experimental data.

Also for Case 2b, Fe^{2+} mass balance is shown in Fig. 5.13a, where the simulated cumulative mass of Fe^{2+} precipitated versus time is calculated using Eq. 5.1. As shown in Fig. 5.13b, the simulated cumulative mass of Fe^{2+} precipitated after 132 d is approximately 21,000 mg, and results equal to the precipitated cumulative mass of Fe^{2+} calculated using the experimental effluent data and Eq. 5.2. Additionally, for 21,000 mg of accumulated mass of Fe^{2+} precipitated, the required stoichiometric cumulative mass of SO_4^{2-} reduced including H_2S lost in the effluent solution would be on the order of 49,000 mg, indicating that the simulated results are consistent in terms of mass stoichiometry.

5.5.4 Reactive Transport for Bioreactor 3

The volumetric discharge for Bioreactor 3 is 144 cm^3/d, which is 5 times lower than that for Bioreactor 1 (i.e., 720 cm^3/d) and 10 times lower than that for Bioreactor 2 (i.e., 1440 cm^3/d). Because of this significantly lower volumetric discharge for Bioreactor 3, the residence time was 31 d, which resulted in only about four pore volumes of flow (PVF) during the 132 d of testing.

5.5.4.1 Concentrations

Simulated SO_4^{2-} and Fe^{2+} effluent concentrations for Bioreactor 3 based on Cases 3a and 3b (Table 5.3) are compared to effluent experimental concentrations in Fig. 5.14. The parameter values used for simulation Cases 3a and 3b are the same as those that provided reasonable approximations to the data for Bioreactors 1 and 2.

As shown in Fig. 5.14a, the experimental data for SO_4^{2-} indicates that between 350 and 650 mg/L SO_4^{2-} were continuously released in the effluent, including ~ 250 mg/L before one PVF. In contrast, in the simulated results, SO_4^{2-} concentrations in the effluent solution are zero until about 85 to 100 d (~ 3 PVF). Therefore, the simulated results for both Cases 3a and 3b provide poor approximations to measured SO_4^{2-} effluent concentrations.

Although the exact cause for this discrepancy is unclear, experimental effluent concentrations for SO_4^{2-} appear to be too high, since (i) significant SO_4^{2-} concentrations were measured in the effluent before one PVF, and (ii) SO_4^{2-} effluent concentrations for Bioreactor 3 were only ~ 50 % lower than those for Bioreactor 2, despite the significant difference in residence times (i.e., 31 d versus 3.1 d). The high effluent concentrations for SO_4^{2-} may be attributable to the release of SO_4^{2-} due to the leaching of the solid materials during the first PVF (e.g., Groudev et al. 1999). In fact, SO_4^{2-} effluent concentrations during the first four PVF also were elevated in the case of Bioreactors 1 and 2 (see Figs. 5.3a,c and 5.11a,c), similarly to what is apparent for Bioreactor 3. Clearly, since Bioreactors 1 and 2 were extended to more than 20, or more than 40 PVF, respectively, the early data pertaining to the first four PVF did not affect the analyses (e.g., see simulation Cases 1b and 1d for Bioreactor 1) as significantly as in the case of Bioreactor

3. As shown in Fig. 5.14b, simulated results for Fe^{2+} (Cases 3a and 3b) are in agreement with measured effluent concentrations for Fe^{2+} that are equal to approximately zero throughout the duration of the experiment. The simulated cumulative mass of Fe^{2+} precipitated in this experiment after 132 d is approximately 3,000 mg, which is equal to the amount calculated based on the experimental results for Fe^{2+}.

5.6 CONCLUSIONS

Experimental effluent concentrations for sulfate (SO_4^{2-}) and ferrous iron (Fe^{2+}) in three open, aerobic-anaerobic, sulfate reducing (SR) bioreactors were approximated using the new biochemical model coupled to flow and contaminant transport. Adjusted parameters for decomposition of polysaccharides (Contois kinetics) in freshly cut alfalfa resulted significantly higher than those previously obtained for leaf mulch, but were consistent with the characteristics of the fresh alfalfa material. In the case of Bioreactors 1 and 2, reasonable temporal approximations were obtained for the experimental concentrations of both SO_4^{2-} and Fe^{2+} in the effluent solution. The model was capable of reasonably simulating the effect of variable residence time (i.e., 6.2, 3.1, and 31 d) on effluent concentrations for Fe^{2+} for all three bioreactors but discrepancies between simulated and experimental results occurred for Bioreactor 3 in the case of SO_4^{2-}.

Comparison of the simulations and experimental data indicated that the kinetically controlled precipitation of iron sulfide, $FeS_{(s)}$, resulted in $FeS_{(s)}$ precipitation not only in the vicinity of the solution inlet (i.e., injection cell), but also near the solution outlet (i.e., drain), due to the particular patterns of flow and transport occurring in the bioreactors. Due to the open system, the volatilization of hydrogen sulfide (H_2S) to the gas phase not

only affected resident concentrations for H_2S, but also caused increases in the effluent concentrations for Fe^{2+}, and retarded the precipitation of $FeS_{(s)}$. Also, due to the open system, the presence of an unknown total thickness of top, non sulfate reducing layer in the bioreactors affected effluent concentrations for SO_4^{2-} and Fe^{2+}.

5.7 ACKNOWLEDGEMENTS

This research was funded by the U. S. EPA Science to Achieve Results (STAR) Program under Grant No. R-82951501-0 as part of the U. S. EPA's *Rocky Mountain Regional Hazardous Substance Research Center*. The authors extend their thanks to Mr. Christian Johnson, Senior Development Engineer, Battelle-PNWD, Richland (WA), for excellent initial RT3D support.

5.8 REFERENCES

Amos, R.T., Mayer, K.U., Blowes, D.W., and Ptacek, C.J. (2004). Reactive transport modeling of column experiments for remediation of acid mine drainage. *Environmental Science and Technology*, 38(11): 3131-3138.

Bechard, G., Yamazaki, H., Gould, W.D., and Bedard, P. (1994). Use of cellulosic substrates for the microbial treatment of acid mine drainage. *Journal of Environmental Quality*, 23(1): 111-116.

Benner, S.G, Blowes, D.W., Ptacek, C.J., and Mayer, K.U. (2002). Rates of sulfate reduction and metal sulfide precipitation in a permeable reactive barrier. *Applied Geochemistry*, 17(1): 301-320.

Boudreau, B.P., and Westrich, J.T. (1984). The dependence of bacterial sulfate reduction

on sulfate concentration in marine environments. *Geochimica et Cosmochimica Acta*, 48(12): 2503-2516.

Chapra, S.C., and Canale, R.P. (2002). *Numerical Methods for Engineers*. 4th Edition, McGraw-Hill, New York, NY.

Christensen, B., Morten, L., and Lien, T. (1996). Treatment of acid mine water by sulfate-reducing bacteria; results from a bench scale experiment. *Water Research*, 30(7): 1617-1624.

Chynoweth, D.P., and Pullammanappallil, P. (1996). Anaerobic digestion of municipal solid waste. *Microbiology of Solid Waste*, A. Palmasano and M.A. Barlaz, eds.,CRC Press, Boca Raton, FL, 77-113.

Clement, T.P. (1997). A Modular Computer Code for Simulating Reactive Multi-species Transport in 3-Dimensional Groundwater Systems RT3D version 1.0. U.S. Department of Energy and Pacific Northwest National Laboratory. PNNL-11720-1997.

Clement, T.P. (2003). RT3D v.2.5 Update Document, What is New in RT3D version 2.5. Electronic document: http://bioprocess.pnl.gov/rt3d.htm.

Contois, D.E. (1959). Kinetics of bacterial growth, relationship between population density and specific growth rate of continuous cultures. *Journal of General Microbiology*, 21(1): 40-50.

Drever, J.I. (1997). *The Geochemistry of Natural Waters – Surface and Groundwater Environments*. 3rd Edition, Prentice-Hall, Upper Saddle River, NJ.

Drury, J.W. (2000). Modeling of sulfate reduction in anaerobic solid substrate bioreactors for mine drainage treatment. *Mine Water and the Environment*, 19(1): 18-28.

Dvorak, D.H., Hedin, R.S., Edenborn, H.M., and McIntire, P.E. (1992). Treatment of metal-contaminated water using bacterial sulfate reduction: results from pilot-scale reactors. *Biotechnology and Bioengineering*, 40(5): 609-616.

Fenchel, T., and Harrison, P. (1976). The significance of bacterial grazing and mineral cycling for the decomposition of particulate detritus. *The Role of Terrestrial and Aquatic Organisms in Decomposition Processes*, J.M. Anderson and A. Macfadyen, eds., Blackwell Scientific Publications, Oxford, UK, 285-299.

Gazea, B., Adam, K., and Kontopoulos, A. (1996). A review of passive systems for the treatment of acid mine drainage. *Minerals Engineering*, 9(1): 23-42.

Gilbert, J.S., Wildeman, T.R., and Ford, K.L. (1999). Laboratory experiments designed to test the remediation properties of materials. Proceedings of the 16th National Meeting of the American Society for Surface Mining and Reclamation, ASMR ed., Scottsdale, AZ, 592-598.

Groudev, S.N., Bratcova, S., and Komnitsas, K. (1999). Treatment of waters polluted with radioactive elements and heavy metals by means of a laboratory passive system. *Minerals Engineering*, 12(3): 261-270.

Hammack, R.W., and Edenborn, H.M. (1992). The removal of nickel from mine waters using bacterial sulfate reduction. *Applied Microbiology and Biotechnology*, 37(5): 674-678.

Harbaugh, A.W., Banta, E.R., Hill, M.C., and McDonald, M.G. (2000). *MODFLOW-2000, the U.S. Geological Survey Modular Ground-Water Model – User Guide to Modularization Concepts and the Ground-Water Flow Process*, USGS Open-File Report 00-92, Reston, VA.

Hemsi, P.S., Shackelford, C.D., and Figueroa, L.A. (2005a). Modeling the influence of decomposing organic solids on sulfate reduction rates for iron precipitation. *Environmental Science and Technology*, 39(9): 3215-3225.

Hemsi, P.S., Shackelford, C.D., and Figueroa, L.A. (2005b). Modeling column experiments for metals precipitation based on sulfate reduction and decomposition of organic solids. *Environmental Science and Technology*. Submitted.

Henriksen, T.M., and Breland, T.A. (2002). Carbon mineralization, fungal and bacterial growth, and enzyme activities as affected by contact between crop residues and soil. *Biology and Fertilization of Soils*, 35(1): 41-48.

Hulshof, A.H., Blowes, D.W., Ptacek, C.J., and Gould, W.D. (2003). Microbial and nutrient investigations into the use of in situ layers for treatment of tailings effluent. *Environmental Science and Technology*, 37(21): 5027-5033.

Langmuir, D. (1997). *Aqueous Environmental Geochemistry*. Prentice-Hall, Upper Saddle River, NJ.

Luptakova, A., and Kusnierova, M (2005). Bioremediation of acid mine drainage contaminated by SRB. *Hydrometallurgy*, 77(1-2): 97-102.

Mayer, K.U., Frind, E.O, and Blowes, D.W. (2002). Multicomponent reactive transport modeling in variably saturated porous media using a generalized formulation for kinetically controlled reactions. *Water Resources Research*, 38(9): 13-1 to 13-21.

Mechemer, S.D., and Wildeman, T.R. (1992). Adsorption compared with sulfide precipitation as metal removal processes from acid mine drainage in a constructed wetland. *Journal of Contaminant Hydrology*, 9(2): 115-131.

Monod, J. (1949). The growth of bacterial cultures. *Annual Review of Microbiology*, 3:

371-394.

MSE Technology Applications (2002). *Final Report-Sulfate Reducing Bacteria Reactive Wall Demonstration.* Mine Waste Technology Program, Activity III, Project 12, U.S. Environmental Protection Agency; U.S. Department of Energy, MWTP-206.

Pollock, D.W. (1994). *User's Guide for MODPATH/MODPATH-PLOT, Version 3: A Particle Tracking Post-Processing Package for MODFLOW, the U.S. Geological Survey Finite-Difference Ground-Water Flow Model,* U.S. Geological Survey, Open-File Report 94-464, Reston, VA.

Postgate, J.R. (1984). *The Sulphate-Reducing Bacteria.* 2nd Edition. Cambridge University Press, Cambridge, UK.

Prasad, D., Wai, M., Berube, P., and Henry, J. (1999). Evaluating substrates in the biological treatment of acid mine drainage. *Environmental Technology*, 20(5): 449-458.

Prommer, H., Barry, D.A., Chiang, W.H., and Zheng, C. (2001). PHT3D – a MODFLOW/MT3DMS-based reactive multi-component transport model. *MODFLOW 2001 and Other Modeling Odysseys*, H. Seo, E. Poeter, and C. Zheng, eds., International Ground-Water Modeling Center, Colorado School of Mines, Golden, CO, 477-483.

Ronen, D., Magaritz, M., Almon, E., and Amiel, A. (1987). Anthropogenic anoxification ("eutrophication") of the water table region of a deep phreatic aquifer. *Water Resources Research*, 23(8): 1554-1560.

Schafer, D., Schafer, W., and Kinzelbach, W. (1998a). Simulation of reactive processes related to biodegradation in aquifers. 1-structure of the three-dimensional reactive

transport model. *Journal of Contaminant Hydrology*, 31(1-2): 167-186.

Schafer, D., Schafer, W., and Kinzelbach, W. (1998b). Simulation of reactive processes related to biodegradation in aquifers. 2-model application to a column study on organic carbon degradation. *Journal of Contaminant Hydrology*, 31(1-2): 187-209.

Shackelford, C. D. (1995). Cumulative mass approach for column testing. *Journal of Geotechnical Engineering*, 121(10): 696-703.

Sposito, G. (1989). *The Chemistry of Soils*. Oxford University Press, Oxford, UK.

Tuttle, J.H., Dugan, P.R., and Randles, C.I. (1969). Microbial sulfate reduction and its potential utility as an acid mine water pollution abatement procedure. *Applied Microbiology*, 17(2): 297-302.

Vavilin, V.A., Rytov, S.V., and Lokshina, L. (1996). A description of hydrolysis kinetics in anaerobic degradation of particulate organic matter. *Bioresource Technology*, 56(1): 229-237.

Zheng, C. (1990). MT3D: *A Modular Three-Dimensional Transport Model for Simulation of Advection, Dispersion and Chemical Reaction of Contaminants in Groundwater Systems*. U.S. Environmental Protection Agency and Robert S. Kerr Environmental Research Laboratory, Ada, OK.

Zheng, C., and Wang, P.P. (1999). MT3DMS: *A Modular Three-Dimensional Multispecies Model for Simulation of Advection, Dispersion, and Chemical Reactions of Contaminants in Groundwater Systems; Documentation and User's Guide*. U.S. Army Corps of Engineers. Contract Report SERDP-99-1, December 1999.

Yabusaki, S., Cantrell, K., Sass, B., and Steefel, C. (2001). Multicomponent reactive transport in an in situ zero-valent iron cell. *Environmental Science and Technology*,

35(7): 1493-1503.

Wakao, N., Takahashi, T., Sakurai, Y., and Shiota, H. (1979). A treatment of acid mine water using sulfate-reducing bacteria. *Journal of Fermentation Technology*, 57(5): 445-452.

Waybrant, K.R., Blowes, D.W., and Ptacek, C.J. (1998). Selection of reactive mixtures for use in permeable reactive walls for treatment of mine drainage. *Environmental Science and Technology*, 32(13): 1972-1979.

Webb, J.S., McGinness, S., and Lappin-Scott, H.M. (1998). Metal removal by sulphate-reducing bacteria from natural and constructed wetlands. *Journal of Applied Microbiology*, 84(2): 240-248.

Westrich, J.T., and Berner, R.A. (1984). The role of sedimentary organic matter in bacterial sulfate reduction: the G model tested. *Journal of Limnology and Oceanography*, 29(2): 236-249.

Whitehead, P.G., and Prior, H (2005). Bioremediation of acid mine drainage: an introduction to the Wheal Jane wetlands project. *Science of the Total Environment,* 338(1-2): 15-21.

Wieder, R.K., Linton, M.N., and Heston, K.P. (1990). Laboratory mesocosm studies of Fe, Al, Mn, Ca, and Mg dynamics in wetlands exposed to synthetic acid coal mine drainage. *Water, Air, and Soil Pollution*, 51(1-2): 181-196.

Table 5.1 – Influent concentrations for sulfate and ferrous iron considered for simulations.

Experiment	Time (d)	Concentration (mg/L) (at the injection cell)	
		SO_4^{2-}	Fe^{2+}
Bioreactors 1, 2, and 3	0-20	1,042.9	193.2
	20-48	1,042.9	217.4
	48-61	1,042.9	200.0
	61-67	1,042.9	195.6
	67-90	1,070.4	195.6
	90-99	1,344.8	195.6
	99-101	1,344.8	214.9
	101-132	1,180.2	214.9

Table 5.2 – Parameter values for different simulation cases for Bioreactor 1.

Case	Materials	Decomposition (Contois kinetics)			Non SR zone	Sulfate Reduction (Monod kinetics)	H_2S Volatiliz. (first-order kinetics)	$FeS_{(s)}$ Precip. (first-order kinetics)	Dispersivity
		Initial [CE] (mg/L)	k_c (d^{-1})	Initial $[X_d]$/[CE]	T (mm)	$[X_{SRB}]$ (mg/L)	k_v (d^{-1})	k_{Fe} (d^{-1})	α_L (mm)
1a	FA	**35,120**	**0.75**	0.005	**30**	50	**0.0; 10**	1.0	**0.0**
1b	FA	**35,120**	**1.50**	0.005	30	50	**0.0; 10**	1.0	0.0
1c	FA	**28,120**	**0.75**	0.005	30	50	**0.0; 10**	1.0	0.0
	EDFA	**7,000**	**4.00**						
1d	FA	**28,120**	**1.50**	0.005	30	50	**0.0; 10**	1.0	0.0
	EDFA	**7,000**	**4.00**						
1e	FA	35,120	1.50	0.005	**10**	50	0.0	1.0	0.0
1f	FA	35,120	1.50	0.005	**20**	50	0.0	1.0	0.0
1g	FA	35,120	1.50	0.005	**40**	50	0.0	1.0	0.0
1h	FA	35,120	1.50	0.005	30	50	0.0	1.0	**20**

FA: freshly cut alfalfa; EDFA: easily decomposable FA.
SR: sulfate reducing.

Table 5.3 – Parameter values for different simulation cases for Bioreactors 2 and 3.

Bioreactor	Case	Materials	Decomposition (Contois kinetics)			Non SR zone	Sulfate Reduction (Monod kinetics)	H_2S Volatiliz. (first-order kinetics)	$FeS_{(s)}$ Precip. (first-order kinetics)
			Initial [CE] (mg/L)	k_c (d^{-1})	Initial $[X_d]$/[CE]	T (mm)	$[X_{SRB}]$ (mg/L)	k_v (d^{-1})	k_{Fe} (d^{-1})
2	2a	FA	**35,120**	**1.50**	0.005	30	50	**0.0; 10**	1.0
	2b	FA	**35,120**	**2.25**	0.005	30	50	**0.0; 10**	1.0
	2c	FA	**28,120**	**1.50**	0.005	30	50	**0.0; 10**	1.0
		EDFA	**7,000**	**4.00**					
	2d	FA	**28,120**	**2.25**	0.005	30	50	**0.0; 10**	1.0
		EDFA	**7,000**	**4.00**					
3	3a	FA	**35,120**	**1.50**	0.005	30	50	0.0	1.0
	3b	FA	**35,120**	**2.25**	0.005	30	50	0.0	1.0

FA: freshly cut alfalfa; EDFA: easily decomposable FA.
SR: sulfate reducing. Note: Dispersivity, α_L, equal to zero.

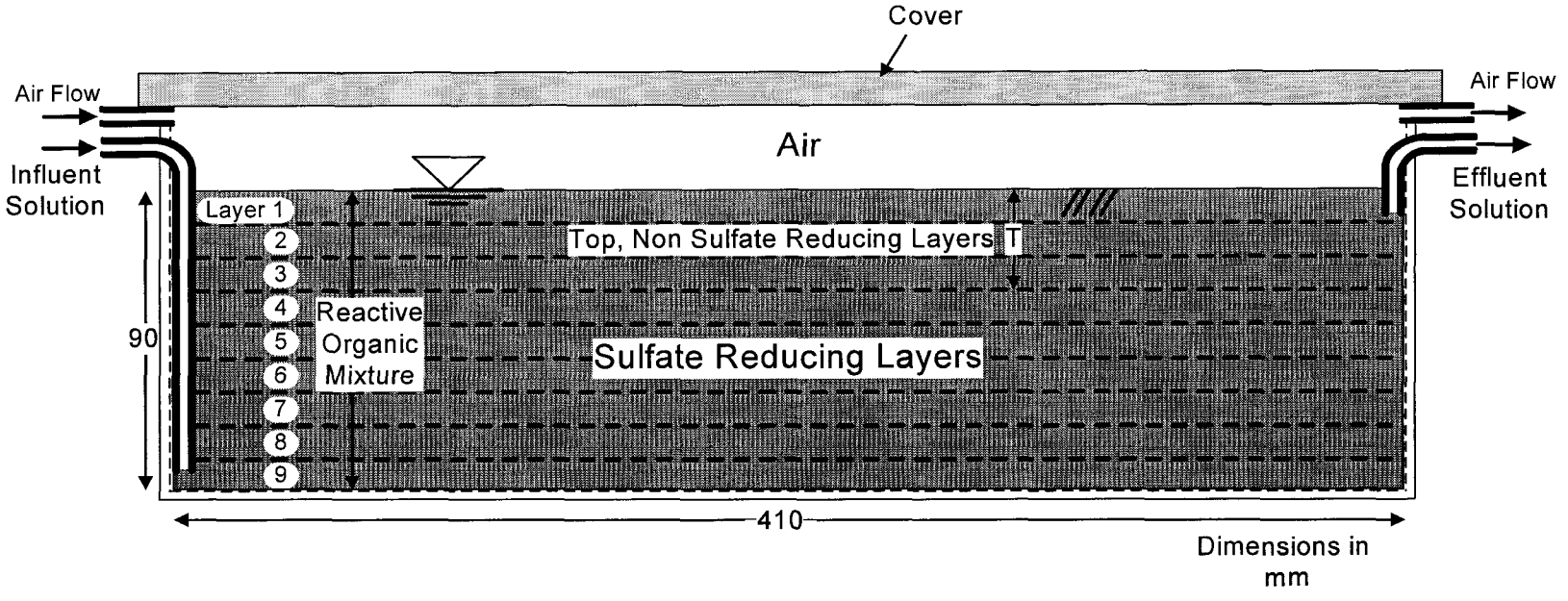

Figure 5.1 – Schematic side view for bioreactors 1, 2, and 3. Note: T = thickness of non sulfate reducing zone.

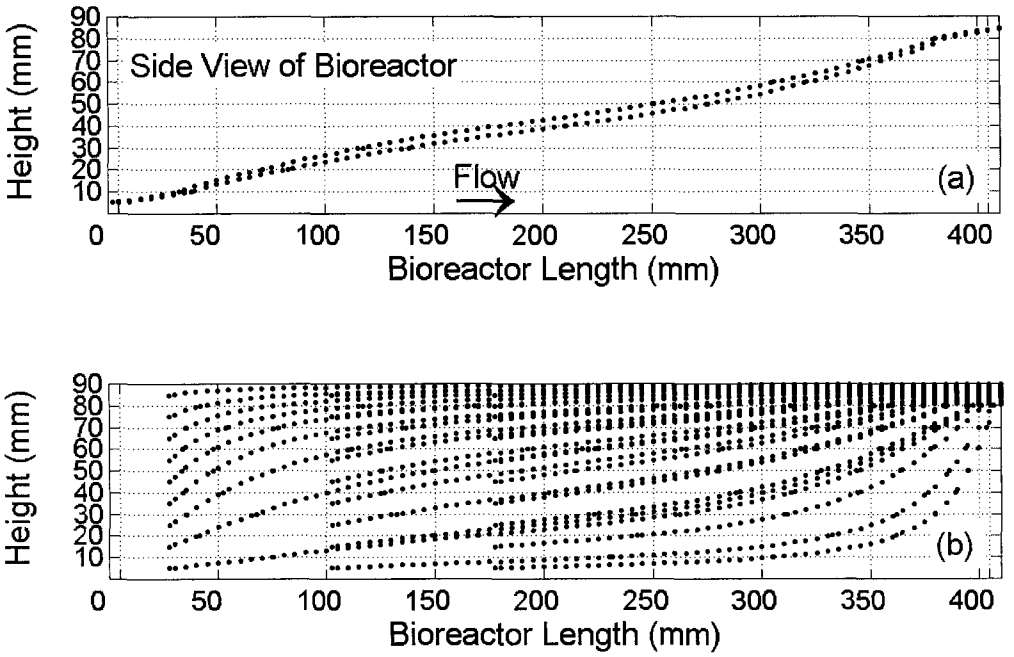

Figure 5.2 – Flow and advective non-reactive transport directions as given by particle tracking: (a) influent (injected) sulfate and ferrous iron, and (b) produced species, such as lactate and H_2S.

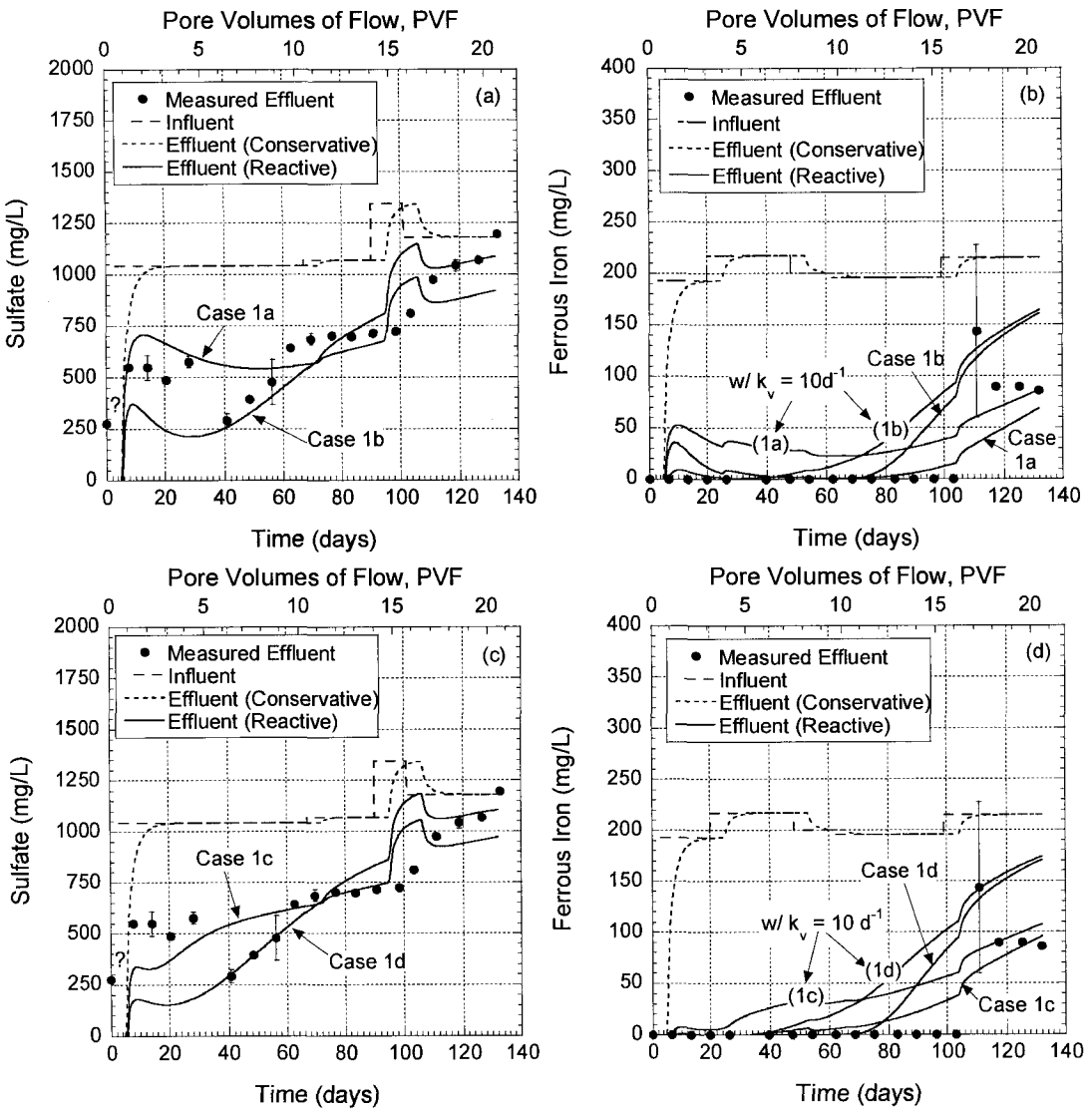

Figure 5.3 – Comparison between simulated and measured effluent concentrations for Bioreactor 1, Cases 1a and 1b: (a) sulfate and (b) ferrous iron, and Cases 1c and 1d: (c) sulfate, and (d) ferrous iron.

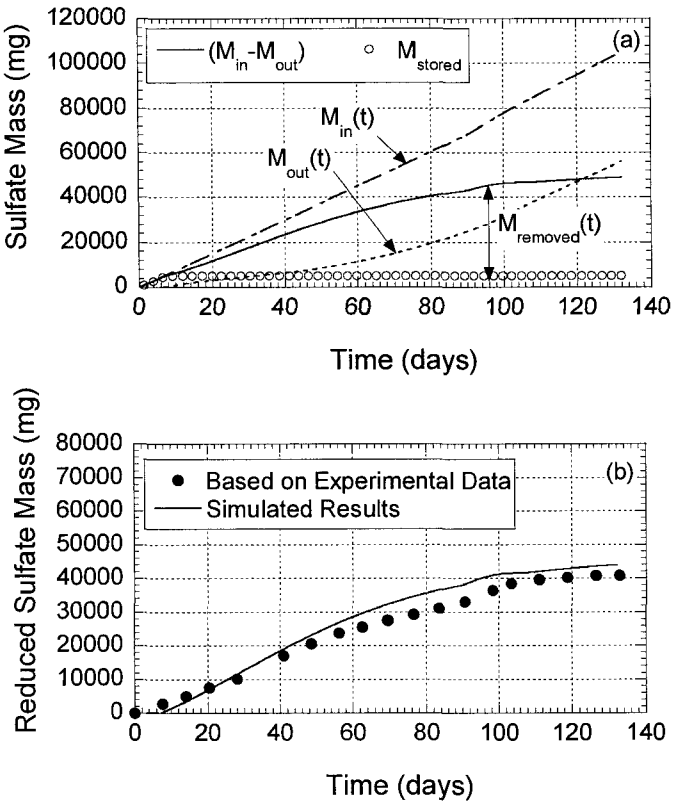

Figure 5.4 – (a) Simulated cumulative masses input (M_{in}), output (M_{out}), stored (M_{stored}), and removed ($M_{removed}$) for sulfate in reactive transport (Case 1b); (b) comparison between simulated (Case 1b) and experimentally based results.

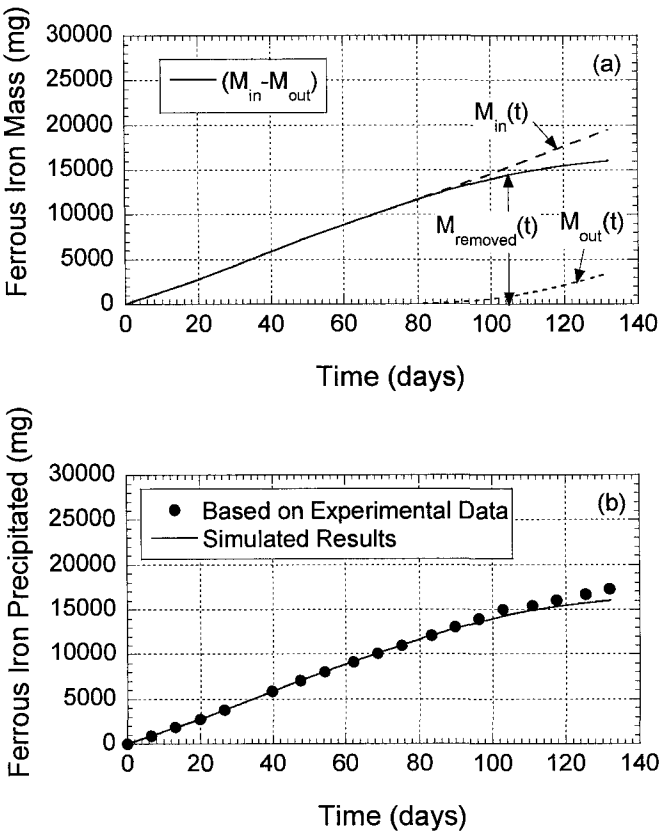

Figure 5.5 – (a) Simulated cumulative masses input (M_{in}), output (M_{out}), and removed ($M_{removed}$) for ferrous iron in reactive transport (Case 1b); (b) comparison between simulated (Case 1b) and experimentally based results. Note: Mass stored neglected.

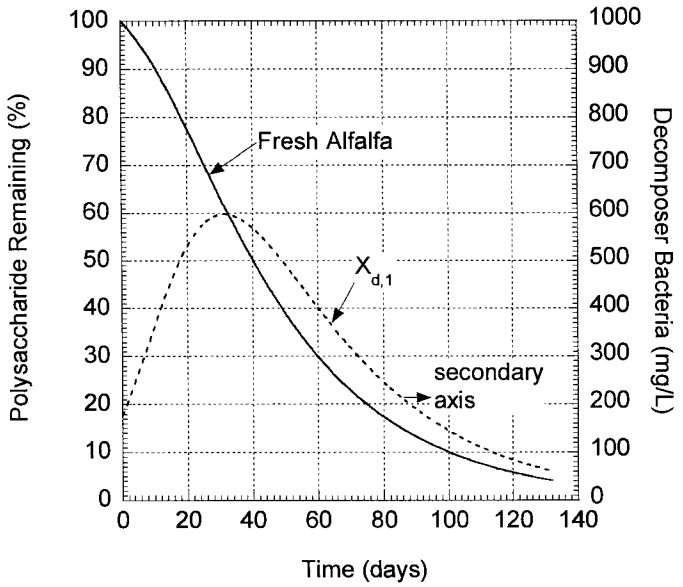

Figure 5.6 – Simulated percentages of initial polysaccharide remaining and concentrations of decomposer bacteria ($X_{d,1}$) in Bioreactor 1 (Case 1b).

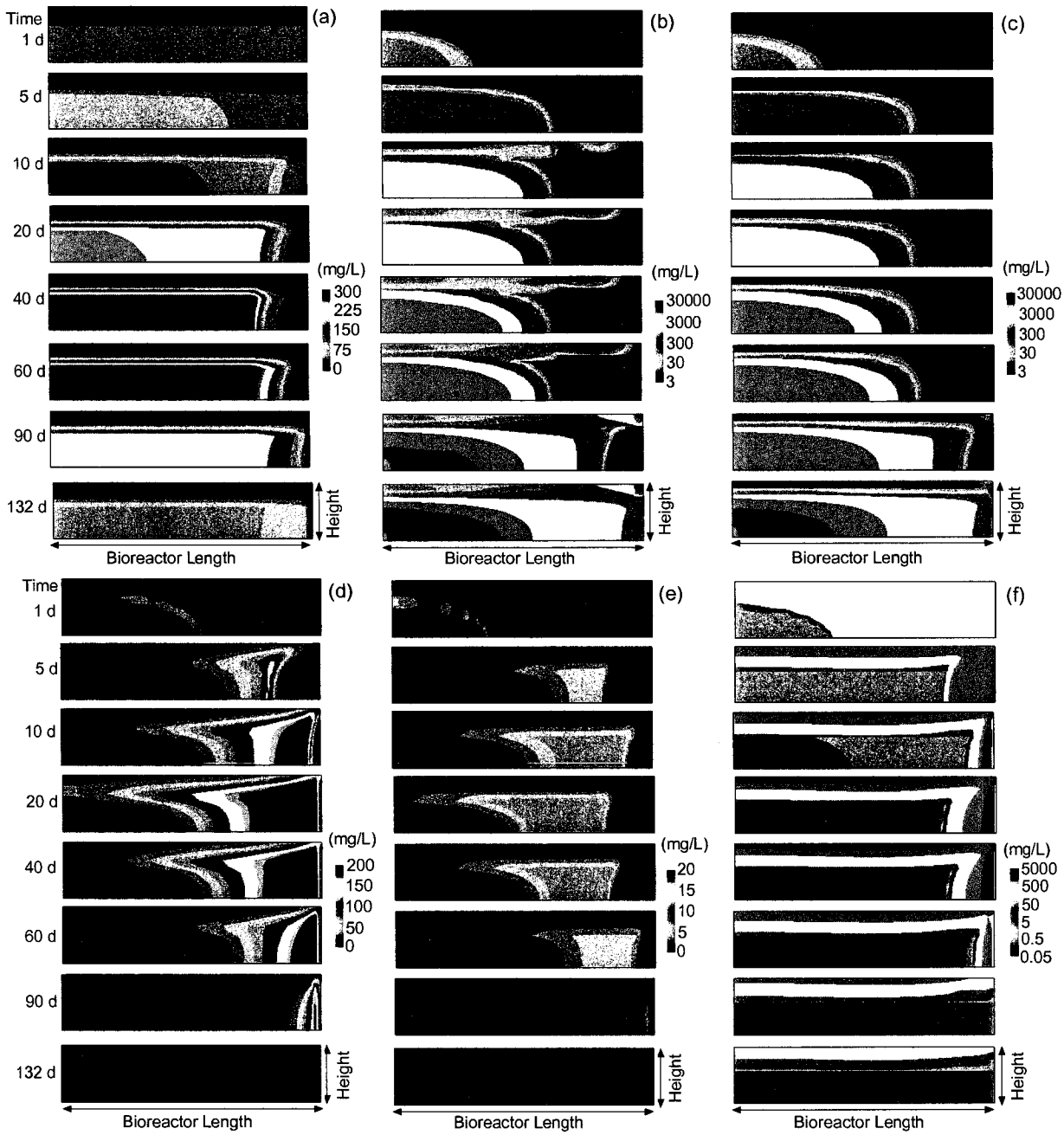

Figure 5.7 – Snapshots (side view) of simulated concentrations in Bioreactor 1 (Case 1b): (a) SRB biomass, (b) iron sulfide ($FeS_{(s)}$) for null volatilization (k_v=0), (c) $FeS_{(s)}$ for k_v=10 d^{-1}, (d) hydrogen sulfide (H_2S) for null volatilization (k_v=0), (e) H_2S for k_v=10 d^{-1}, and (f) lactate.

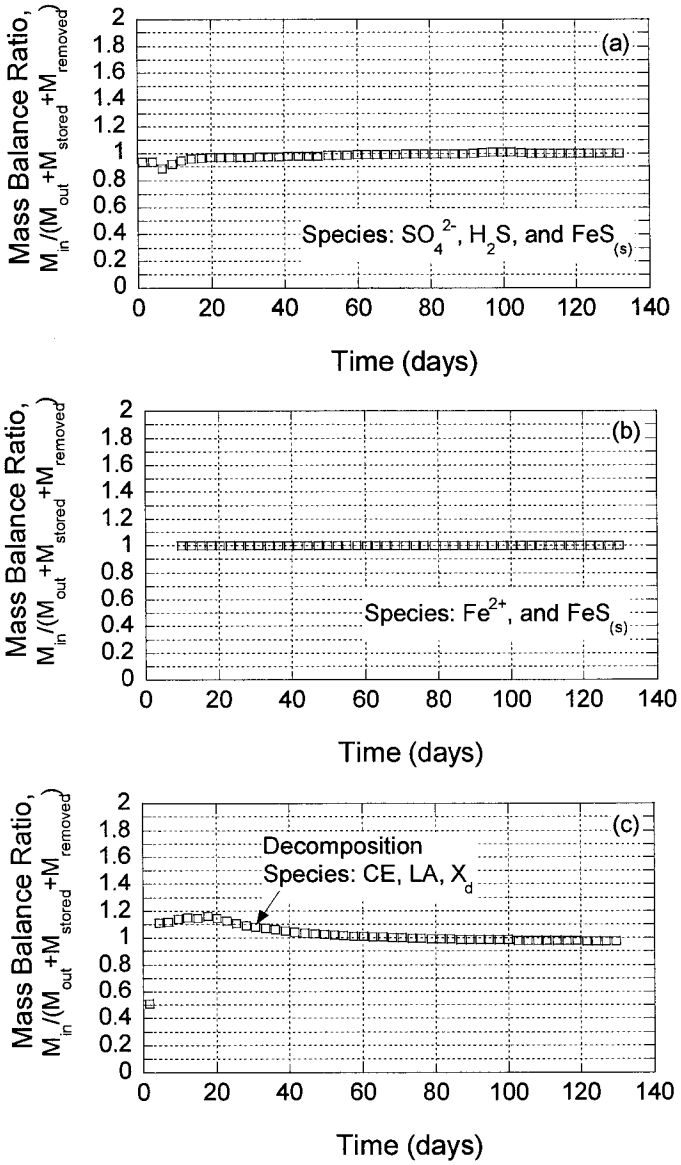

Figure 5.8 – Mass balance ratios for Bioreactor 1, simulation Case 1b, (a) sulfur, (b) iron, and (c) carbon.

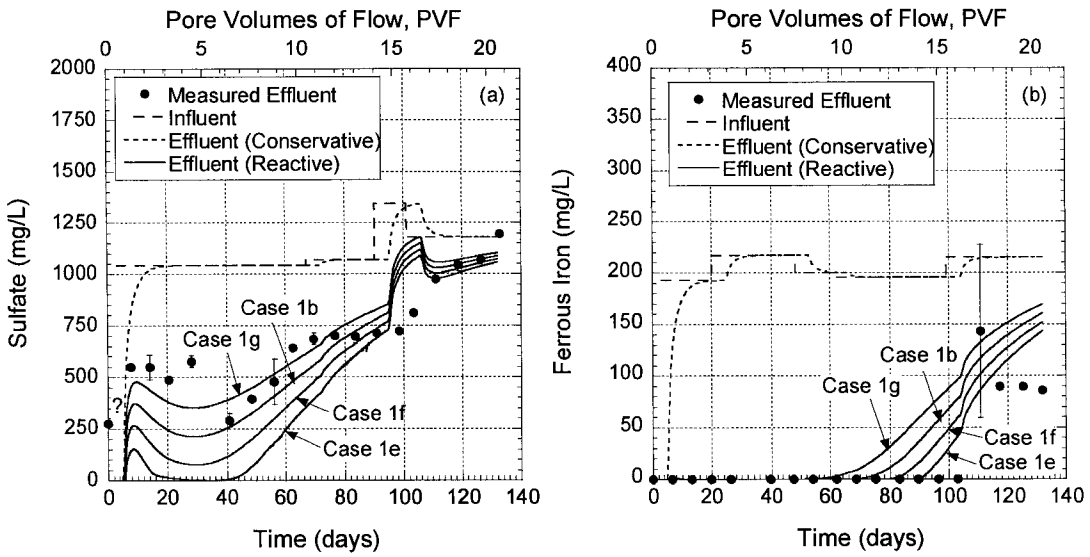

Figure 5.9 – Effect of the thickness of the non sulfate reducing layer (T) on simulated effluent concentrations for (a) sulfate, and (b) ferrous iron, for Bioreactor 1 (Cases 1b, 1e, 1f, 1g).

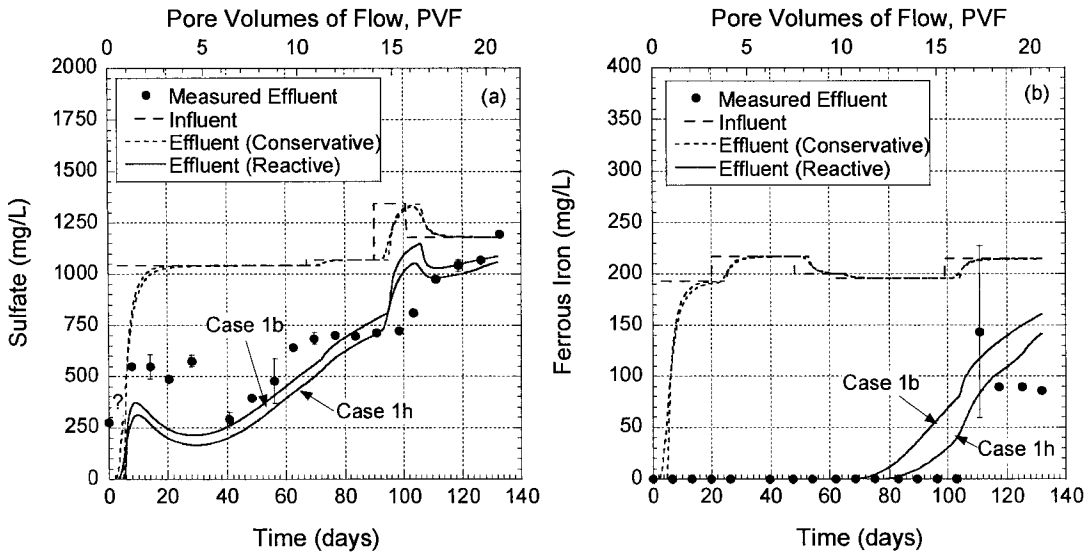

Figure 5.10 – Effect of the longitudinal dispersivity (α_L) on simulated effluent concentrations for (a) sulfate, and (b) ferrous iron, for Bioreactor 1 (Cases 1b and 1h).

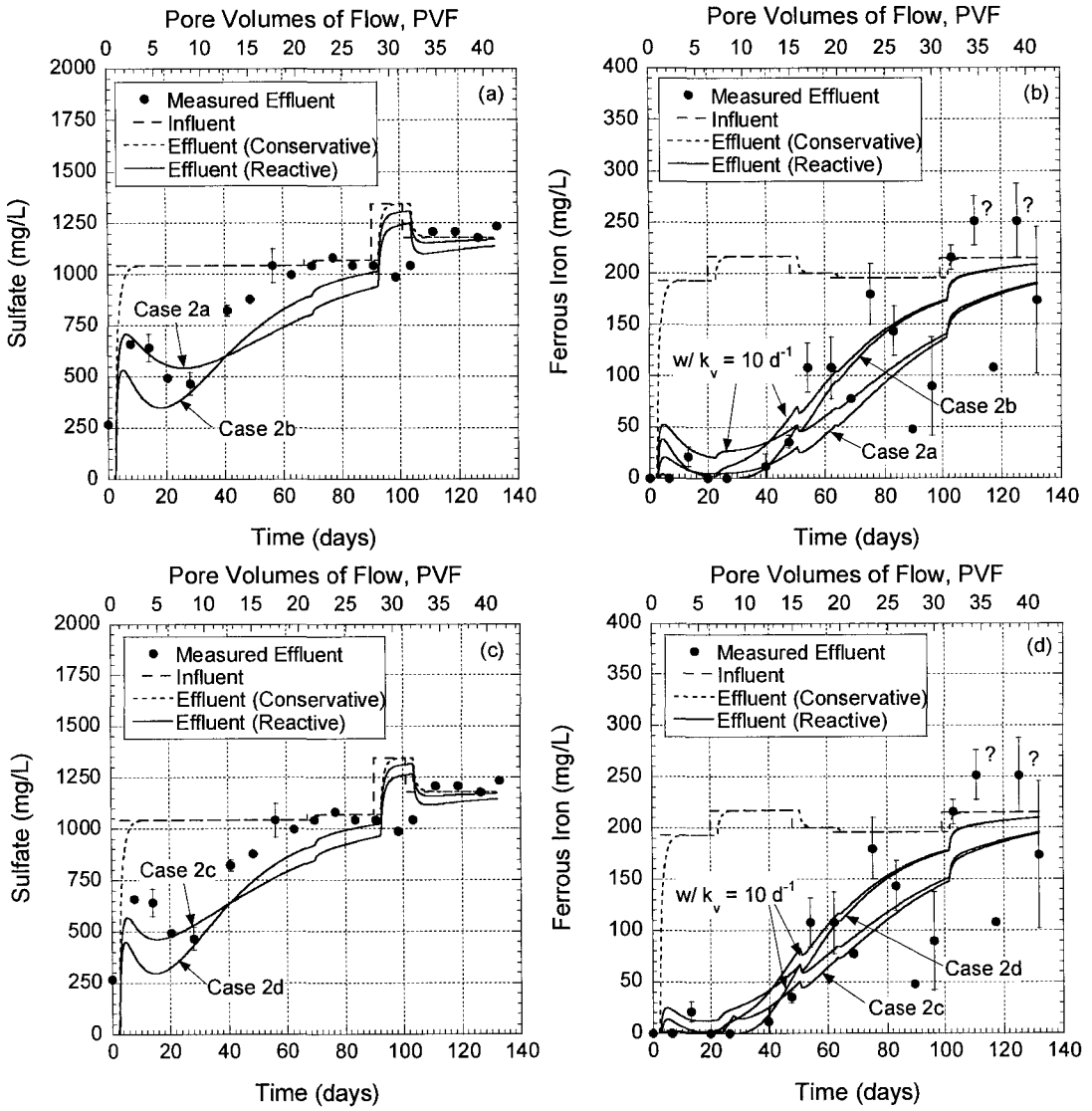

Figure 5.11 – Comparison between simulated and measured effluent concentrations for Bioreactor 2, Cases 2a and 2b: (a) sulfate and (b) ferrous iron, and Cases 2c and 2d: (c) sulfate, and (d) ferrous iron.

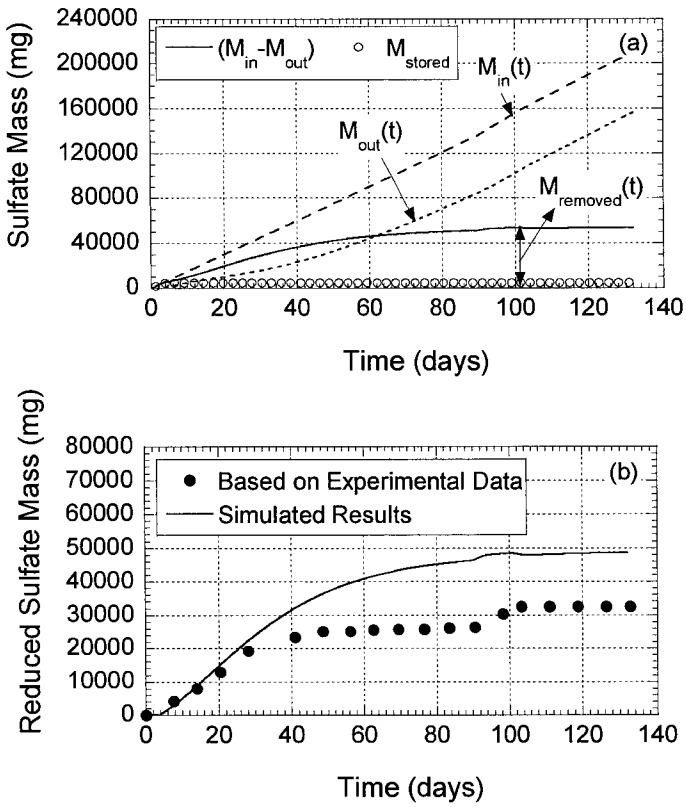

Figure 5.12 – (a) Simulated cumulative masses input (M_{in}), output (M_{out}), stored (M_{stored}), and removed ($M_{removed}$) for sulfate in reactive transport (Case 2b); (b) comparison between simulated (Case 2b) and experimentally based results.

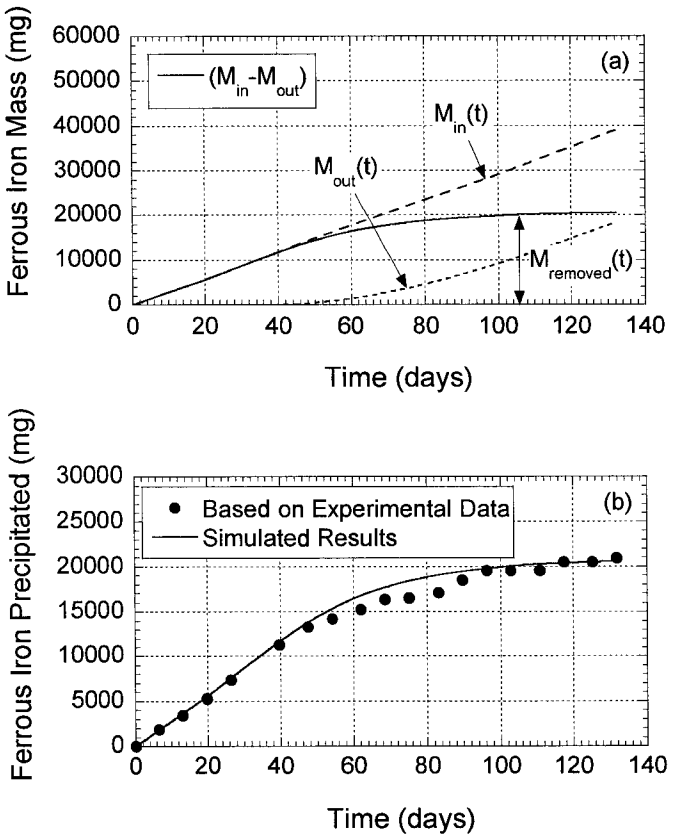

Figure 5.13 – (a) Simulated cumulative masses input (M_{in}), output (M_{out}), and removed ($M_{removed}$) for ferrous iron in reactive transport (Case 2b); (b) comparison between simulated (Case 2b) and experimentally based results. Note: Mass stored neglected.

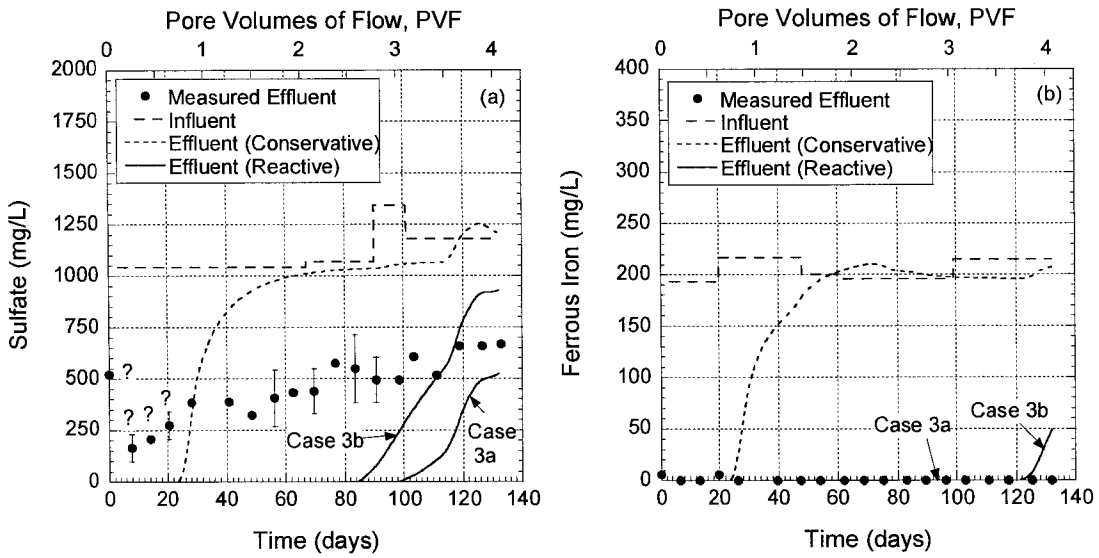

Figure 5.14 – Comparison between simulated and measured effluent concentrations for Bioreactor 3, (a) sulfate (Cases 3a and 3b), and (b) ferrous iron (Cases 3a and 3b).

CHAPTER 6

AN EVALUATION OF THE INFLUENCE OF AQUIFER HETEROGENEITY ON PERMEABLE REACTIVE BARRIER DESIGN

ABSTRACT: The influence of heterogeneity in aquifer hydraulic conductivity (K) on contaminant plume patterns and the required thickness and length of permeable reactive barriers (PRBs) used for *in-situ* remediation is evaluated using stochastic modeling. The results provide a quantitative means for evaluating the effects of (i) the level of aquifer heterogeneity as reflected by the standard deviation of the logarithm of K, σ_{lnK}, (ii) the aquifer correlation structure anisotropy represented by the ratio of correlation lengths, λ_x/λ_y, and (iii) D_{PRB} representing the distance from the contaminant source zone to the PRB. In terms of PRB thickness, a probabilistic factor of safety related to uncertainty in influent groundwater seepage velocities ($FS_{1,90}$) at the location of the PRB is quantified. In terms of PRB length, a probabilistic factor of safety related to uncertainty in the length of a PRB required to capture the contaminant plume, defined as the capture length ratio (CLR), is quantified. The mean and standard deviation of $FS_{1,90}$ significantly increase as σ_{lnK} increases from 0.2 to 1.6, and slightly increase as λ_x/λ_y increases from 1.0 to 3.0 and D_{PRB} increases from 15 to 45 m. The values for the factor of safety for PRB thickness versus σ_{lnK} compare favorably with previously published values based on a different methodology. The mean and standard deviation of CLR increase with increasing σ_{lnK} and with increasing D_{PRB}, and decrease slightly with increasing λ_x/λ_y. Finally, the ranges in CLR are correlated with strongly-divergent and strongly-convergent plume patterns.

Key Words: Aquifer heterogeneity, Groundwater capture zone, Hydraulic conductivity, Particle tracking, Permeable reactive barrier, Synthetic aquifers, Stochastic aquifers, Turning bands.

6.1 INTRODUCTION

Permeable reactive barriers (PRBs) are subsurface emplacements of reactive materials designed to intercept a contaminant plume, provide a flow path through the reactive media, and transform the contaminants into environmentally acceptable forms to achieve remediation goals down gradient of the PRB (US EPA 1998). Remediation goals typically include contaminant effluent concentrations in compliance with prescribed maximum contaminant levels (i.e., MCLs). Properly designed and constructed PRBs have minimal impact on the natural groundwater gradient (i.e., unimpeded flow), and have low operational and maintenance costs for extended periods of time (i.e., except for the costs associated with monitoring). Zero-valent iron (Fe^0) has been used as the reactive material for the majority of constructed PRBs to promote the reductive dehalogenation of volatile organic compounds (VOCs), reduce mobile and toxic oxyanions of chromium (CrO_4^{2-}), arsenic ($H_2AsO_4^-$), and selenium ($HSeO_4^-$) into immobile precipitates, and treat radionuclide and nitrate bearing ground waters (e.g., US EPA 1998, O'Hannesin and Gilham 1998, US EPA 2002). Biochemical systems based on the decomposition of emplaced solid organic materials oriented towards the remediation of nitrate, sulfate, and heavy metals (acid mine drainage) from impacted ground waters also have been used as PRBs (e.g., Thombre et al. 1997, Benner et al. 1997, Robertson et al. 2000, US EPA 2002, Groudev et al. 2003, Hemsi et al. 2005).

In the field, aquifer heterogeneity inherently affects the performance of PRBs. Heterogeneity induces preferential pathways of flow and contaminant transport (channeling) that expose the PRB to spatially variable groundwater seepage velocities, with localized values that may be sufficiently high such that the required PRB thickness

is greater than that for a homogenous aquifer. Additionally, aquifer heterogeneity may induce divergent flow patterns that require the length of the PRB to be greater than that for a homogenous aquifer.

The primary objective of this study is to evaluate the influence of aquifer heterogeneity on plume patterns and on the required thickness and length of PRBs. The approach is based on numerical modeling of flow and particle tracking for 650 synthetic stochastic heterogeneous aquifers pertaining to different simulation cases. The results include (i) identification of plume pattern categories with frequencies of occurrence, (ii) quantification of a probabilistic factor of safety for scaling the PRB thickness, and (iii) quantification of a probabilistic factor of safety for scaling the PRB length. The evaluation is limited to PRBs consisting of a continuous trench subjected to two-dimensional horizontal flow within a heterogeneous aquifer (i.e., funnel-and-gate scenarios for PRBs and injected subsurface treatment zones are not evaluated). Also, the effects of factors that can influence PRB design and performance other than aquifer heterogeneity, such as the seasonal variability in the direction and magnitude of the aquifer hydraulic gradient, temporal variability in reactivity and biological and mineral fouling (e.g., Li et al. 2005), are not evaluated in this study. Finally, *a piori* characterization of the *in-situ* distribution of K in a given aquifer of interest will be required before the results of this study can be used (e.g., Pfleiderer and Moltyaner 1993, Gavaskar et al. 1998, Zheng and Bennett 2002).

6.2 BACKGROUND

6.2.1 PRB Design Based on Homogenous Aquifers

The most simplistic approach to PRB design is based on the assumptions of a homogeneous aquifer and PRB, uniform flow perpendicular to the PRB, uniform contaminant residence time within the PRB, and the validity of relatively simple reaction mechanisms within the PRB, such as first-order kinetics in the case of VOC degradation by Fe^0 (Gavaskar et al. 1998, US EPA 1998). In this case, a closed-form analytical solution for the minimum PRB thickness based on steady-state one-dimensional advective-dispersive transport with first-order reaction kinetics can be written as follows (e.g., Eykholt and Sivavec 1995):

$$T_{PRB,Homog} = \frac{2\,D\,\ln\left(C_{in}/C_{eff}\right)}{\sqrt{v^2 + 4kD} - v} = \frac{2\,D\,\ln\left(C_o/MCL\right)}{\sqrt{v^2 + 4kD} - v} \tag{6.1}$$

where $T_{PRB,Homog}$ is the PRB thickness, C_{in} and C_{eff} are the influent and effluent contaminant concentrations, respectively, C_o is the source-zone concentration, MCL is the maximum contaminant level (i.e., $C_{in} = C_o$, and $C_{eff} = MCL$), k is the first-order degradation rate coefficient, D is the coefficient of hydrodynamic dispersion, and v is the uniform seepage velocity based on Darcy's law. Also, the analytical plug-flow solution (i.e., without considering hydrodynamic dispersion) can be written as follows (e.g., Eykholt and Sivavec 1995, Elder et al. 2002):

$$T_{PRB,Homog} = \frac{v\,\ln\left(C_{in}/C_{eff}\right)}{k} = \frac{v\,\ln\left(C_o/MCL\right)}{k} \tag{6.2}$$

which is a classic first-order kinetic expression with $T_{PRB,Homog}/v$ representing the reaction

time. Eykholt and Sivavec (1995) used Eq. 6.2 with $C_{in}/C_{eff} = 1000$ for several different values of v and k resulting in PRB thicknesses ranging from 0.003048 to 3.048 m (0.01 to 10 ft).

A factor of safety commonly is used in conjunction with Eqs. 6.1 or 6.2 to account for uncertainty in flow and reactivity, primarily due to aquifer and PRB heterogeneity, hydraulic gradient variability, and temporal and spatial changes in the reactivity of the Fe^0 (Eykholt 1997, Elder 2000, Elder et al. 2002). Typical factors of safety are on the order of two, but values as high as 10 have been reported in conjunction with higher levels of heterogeneity in aquifer K.

The length of a PRB in a homogeneous aquifer is equal to the width of the source zone if the PRB is placed perpendicular to the direction of flow and centered with respect to the source zone. A factor of safety also can be used to increase the length of the PRB to account for variability in plume capture zones due to aquifer heterogeneity and variability in the direction of the hydraulic gradient. In contrast, consideration of the length of the PRB is irrelevant in cases where PRBs are laterally keyed to bedrock (e.g., Benner et al. 1997, Groudev et al. 2003).

6.2.2 PRB Design Based on Heterogeneous Aquifers

The simple analytical solutions (e.g., Eqs. 6.1 and 6.2) generally are not applicable in the case where the contaminant degradation within the PRB does not follow simple (e.g., first-order) kinetics. In addition, the effects of aquifer heterogeneity on groundwater flow and contaminant transport (i.e., preferential flow and channeling) typically are taken into account through the use of numerical modeling (e.g., Poeter and Gaylord 1990, Moreno and Tsang 1994, Zheng and Jiao 1998, Gavaskar et al. 1998,

Elder 2000, Bilbrey and Shafer 2001, Elder et al. 2002, Zheng and Bennett 2002). For example, flow channeling can be represented macroscopically by longitudinal and transverse macroscopic dispersions that are regional properties of the heterogeneous aquifer, and proportional to σ^2_{lnK} (e.g., Gelhar et al. 1992, Gelhar 1993, Zheng and Bennett 2002), such that the standard deviation of the logarithm of the aquifer K, or σ_{lnK}, is likely to be a major aquifer parameter affecting the design of PRBs.

Different methodologies have been used to evaluate the effect of aquifer heterogeneity on the required PRB thickness. For example, Eykholt (1997) performed a Monte Carlo analysis using Eq. 6.2 to simulate the probabilistic distribution of C_{eff} as a function of v, C_{in}, and k that were assumed to follow given probabilistic distributions. The value of the PRB thickness (T_{PRB}) was iterated until $C_{eff}/C_{in} < 0.001$ was obtained. A factor of safety (FS) was defined by dividing T_{PRB} by the hypothetical PRB thickness associated with the mean values in the assumed distributions of the input variables. The process was repeated for a number of combinations of input variables, as well as for a number of standard deviations for the distributions of the input variables. The final values of FS for scaling T_{PRB} ranged from about 2 to 6, with the higher values being associated with higher standard deviations of groundwater seepage velocity (v), as expected.

Eykholt et al. (1999) evaluated the impacts of aquifer heterogeneity and variability in the reactivity of Fe^0 on effluent VOC concentrations leaving a homogeneous PRB. The methodology was based on flow and particle tracking in heterogeneous aquifers considering different heterogeneity levels, i.e., σ_{lnK} = 0.5 to 2.0, and Monte Carlo analyses considering first-order VOC degradation. A discussion of different compensating factors for reducing the vulnerability of PRBs is provided.

However, the study appears to be based on a relatively small number of aquifer realizations for each case (i.e., < 5).

Elder (2000) and Elder et al. (2002) performed numerical modeling of flow and contaminant transport in three-dimensional synthetic heterogeneous aquifers generated by stacking 20 layers of spatially-correlated K obtained with a Turning Bands algorithm (Tompson et al. 1989). First-order contaminant degradation kinetics within the PRB was considered, and the spatial distributions of C_{in} and C_{eff} were obtained based on contaminant transport modeling for different simulation scenarios of aquifer and PRB heterogeneity in terms of K and reactivity (~ 10 aquifer realizations were used for each simulation case). The parameter σ_{lnK} was identified as having the greatest impact on the distributions of C_{in} and C_{eff} and on the performance of the PRB. Elder (2000) regressed empirical correlations relating the required FS for scaling T_{PRB} to σ_{lnK}, K_g (geometric mean of K in the heterogeneous aquifer), λ_x (longitudinal correlation length), and a probability of failure. Also, varying σ_{lnK} affected the PRB performance more significantly than varying the PRB hydraulic conductivity (K_{PRB}) or reactivity, which is consistent with the observation that the contaminant residence time within the PRB is controlled by aquifer K when K_{PRB} is approximately five times greater than K_g (Gavaskar et al. 1998, Elder et al. 2002). Finally, the effects of the aquifer correlation structure and anisotropy were found to be minor (Elder et al. 2002).

Bilbrey and Shafer (2001) performed numerical modeling of flow and particle tracking in 15 moderately heterogeneous aquifers (σ_{lnK} = 1.0) containing a funnel-and-gate system to evaluate the variability in the downstream capture width of the funnel-and-gate caused by aquifer heterogeneity. Predicted meandering pathlines in heterogeneous

aquifers, following the paths of least resistance to flow, resulted in downstream capture widths not only varying in size, but also shifting positions within the aquifer. Bilbrey and Shafer (2001) proposed the use of a design factor of safety for increasing the funnel-and-gate dimensions due to aquifer heterogeneity.

Benner et al. (2001) performed numerical modeling of flow and particle tracking to study the spatial variability of contaminant residence time within a PRB considering layered aquifer systems, i.e., discretely heterogeneous aquifers composed of approximately four adjacent homogeneous layers with different values of K, and a total of 18 different simulations. The results showed the expected behavior of critical contaminant residence times occurring in conjunction with scenarios where aquifer layers with high K are intercepted by the PRB.

6.3 METHODOLOGY

6.3.1 Synthetic Aquifers

The approach adopted in this study is based on numerical modeling of steady-state flow and particle-tracking using MODFLOW 2000, version 1.7 (Harbaugh et al. 2000) and MODPATH, version 4.2 (Pollock 1994) in conjunction with 650 synthetic stochastic heterogeneous aquifers produced using the Turning Bands method (Tompson et al. 1989, Elder 2000), and different simulation cases corresponding to different sets of input parameters. Two-dimensional synthetic stochastic heterogeneous aquifers were generated as per Elder et al. (2002) using a Turning Bands algorithm implemented by Tompson et al. (1989) and modified by Elder (2000). Although other methodologies for generating heterogeneous aquifers, such as the sequential Gaussian simulation (sgsim)

program (Deutsch and Journel 1998) employed by Bilbrey and Shafer (2001), could have been used in this study, the Turning Bands method was selected on the basis of Elder (2000) who recommended the Turning Bands method as a robust tool for simulating synthetic stochastic heterogeneous aquifers. Additional explanation of the Turning Bands method is given by Mantoglu and Wilson (1982).

Each cell in the discretized domain is assigned an outcome of the random variable K assuming that the probability density function of K is log normal (e.g., Freeze and Cherry 1979), and that K values are spatially correlated along the two domain directions (i.e., x- and y-directions). In this case, the logarithm of K is described by a mean (μ_{lnK}) and a standard deviation (σ_{lnK}) (Aitchison and Brown 1957). Also, K_g can be defined as $e^{\mu lnK}$, such that 95.2 % of all K values fall within the interval $K_g/\exp(2\sigma_{lnK}) < K < K_g \times \exp(2\sigma_{lnK})$. The spatial autocorrelation between values of K at different domain cells is based on the assumption of an exponential autocorrelation function along each domain direction. Based on exponential autocorrelation functions, values of K in different cells become practically uncorrelated (autocorrelation < 0.05) when the separation distance between the cells is greater than ~ 3λ.

Statistically meaningful aquifer realizations using the Turning Bands method require the domain length along each direction to be greater than 25 times the value of λ along that direction, and the grid-discretization size along each direction to be less than 0.2 times λ for that direction (Ababou et al. 1989). These requirements are more stringent than those in Tompson et al. (1989), who recommend a domain length > 20λ and grid-discretization size < 0.5λ. Random seed numbers for the Turning Bands algorithm were selected following the guidelines provided with the Turning Bands algorithm; i.e., odd

integer seed numbers that are less than 2^{20}.

Representative values for correlation lengths (λs) for different types of aquifer materials are given in Elder et al. (2002). Based on the values for λ reported in Elder et al. (2002) and the aforementioned considerations, the longitudinal correlation length λ_x was assumed in this study to be equal to 3.0 m, whereas the transverse correlation length λ_y was considered to vary to provide correlation structure anisotropy ratios (λ_x/λ_y) of 1.0, 1.5, and 3.0 (i.e., λ_y = 3.0, 2.0, and 1.0 m, respectively). Two examples of heterogeneous aquifers are illustrated in Fig. 6.1, one isotropic (Fig. 6.1a), and one anisotropic with λ_x/λ_y = 3.0 (Fig. 6.1b). Since two-dimensional synthetic aquifers were employed, the correlation structure in the flow domains was considered fixed along the vertical direction; i.e., perfect correlation in a vertical column of cells with the vertical correlation length equal to the cell thickness.

6.3.2 Modeling Flow and Particle Tracking

A cross-section schematic of the physical scenario being considered is shown in Fig. 6.2, and an isometric view of the aquifer model domain is shown in Fig. 6.3. Three-dimensional aquifer domains consisted of a top, unconfined heterogeneous layer with dimensions 80 m x 70 m and comprising 800 rows (parallel to the x direction) and 700 columns (Fig. 6.3). The grid size of 0.1 m along both domain directions was within the range of grid sizes (0.05 to 0.40 m) used by Elder et al. (2002). Constant-head boundary conditions were applied to the first and last columns in the domain, resulting in an imposed hydraulic gradient parallel to the x direction of 0.01. Locally, the hydraulic gradient is heterogeneously distributed throughout the aquifer due to heterogeneity in aquifer K (e.g., Zheng and Jiao 1998). A centered, 15-m-long source zone was defined

near the up-gradient side of the domain, parallel to the y direction, and consisting of 76 adjacent tracking particles (Fig. 6.3). This number of particles was chosen after verifying that particle tracking results were the same for either 76 or 151 particles. The use of 76 particles resulted in smaller MODPATH output files and a concomitant reduction in computational memory requirements.

The influent side of the PRB was assumed to be located at a variable distance D_{PRB} (= 15, 30, or 45 m) down gradient of the source zone. The distance between the source zone and the PRB was significantly greater than the minimum of ~ $2\lambda_x$ recommended for more realistic simulations subject to flow channeling (Elder 2000).

For all flow simulations, the maximum acceptable value for the volumetric budget discrepancy was 0.1 %. The preconditioned conjugate gradient (PCG) algorithm (Hill 1990) was employed as the MODFLOW 2000 solver (PCG package, Harbaugh et al. 2000), and proved capable of solving flow in heterogeneous aquifers within the volumetric budget discrepancy of usually ~ 0.05 %. In some cases, particularly in the cases with higher values of σ_{lnK}, the input PCG parameters, including the prescribed maximum numbers of inner and outer iterations and the damping and relaxation parameters, were varied slightly to ensure the required accuracy of the solution. Since MODPATH was used in conjunction with steady-state results for flow, the input of a transport time step discretization was not required, as described by Pollock (1994).

The number of aquifers used for each simulation case was a compromise between having a sufficient number of aquifers to provide adequate probabilistic distributions of the results while limiting the number of aquifers due to the practical constraints of time and computational memory. The number of aquifers for each simulation case was defined

incrementally until the level of variation in the results (i.e., in the parameters of the resulting probabilistic distributions) detected upon addition of new aquifer realizations was considered to be insignificant. The required number of aquifer realizations and simulations for each simulation case varied with the level of aquifer heterogeneity (i.e., σ_{lnK}). The total number of aquifers utilized in this study was 650, with 45 aquifers for σ_{lnK} = 0.2, 50 aquifers for σ_{lnK} = 0.4, 120 aquifers for σ_{lnK} = 0.8 (including different simulation cases), and 200 aquifers for σ_{lnK} = 1.6.

Graphical visualizations of aquifers and flow solutions were obtained with the three-dimensional software ModelViewer, version 1.0 (U.S. Geological Survey, March 2002), described in Hsieh and Winston (2002). MATLAB® version 6.5 (The MathWorks, Inc., Natick, MA) was employed to develop algorithms for handling data and performing calculations.

6.3.3 Simulation Cases

The primary objectives of the study were to evaluate the effects of (i) the level of aquifer heterogeneity (σ_{lnK}), (ii) the aquifer correlation structure anisotropy (λ_x/λ_y), and (iii) the distance between the source zone and the PRB (D_{PRB}) on the PRB design. The simulation cases performed to achieve these objectives are summarized in Table 6.1.

Simulation Case A represents the baseline case against which the other simulation cases are compared. Aquifers pertaining to Case A are characterized by μ_{lnK} = –9.2 corresponding to $K_g = 1.0 \times 10^{-4}$ m/s, which is consistent with medium-to-coarse sands, isotropic K with $\lambda_x = \lambda_y$ = 3.0 m, and a moderate level of aquifer heterogeneity with σ_{lnK} = 0.8. Also, D_{PRB} in this case was 30 m.

Simulation Cases B1, B2, and B3 were performed to evaluate the effect of the level of aquifer heterogeneity on PRB design. Values for all input parameters were identical to those for baseline Case A, except that σ_{lnK} was changed from 0.8 for Case A to 0.2, 0.4, and 1.6 for Cases B1, B2, and B3, respectively. Aquifers with $\sigma_{lnK} > 1.6$ were not considered in this study because (i) the results of Elder (2000) indicated that increasing σ_{lnK} from 2.0 to 4.0 had a comparatively smaller effect on the PRB design than increasing σ_{lnK} from 1.0 to 2.0, (ii) values of σ_{lnK} typically are < 1.44 for sands and < 2.1 for sands and gravels (Elder et al. 2002), and (iii) the fact that (as shown later) scaling factors for the PRB thickness in aquifers with $\sigma_{lnK} = 1.6$ were found to be sufficiently high such that the use of PRBs in aquifers with $\sigma_{lnK} > 1.6$ likely is not a practical solution for *in situ* remediation.

Simulation Cases C1 and C2 were performed to evaluate the effect of the aquifer correlation structure on the PRB design via the magnitude of the correlation structure anisotropy ratio λ_x/λ_y. The values for all parameters in Cases C1 and C2 were identical to those for baseline Case A, except that λ_y was changed from 3.0 m in Case A to 2.0 m for Case C1 and 1.0 m for Case C2 resulting in correlation structure anisotropy ratios, λ_x/λ_y, of 1.5 and 3.0, respectively.

Simulation Cases D1 and D2 were performed to evaluate the effect of the distance between the source zone and the PRB on the PRB design. The values for all parameters in Cases D1 and D2 were identical to those for baseline Case A, except that D_{PRB} was changed to 15 m for Case D1 and 45 m for Case D2.

6.3.4 Factor of Safety Approach

Probabilistic factors of safety for PRB design are defined as scaling factors by which a PRB thickness or length associated with a simplified scenario (i.e., homogeneous aquifer with $K = K_g$, negligible variability in hydraulic gradient, negligible PRB fouling, etc.) can be multiplied in order to take into account uncertainty associated with more realistic scenarios, such as those taking into account aquifer heterogeneity. In general, a global or overall factor of safety can be defined as follows:

$$FS = \prod_{i=1}^{n} FS_i = FS_1 \times FS_2 \times FS_3 \times ... \times FS_n \tag{6.3}$$

where FS is the global factor of safety for scaling the PRB thickness or extension in length, and FS_i are partial factors of safety related to the uncertainty associated with different factors. A partial factor of safety is considered in this study with respect to the effect of aquifer heterogeneity on the thickness of a PRB, viz., a partial factor of safety associated with variability in influent groundwater seepage velocities (FS_I). Thus, the global factor of safety with respect to PRB thickness, FS_T, is simply represented in this study by FS_I. The global factor of safety with respect to PRB length, FS_L, is represented in this study by the partial factor of safety associated with the variability in required capture zone length, which is referred to herein as the capture length ratio, CLR, such that FS_L = CLR. Other possible partial factors of safety (e.g., related to PRB reactivity or the hydraulic gradient) are not evaluated in this study.

6.4 RESULTS AND DISCUSSION

6.4.1 Plume Patterns

As shown in Fig. 6.4, plume patterns are influenced by the level of aquifer heterogeneity (i.e., magnitude of σ_{lnK}), with distinct plume patterns developed as a function of σ_{lnK}. Distinct contrasts between divergent and convergent plume patterns occur for the simulation cases with higher σ_{lnK} (i.e., Cases A and B3), whereas the contrast attenuates for lower values of σ_{lnK} (Cases B1 and B2). As illustrated by the plume patterns shown in Fig. 6.5 resulting from considering the highest level of aquifer heterogeneity evaluated in this study (i.e., Case B3 with σ_{lnK} = 1.6), plume patterns can be categorized qualitatively as strongly divergent, divergent, hybrid, convergent, and strongly convergent. Examples of strongly divergent and strongly convergent plumes occurring for Case B3 are shown in Figs. 6.6 and 6.7, respectively, for the purpose of illustrating the variability in plume morphology observed in this study. Finally, frequencies of occurrence for the different plume pattern categories are summarized in Fig. 6.8 for Cases A and B3. For Case B3 with σ_{lnK} of 1.6, 24 % of all heterogeneous aquifers produced either strongly divergent or strongly convergent plumes, each with approximately a 12 % frequency of occurrence. Also, for Case A with σ_{lnK} of 0.8, divergent and convergent plumes with approximately equal frequencies of occurrence (i.e., 52 and 48 %) were observed.

6.4.2 Thickness of a PRB

The factor of safety associated with the variability in influent seepage velocities due to aquifer heterogeneity, FS_1, is evaluated on the basis of probabilistic distributions of longitudinal groundwater seepage velocities (v_x) arriving at the location of the PRB normalized with respect to the uniform velocity that would be associated with the homogeneous aquifer with $K = K_g$, i.e.:

$$FS_1 = \frac{T_{PRB}}{T_{PRB,Homog}} = \frac{v_x}{v_{x,Homog}} \tag{6.4}$$

where $T_{PRB,Homog}$, T_{PRB}, $v_{x,Homog}$, and v_x are the PRB thicknesses and seepage velocities associated with homogeneous and heterogeneous aquifers, respectively. The purpose of FS_1 is to ensure an adequate residence time for the PRB located within the heterogeneous aquifer (by definition, $FS_1 = 1$ for a homogeneous aquifer). The variable v_x is probabilistic and characterized by a frequency distribution for each heterogeneous aquifer since each tracked particle in the aquifer arrives at the location of the PRB with a different v_x. The 90^{th}-percentile value of FS_1, referred to herein as $FS_{1,90}$, for each heterogeneous aquifer is adopted as a representative value, which is similar to the approach used by Elder (2000) for the variable C_{eff}. The probabilistic distributions of $FS_{1,90}$ can be developed based on the ensemble of all heterogeneous aquifers belonging to a given simulation case or category.

The distributions of seepage velocities (v_x and v_y) for particles arriving at the location of the PRB are shown in Fig. 6.9 for Cases B1 ($\sigma_{lnK} = 0.2$), B2 ($\sigma_{lnK} = 0.4$), A ($\sigma_{lnK} = 0.8$), and B3 ($\sigma_{lnK} = 1.6$), as σ_{lnK} is the parameter that most significantly affects the distributions of v_x and v_y. The results for Cases C1, C2, D1, and D2 with $\sigma_{lnK} = 0.8$ are similar to those for Case A and, therefore, are not shown. Each line in a plot in Fig. 6.9 represents the distribution for the 76 particles in one heterogeneous aquifer, and each plot represents the results for the ensemble of all heterogeneous aquifers for a simulation case. The distributions of v_x and v_y in the plots spread more significantly as the magnitude of σ_{lnK} increases from 0.2 to 1.6. This spreading is inherently related to the

magnitude of σ_{lnK} as opposed to the number of aquifer realizations (e.g., compare Figs. 6.9a and b, both of which are based on approximately the same number of aquifer realizations). As shown in Fig. 6.9, due to preferential flow, the longitudinal seepage velocities, v_x, for the heterogeneous aquifers are often significantly higher than the v_x of 3 x 10^{-6} m/s (and $v_y = 0$) that would be associated with the homogeneous aquifer with K = K_g for the same hydraulic gradient and porosity.

The distributions of FS_1 for particles arriving at the location of the PRB are shown in Fig. 6.10 for simulation Cases A and B1 to B3, each plot representing the collection of FS_1 distributions for all heterogeneous aquifers in the simulation case (plots for Cases C1, C2, D1, and D2 are similar and therefore are not shown). The distributions of FS_1 spread more significantly as the magnitude of σ_{lnK} increases from 0.2 to 1.6 in a manner similar to that for v_x. As shown in Fig. 6.10a, the range for the 90th-percentile values of FS_1 (i.e., $FS_{1,90}$) can be established for each simulation case on the basis of the results for all aquifers in the case.

Particle tracking results (v_x distributions) considering either 76 or 151 tracked particles for two examples of heterogeneous aquifers (Cases A and B3) are shown for comparison in Fig. 6.11. As previously noted, the use of 76 particles was preferred in this study since the results using 76 particles are virtually identical to those using 151 particles.

Probabilistic incremental and cumulative distributions of $FS_{1,90}$ are shown in Fig. 6.12 for all cases. The mean, standard deviation, and skewness of the $FS_{1,90}$ distributions determined from the data increase as the level in aquifer heterogeneity (i.e., σ_{lnK}) increases, with mean values for $FS_{1,90}$ of 1.60, 1.91, 2.71, and 5.14 corresponding to σ_{lnK}

values of 0.2 (Case B1), 0.4 (Case B2), 0.8 (Case A), and 1.6 (Case B3), respectively. The mean and standard deviation of the $FS_{1,90}$ distributions also tend to increase as the correlation structure anisotropy ratio, λ_x/λ_y, increases, with mean values for $FS_{1,90}$ of 2.71, 2.87, and 3.74 corresponding to λ_x/λ_y values of 1.0 (Case A), 1.5 (Case C1), and 3.0 (Case C2), respectively. A clear trend for skewness was not observed for these results (i.e., comparing Cases A, C1, and C2). Finally, the values for the mean and standard deviation of the $FS_{1,90}$ distributions increase slightly, whereas the skewness decreases, as the distance from the source zone to the PRB, D_{PRB}, increases, with mean values for $FS_{1,90}$ of 2.64, 2.71, and 2.74 corresponding to D_{PRB} values of 15 m (Case D1), 30 m (Case A), and 45 m (Case D2), respectively.

The trends in $FS_{1,90}$ as a function of the level of aquifer heterogeneity, the correlation structure anisotropy ratio, and the distance from the source zone to the PRB are shown in Fig. 6.13. Based on the results shown in Fig. 6.13, σ_{lnK} appears to have a greater effect on $FS_{1,90}$ than either λ_x/λ_y or D_{PRB}, i.e., for the ranges of values for σ_{lnK}, λ_x/λ_y, and D_{PRB} considered in this study. For the highest level of aquifer heterogeneity evaluated in this study (i.e., $\sigma_{lnK} = 1.6$), $FS_{1,90}$ (Fig. 6.13a) is on the order of 5.0 (mean) to 10 (mean plus two standard deviations), comparing favorably with values given by an empirical correlation in Elder (2000) that relates the factor of safety for scaling the PRB thickness to σ_{lnK}, μ_{lnK}, λ_x, and to an input probability of failure, although the methodology employed in the present study is significantly different than that used by Elder (2000).

6.4.3 Length of a PRB

The capture length ratio (CLR) is evaluated on the basis of probabilistic distributions of the required capture zone lengths at the location of the PRB normalized with respect to the width of the source zone (i.e., direction parallel to the length of the PRB), i.e.:

$$CLR = \frac{L_{PRB}}{L_{PRB,Homog}} = \frac{L_{PRB}}{W_S} \tag{6.5}$$

where $L_{PRB,Homog}$ and L_{PRB} are the required PRB lengths associated with homogeneous and heterogeneous aquifers, respectively, and W_S is the width of the source zone. By definition, CLR = 1 in a homogenous aquifer. The length L_{PRB} is a probabilistic variable characterized by a frequency distribution for each ensemble of aquifers in a given simulation case. The definition of a required L_{PRB} assumes the PRB to be placed perpendicular to the general hydraulic gradient direction for the entire aquifer, and centered and parallel with respect to the source zone. The PRB is assumed symmetrical with respect to a center line such that the longer required half of L_{PRB} dictates the total L_{PRB} (i.e., the required L_{PRB} equals twice the longer half).

Probabilistic incremental and cumulative distributions of CLR are shown in Fig. 6.14 for all cases. The mean and standard deviation of the CLR distributions obtained from the data increase with increasing level of aquifer heterogeneity (i.e., σ_{lnK}), with mean values for CLR of 1.09, 1.14, 1.24, and 1.54 corresponding to σ_{lnK} values of 0.2 (Cases B1), 0.4 (Case B2), 0.8 (Case A), and 1.6 (Case B3), respectively. Additionally, CLR distributions are positively skewed for all heterogeneity levels, with skewness generally decreasing with increasing σ_{lnK}. The trend of decreasing skewness with

increasing σ_{lnK} can be explained on the basis of the convergent and strongly convergent plume patterns that result in some values of CLR < 1.0 for Cases A and B3.

The mean and standard deviation of the CLR distributions slightly decrease with increasing correlation structure anisotropy ratio, λ_x/λ_y, with mean values for CLR of 1.24, 1.20, and 1.16 corresponding to λ_x/λ_y values of 1.0 (Cases A), 1.5 (Case C1), and 3.0 (Case C2), respectively. These results are consistent with the fact that, as λ_y decreases, particle trajectories become less meandering (intuitively, there is less transverse macroscopic dispersion), resulting in shorter capture zone lengths at the PRB location. In this case, no clear trend for skewness was obtained with respect to increasing λ_x/λ_y.

Finally, the mean and standard deviation of the CLR distributions increase with increasing distance from the source zone to the PRB, D_{PRB}, with mean values of 1.13, 1.24, and 1.33 corresponding to D_{PRB} values of 15 m (Case D1), 30 m (Case A) and 45 m (Case D2), respectively. These results are consistent with the expected behavior since locating the PRB further down-gradient with respect to the source zone results in a broader plume to be encompassed by the PRB. Also, no clear trend for skewness with respect to increasing D_{PRB} was obtained.

Values of CLR corresponding to the mean and mean plus one and two standard deviations are plotted as a function of the level of aquifer heterogeneity (i.e., σ_{lnK}), the correlation structure anisotropy ratio (λ_x/λ_y), and the distance from the source zone to the PRB (D_{PRB}) in Fig. 6.15. As shown in Fig. 6.15, CLR is affected significantly by the level of aquifer heterogeneity (i.e., σ_{lnK}), and both λ_x/λ_y and D_{PRB} also have noticeable effects on CLR. For example, considering the values of CLR corresponding to the mean plus two standard deviations, a CLR value of ~ 2.7 results for Case B3 with σ_{lnK} of 1.6, whereas a

CLR value of ~ 2.0 results for Case A with σ_{lnK} of 0.8. Finally, CLR also can provide a quantitative means for categorizing plume patterns as shown in Figs. 6.6 and 6.7. For example, CLR ranges from ~ 2 to ~ 3 when strongly divergent plumes occur with Case B3, whereas CLR ranges from only ~ 0.3 to ~ 0.5 when strongly convergent plumes occur with Case B3. Thus, CLR values < 1 imply convergent plume patterns, whereas CLR values > 1 imply divergent plume patterns.

6.5 CONCLUSIONS

The influence of heterogeneity in aquifer hydraulic conductivity (K) on plume patterns and the required thickness and length of PRBs was evaluated using stochastic modeling. In terms of PRB thickness, a probabilistic factor of safety related to uncertainty in influent groundwater seepage velocities (FS_1) was quantified, and in terms of PRB length, a factor of safety defined as the capture length ratio (CLR) was quantified. The influences of the level of aquifer heterogeneity (i.e., magnitude of σ_{lnK}), the correlation structure anisotropy ratio (λ_x/λ_y), and the distance from the source zone to the PRB (D_{PRB}) on FS_1 and CLR were evaluated. For the ranges in values of σ_{lnK}, λ_x/λ_y, and D_{PRB} considered in this study, the level of aquifer heterogeneity (i.e., σ_{lnK}) had the greatest effect on the factors of safety. However, the effects of λ_x/λ_y and D_{PRB} on the required length of PRBs were noticeable and greater than the relatively minor effects of λ_x/λ_y and D_{PRB} on the required thickness of PRBs.

The main implications of the present study are that quantified factors of safety for scaling the thickness and length of PRBs in heterogeneous aquifers significantly impact the PRB design. Considering the highest level of aquifer heterogeneity evaluated in this

study (σ_{lnK} = 1.6), the factor of safety for PRB thickness, $FS_{1,90}$, was on the order of 5.0 for mean partial factor of safety, and 10 for mean plus two standard deviations. The trends versus σ_{lnK} showed relatively good correlation with previously published values based on a different methodology. Also, for σ_{lnK} = 1.6, the global factor of safety for PRB length, FS_L (= CLR), corresponding to the mean plus two standard deviations in CLR was on the order of 2.7.

Based on the magnitudes of scaling factors obtained in this study, the required thickness and length of a PRB located in a heterogeneous aquifer can be expected to significantly differ from values evaluated on the basis of a homogeneous aquifer (i.e., K = K_g). Thus, *in-situ* characterization of the aquifer in which the PRB is to be constructed is extremely important. In cases where aquifer heterogeneity is significant (e.g., σ_{lnK} > 1.6), the effect of the aquifer heterogeneity may be to the extent that the use of PRBs for *in-situ* remediation is rendered impractical, requiring the consideration of other remediation technologies. In addition, other possible sources of uncertainty not evaluated in this study, such as variability in PRB reactivity and fouling, may impact the design and performance of PRBs.

6.6 ACKNOWLEDGEMENTS

This research was funded by the U. S. EPA Science to Achieve Results (STAR) Program under Grant No. R-82951501-0 as part of the U. S. EPA's *Rocky Mountain Regional Hazardous Substance Research Center*. The authors thank the anonymous Associate Editor and two reviewers, and acknowledge Prof. Craig Benson (University of Wisconsin-Madison) and Dr. Carl Elder (GeoSyntec Consultants, Boston) for initial

assistance with the Turning Bands and Dr. Andrea Dominijanni (Politecnico di Torino, Italy) for initial assistance with MATLAB.

6.7 REFERENCES

Ababou, R., McLaughlin, D., Gelhar, L.W., and Tompson, A.F. (1989). Numerical simulation of three-dimensional saturated flow in randomly heterogeneous porous media. *Transport in Porous Media*, 4(6): 549-565.

Aitchison, J., and Brown, J.A.C. (1957). *The Lognormal Distribution, with Special Reference to its Use in Economics*, Cambridge University Press, Cambridge (UK).

Benner, S.G., Blowes, D.W., and Ptacek, C.J. (1997). A full-scale porous reactive wall for prevention of acid mine drainage. *Ground Water Monitoring and Remediation*, 17(4): 99-107.

Benner, S.G., Blowes, D.W., and Molson, J.W. (2001). Modeling preferential flow in reactive barriers: implications for performance and design. *Ground Water*, 39(3): 371-379.

Bilbrey, L.C., and Shafer, J.M. (2001). Funnel-and-gate performance in a moderately heterogeneous flow domain. *Ground Water Monitoring and Remediation*, 21(3): 144-151.

Deutsch, C.V., and Journel, A.G. (1998). *GSLIB: Geostatistical Software Library and User's Guide,* Oxford University Press, New York (NY).

Elder, C.R. (2000). *Evaluation and Design of Permeable Reactive Barriers Amidst Heterogeneity*. Ph.D. Dissertation presented at the University of Wisconsin at Madison.

Elder, C.R., Benson, C.H., and Eykholt, G.R. (2002). Effects of heterogeneity on influent and effluent concentrations from horizontal permeable reactive barriers. *Water Resources Research*, 38(8): 27-1:27-19.

Eykholt, G.R. (1997). Uncertainty-based scaling of iron reactive barriers. *In Situ Remediation of the Geoenvironment*, J. Evans, ed., American Society of Civil Engineers, New York (NY), p. 41-45.

Eykholt, G.R., Elder, C.R., and Benson, C.H. (1999). Effects of aquifer heterogeneity and reaction mechanism uncertainty on a reactive barrier. *Journal of Hazardous Materials,* 68(1-2): 73-96.

Eykholt, G.R., and Sivavec, T.M. (1995). Contaminant transport issues for reactive permeable barriers. *Geoenvironment 2000: Characterization, Containment, Remediation, and Performance in Environmental Geotechnics*, D. Daniel and Y. Acar, eds., American Society of Civil Engineers, New York (NY), p. 1608-1621.

Freeze, R.A., and Cherry, J.A. (1979). *Groundwater,* Prentice-Hall, Englewood Cliffs (NJ).

Gavaskar, A.R., Gupta, N., Sass, B.M., Janosy, R.J., and O'Sullivan. D. (1998). *Permeable Barriers for Groundwater Remediation: Design, Construction, and Monitoring*, Battelle Press, Columbus (OH).

Gelhar, L.W. (1993). *Stochastic Subsurface Hydrology*, Prentice Hall, Englewood Cliffs (NJ).

Gelhar, L.W., Welty, C., and Rehfeldt, K.R. (1992). A critical review of data on filed-scale dispersion in aquifers. *Water Resources Research*, 28(7) 1955-1974.

Groudev, S., Nicolova, M., Spasova, I., and Schutte, R. (2003). Treatment of waters from

a copper mine by means of a permeable reactive barrier. *Fifty Years of the University of Mining and Geology "St. Ivan Rilski"*, University of Mining and Geology, Sofia (Bulgaria), Volume 46, Part II, Section Mining and Mineral Processing, p. 229-231.

Harbaugh, A.W., Banta, E.R., Hill, M.C., and McDonald, M.G. (2000). *MODFLOW-2000, the U.S. Geological Survey Modular Ground-Water Model - User Guide to Modularization Concepts and the Ground-Water Flow Process*, U.S. Geological Survey, Open-File Report 00-92, Reston (VA).

Hemsi, P.S., Shackelford, C.D., and Figueroa, L.A. (2005). Modeling the influence of decomposing organic solids on sulfate reduction rates for iron precipitation. *Environmental Science and Technology,* 39(9): 3215-3225.

Hill, M.C. (1990). *Preconditioned Conjugate-Gradient 2 (PCG2), A Computer Program for Solving Ground-Water Flow Equations*, U.S. Geological Survey, Water Resources Investigations Report 90-4048, Denver (CO).

Hsieh, P.A., and Winston, R.B. (2002). *User's Guide to Model Viewer, a Program for Three-Dimensional Visualization of Ground-Water Model Results,* U.S. Geological Survey, Open-File Report 02-106, Menlo Park (CA).

Li, L., Benson, C.H., and Lawson, E.M. (2005). Impact of mineral fouling on hydraulic behavior of permeable reactive barriers. *Ground Water*, 43(4): 582-596.

Mantoglu, A., and Wilson, J.L. (1982). The turning bands method for simulation of random fields using line generations by a spectral method. *Water Resources Research*, 18(5): 1379-1394.

Moreno, L., and Tsang, C.F. (1994). Flow channeling in strongly heterogeneous porous media: a numerical study. *Water Resources Research*, 30(3): 1421-1430.

O'Hannesin, S.F., and Gillham, R.W. (1998). Long-term performance of an in situ "iron wall" for remediation of VOCs. *Ground Water*, 36(1): 164-170.

Pfleiderer, S., and Moltyaner, G.L. (1993). The use of velocity and conductivity data for the quantification of heterogeneity: a comparison. *Water Resources Research*, 29(12): 4151-4156.

Poeter, E., and Gaylord, D.R.(1990). Influence of aquifer heterogeneity on contaminant transport at the Hanford site. *Ground Water*, 28(6): 900-909.

Pollock, D.W. (1994). *User's Guide for MODPATH/MODPATH-PLOT, Version 3: A Particle Tracking Post-Processing Package for MODFLOW, the U.S. Geological Survey Finite-Difference Ground-Water Flow Model,* U.S. Geological Survey, Open-File Report 94-464, Reston (VA).

Robertson, W.D., Blowes, D.W., Ptacek, C.J. and Cherry, J.A. (2000). Long-term performance of in situ reactive barriers for nitrate remediation, *Ground Water*, 38 (5): 689-695.

Thombre, M.S., Thomson, B.M., and Barton, L.L. (1997). Use of a permeable biological barrier for groundwater remediation at a uranium mill tailings remedial action (UMTRA) site. *International Containment Technology Conference*, U.S. Department of Energy, U.S. Environmental Protection Agency, and Florida State University, St. Petersburg (FL).

Tompson, A.F., Ababou, R., and Gelhar, L.W. (1989). Implementation of the three-dimensional turning bands random field generator. *Water Resources Research*, 25(10): 2227-2243.

US EPA (1998). *Permeable Reactive Barrier Technologies for Contaminant*

Remediation, EPA/600/R-98/125, Washington DC.

US EPA (2002). *Field Applications of In Situ Remediation Technologies: Permeable Reactive Barriers,* Office of Solid Waste and Emergency Response, Washington DC.

Zheng, C., and Bennett, G.D. (2002). *Applied Contaminant Transport Modeling*, 2nd Edition, John Wiley and Sons, New York (NY).

Zheng, C., and Jiao, J.J. (1998). Numerical simulation of tracer tests in heterogeneous aquifers. *Journal of Environmental Engineering*, 124(6): 510-516.

Table 6.1 – Input parameter values for different simulation cases.

Case	Purpose	Input Parameter Values[1]					
		K_g (m/s)	σ_{lnK}	λ_x (m)	λ_y (m)	λ_x/λ_y	D_{PRB} (m)
A	Baseline Case	**1.0×10^{-4}**	**0.8**	**3.0**	**3.0**	**1.0**	**30**
B1	Heterogeneity in K	1.0×10^{-4}	**0.2**	3.0	3.0	1.0	30
B2		1.0×10^{-4}	**0.4**	3.0	3.0	1.0	30
B3		1.0×10^{-4}	**1.6**	3.0	3.0	1.0	30
C1	Correlation Structure	1.0×10^{-4}	0.8	3.0	**2.0**	**1.5**	30
C2		1.0×10^{-4}	0.8	3.0	**1.0**	**3.0**	30
D1	Distance from Source	1.0×10^{-4}	0.8	3.0	3.0	1.0	**15**
D2		1.0×10^{-4}	0.8	3.0	3.0	1.0	**45**

[1] K_g = geometric mean of K, σ_{lnK} = standard deviation of the logarithm of K, λ_x = correlation length of K along the x direction, λ_y = correlation length of K along the y direction, and D_{PRB} = distance from the source zone to the PRB.

Table 6.2 – Summary of results.

Case	Results	
	Factor of Safety $FS_{1,90}$	Capture Length Ratio, CLR
A	2.71 ± 0.75	1.24 ± 0.32
B1	1.60 ± 0.10	1.09 ± 0.08
B2	1.91 ± 0.23	1.14 ± 0.15
B3	5.14 ± 2.54	1.54 ± 0.60
C1	2.87 ± 0.71	1.20 ± 0.26
C2	3.74 ± 0.80	1.16 ± 0.24
D1	2.64 ± 0.72	1.13 ± 0.22
D2	2.74 ± 0.86	1.33 ± 0.35

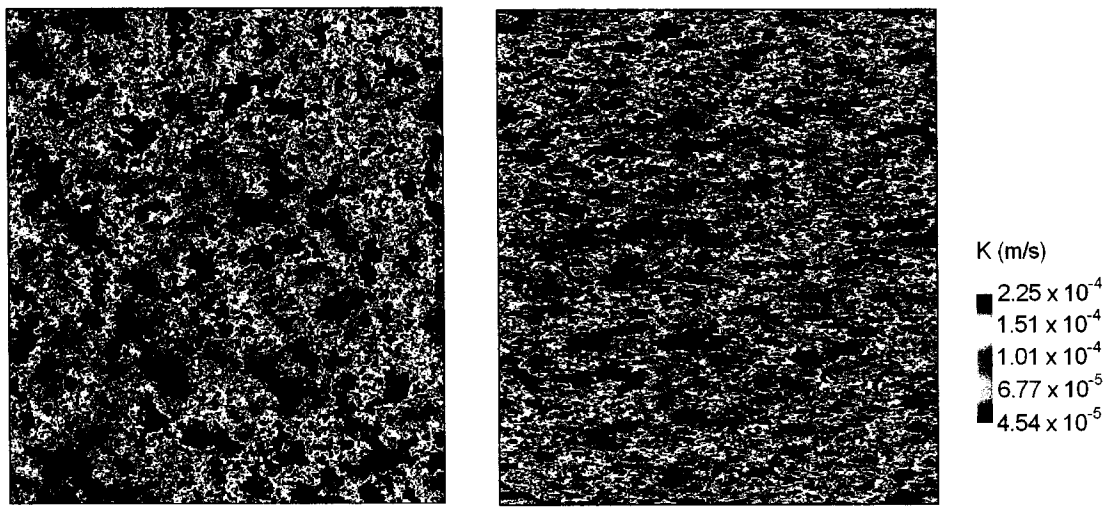

Figure 6.1 – Examples of the effect of correlation structure on hydraulic conductivity domains (plan views): (left) isotropic correlation structure ($\lambda_x/\lambda_y = 1.0$; Case A), and (right) anisotropic correlation structure ($\lambda_x/\lambda_y = 3.0$; Case C2). Note: color scale ranging from $K_g/\exp(\sigma_{lnK})$ to K_g x $\exp(\sigma_{lnK})$.

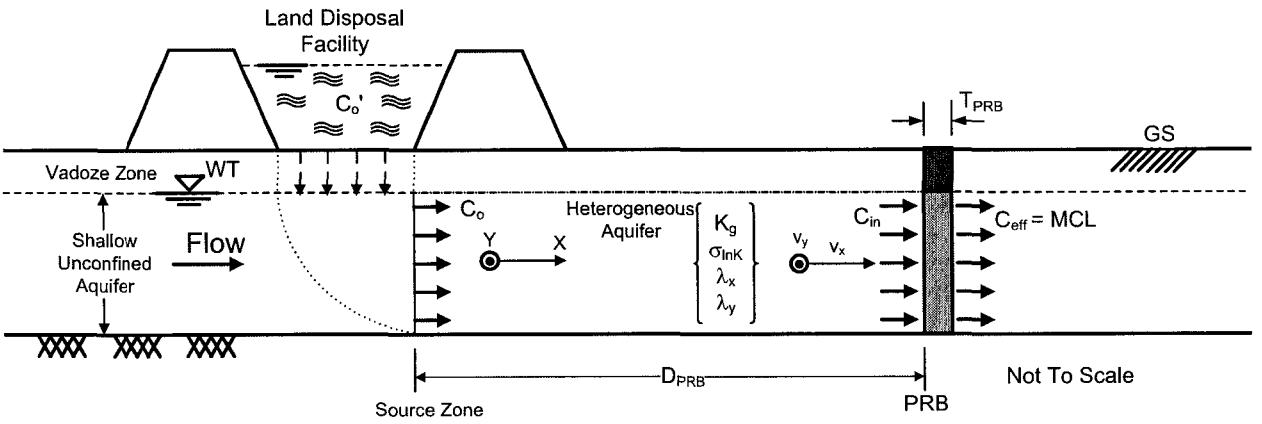

Figure 6.2 – Cross-sectional schematic of the flow scenario pertaining to this study, depicting the shallow unconfined aquifer, the model source zone, and the PRB.

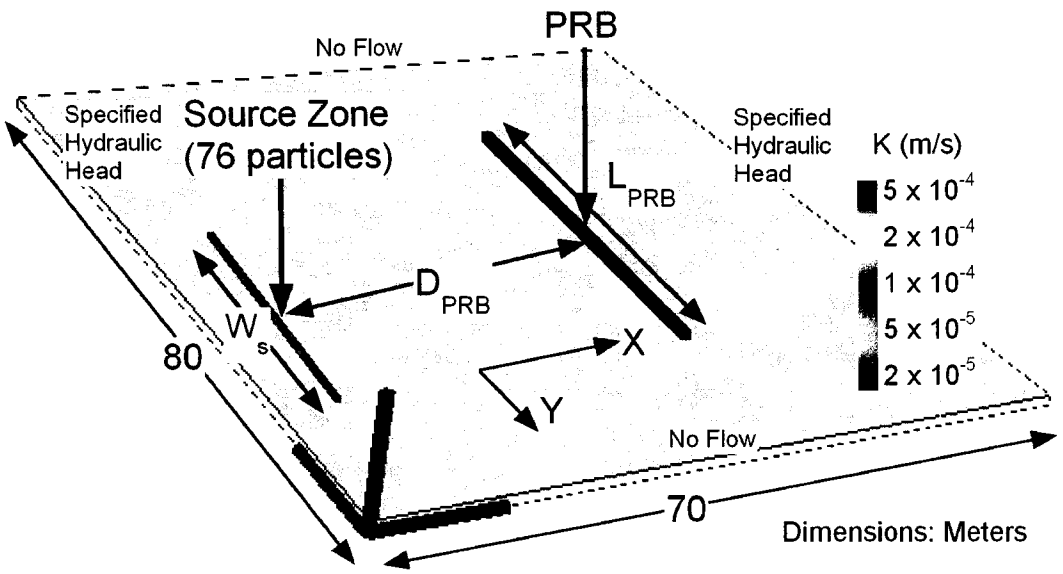

Figure 6.3 – Isometric view of the flow scenario, illustrating the model geometry, dimensions, boundary conditions, source zone, and PRB.

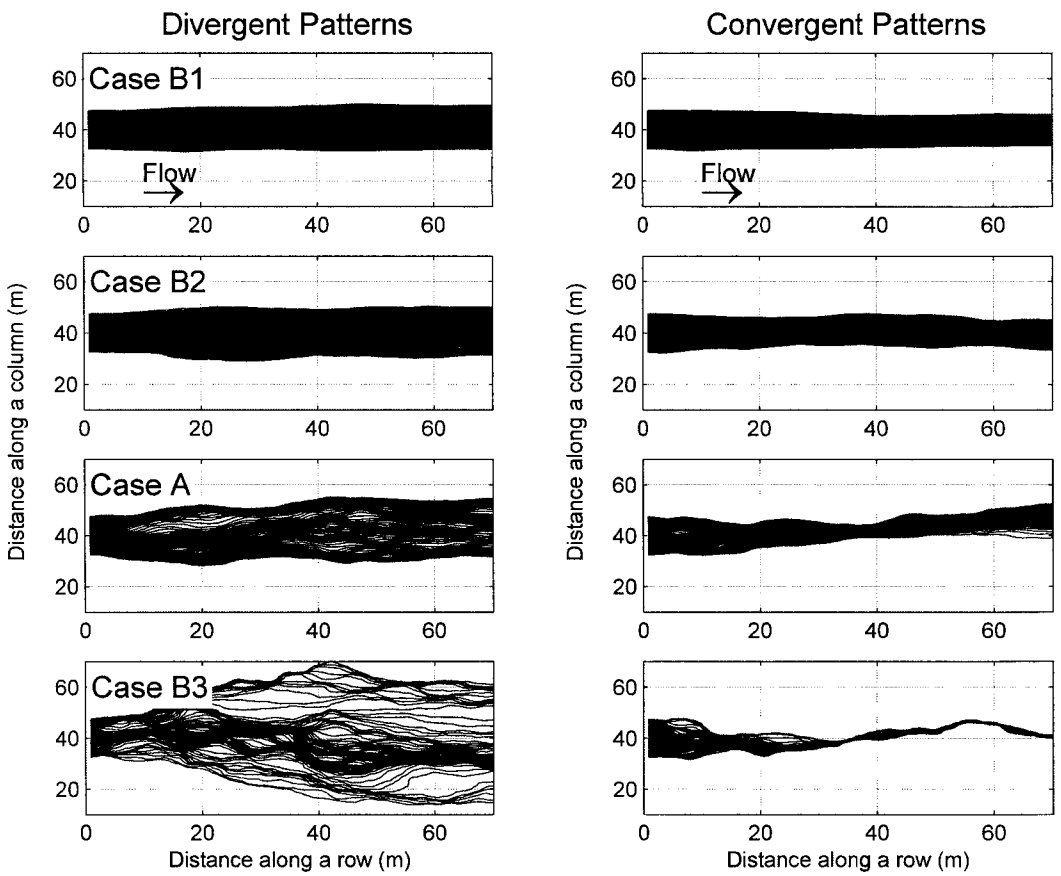

Figure 6.4 – Contrasts between divergent and convergent plumes resulting from different levels of aquifer heterogeneity: Case B1 (σ_{lnK} = 0.2), Case B2 (σ_{lnK} = 0.4), Case A (σ_{lnK} = 0.8), and Case B3 (σ_{lnK} = 1.6).

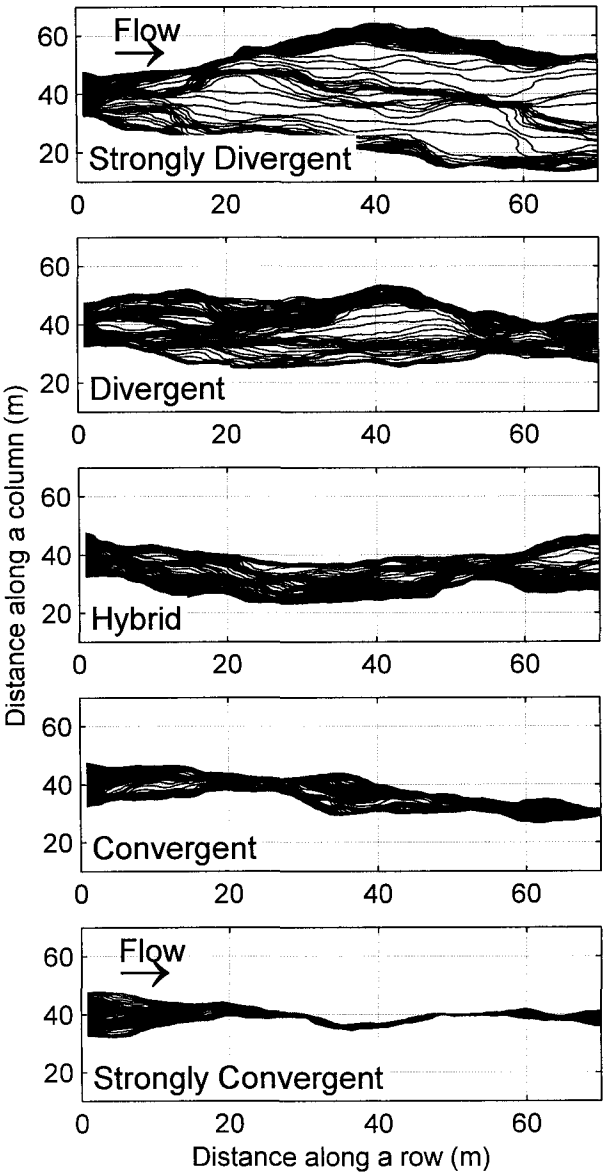

Figure 6.5 – Qualification of possible plume pattern categories developed in heterogeneous aquifers.

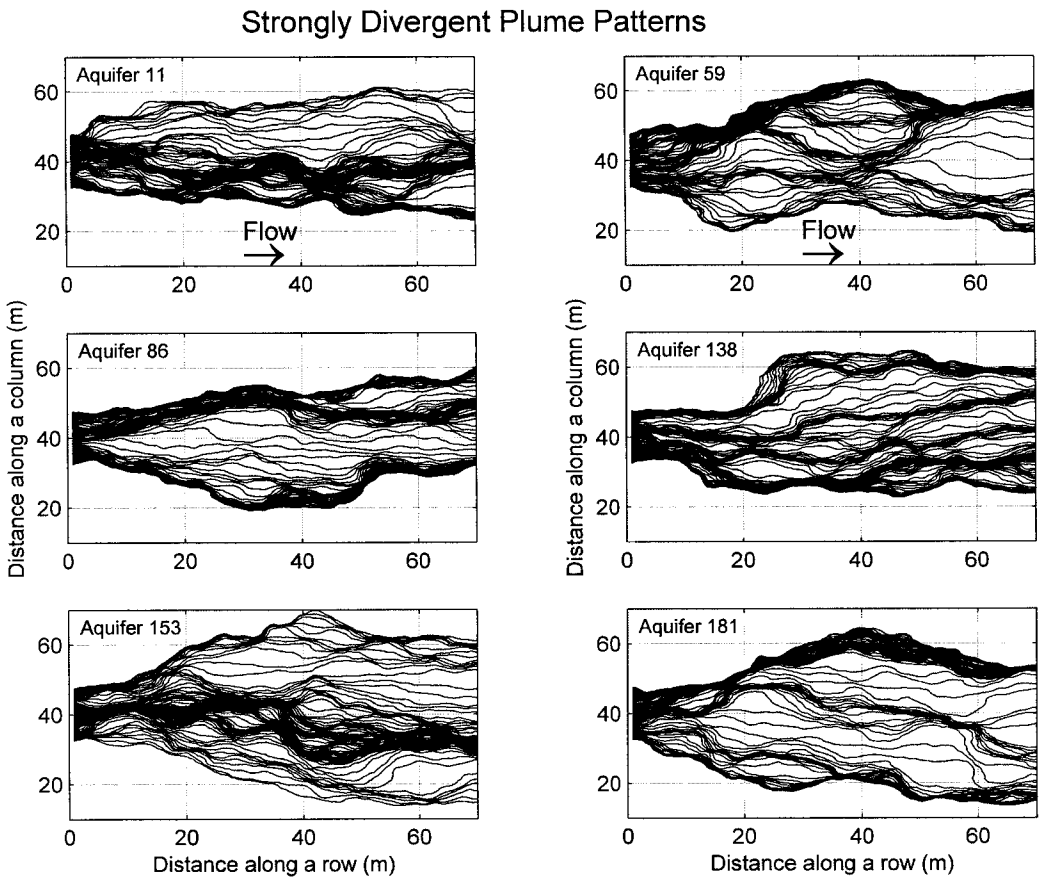

Figure 6.6 – Examples of divergent plume pattern variability resulting from the highest level of aquifer heterogeneity considered in this study (i.e., $\sigma_{lnK} = 1.6$, Case B3).

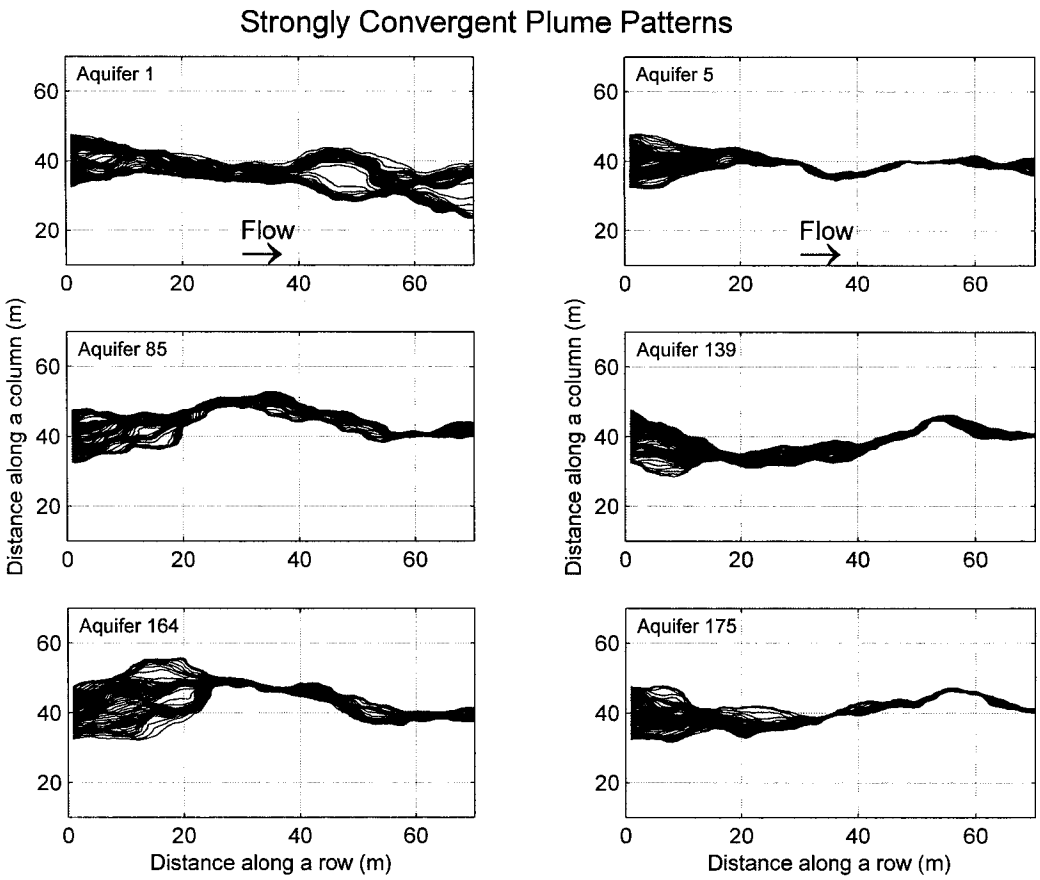

Figure 6.7 – Examples of convergent plume pattern variability resulting from the highest level of aquifer heterogeneity considered in this study (i.e., $\sigma_{\ln K} = 1.6$, Case B3).

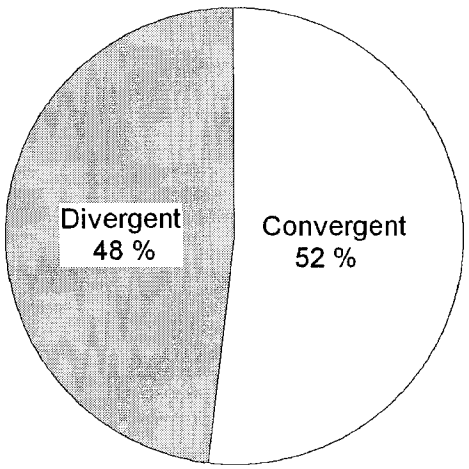

Case A

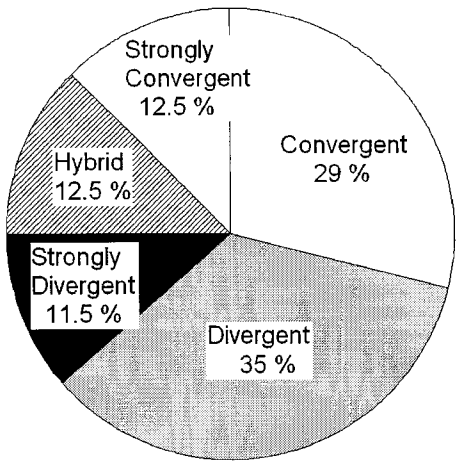

Case B3

Figure 6.8 – Frequency of occurrence of plume pattern categories for Cases A (σ_{lnK} = 0.8) and B3 (σ_{lnK} = 1.6).

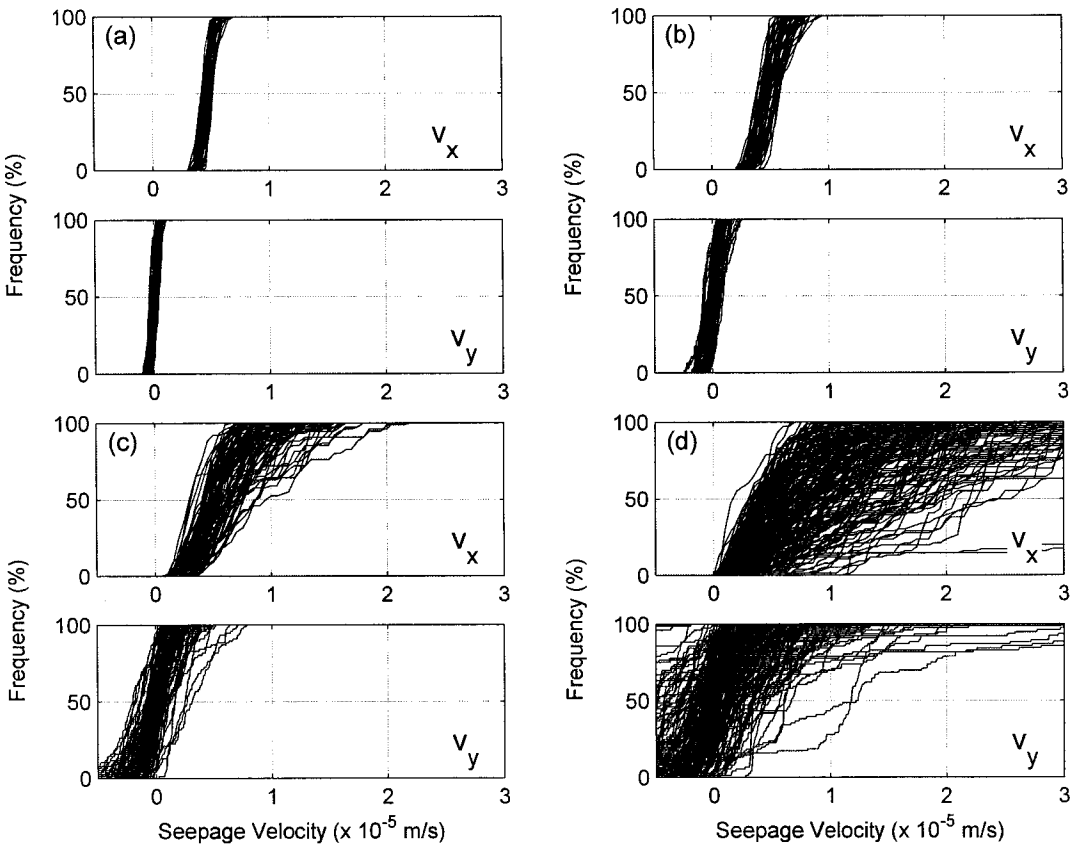

Figure 6.9 – Distributions of particle seepage velocities v_x and v_y for particles arriving at the location of the PRB: (a) $\sigma_{lnK} = 0.2$ (Case B1), (b) $\sigma_{lnK} = 0.4$ (Case B2), (c) $\sigma_{lnK} = 0.8$ (Case A), and (d) $\sigma_{lnK} = 1.6$ (Case B3).

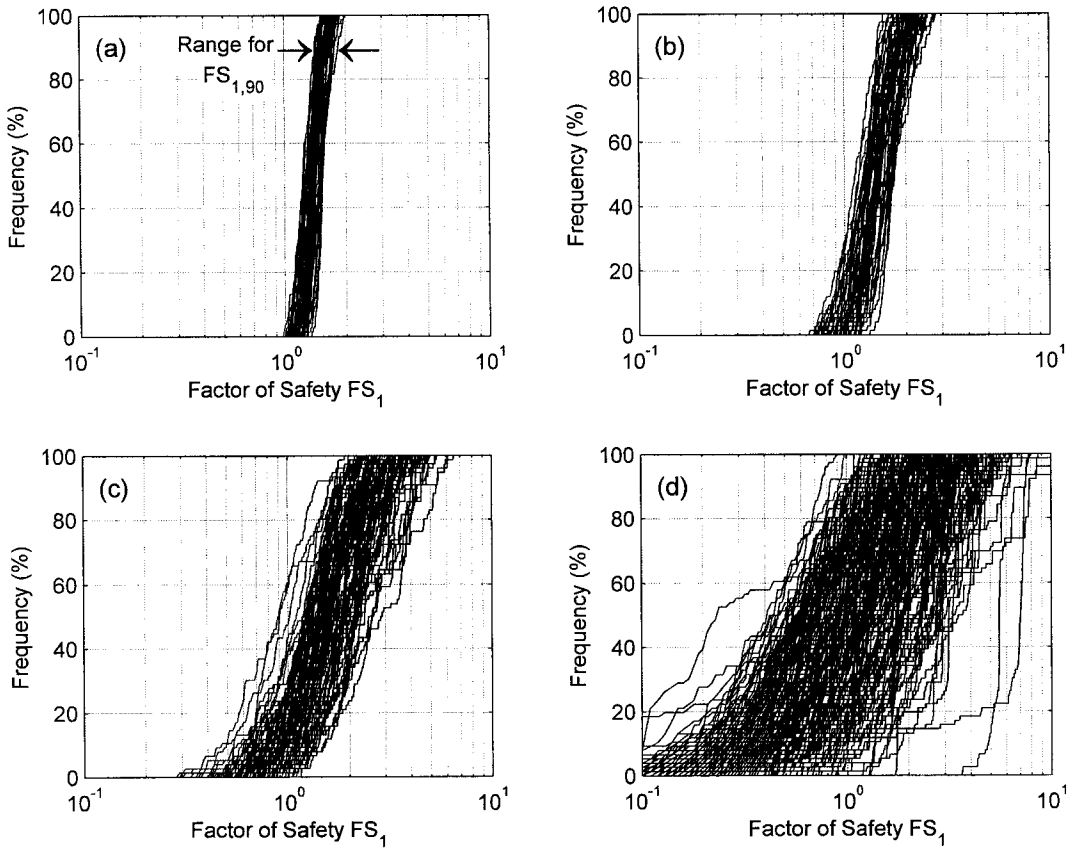

Figure 6.10 – Distributions of factor of safety FS_1 for particles arriving at the location of the PRB: (a) $\sigma_{lnK} = 0.2$ (Case B1), (b) $\sigma_{lnK} = 0.4$ (Case B2), (c) $\sigma_{lnK} = 0.8$ (Case A), and (d) $\sigma_{lnK} = 1.6$ (Case B3).

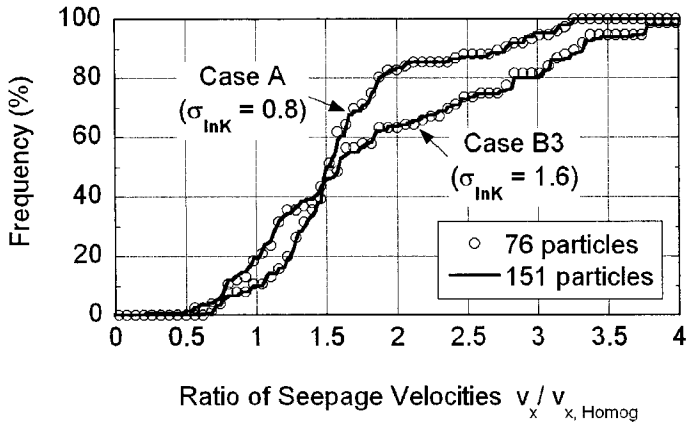

Figure 6.11 – Particle tracking results considering 76 versus 151 particles.

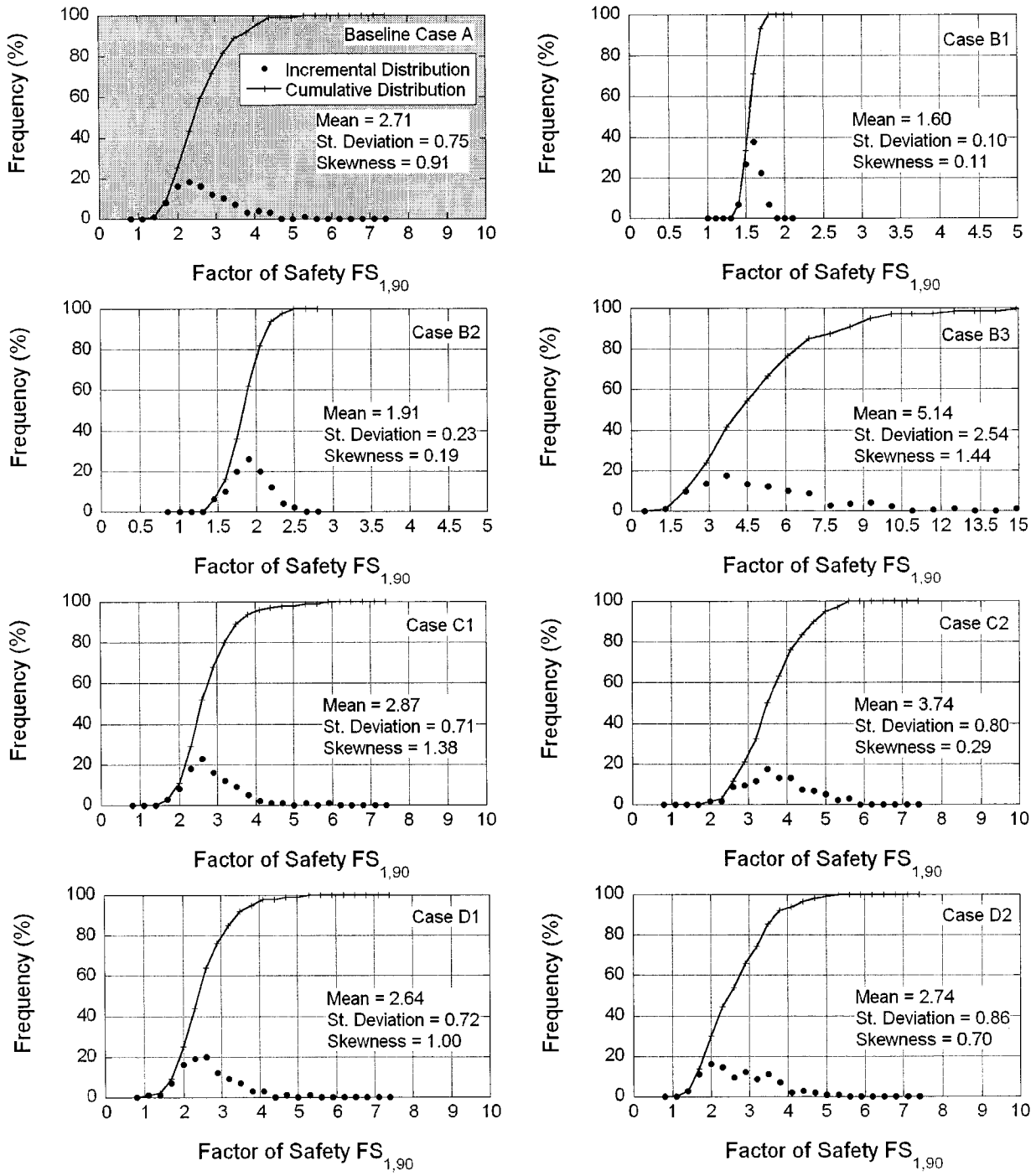

Figure 6.12 – Frequency distributions of $FS_{1,90}$ for scaling the PRB thickness (refer to Table 1 for parameter sets used for simulation cases).

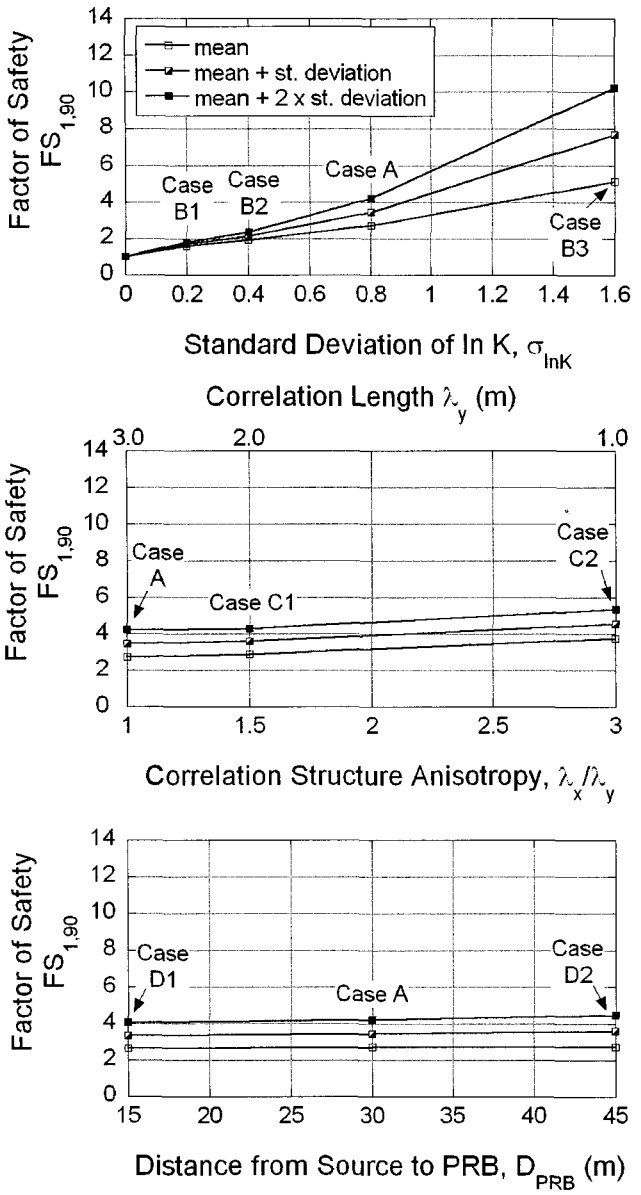

Figure 6.13 – Effects of level of aquifer heterogeneity (σ_{lnK}), correlation structure anisotropy, and distance from source to PRB on the factor of safety $FS_{1,90}$ for scaling the PRB thickness (refer to Table 1 for parameter sets used for simulation cases).

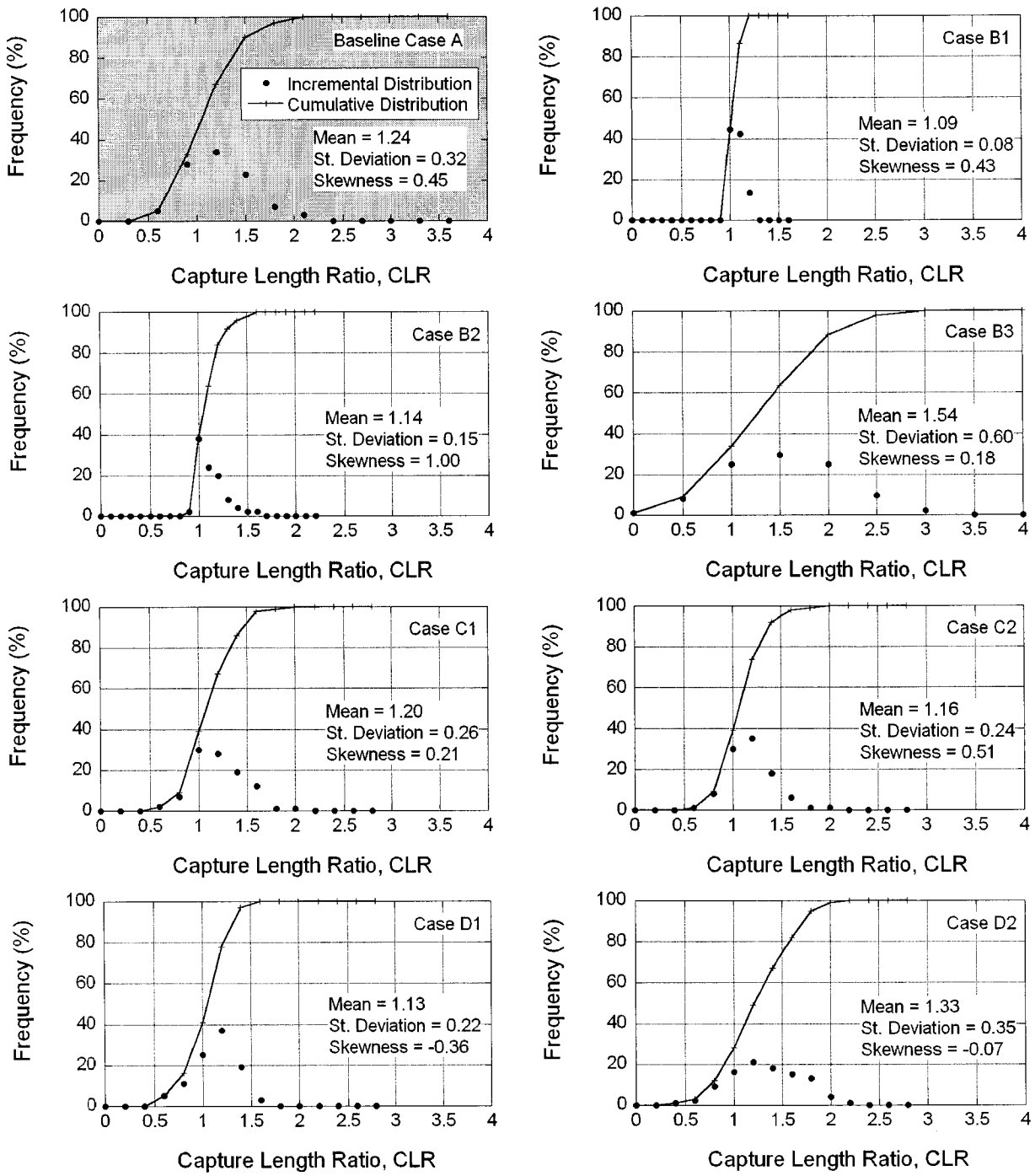

Figure 6.14 – Frequency distributions for capture length ratio for scaling the PRB length (refer to Table 1 for parameter sets used for simulation cases).

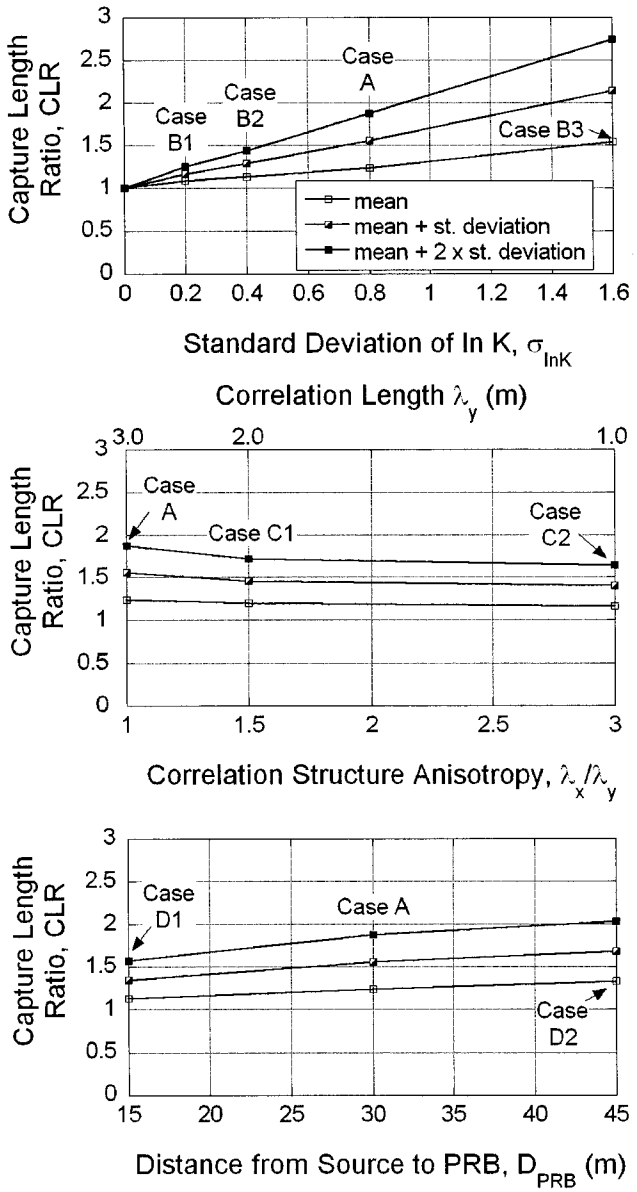

Figure 6.15 – Effects of level of aquifer heterogeneity (σ_{lnK}), correlation structure anisotropy, and distance from source to PRB on the capture length ratio for scaling the PRB length (refer to Table 1 for parameter sets used for simulation cases).

CHAPTER 7

EFFECT OF SEASONAL TEMPERATURE VARIABILITY ON BIOREMEDIATION OF ACID MINE DRAINAGE IN A PERMEABLE REACTIVE BARRIER

ABSTRACT: A biochemical model coupled to flow and transport is applied to simulate trends in field derived data from a field-scale permeable reactive barrier (PRB), with emphasis on the effect of seasonal temperature variability on acid mine drainage (AMD) bioremediation in the PRB. Seasonal temperature variability influences primarily the simulated degradability and longevity of decomposable organic materials, consequently affecting the behavior of the PRB. Dispersive components of influent mass fluxes for SO_4^{2-} and Fe^{2+} are affected by seasonality, with greater dispersive mass fluxes occurring during the warmer months, because aqueous concentrations immediately inside the PRB approach zero during the warm season due to more intensified bacterial activity, creating greater concentration gradients and dispersive mass fluxes at the influent side of the PRB in this case. However, the most significant impact of seasonal temperature variability occurs in terms of effluent mass fluxes for SO_4^{2-} and Fe^{2+} exiting the PRB, which peak during the colder months of the year in response to lower bacterial activity within the PRB, for both decomposer and sulfate reducing bacteria. Thus, although the PRB is capable of achieving remediation of the AMD plume during the warmer seasons, peaks of effluent mass fluxes may be expected during the winter. As a result, model simulations that include seasonal temperature variability provide important insight into the behavior of

full-scale PRBs, the performance of which may be restricted in the field by cold temperatures.

Key Words: Acid mine drainage, Bioremediation, Decomposition kinetics, Permeable Reactive Barrier, Polysaccharide decomposition, Seasonality, Sulfate reduction, Temperature.

7.1. INTRODUCTION

Several field applications of sulfate (SO_4^{2-}) reducing permeable reactive barriers (PRBs) for *in-situ* remediation of acid mine drainage (AMD) have been reported (e.g., Benner et al. 2002, Groudev et al. 2003). These systems are designed to treat AMD effluents emanating from tailings impoundments by SO_4^{2-} reduction, precipitation of metals, and alkalinity generation, coupled to decomposition of solid organic materials emplaced into the PRB. Among the reported field-scale sulfate reducing PRBs is the first full-scale system constructed in August 1995 at the Nickel Rim mine site near Sudbury, Ontario, Canada, with monitoring data for the first three monitoring events of the operation of this system reported in detail by Benner et al. (1997, 1999, 2002).

For the PRB at the Nickel Rim mine, the experimental rate of bacterially mediated SO_4^{2-} reduction was modeled by Benner et al. (2002) assuming that the rate of SO_4^{2-} reduction is equal to a constant multiplied by a hyperbolic term that accounts for SO_4^{2-} limitation. For the Nickel Rim PRB, an average rate constant of 12 mg SO_4^{2-}/L-d was obtained by fitting the SO_4^{2-} data for the third year of operation (1998) and considering an average groundwater temperature of 9 °C. Rates of SO_4^{2-} reduction during the winter were found to be approximately equal to 50 % of the rates of SO_4^{2-} reduction occurring during the summer (Benner et al. 2002) and, thus, Benner et al. (2002) fitted these rates of SO_4^{2-} reduction using an Arrhenius model. However, since the model does not relate rates of SO_4^{2-} reduction to rates of the precursor process of decomposition of solid organic materials, some difference in predictions of long-term behavior may be expected relative to the use of a more mechanistic model considering SO_4^{2-} reduction linked to solid

decomposition. Also, since decomposition of solid organic materials is significantly affected by temperature (e.g., Katterer et al. 1998), a model in which rates of SO_4^{2-} reduction are linked to rates of solid decomposition is a more fundamental approach for representing the effect of seasonal temperature variability on the performance of SO_4^{2-} reducing PRBs.

As a result, this Chapter presents applications of a biochemical model previously described in Chapter 2 that includes sulfate reduction and metals precipitation with sulfate reduction kinetics coupled to, and limited by, the decomposition of solid (particulate) organic materials for simulating trends in field derived data from the Nickel Rim PRB. For simulating such field conditions, emphasis in the application of the model is placed on the effect of seasonal temperature variability, since temperature directly affects bacterial activity for decomposer and SO_4^{2-} reducing bacteria and, as a result, is expected to play a significant role on the extent of AMD remediation occurring within the PRB.

7.2. BACKGROUND

The effect of temperature on kinetic rate constants for generic chemical and biological reactions may be assessed using the Arrhenius equation (e.g., Drever 1997, Benner et al. 2002), as follows:

$$\log\frac{k_2}{k_1} = \frac{E_a}{2.303R}\left[\frac{1}{T_1} - \frac{1}{T_2}\right] \tag{7.1}$$

where k_1 and k_2 are the rate constants at temperatures T_1 and T_2, respectively, R is the universal gas constant (= 8.314 x 10^{-3} kJ mol^{-1} K^{-1}), and E_a is the activation energy of the

chemical or biological reaction. Despite all the complex steps involved in SO_4^{2-} reduction, Benner et al. (2002) report an effective E_a value that falls within the relatively narrow range 40±20 kJ/mol. However, an effective E_a value has not been defined by Benner et al. (2002) for the precursor and rate limiting process of decomposition of polysaccharides in solid organic materials (e.g., municipal compost, leaf mulch, and wood chips), preventing the application of Eq. 7.1 to decomposition.

Specifically for the problem of defining temperature-dependent rate coefficients for organic matter decomposition, Katterer et al. (1998) employed an exponential Q_{10} model as follows:

$$\frac{k_{c,2}}{k_{c,1}} = (Q_{10})^{(T_2-T_1)/10} \tag{7.2}$$

where $k_{c,1}$ and $k_{c,2}$ are decomposition rate coefficients at temperatures T_1 and T_2, respectively, and Q_{10} is a temperature coefficient (van't Hoff 1898) that increases with decreasing temperature, i.e., Q_{10} is ~ 2.5 at 20 °C and ~ 8.0 at 0 °C (Katterer et al. 1998). The exponential Q_{10} model with Q_{10} equal to 2.0 corresponding to intermediate temperatures ranging from 5 to 35 °C is identical to the common "rule of thumb" whereby rate constants for generic chemical and biological reactions are assumed to decline by 50 % for every 10-°C decrease in temperature (Rittman and McCarty 2001).

Application of the "rule of thumb" (i.e., or assuming Q_{10} equal to 2.0) for the purpose of adjusting rate coefficients for decomposition of polysaccharides in municipal compost, leaf mulch, and wood chips at 25 °C of 6.0 d^{-1}, 0.5 d^{-1}, and 0.3 d^{-1}, respectively, to values more applicable to 15 and 5 °C is illustrated in Fig. 7.1. The limitation in this

approach is evident by the observation that Q_{10} should be greater (e.g., 8.0) at lower temperatures (e.g., 0 °C), i.e., rate coefficients should decline to zero as temperature goes to zero. As shown in Fig. 7.1, a new exponential fit for decomposition rate coefficients (k_c) versus temperature, whereby rate coefficients k_c decline to zero as the temperature goes to zero, may be written as follows:

$$k_c(T) = a\, T^{0.825} \tag{7.3}$$

where k_c is the decomposition rate coefficient, T is temperature in °C, and a is a fitting coefficient that depends on the decomposable material (Fig. 7.1). This model for declining k_c with T has a coefficient of correlation of 0.95 with respect to k_c values obtained using the "rule of thumb" between 5 and 25 °C. Vertically averaged groundwater temperatures from zero to 3.6 m of depth at the location of the PRB vary from ~ 15 °C in the warmer season of the year to only ~ 3 °C in the colder season of the year (Benner et al. 2002). The fitted exponential model (Eq. 7.3) will be used to evaluate k_c values for solid decomposition as a function of temperature since this is the only of the models shown in Fig. 7.1 in which k_c declines to zero as T goes to zero.

7.3. BASIS FOR EVALUATION

Field derived data for the PRB at the Nickel Rim mine site are used for the purpose of adjusting model parameter values to values that are expected to be more representative of the field conditions relative to the parameter values used in Chapter 4 on the basis of laboratory data. The comparisons between simulated results and field data are based on

three sets of field derived data, with one set pertaining to each of the first three annual monitoring events in the PRB. The data sets consist of influent, resident (i.e., within the PRB), and effluent concentrations for sulfate (SO_4^{2-}) and ferrous iron (Fe^{2+}), and include data sets for the monitoring events that occurred in September 1996 (i.e., after 13 months of operation), October 1997 (i.e., after 26 months), and October 1998 (i.e., after 38 months) (Benner et al. 2002). In addition, influent, resident, and effluent concentrations for calcium (Ca^{2+}) and hydrogen sulfide (H_2S) are available for September 1996 (Benner et al. 1999).

The simulated behaviors for decomposable polysaccharides, organic substrates, resident bacterial populations (i.e., decomposers and SRB), and solid-phase precipitates ($FeS_{(s)}$, calcite, and siderite) also are obtained. For the simulations reported herein, model parameter values are adopted initially on the basis of laboratory derived data (Chapter 4) and subsequently adjusted to approximate the field derived PRB data. The primary parameter values adjusted herein are those related to decomposition of municipal compost, leaf mulch, and wood chips based on particle size of organic materials and seasonal variations in temperature.

A schematic plan view of the Nickel Rim PRB is provided in Fig. 7.2 (Benner et al. 2002). An isometric view depicting the model geometry, and the assumed locations of source zone, initial AMD plume, and PRB is provided in Fig. 7.3.

As shown in Fig. 7.3, the Nickel Rim PRB is 20 m long (transverse to flow), 4.0 m in thickness (parallel to flow), and 3.6 m in depth. The PRB length and depth are restricted by the presence of bedrock on the sides and base of the alluvium valley (Fig. 7.2). The total and pore volumes for the PRB are approximately 288 m^3 and 115.2 m^3, respectively,

corresponding to a porosity of 0.4 (Benner et al. 1999). The specific discharge, interstitial groundwater seepage velocity, and solution residence time within the PRB are approximately 0.0176 m/d, 0.044 m/d, and 90 days, respectively (Benner et al. 1999, 2002).

Only the longer term (13 to 38 months) PRB reactivity and SRB growth coupled to, and limited by, the decomposition of solid organic materials is simulated, and dissolved organic substrates (e.g., lactate or $C_3H_5O_3^-$) are assumed to be absent from both the influent solution and the initial pore-space solution in the PRB. The initial equivalent SRB biomass concentration adopted in this study is assumed to incorporate the effect of the initial acclimatization period. Uniform initial distributions of organic decomposable materials and bacterial populations within the PRB are assumed for the simulations.

Vertically averaged groundwater temperatures at the location of the PRB (i.e., from zero to 3.6 m of depth) vary significantly throughout the year, i.e., from ~ 15 ^{o}C in the warmer season to only ~ 3 ^{o}C in the colder season of the year (Benner et al. 2002). Thus, since temperature affects bacterial activity, such seasonality is expected to play an important role in the PRB performance throughout the year. The effect of seasonality is incorporated by considering time-dependent (i.e., warmer/colder seasons) rate coefficients for the bacterial processes in the model, particularly for the rate-limiting process of decomposition of solid organic materials.

The Nickel Rim PRB was filled with 49 % organic materials, 50 % pea gravel, and 1 % limestone, all by volume. The organic materials are comprised of ~ 41 % municipal compost, 41 % leaf mulch, and 18 % wood chips, also all by volume. For simulation, the initial equivalent concentrations (i.e., dry mass/pore volume) of organic materials in the

PRB were calculated using an estimated dry density of organic materials (see section 7.5.2).

As reported by Benner et al. (1999), the influent ground water contained Al^{3+} (~ 35 mg/L), Mn^{2+} (~ 9 mg/L), Ni^{2+} (~ 7.7 mg/L), and Zn^{2+} (~ 0.3 mg/L). However, these metals are neglected for simulation since the precipitation of Mn^{2+}, Ni^{2+}, and Zn^{2+} with H_2S is negligible relative to that for Fe^{2+} (i.e., since influent Fe^{2+} ranges from 600 - 650 mg/L), and the removal of Al^{3+} is usually not attributed to precipitation as a sulfide phase but rather is related to the precipitation of amorphous $Al(OH)_3$ and/or cation exchange and organic binding (Drever 1997, Langmuir 1997, Weider et al. 1990). Within the PRB, the solution pH ranges from 6.5 to 7.0 (Benner et al. 1999), which is consistent with the range in pH assumed for the model. Also, the possibility of sorption of Fe^{2+} to the surfaces of the organic materials, which are likely to be negatively charged for the range of pH in the PRB (e.g., Sposito 1989), is not considered in this study.

Geochemical modeling based on groundwater composition in the vicinity of the PRB was used to calculate vertically averaged saturation indices for selected minerals (Benner et al. 1999). Within the PRB, ground water is near saturation with respect to siderite ($FeCO_{3(s)}$), and supersaturated with respect to calcite ($CaCO_{3(s)}$), dolomite ($CaMg(CO_3)_{2(s)}$), rhodochrosite ($MnCO_{3(s)}$), and amorphous $Al(OH)_{3(s)}$. Also, the solution is supersaturated with respect to amorphous $FeS_{(s)}$, which is in agreement with the observed 1-to-1 Fe-to-S stoichiometry in black precipitates formed in the PRB (Benner et al. 1999), and under saturated with respect to gypsum ($CaSO_4.2H_2O_{(s)}$). Elevated Ca^{2+} concentrations entering the PRB are attributed to the aquifer, and remain approximately unaffected by $CaCO_{3(s)}$ dissolution within the sand zone existing immediately up gradient

of the PRB. High influent Ca^{2+} combined with high alkalinity (e.g., HCO_3^-) generated within the PRB result in the tendency to precipitate $CaCO_{3(s)}$, $FeCO_{3(s)}$, and other carbonate solids. As a result, influent Ca^{2+} on the order of 500 mg/L was considered in this study. Since degassing was observed to occur above the PRB (Benner et al. 2002), the possibility of H_2S volatilization to the gas phase is included in most simulations reported in this study.

7.4. MODEL DESCRIPTION AND SOLUTION

The mathematical model used in this study is described in Chapter 2 (and Hemsi et al. 2005) and includes (i) anaerobic decomposition of polysaccharides in solid organic materials based on Contois kinetics (Contois 1959), (ii) SO_4^{2-} reduction based on incomplete oxidation of lactate, including SRB growth via Monod kinetics (Monod 1949), (iii) kinetically controlled precipitation of Fe^{2+} mono sulfide, (iv) partial volatilization of H_2S to the gas phase, and (iv) reversible kinetically controlled dissolution-precipitation of $CaCO_{3(s)}$ and $FeCO_{3(s)}$. Steady-state flow and multi-species reactive contaminant transport were modeled using MODFLOW 2000 version 1.7 (Harbaugh et al. 2000) and RT3D version 2.5 (Clement 1997, 2003), with transport coupled in time to user defined biochemical reactions. Transport time steps on the order of 0.015 d were implemented based on consideration of the requirements for advection, dispersion, sink/source mixing (e.g., Zheng and Wang 1999), and reactions. Multiple reaction time steps for the Runge-Kutta-Fehlberg algorithm used for solving the reaction component are allowed within each transport time step, and the component of the simulation using RT3D stops if more than 3000 reaction time steps are required within each transport time step (Clement 1997).

The aquifer containing the PRB (Figure 7.3) was modeled as a discretized domain

with grid discretization consisting of one 3.6-m-thick layer, 40 0.5-m-wide rows (parallel to the direction of flow), and 230 columns (i.e., transverse to the direction of flow) with variable widths. Column widths were gradually increased from 0.05 m at and near the center of the domain, where the PRB was located, to 0.4 m near the model boundaries, with width expansion factors between any two adjacent columns of less than 1.2. The refinement of the finite difference grid near the center of the domain is required for more accurate transport results, i.e., SO_4^{2-} and Fe^{2+} influent, resident, and effluent concentrations in the vicinity of the PRB. Constant hydraulic-head boundary conditions for flow are imposed at both the up gradient and down gradient boundaries of the domain. Constant-concentration boundary conditions for transport are imposed for SO_4^{2-}, Fe^{2+}, Ca^{2+}, and HCO_3^- at the cells corresponding to the AMD source zone (see Fig. 7.3).

Initial conditions for SO_4^{2-} and Fe^{2+} are given by the assumed initial location of the AMD plume (Fig. 7.3), which was obtained by first simulating conservative transport of SO_4^{2-} and Fe^{2+} emanating from the source zone (Fig. 7.3) for 450 d in the aquifer without the presence of the PRB. Following the simulation for conservative transport, reactive transport simulations used the final SO_4^{2-} and Fe^{2+} plume location as the initial conditions for SO_4^{2-} and Fe^{2+}. The reactive transport simulations also included the PRB, which was assumed to be installed in the aquifer at a location 4.5 m down gradient of the front of the SO_4^{2-} and Fe^{2+} plume (Fig. 7.3). Such an assumption reflects the practical scenario of locating the PRB ahead of the plume (i.e., whenever possible) to allow for construction of the PRB. For the groundwater seepage velocity of 0.04 m/d, 4.5 m corresponds to approximately 100 d required for the front of the plume to reach the PRB.

7.5. INITIAL CONCENTRATIONS AND PARAMETER VALUES

Initial concentrations and parameter values used in this study for all simulation cases are summarized in Table 7.1. Further details regarding the bacterial populations, polysaccharide decomposition, sulfate reduction, sulfide precipitation, hydrogen sulfide volatilization, and dissolution-precipitation of calcite and siderite follow.

7.5.1. Bacterial Populations

The equivalent biomass concentration by dry mass of polysaccharide decomposer bacteria colonizing each decomposable polysaccharide ranges from 0.1 to 10 mg biomass/g of dry polysaccharide, based on cell coverage ranging from approximately 10^9 to 10^{10} cells/g of dry detritus, and considering from 10^{-10} to 10^{-9} mg per cell on a dry mass basis (e.g., Fenchel and Harrison 1976). A cell coverage ranging from 2 to 15 cells/100 μm^2 of fiber of decomposable detritus is obtained assuming fibers with a 2-mm diameter, 5-mm length, and ~ 3 mg/fiber (Fenchel and Harrison 1976, Henriksen and Breland 2002). Intermediate equivalent concentrations corresponding to concentration ratios by dry mass of decomposer bacteria to decomposable polysaccharide, $[X_d]/[CE]$, ranging from 5×10^{-3} to 1×10^{-2} are used for the simulations.

The equivalent biomass concentration by dry mass for SRB that are incomplete oxidizers of lactate (e.g., *Desulfovibrio vulgaris*) was estimated to range from 1 to 1000 mg biomass/L of pore liquid when SO_4^{2-} reduction is active. This range is based on the converted abundance ranging from 10^7 to 10^9 cells/mL of pore liquid that is in agreement with measurements reported by Benner et al. (2002) for the Nickel Rim PRB. Based on from 10^{-10} to 10^{-9} mg/cell by dry mass corresponding to cylindrical cells with a height of

2.35 μm and a diameter of 0.75 μm (Postage 1984), an intermediate value of 50 mg biomass/L of pore liquid is used for the simulations.

7.5.2. Polysaccharide Decomposition

The amounts of total organic materials emplaced in the PRB (i.e., municipal compost, leaf mulch, and wood chips) were reported only on a volume basis by Benner et al. (1997, 1999). In order to estimate the amounts of total organic materials on a dry mass basis, a dry density of organic materials of 0.4 g/cm^3 was assumed (e.g., http://simetric.co.uk). Additionally, the amounts of anaerobically decomposable polysaccharides within total organic materials were estimated on the basis of representative percentages reported in Chapter 2. The resulting initial amounts of decomposable polysaccharides in municipal compost, leaf mulch, and wood chips were estimated as 8.0, 60.0, and 27.0 g/L, respectively, all with respect to the volume of pore liquid within the PRB (Table 7.1). Based on the pore volume of 115.2 m^3, the total dry masses of municipal compost, leaf mulch, and wood chips required to fill the PRB are estimated as 900, 6,900, and 3,000 kg, respectively. With respect to the kinetics of polysaccharide decomposition, Contois kinetic parameter values for polysaccharide decomposition were initially taken from Chapter 4, and subsequently adjusted considering the effects of the particle size of organic materials and seasonal temperature variation.

7.5.3 Sulfate and Sulfide

Monod parameters for SRB growth on lactate were taken as per Chapter 4, with a temperature adjustment, resulting in a maximum specific SRB growth rate (μ_{SRB}) equal to

2.0 d^{-1}, and half-saturation constants for lactate (K_V) and sulfate (K_{SO}) of 5.0 and 2.0 mg/L, respectively. Kinetically controlled precipitation of Fe^{2+} mono sulfide, modeled using first-order kinetics, included a first-order rate coefficient (i.e., k_{Fe}) equal to 1.0 d^{-1} (Table 7.1), as per Chapter 4. Kinetically controlled volatilization of hydrogen sulfide (H_2S), modeled using first-order kinetics, included a variable first-order rate coefficient (i.e., k_v), equal to zero, 1.0 d^{-1}, or 100 d^{-1} in selected simulations (Table 7.1).

7.5.4 Calcite and Siderite

Reversible dissolution of $CaCO_{3(s)}$ and precipitation of $FeCO_{3(s)}$ were modeled using modified first-order kinetics (Chapter 2). The initial dry mass of $CaCO_{3(s)}$ was assumed as equal to 10,000 mg $CaCO_{3(s)}$/L (Table 7.1). Dissolution rate coefficients for $CaCO_{3(s)}$ and $FeCO_{3(s)}$ were reduced with respect to those used in Chapter 4, to incorporate the effect of the lower temperature in the PRB. Those rate coefficients were assumed as 30 mg/L-d and 20 mg/L-d for calcite and siderite, respectively. Also, solubility products for $CaCO_{3(s)}$ of $10^{1.85}$ and for $FeCO_{3(s)}$ of $10^{-0.56}$ were adopted from Drever (1997).

7.6. RESULTS AND DISCUSSION

7.6.1. Adjusting Field Decomposition Kinetics

7.6.1.1. Concentrations

Comparisons of simulated results and field derived data for SO_4^{2-} and Fe^{2+} are shown in Fig. 7.4 where the simulated results are based on variable Contois rate coefficients, k_c, for decomposition of compost, leaf mulch, and wood chips (Cases 1 to 4;

Table 7.1). The field derived data consist of vertically averaged concentration profiles across the central line of the PRB. When comparing simulated results to field derived SO_4^{2-} and Fe^{2+} data, the data point for distance of 5.0 m down gradient of the PRB will be neglected. The reason for neglecting this data is because the SO_4^{2-} and Fe^{2+} concentrations at this point are increased due to the infiltration of surface water contaminated by AMD in the site (Benner et al. 1999), a fact that was not included in the model. Another simulation case (data not shown) using Contois rate coefficients, k_c, identical to those used in Chapter 4 (i.e., k_c equal to 6.0 d^{-1}, 0.5 d^{-1}, and 0.3 d^{-1}, for compost, leaf mulch, and wood chips, respectively) resulted in poor approximations of SO_4^{2-} and Fe^{2+} data with time (i.e., at 13 months, simulated concentrations abruptly declined to zero and, at 38 months, simulated concentrations were higher than the field data). That is, for parameter values directly taken from Chapter 4, poor approximations of longevity of organic materials in the PRB were obtained.

The results for the first simulation case in Fig. 7.4 (Case 1; Table 7.1) reflect the use of reduced decomposition parameter values relative to those previously used in the simulations for the column tests (Chapter 4) on the basis of the effect of particle size on decomposition kinetics (e.g., Humphrey 1979). That is, because the diameters for the partly degraded leaf much and wood chip chunks emplaced in the PRB are on the order of 0.5 to 3.0 cm (Benner et al. 2002), which are at least two times greater than those for the same materials in the 5-cm-diameter column tests (Chapter 4), decomposition rate coefficients used for simulating the column test results (Chapter 4) were reduced by a factor of two for simulation Case 1, i.e., considering the rate of decomposition of organic materials as being inversely proportional to particle size (Humphrey 1979), as shown in

Fig. 7.5. Thus, the resulting decomposition rate coefficients for simulation Case 1 were equal to 3.0 d^{-1}, 0.25 d^{-1}, and 0.15 d^{-1}, for compost, leaf mulch, and wood chips, respectively.

However, the results for simulation Case 1 still do not provide a favorable approximation of the field derived data. On the contrary, simulated results obtained for Case 1 still over predict SO_4^{2-} reduction and Fe^{2+} precipitation when compared to data for the monitoring event at 13 months (1996), also under predicting the longer-term sustainability of SO_4^{2-} reduction in the PRB, i.e., when compared to data for the monitoring event at 38 months (1998). The reason for the discrepancy is that the additional corrections on k_c due to the effect of seasonal temperature variability have not yet been included in simulation Case 1.

Vertically averaged groundwater temperatures ranging from ~ 15 °C (warmer season) to only ~ 3 °C (colder season) are at least 10 °C lower than the temperature in the column tests reported in Chapter 4 (i.e., 25 °C). Thus, k_c values for simulation Cases 2 to 4 were reduced in comparison to those values used for simulation Case 1 by factors of 1.33 (Case 2), 2.0 (Case 3), and 4.0 (Case 4). For example, the k_c values for Case 3 are equal to 1.5 d^{-1}, 0.125 d^{-1}, and 0.075 d^{-1} for compost, leaf mulch, and wood chips, respectively (Case 3; Table 7.1). In addition, simulation Cases 2 to 4 include seasonality effects by considering each year to be separated into two seasons, with a warmer season ranging from April through September (6 months), and a colder season ranging from October through March (6 months). Since colder months are characterized by average groundwater temperatures of only ~ 3 °C, k_c coefficients during these months were reduced further relative to values of k_c for the warm months. On the basis of the regressed exponential fit

(k_c versus temperature) shown in Fig. 7.1, cold-season k_c values are four times lower than warm-season k_c values.

On the basis of the results shown in Fig. 7.4, simulation Case 3 appears to provide the best overall approximation to field derived data for all three monitoring events. Also, 15-°C rate coefficients for Case 3 are 50 % of the values for Case 1, which agrees with the "rule of thumb" whereby coefficients are divided by a factor of two for every 10-°C drop in temperature (Rittman and McCarty 2001).

7.6.1.2 Cumulative Mass

Influent and effluent mass fluxes, and influent, effluent, and stored cumulative masses for the conservative transport of SO_4^{2-} through the PRB are shown in Fig. 7.6. As shown in Fig. 7.6b, during the total simulation time of 1080 d, ~ 3,400 kg of SO_4^{2-} entered the PRB.

The influent and effluent mass fluxes as well as the influent, effluent, and removed cumulative masses for SO_4^{2-} over time (from August 1995 to October 1998) based on simulation Case 3 for reactive transport of SO_4^{2-} through the PRB are shown in Figs. 7.7a, b, and c, respectively. The simulated cumulative mass of SO_4^{2-} removed versus time (i.e., Fig. 7.7c) is calculated using a cumulative mass approach based on integrated mass flux components (e.g., Shackelford 1994, 1995), as follows:

$$M_{removed}(t) = An \{ \underbrace{\int_0^t [vC_{in}(t) + D(\partial C_{in} / \partial x)]dt}_{M_{in}(t)} - \underbrace{\int_0^t [vC_{eff}(t)]dt}_{M_{out}(t)} \} \qquad (7.4)$$

where $M_{removed}$ is the mass removed, A and n are the PRB cross-sectional area and the medium porosity, respectively, D is the coefficient of hydrodynamic dispersion, and C_{in} and C_{eff} are influent and effluent (simulated) concentrations, respectively.

As shown in Fig. 7.7a, the influent SO_4^{2-} mass flux based on simulation Case 3 that includes advective and dispersive mass flux components (Eq. 7.4), with the dispersive component of transport being a relatively small component of the total mass flux (< 5 %, Fig. 7.7a), provides results that are similar to those based on conservative transport (Fig. 7.6a). Moreover, as shown in Fig. 7.7a, seasonality affects the dispersive mass flux entering the PRB, which increases during the warmer months due to the increase in decomposition and SO_4^{2-} reduction within the PRB during the warmer months resulting, in turn, in an increase in the SO_4^{2-} concentration gradient towards the PRB during this period.

As shown in Fig. 7.7b, seasonality plays a significant role on the effluent mass flux of SO_4^{2-} exiting the PRB. In this case, peaks in SO_4^{2-} effluent concentrations (i.e., equivalent to effluent mass fluxes on the order of ~ 2,700 – 2,900 g SO_4^{2-}/d) occur during some of the cold months of the year (e.g., January to April, Fig. 7.7b), which is consistent with a decline in SO_4^{2-} reduction during the cold season. Thus, although the PRB is capable of achieving remediation of SO_4^{2-} during the warmer season, significant peaks in SO_4^{2-} may occur during the winter, which is consistent with observations made by Benner et al. (2002), with significant practical implications. As shown in Fig. 7.7c, during the total simulation time of 1080 d, ~ 2,500 kg of SO_4^{2-} were removed in the PRB (i.e., both reduced or transformed and stored), with variable rates of removal affected by seasonality in temperature (Fig. 7.7c).

Influent and effluent mass fluxes as well as influent, effluent, and stored

cumulative masses for the conservative transport of Fe^{2+} through the PRB are shown in Fig. 7.8. As shown in Fig. 7.8a, the influent mass flux of Fe^{2+} into the PRB reaches ~ 770 g/d, and ~ 680 kg of Fe^{2+} entered the PRB from the aquifer (i.e., source zone) during the total simulation time of 1080 d.

As shown in Fig. 7.9a, the influent Fe^{2+} mass flux for simulation Case 3 including both advective and dispersive mass flux components (Eq. 7.4) is similar to the simulated influent Fe^{2+} mass flux based on conservative transport (Fig. 7.9a). In this case, the dispersive mass flux corresponds to ~ 8 % of the total mass flux during the warmer months, and to only about 3 % during the cold season, since Fe^{2+} is almost entirely precipitated and the aqueous concentration of Fe^{2+} immediately inside the PRB approaches zero during the warm season, creating a large concentration gradient for Fe^{2+} and, consequently, a greater dispersive mass flux at the influent side of the PRB.

As shown in Fig. 7.9b, seasonality also plays a significant role on the effluent mass flux for Fe^{2+} exiting the PRB, since peaks in this effluent mass flux correlate with the colder seasons (i.e., on the order of 30, 290, and 350 g Fe^{2+}/d for the first, second, and third cold seasons, respectively), when bacterial activity within the PRB is expected to decline. Thus, although the PRB achieves a significant removal of Fe^{2+} during the warmer seasons (i.e., almost 100 % up to 1080 d for simulation Case 3), Fe^{2+} emanates from the PRB during the winter months as a result of low bacterial activity. As shown in Fig. 7.9c, during the total simulation period of 1080 d, ~ 640 kg of Fe^{2+} were removed, either by precipitation or storage within the PRB (simulation Case 3).

7.6.1.3 Other Simulated Species

For simulation Case 3, concentrations for $FeS_{(s)}$ are shown as a function of time (i.e., first, second, and third years) and distance in Fig. 7.10. The maximum concentrations of precipitated $FeS_{(s)}$ occur at the influent face of the PRB, which is consistent with the results of simulations for different precipitates in a zero valent iron PRB (e.g., Yabusaki et al. 2001). As shown in Fig. 7.11, the cumulative mass of $FeS_{(s)}$ and Fe^{2+} removed by sulfide precipitation achieved approximately 1,040 and 650 kg in 1080 d (i.e., from August 1995 to October 1998) for simulation Case 3. The results of simulation Case 3 shown in Fig. 7.12 indicate nearly uniform SRB concentrations developing in the PRB throughout all three years, except for the SRB near the effluent side of the PRB, which is significantly lower than those elsewhere in the barrier.

7.6.2 Impact of Seasonality

As shown in Table 7.1, simulation Case 5 is the same as simulation Case 3 except there is no consideration of seasonality in temperature, and parameter values for warmer conditions (i.e., average temperature of 15 °C) are assumed to occur throughout the entire year. As shown in Fig. 7.13, simulation results based on Cases 3 and 5 provide similar SO_4^{2-} and Fe^{2+} influent, resident, and effluent concentrations for time equal to13 months (i.e., Figs. 7.13a,b). However, the simulated results for Cases 3 and 5 deviate for later times, as shown in Figs. 7.13c-f.

The results for simulation Case 5 are based on higher decomposition parameter values during the year, since there is no reduction in decomposition parameter values during the cold season. As a result, simulated SO_4^{2-} and Fe^{2+} resident and effluent concentrations based on simulation Case 5 are higher than those for Case 3 after the first

13 months of the simulation period (see Figs. 7.13c-f,). This difference can be attributed to the difference in the lifetimes of the decomposable organic materials between simulation Cases 3 and 5. Since simulation Case 5 contains higher decomposition parameter values, organic materials decompose more rapidly and remain at lower concentrations later on (e.g., 26 or 38 months), reducing the overall long-term performance of the PRB. For an earlier period (e.g., 8 months), simulated SO_4^{2-} and Fe^{2+} resident and effluent concentrations are lower for simulation Case 5 than for simulation Case 3 (data not shown), denoting more SO_4^{2-} reduction and Fe^{2+} precipitation for simulation Case 5 during this period.

The simulated behaviors of decomposable polysaccharides [$n(C_6H_{10}O_5)$] in leaf mulch and wood chips with time are shown in Fig. 7.14. In Figs. 7.14a and 7.14c, simulated polysaccharide decompositions based on simulation Cases 3 and 5 are compared for time frames of approximately three years. In Figs. 7.14b and 7.14d, the longer-term polysaccharide decomposition behavior based only on simulation Case 3 is extrapolated for time frames beyond 13 years.

As shown in Figs. 7.14a and 7.14c, simulated polysaccharide decomposition in leaf mulch and wood chips is significantly affected by the seasonality in temperature (e.g., compare simulation Case 3 including seasonality with simulation Case 5 excluding seasonality). For example, at two years, simulated percentages of decomposable polysaccharides remaining in leaf mulch and wood chips are on the order of 30 % for Case 5 versus 50 % for Case 3 (Fig. 7.14a), and 55 % for Case 5 versus 73 % for Case 3 (Fig. 7.14c), respectively. For Case 3, slower decomposition kinetics occurring during cold seasons is evident in Figs. 7.14a and 7.14c.

As shown in Figs. 7.14b and 7.14d, the results of the simulated longer-term behavior of polysaccharide decomposition in leaf mulch and wood chips suggest that polysaccharides in leaf mulch in the PRB are depleted after ~ 11 years (Fig. 7.14b), whereas in wood chips polysaccharides last for more than 13 years. Additionally, exponential curve fittings of these simulated results are shown in Figs. 7.14b and 7.14d. Exponential functions in the form of percentage remaining (PR) versus time were considered appropriate since the PR not only declines with time, but also the rate of decomposition given by dPR/dt declines with time, as expected (e.g., Janssen 1984).

7.6.3 Effect of Hydrogen Sulfide Volatilization

Degassing, probably including $H_2S_{(g)}$ (i.e., gas-phase hydrogen sulfide) occurred above the PRB (Benner et al. 2002). As shown in Table 7.1, simulation Cases 6 and 7 consider different values for the first-order rate coefficient for volatilization of liquid-phase H_2S (i.e., k_v = 1 d^{-1} and zero, for Cases 6 and 7, respectively) as compared to the value assumed for simulation Case 3 (i.e., 100 d^{-1}). Therefore, the effect of H_2S volatilization on simulated influent, resident, and effluent concentrations for Fe^{2+} can be observed by comparing the results for simulation Cases 3, 6, and 7. As assumed in the model, H_2S volatilization does not affect SO_4^{2-} and, therefore, the results for SO_4^{2-} are the same in simulation Cases 3, 6, and 7.

As shown in Fig. 7.15, resident and effluent concentrations for Fe^{2+} increase with increasing k_v (i.e., are greater for Case 3 relative to Cases 6 and 7) due to the competition between volatilization and $FeS_{(s)}$ precipitation for H_2S. As also shown in Fig. 7.15, the results for Fe^{2+} obtained for Case 6 (k_v = 1 d^{-1}) are practically identical to those obtained

for Case 7 (k_v = 0), indicating that the extent of kinetic limitation to FeS(s) precipitation imposed by volatilization with k_v = 1 d^{-1} is negligible. Concentrations of H_2S in the PRB vary significantly depending on the assumed value of k_v (i.e., Cases 3, 6, and 7). The levels of H_2S in solution increase by an order of magnitude from Case 3 to 6 (i.e., for k_v decreasing from 100 to 1 d^{-1}), and by two to three orders of magnitude from Case 6 to 7 (i.e., for k_v decreasing from 1 d^{-1} to zero).

7.6.4 Effect of Siderite Precipitation

As shown in Table 7.1, simulation Cases 8 and 9 include siderite ($FeCO_{3(s)}$) precipitation as a second significant sink for Fe^{2+} in the model. For both cases, the precipitation of $FeCO_{3(s)}$ is assumed to be linked to the dissolution of an initial mass of calcite ($CaCO_{3(s)}$) amounting to 10 g $CaCO_{3(s)}$/L in the PRB (Benner et al. 2002), resulting in the release of HCO_3^- in solution. As shown in Figs. 7.16a-c, field derived effluent concentrations for Fe^{2+} are from 100 to 300 mg/L greater than those concentrations resulting from simulation Case 3. Thus, consideration of an additional sink for Fe^{2+} ($FeCO_{3(s)}$ precipitation, Cases 8 and 9) will increase this discrepancy between simulated results and field data for Fe^{2+}. However, the precipitation of $FeCO_{3(s)}$ is reported by Benner et al. (2002) and, therefore, is also included herein.

Cases 8 and 9 differ in that different rate coefficients for H_2S volatilization are used, i.e., k_v = 100 d^{-1} for Case 8, and k_v = 1 d^{-1} in Case 9 (Table 7.1). The volatilization of H_2S affects the kinetics of Fe^{2+} precipitation with H_2S (i.e., $FeS_{(s)}$ precipitation) which, in turn, competes with $FeCO_{3(s)}$ precipitation for Fe^{2+} in solution. As assumed in the model, $FeCO_{3(s)}$ precipitation does not affect SO_4^{2-} and, therefore, the results for SO_4^{2-} are the

same for Cases 3, 8, and 9.

As shown in Fig. 7.16, resident and effluent concentrations for Fe^{2+} are lower for Cases 8 and 9 relative to those for Case 3, due to the precipitation $FeCO_{3(s)}$. However, this difference decreases with time, such that for 26 months (Figs. 7.16b,c) simulated results for Cases 8 and 9 are closer to those for Case 3 than for 13 months (Fig. 7.16a).

The simulated equivalent concentrations for the solid phases $FeS_{(s)}$, $CaCO_{3(s)}$, and $FeCO_{3(s)}$ for Cases 8 and 9 are shown in Figs. 7.17. As shown in Figs. 7.17a,b, the amount of $FeS_{(s)}$ precipitated based on simulation Case 8 (Fig. 7.16a) is lower over time than that based on simulation Case 9 (Fig. 7.17b), due to greater H_2S volatilization in Case 8 (i.e., k_v = 100 d^{-1} versus 1.0 d^{-1} in Case 9). Also, as shown in Figs. 7.17c-f, more $CaCO_{3(s)}$ dissolves and more $FeCO_{3(s)}$ precipitates in the PRB for Case 8 compared to Case 9, an observation that is attributable to lower precipitation of Fe^{2+} with H_2S based on simulation Case 8.

Cumulative masses of dissolved $CaCO_{3(s)}$ and precipitated $FeS_{(s)}$ and $FeCO_{3(s)}$ versus time up to 1080 d for Cases 8 and 9 are shown in Figs. 7.18a and 7.18b, respectively. As shown in Fig. 7.18a, for the assumptions in simulation Case 8 (Table 7.1), the cumulative mass of $FeCO_{3(s)}$ precipitated over time is greater than that for $FeS_{(s)}$, e.g., 700 kg $FeCO_{3(s)}$ versus 590 kg $FeS_{(s)}$ at three years. However, Benner et al. (2002) reported that at ~ 23 months, only ~ 30 % of the total precipitated Fe^{2+} occurred in a non-sulfidic form, i.e., on the basis of calculated S-to-Fe ratios of precipitates and solid-phase extractions. As shown in Fig. 7.18b, for the assumptions in simulation Case 9 (Table 7.1), i.e., less H_2S volatilization favoring more precipitation of $FeS_{(s)}$, the cumulative mass of precipitated $FeS_{(s)}$ is greater than that for $FeCO_{3(s)}$. For example, 780 kg $FeS_{(s)}$ versus 510

kg $FeCO_{3(s)}$ at three years, and 410 kg $FeS_{(s)}$ versus 380 kg $FeCO_{3(s)}$ at 23 months. The later is equivalent to ~ 30 % of the cumulative precipitated Fe^{2+} removed in non-sulfidic form. As shown in Fig. 7.19a, simulated results for calcium (Ca^{2+}) based on simulation Cases 8 and 9 compare favorably to field derived data at 12 months, the same occurring for the simulated concentrations for H_2S for Case 9 (i.e., H_2S concentrations after uptake of H_2S in $FeS_{(s)}$ precipitation), i.e., as shown in Fig. 7.19b.

7.6.5 Effect of Aquifer Dispersivity

As shown in Table 7.1, simulation Case 10 is based on parameter values identical to those for Case 3, except for the assumed longitudinal dispersivity, α_L, of the aquifer. In Case 10, α_L is assumed equal to 0.5 m, i.e., five times greater than that assumed for Case 3. As shown in Fig. 7.20, the effect of the value of α_L on simulated influent, resident, and effluent concentrations for SO_4^{2-} and Fe^{2+} may be significant, particularly at earlier times, e.g., comparing the simulated results at 13 months (Figs. 7.20a,b) versus those at 38 months (i.e., Figs. 7.20e,f). However, the value of α_L does not appear to significantly affect the major trends in the simulated results.

7.7 CONCLUSIONS

A biochemical model coupled to flow and transport was used for simulating trends in data from a field-scale permeable reactive barrier (PRB) for bioremediation of acid mine drainage (AMD) at Nickel Rim, Ontario, Canada, with emphasis on the effect of seasonal temperature variations on the extent of AMD remediation in the PRB. The biochemical model differs from previous models used for such simulations in that sulfate

reduction and metals precipitation kinetics are coupled to, and limited by, the decomposition of solid (particulate) organic materials. Simulated results were compared to field derived data pertaining to three monitoring events of the PRB, i.e., at 13 month of operation (1996), at 26 months of operation (1997), and at 38 months of operation (1998).

The effect of seasonal temperature variation was incorporated in the model by adding the capability of time-dependant reaction rate constants in RT3D, and adjusting parameter values for biological processes. Seasonal temperature variation influenced the simulated longevity of decomposable organic materials which, in turn, affected the performance of the system (i.e., effluent concentrations and mass fluxes for SO_4^{2-} and Fe^{2+}) since decomposition is precursor, and rate limiting, to SO_4^{2-} reduction and metal precipitation. Simulated decomposition of polysaccharides in leaf mulch and wood chips was significantly affected by the presence of seasonality in temperature. For example, at 26 months, simulated percentages of decomposable polysaccharides remaining in leaf mulch and wood chips were on the order of 30 and 55 % when seasonality was not included, versus 50 and 73 % when seasonality was included. Based on the simulated results considering seasonality in temperature, polysaccharides in leaf mulch and wood chips were estimated to last within the PRB for ~ 11 and more than 13 years, respectively.

During the total simulation time of 1080 d (from August 1995 to October 1998), approximately 3,400 kg of SO_4^{2-} and 680 kg of Fe^{2+} entered the PRB from the source zone in the aquifer. During this period, approximately 2,500 kg of SO_4^{2-} and 640 kg of Fe^{2+} were removed within the PRB, either transformed or stored. Dispersive components of influent mass fluxes for SO_4^{2-} and Fe^{2+} were significantly affected by seasonality, and were greater during the warmer months, since aqueous concentrations immediately inside

the PRB approached zero during the warm season (due to more intensified bacterial activity) creating greater concentration gradients and dispersive mass fluxes at the influent side of the PRB.

Seasonality also played a significant role on effluent mass fluxes for SO_4^{2-} and Fe^{2+} exiting the PRB, which peaked during the colder months of the year. In the case of SO_4^{2-}, such peaks were on the order of 2,700 – 2,900 g SO_4^{2-}/d and, in the case of Fe^{2+}, 30, 290, and 350 g Fe^{2+}/d for the first, second, and third cold seasons. Therefore, although the PRB completely removed the AMD plume during the warmer seasons, peaks in effluent concentrations may be expected during cold seasons. Thus, the computational modeling performed in this study has provided important insight into potential limitations to AMD remediation in PRBs that may occur as a consequence of cold environments.

7.8 ACKNOWLEDGEMENTS

This research was funded by the U. S. EPA Science to Achieve Results (STAR) Program under Grant No. R-82951501-0 as part of the U. S. EPA's *Rocky Mountain Regional Hazardous Substance Research Center*. The author extends his thanks to Mr. Christian Johnson, Senior Development Engineer, Battelle-PNWD, Richland (WA), for helping develop a customized version of RT3D with time-dependent kinetic parameter values.

7.9 REFERENCES

Benner, S.G, Blowes, D.W., Ptacek, C.J., and Mayer, K.U. (2002). Rates of sulfate reduction and metal sulfide precipitation in a permeable reactive barrier. *Applied*

Geochemistry, 17(1): 301-320.

Benner, S.G., Blowes, D.W., and Ptacek, C.J. (1997). A full-scale porous reactive wall for prevention of acid mine drainage. *Ground Water Monitoring and Remediation*, 17(4): 99-107.

Benner, S.G., Blowes, D.W., Gould, W.D., Herbert, R.B. and C. J. Ptacek (1999). Geochemistry of a permeable reactive barrier for metals and acid mine drainage. *Environmental Science and Technology*, 33(16): 2793-2799.

Clement, T.P. (1997). A Modular Computer Code for Simulating Reactive Multi-species Transport in 3-Dimensional Groundwater Systems RT3D version 1.0. U.S. Department of Energy and Pacific Northwest National Laboratory. PNNL-11720-1997.

Clement, T.P. (2003). RT3D v.2.5 Update Document, What is New in RT3D version 2.5. Electronic document: http://bioprocess.pnl.gov/rt3d.htm.

Contois, D.E. (1959). Kinetics of bacterial growth, relationship between population density and specific growth rate of continuous cultures. *Journal of General Microbiology*, 21(1): 40-50.

Drever, J.I. (1997). *The Geochemistry of Natural Waters – Surface and Groundwater Environments*. 3rd Edition, Prentice-Hall, Upper Saddle River, NJ.

Fenchel, T., and Harrison, P. (1976). The significance of bacterial grazing and mineral cycling for the decomposition of particulate detritus. *The Role of Terrestrial and Aquatic Organisms in Decomposition Processes*, J.M. Anderson and A. Macfadyen, eds., Blackwell Scientific Publications, Oxford, UK, 285-299.

Groudev, S., Nicolova, M., Spasova, I., and Schutte, R. (2003). Treatment of waters from

a copper mine by means of a permeable reactive barrier. *Fifty Years of the University of Mining and Geology "St. Ivan Rilski"*, University of Mining and Geology, Sofia (Bulgaria), Volume 46, Part II, Section Mining and Mineral Processing, 229-231.

Harbaugh, A.W., Banta, E.R., Hill, M.C., and McDonald, M.G. (2000). *MODFLOW-2000, the U.S. Geological Survey Modular Ground-Water Model – User Guide to Modularization Concepts and the Ground-Water Flow Process*, USGS Open-File Report 00-92, Reston, VA.

Hemsi, P.S., Shackelford, C.D., and Figueroa, L.A. (2005). Modeling the influence of decomposing organic solids on sulfate reduction rates for iron precipitation. *Environmental Science and Technology*, 39(9): 3215-3225.

Henriksen, T.M., and Breland, T.A. (2002). Carbon mineralization, fungal and bacterial growth, and enzyme activities as affected by contact between crop residues and soil. *Biology and Fertilization of Soils*, 35(1): 41-48.

Humphrey, A. E. (1979). The Hydrolysis of Cellulosic Materials to Useful Products. *Hydrolysis of Cellulose: Mechanisms of Enzymatic and Acid Catalysis*, Chapter 2, Advances in Chemistry Series, No. 181, American Chemical Society, Washington D.C., 25-53.

Janssen, B.H. (1984). A simple method for calculating decomposition and accumulation of young soil organic matter. *Plant and Soil*, 76(1-3):297-304.

Katterer, T., Reichtein, M., Andren, O., and Lomander, A. (1998). Temperature dependence of organic matter decomposition: a critical review using literature data analyzed with different models. *Biology and Fertility of Soils*, 27(3):258-262.

Langmuir, D. (1997). Aqueous Environmental Geochemistry. Prentice-Hall, Upper Saddle

River, NJ.

Monod, J. (1949). The growth of bacterial cultures. *Annual Review of Microbiology*, 3: 371-394.

Postgate, J.R. (1984). *The Sulphate-Reducing Bacteria.* 2nd Edition. Cambridge University Press, Cambridge, UK.

Rittman, B.E., and McCarty, P.L. (2001). *Environmental Biotechnology: Principles and Applications*. McGraw-Hill, NewYork, NY.

Shackelford, C. D. (1994). Critical concepts for column testing. *Journal of Geotechnical Engineering*, 120(10): 1804-1828.

Shackelford, C. D. (1995). Cumulative mass approach for column testing. *Journal of Geotechnical Engineering*, 121(10): 696-703.

Sposito, G. (1989). *The Chemistry of Soils*. Oxford University Press, Oxford, UK.

Wieder, R.K., Linton, M.N., and Heston, K.P. (1990). Laboratory mesocosm studies of Fe, Al, Mn, Ca, and Mg dynamics in wetlands exposed to synthetic acid coal mine drainage. *Water, Air, and Soil Pollution*, 51(1-2): 181-196.

Yabusaki, S., Cantrell, K., Sass, B., and Steefel, C. (2001). Multicomponent reactive transport in an in situ zero-valent iron cell. *Environmental Science and Technology*, 35(7): 1493-1503.

Zheng, C., and Wang, P.P. (1999). MT3DMS: *A Modular Three-Dimensional Multispecies Model for Simulation of Advection, Dispersion, and Chemical Reactions of Contaminants in Groundwater Systems; Documentation and User's Guide*. U.S. Army Corps of Engineers. Contract Report SERDP-99-1, December 1999.

Table 7.1 – Parameter values in different simulation cases considered for simulation.

Case	Materials	Decomposition (Contois kinetics)			Sulfate Reduct. (Monod kinetics)	Precipitation (first-order kinetics)			$H_2S_{(g)}$ volatilization	Dispersivity	Seasonality
						$FeCO_{3(s)}$		$FeS_{(s)}$			
		Initial [CE] (mg/L)	k_c (d^{-1})	Initial $[X_d]$/[CE]	$[X_{SRB}]$ (mg/L)	Initial $CaCO_{3(s)}$ (g/L)		k_{Fe} (d^{-1})	k_{vol} (d^{-1})	α_L (mm)	
1	MC	8,000	**3.0**	0.01	50	**No**	**0.0**	1.0	**100**	**100**	**No**
	LM	60,000	**0.25**	0.005							
	WC	27,000	**0.15**								
2	MC	8,000	**2.25**	0.01	50	No	0.0	1.0	100	100	**Yes**
	LM	60,000	**0.1875**	0.005							
	WC	27,000	**0.1125**								
3	MC	8,000	**1.5**	0.01	50	No	0.0	1.0	100	100	**Yes**
	LM	60,000	**0.125**	0.005							
	WC	27,000	**0.075**								
4	MC	8,000	**0.75**	0.01	50	No	0.0	1.0	100	100	**Yes**
	LM	60,000	**0.0675**	0.005							
	WC	27,000	**0.0375**								
5	MC	8,000	1.5	0.01	50	No	0.0	1.0	100	100	**No**
	LM	60,000	0.125	0.005							
	WC	27,000	0.075								
6	MC	8,000	1.5	0.01	50	No	0.0	1.0	**1.0**	100	Yes
	LM	60,000	0.125	0.005							
	WC	27,000	0.075								
7	MC	8,000	1.5	0.01	50	No	0.0	1.0	**0.0**	100	Yes
	LM	60,000	0.125	0.005							
	WC	27,000	0.075								
8	MC	8,000	1.5	0.01	50	**Yes**	**10**	1.0	**100**	100	Yes
	LM	60,000	0.125	0.005							
	WC	27,000	0.075								
9	MC	8,000	1.5	0.01	50	**Yes**	**10**	1.0	**1.0**	100	Yes
	LM	60,000	0.125	0.005							
	WC	27,000	0.075								
10	MC	8,000	1.5	0.01	50	No	0.0	1.0	100	**500**	Yes
	LM	60,000	0.125	0.005							
	WC	27,000	0.075								

MC: municipal compost; LM: leaf mulch; and WC: wood chips.

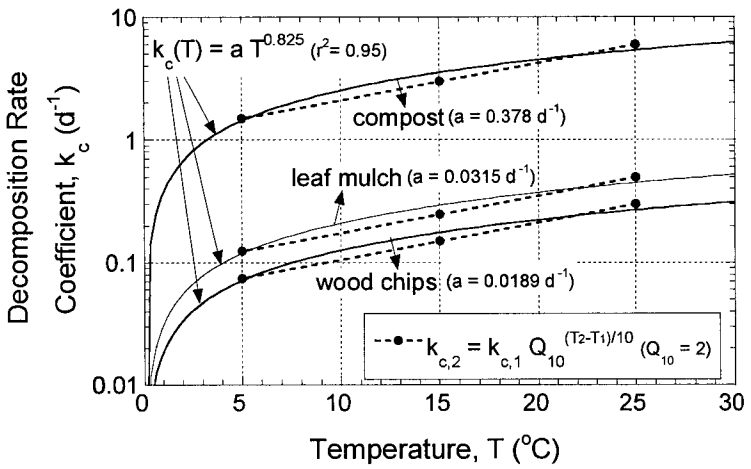

Figure 7.1 – Decomposition rate coefficient, k_c, as a function of temperature, including the exponential Q_{10} model and a new fitted exponential regression.

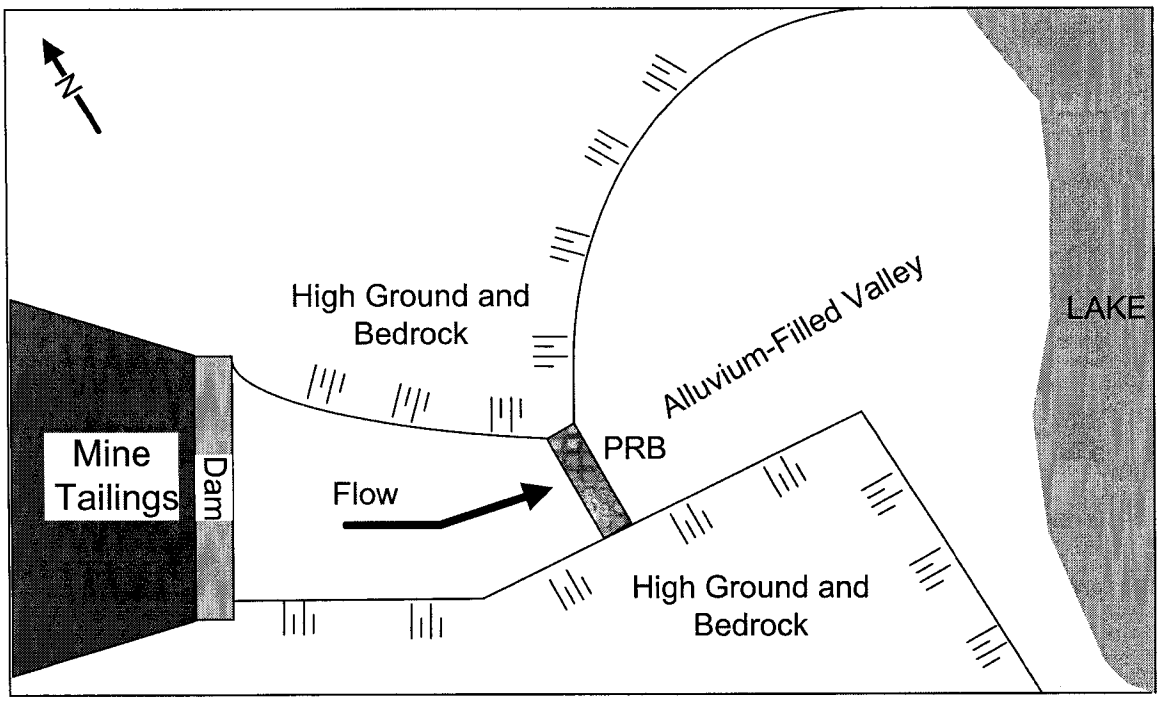

Figure 7.2 – Map view of the Nickel Rim mine site in Ontario (Canada) (Benner et al. 2002).

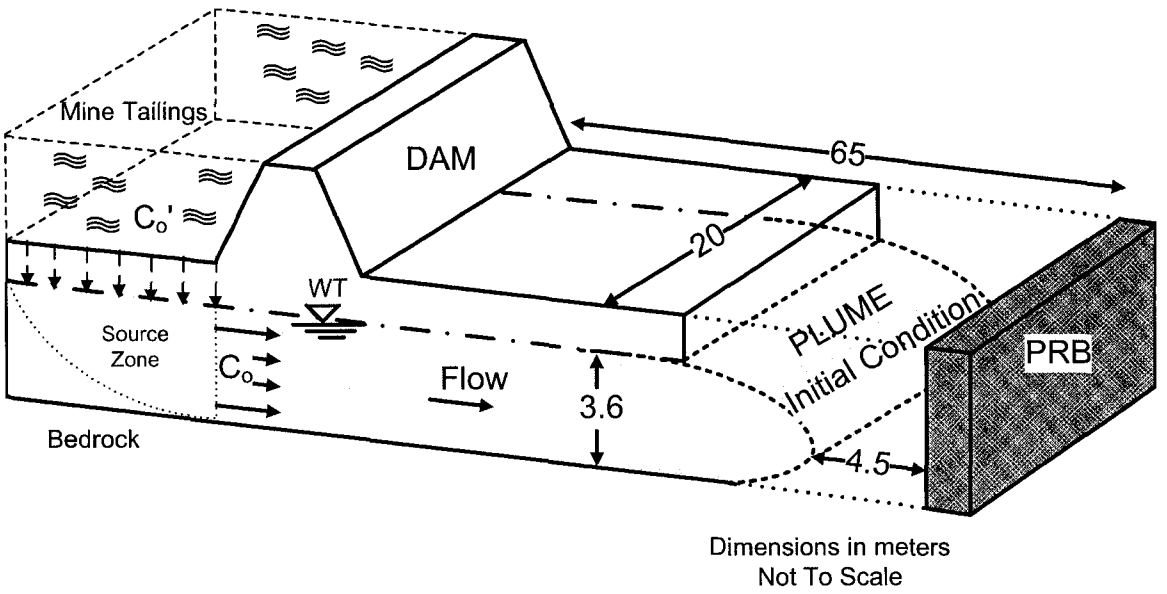

Figure 7.3 – Isometric view showing model dimensions, source zone, PRB, and the initial AMD plume assumed for simulation.

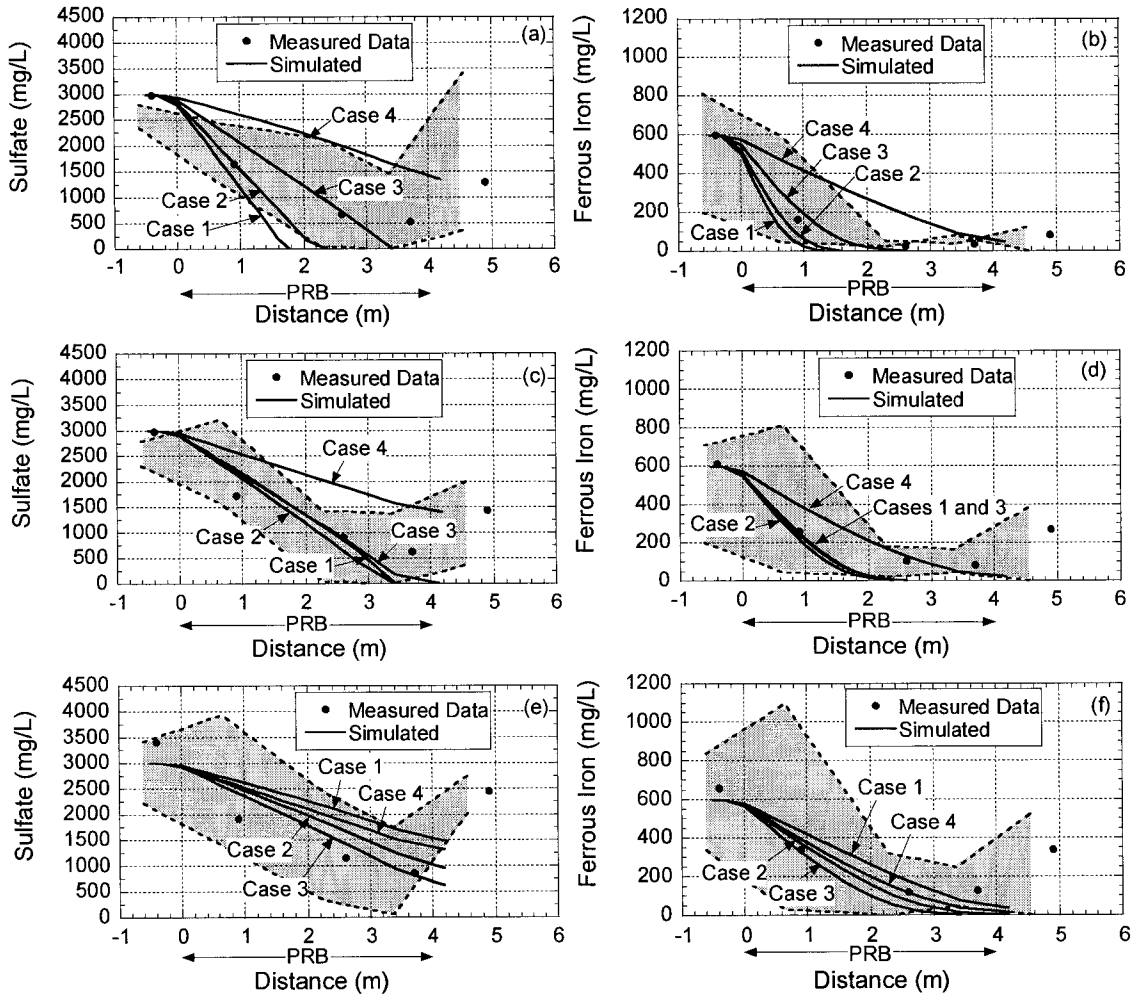

Figure 7.4 – Measured and simulated (Cases 1 to 4) concentration profiles for sulfate and ferrous iron across the central line of the PRB: (a) and (b) September 1996, (c) and (d) October 1997, and (e) and (f) October 1998.

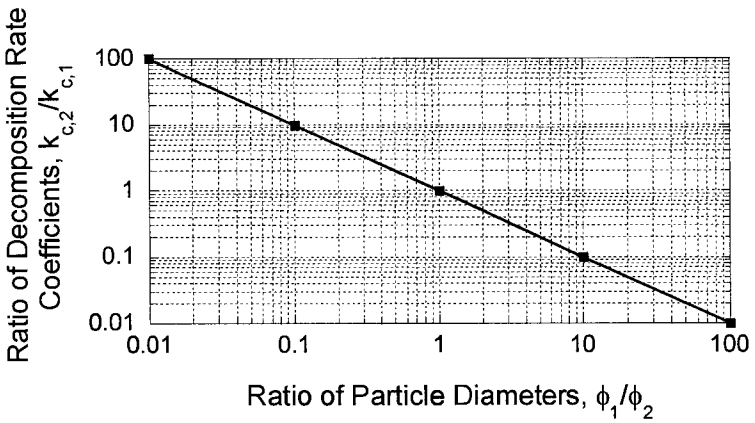

Figure 7.5 – Decomposition rate coefficient, k_c, as a function of particle size of decomposable organic materials (Humphrey 1979).

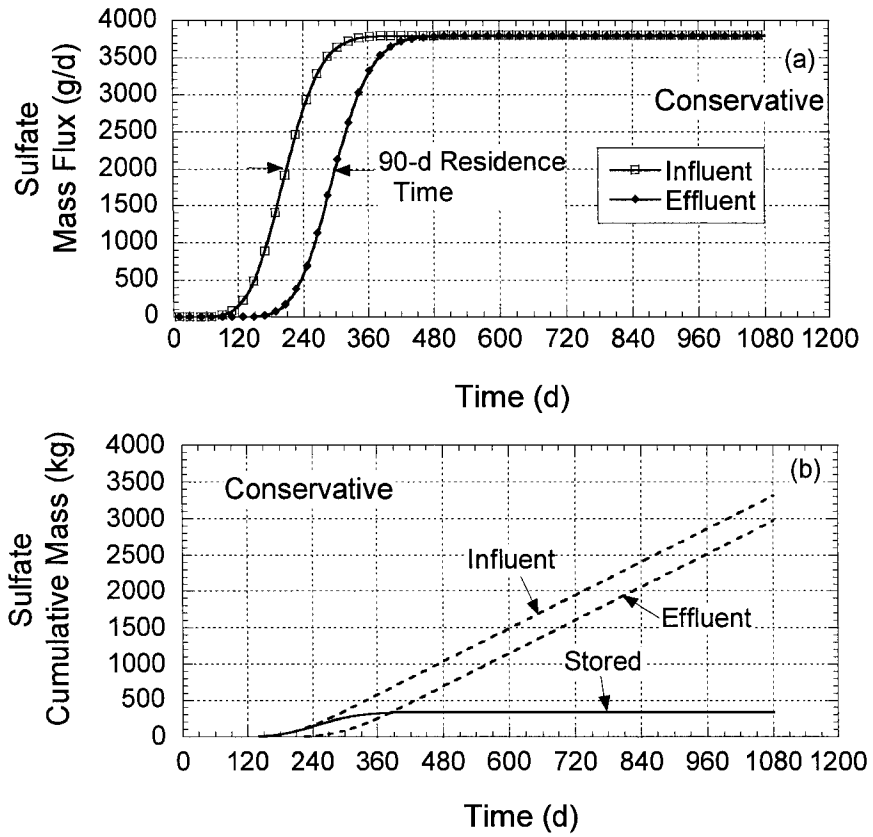

Figure 7.6 – Simulated results for conservative transport of sulfate: (a) influent and effluent mass fluxes, and (b) influent, effluent, and stored cumulative masses.

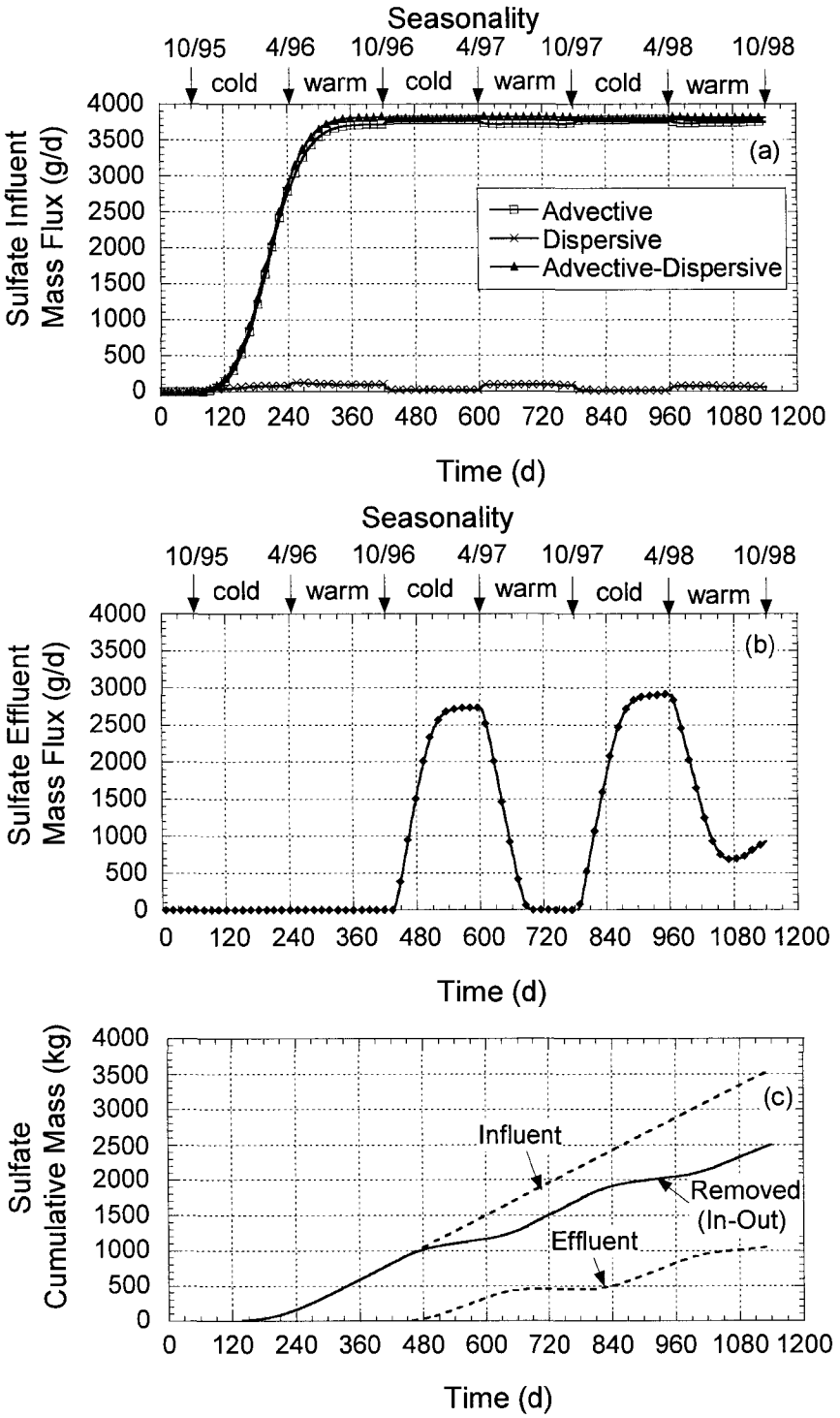

Figure 7.7 – Simulated results for reactive transport (Case 3) of sulfate: (a) influent mass fluxes, (b) effluent mass flux, and (c) influent, effluent, and removed cumulative masses.

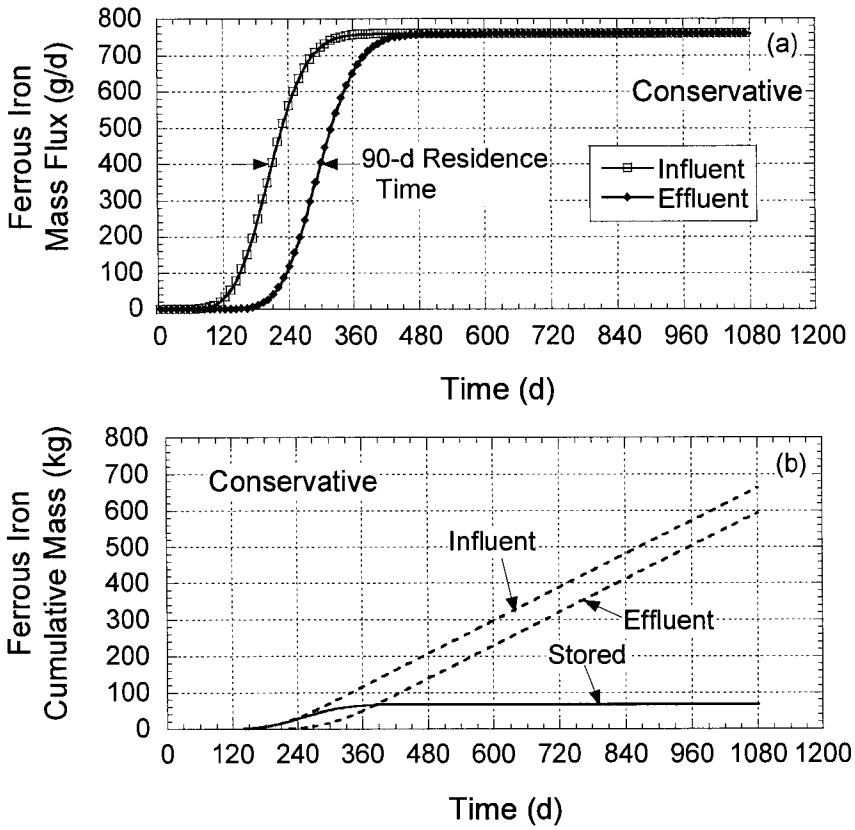

Figure 7.8 – Simulated results for conservative transport of ferrous iron: (a) influent and effluent mass fluxes, and (b) influent, effluent, and stored cumulative masses.

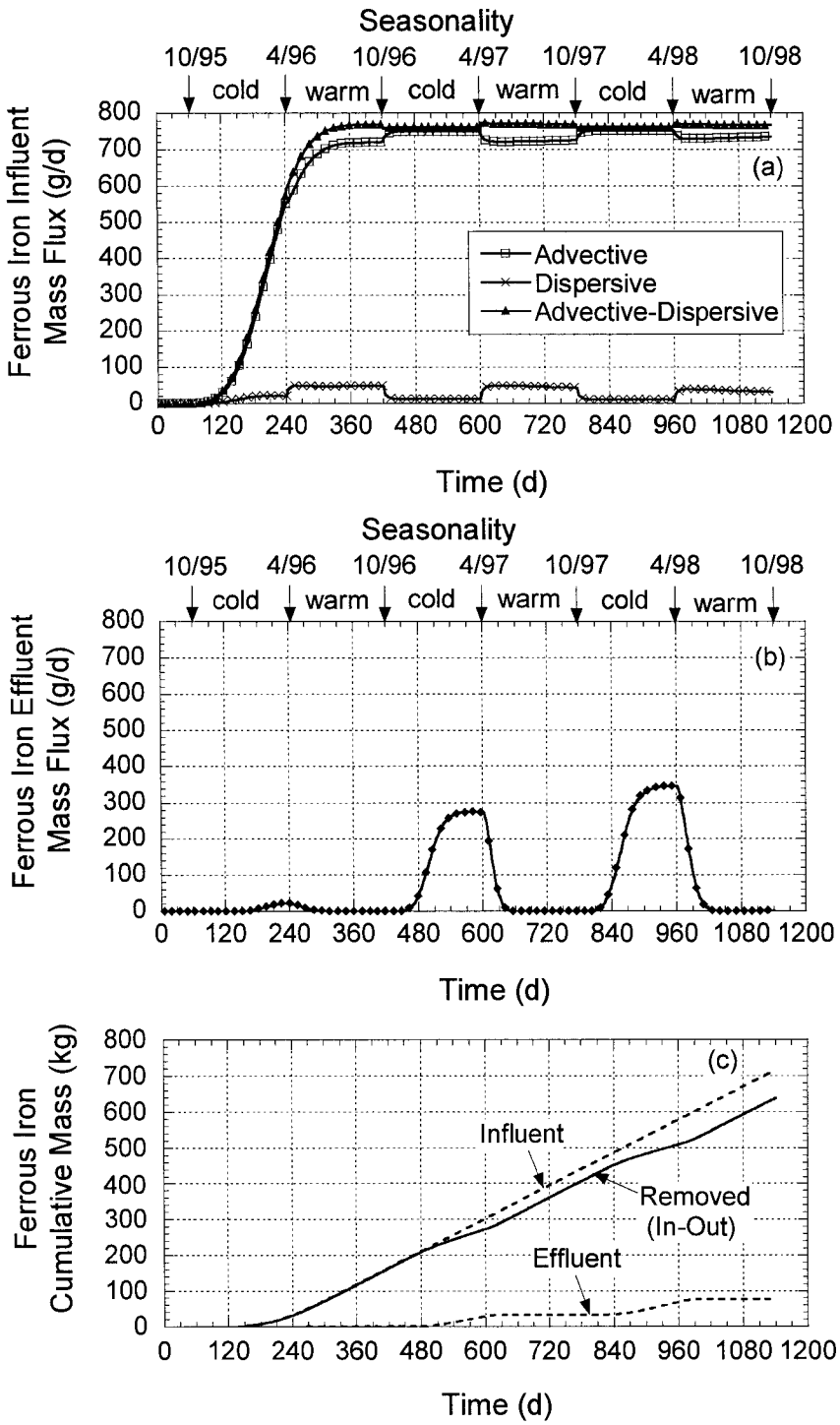

Figure 7.9 – Simulated results for reactive transport (Case 3) of ferrous iron: (a) influent mass fluxes, (b) effluent mass flux, and (c) influent, effluent, and removed cumulative masses.

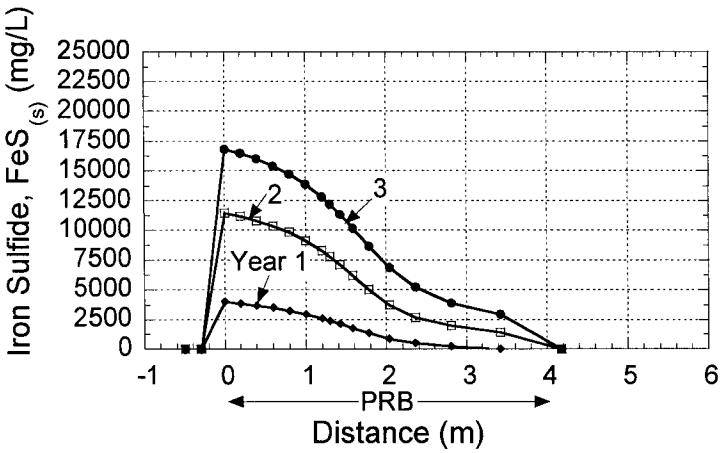

Figure 7.10 – Simulated equivalent concentrations for iron sulfide ($FeS_{(s)}$) precipitate (Case 3).

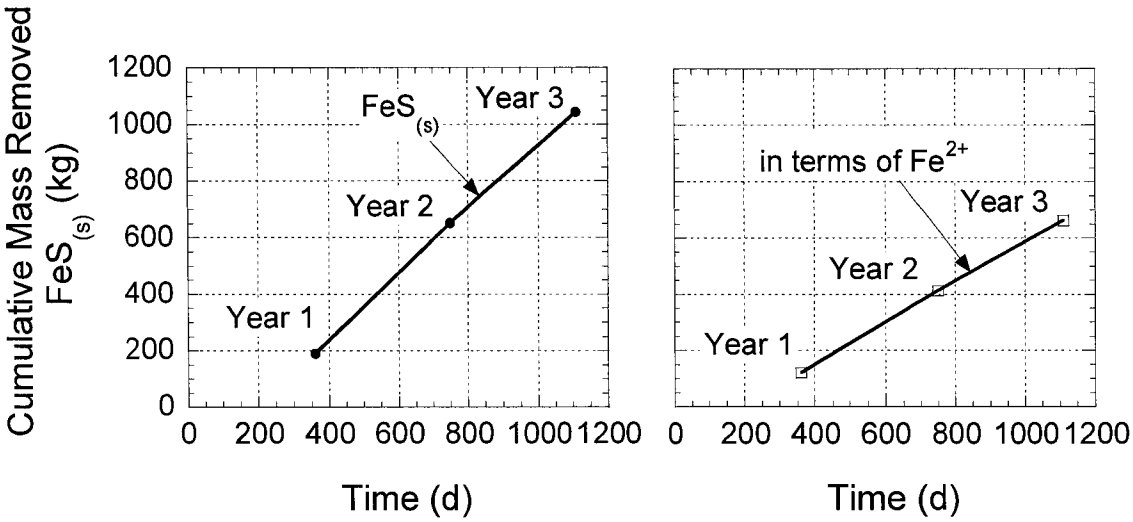

Figure 7.11 – Simulated cumulative masses of $FeS_{(s)}$ and Fe^{2+} precipitated in the PRB over time (Case 3).

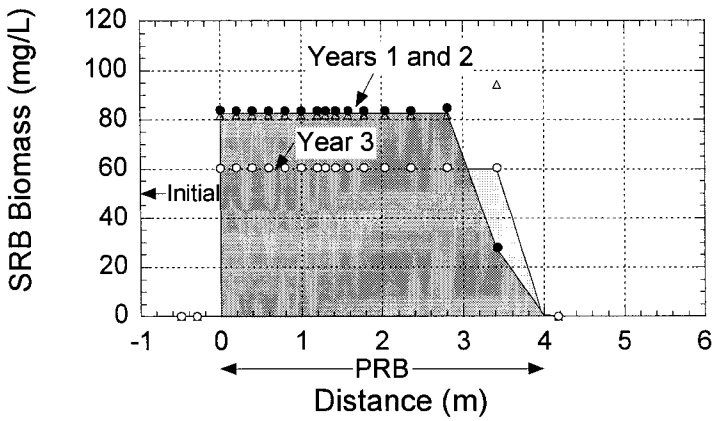

Figure 7.12 – Simulated SRB biomass concentrations in the PRB over time (Case 3).

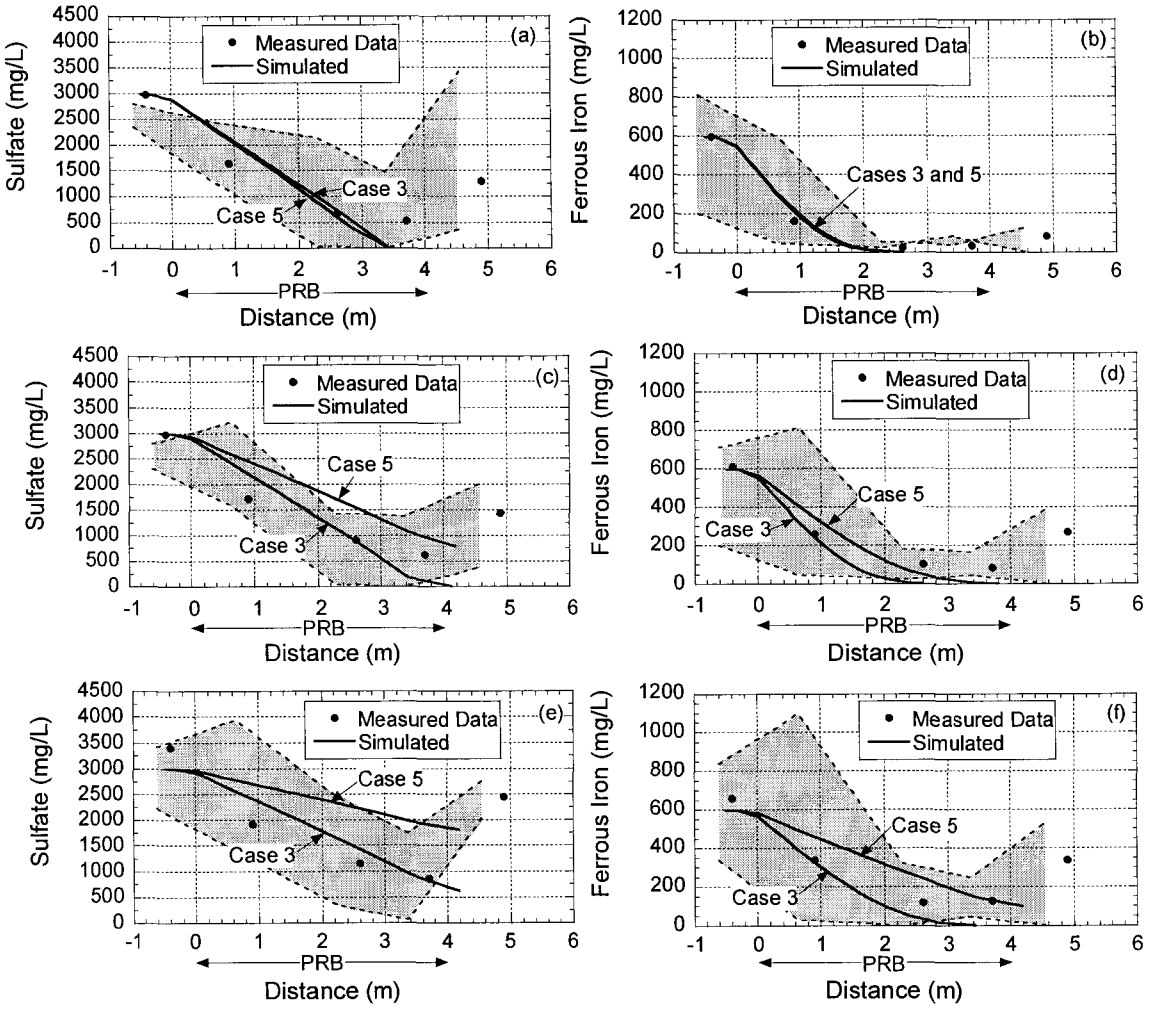

Figure 7.13 – Measured and simulated (Cases 3 and 5) concentration profiles for sulfate and ferrous iron across the central line of the PRB: (a) and (b) September 1996, (c) and (d) October 1997, and (e) and (f) October 1998.

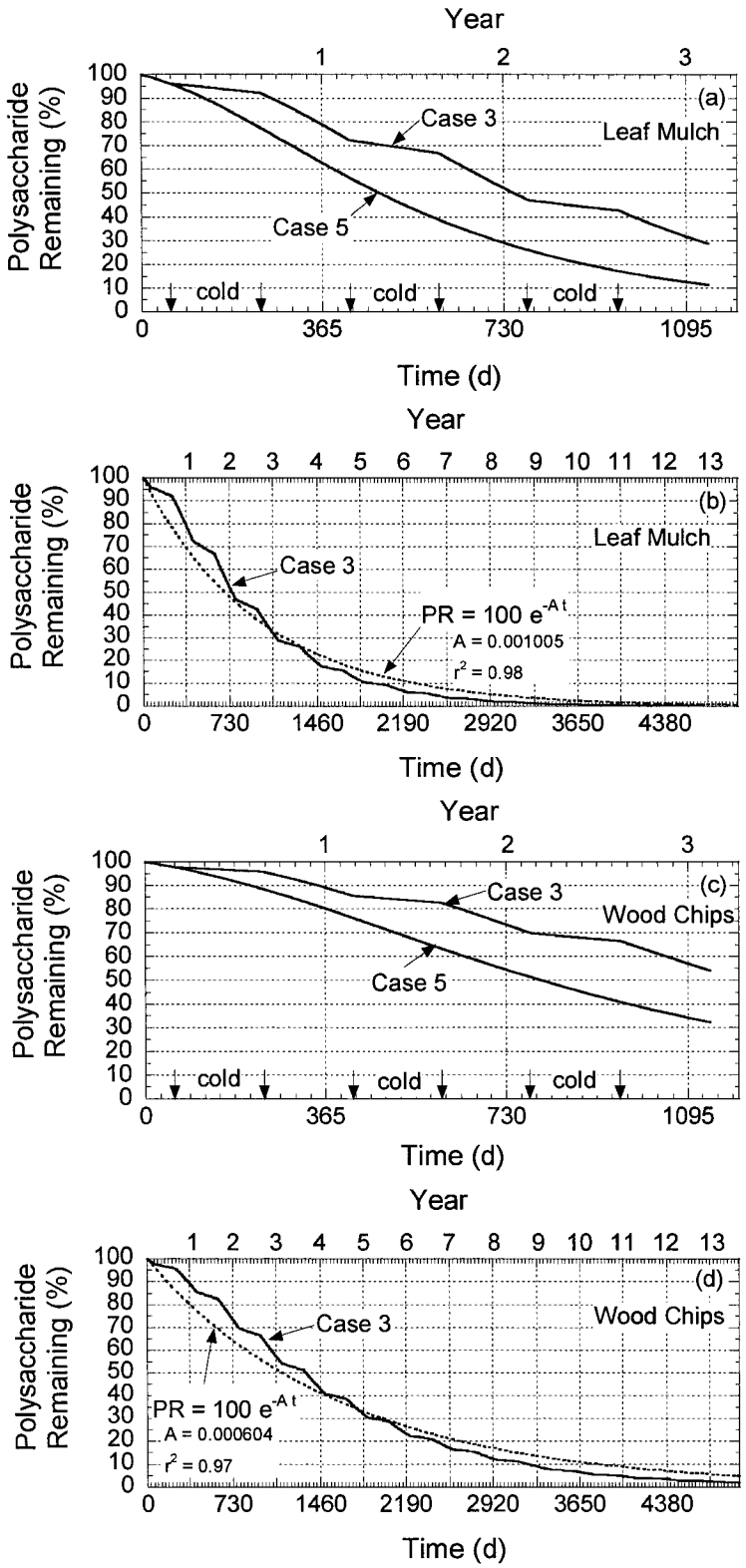

Figure 7.14 – Simulated percentages of polysaccharides remaining: (a) leaf mulch, for time of approximately 3 years (Cases3 and 5), (b) leaf mulch, longer term (Case 3), (c) wood chips, for time of approximately 3 years (Cases 3 and 5), and (d) wood chips, longer term (Case 3).

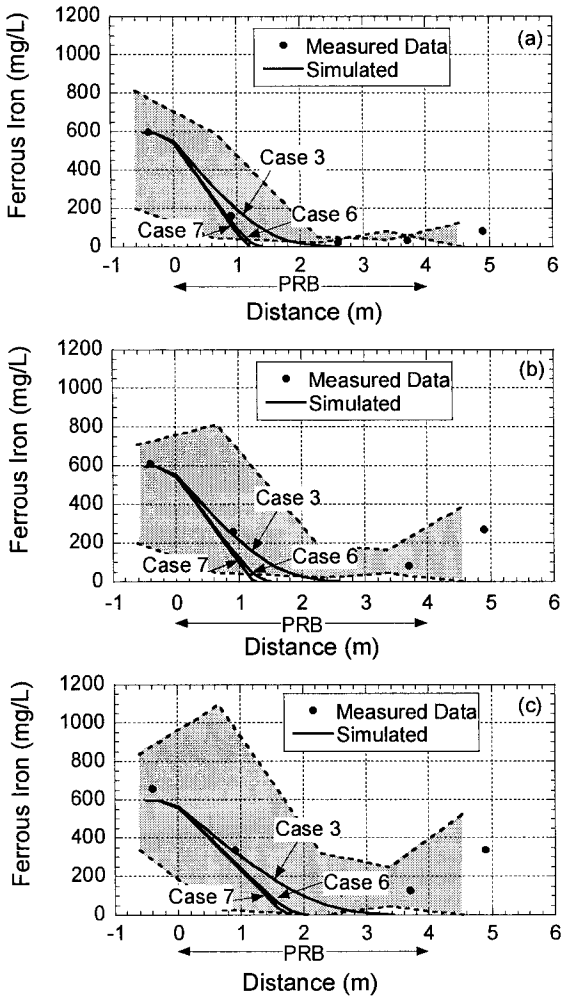

Figure 7.15 – Measured and simulated (Cases 3, 6, and 7) concentration profiles for ferrous iron across the central line of the PRB: (a) September 1996, (b) October 1997, and (c) October 1998.

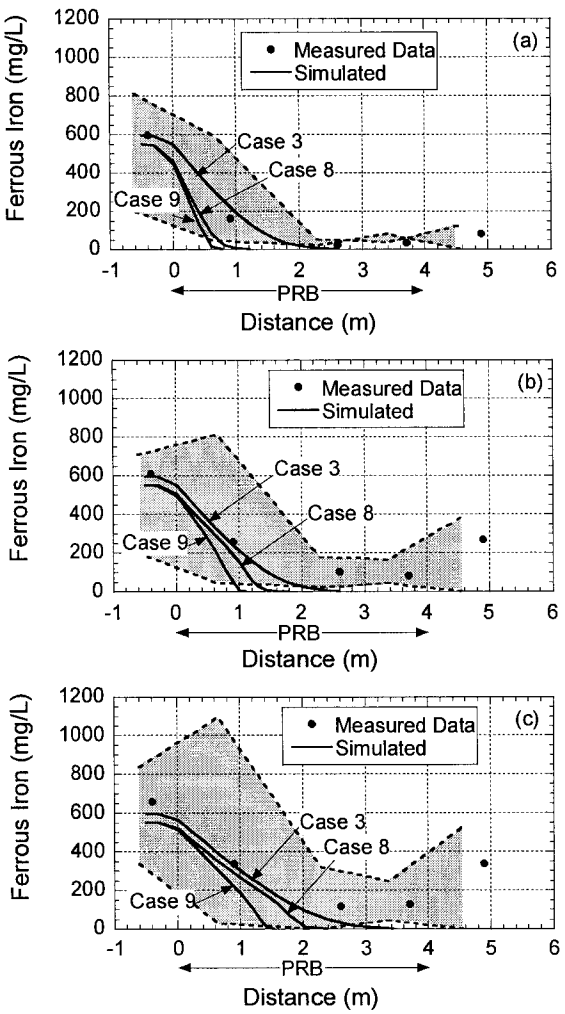

Figure 7.16 – Measured and simulated (Cases 3, 8, and 9) concentration profiles for ferrous iron across the central line of the PRB: (a) September 1996, (b) October 1997, and (c) October 1998.

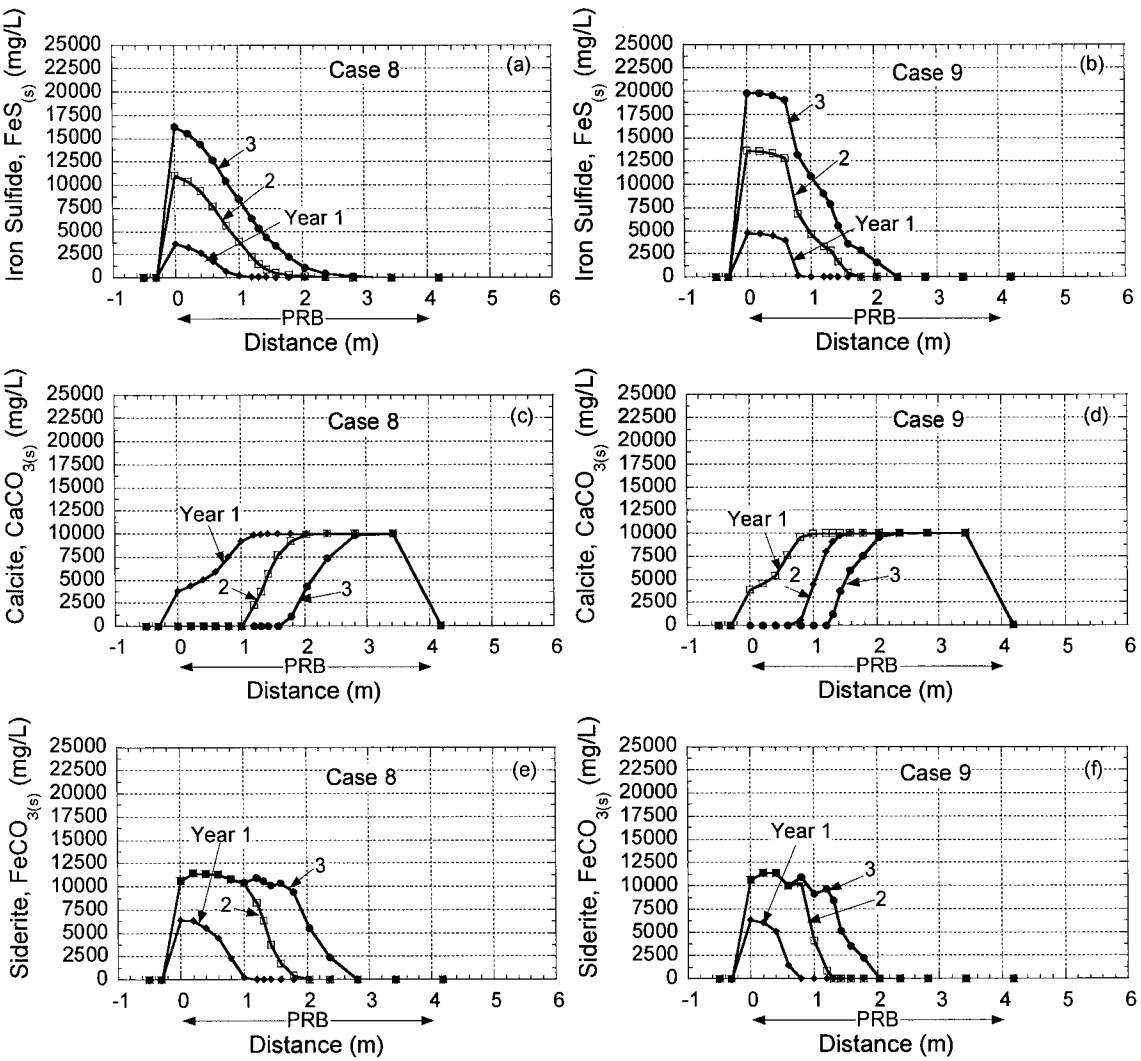

Figure 7.17 – Simulated concentration profiles across the central line of the PRB: (a) $FeS_{(s)}$, Case 8, (b) $FeS_{(s)}$, Case 9, (c) $CaCO_{3(s)}$, Case 8, (d) $CaCO_{3(s)}$, Case 9, (e) $FeCO_{3(s)}$, Case 8, and (f) $FeCO_{3(s)}$, Case 9.

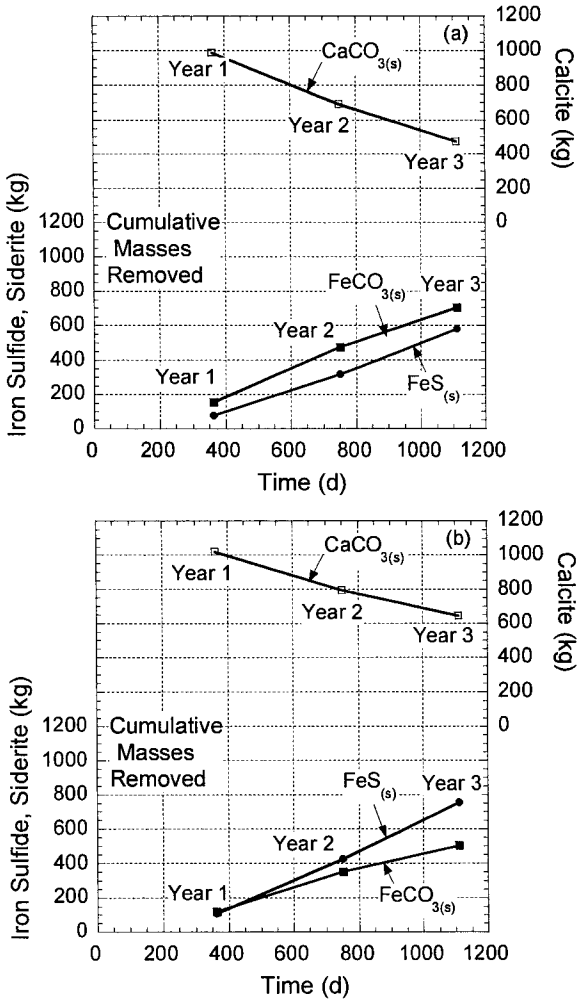

Figure 7.18 – Simulated cumulative masses of $FeS_{(s)}$ and $FeCO_{3(s)}$ precipitated and of $CaCO_{3(s)}$ dissolved in the PRB over time: (a) Case 8, and (b) Case 9.

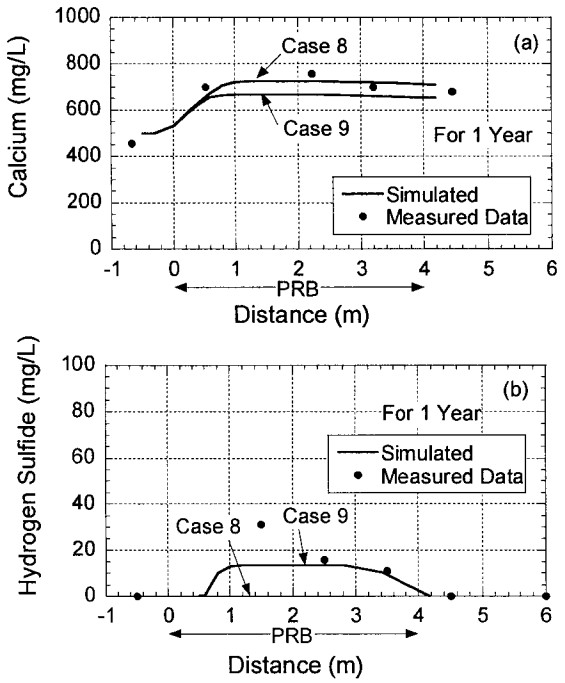

Figure 7.19 – Measured and simulated (Cases 8 and 9) concentration profiles across the central line of the PRB for September 1996: (a) calcium, and (b) hydrogen sulfide.

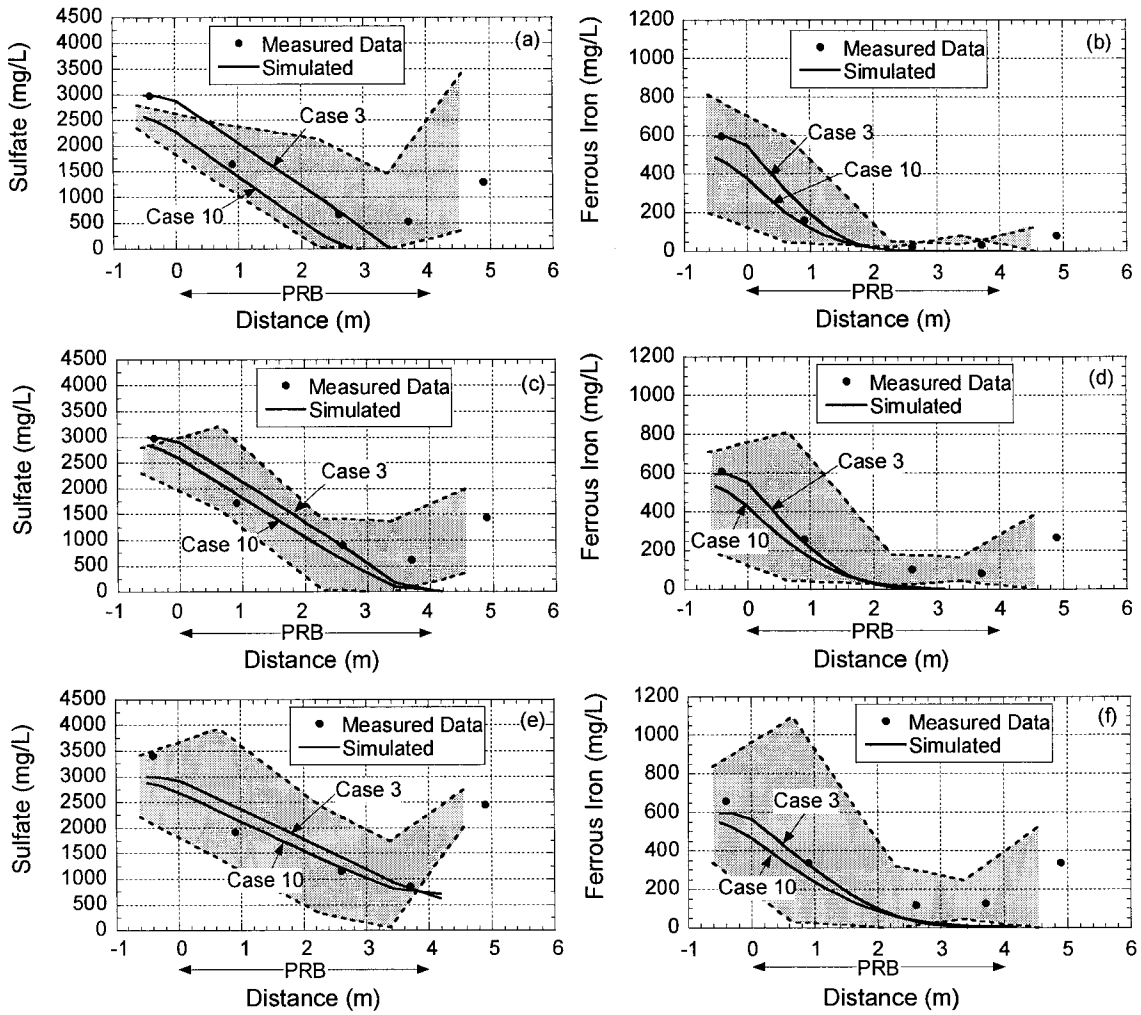

Figure 7.20 – Measured and simulated (Cases 3 and 10) concentration profiles for sulfate and ferrous iron across the central line of the PRB: (a) and (b) September 1996, (c) and (d) October 1997, and (e) and (f) October 1998.

CHAPTER 8

SUMMARY AND CONCLUSIONS

8.1 SUMMARY

A new biochemical model for quantifying bioremediation of acid mine drainage (AMD) based on SO_4^{2-} reduction and precipitation of metals coupled to, and limited by, the decomposition of solid organic materials (e.g., leaf mulch compost, wood chips, sawdust, alfalfa) was formulated and solved either as a stand-alone algorithm or coupled to flow and multi-species contaminant transport (i.e., MODFLOW with RT3D). The model included the primary processes of (i) decomposition of polysaccharides in solid organic materials, (ii) SO_4^{2-} reduction based on lactate, (iii) precipitation of insoluble metal sulfides, (iv) partial volatilization of hydrogen sulfide (H_2S) to the gas phase, and (v) reversible dissolution-precipitation of calcite ($CaCO_{3(s)}$) and metal carbonates (e.g., siderite, $FeCO_{3(s)}$). The model was evaluated and calibrated using experimental data obtained from the literature pertaining to four batch-equilibrium (no-flow) tests, two closed-system column tests, three open-system bioreactor tests, and a full-scale PRB. The comparisons with experimental data provided insight into the effects of different model kinetics, slow decomposition of solids, multiple-phase precipitation, and seasonal temperature variability, as well as the appropriate ranges of values for a variety of model parameters.

In addition, a quantification of the influence of heterogeneity in aquifer hydraulic conductivity (K) on the design and performance of PRBs was performed using computational modeling of flow and particle tracking (i.e., MODFLOW with MODPATH) in conjunction with 650 synthetic stochastic heterogeneous aquifers generated using the Turning Bands method. Newly defined probabilistic factors of safety for scaling both the PRB thickness and length amidst heterogeneity were quantified considering different levels of aquifer heterogeneity, correlation structure anisotropy ratios, and distances from source zone to PRB. The effects of preferential flow and contaminant transport also were apparent in strongly divergent and strongly convergent plume patterns resulting from the highest level of aquifer heterogeneity (i.e., standard deviation of logarithm of K, σ_{lnK}, equal to 1.6). The significant magnitudes of required factors of safety for PRB design obtained in this study highlighted the importance of site characterization as a prerequisite to PRB design.

8.2 CONCLUSIONS

First, the concepts, assumptions, and mathematics of the new model for bioremediation of AMD based on sulfate (SO_4^{2-}) reduction and metals precipitation coupled to, and limited by, the decomposition of solid organic materials were presented (Chapter 2). In an illustrative example using the model coupled to flow and contaminant transport the bioremediation of influent SO_4^{2-}, ferrous iron (Fe^{2+}), and zinc (Zn^{2+}) was modeled for a hypothetical column test. The model was verified to be operational, requiring experimental data for evaluation and calibration of parameter values.

Second, using the model as a stand-alone algorithm, approximations of experimental data pertaining to two single-substrate and two multiple-substrate batch equilibrium (no-flow) experiments in the literature were performed for evaluation and calibration of parameter values under batch conditions (Chapter 3). Contois kinetics for polysaccharide decomposition in series with Monod kinetics for SO_4^{2-} reduction based on lactate satisfactorily approximated rates of SO_4^{2-} reduction varying from 15 - 50 mg SO_4^{2-}/L-d (Batch test 1), 40 - 80 mg SO_4^{2-}/L-d (Batch tests 2 and 3) and 80 - 100 mg SO_4^{2-}/L-d (Batch test 4), allowing for calibration of several parameter values. As initially expected, parameter values for Contois decomposition of cellulose at 35 °C taken from the literature had to be reduced in order to provide reasonable approximation to the experimental data collected at the testing temperature of 25 °C. When Contois kinetics for polysaccharide decomposition was replaced by first-order kinetics, comparatively poorer approximations of rates of SO_4^{2-} reduction were obtained, indicating that Contois kinetics is a better model for decomposition in these systems than first-order kinetics. Instantaneous precipitation of $FeS_{(s)}$ provided a good approximation to experimental Fe^{2+} data for cellulose-based experiment, for the same parameter set that approximated SO_4^{2-} data. However, for the other experiments, kinetic limitation to $FeS_{(s)}$ precipitation was required, i.e., since instantaneous precipitation resulted in simulated Fe^{2+} concentrations lower than the experimental ones.

Third, using the model coupled to flow and contaminant transport, approximations of experimental data pertaining to two closed-system column tests reported in the literature were performed for evaluation and calibration of parameter values representative of flowing conditions (Chapter 4). Adjusted Contois rate

coefficients for decomposition of organic solids in the columns resulted ~ 25 % lower than decomposition rate coefficients used in Chapter 3 for the same materials. However, this finding was considered consistent with the difference in the solid:solution ratios between column and batch scenarios. Experimental data consisting of effluent concentrations for SO_4^{2-}, Fe^{2+}, and hydrogen sulfide (H_2S) in one column were approximated using the model including both $FeS_{(s)}$ precipitation (i.e., linked to SO_4^{2-} reduction and decomposition of polysaccharides) and $FeCO_{3(s)}$ precipitation linked to the dissolution of calcite ($CaCO_{3(s)}$). Calcite was depleted from the column after approximately 230 d (15 pore volumes of flow), such that the longer-term (> 250 d) removal of influent Fe^{2+} was exclusively due to the precipitation of the sulfidic phase. A cumulative mass analysis indicated that approximately 8,000 mg of SO_4^{2-} were reduced in the column, 2,700 mg of Fe^{2+} were precipitated as $FeS_{(s)}$ throughout the duration of the test (i.e., 425 d), and approximately 1,900 mg Fe^{2+} were precipitated as $FeCO_{3(s)}$ until 230 d. For the other column, effluent concentrations for SO_4^{2-}, Fe^{2+}, and Zn^{2+} were approximated with SO_4^{2-} reduction limited by decomposition of polysaccharides in wood chips. The competitive precipitation of Fe^{2+} and Zn^{2+} was modeled with a first-order rate coefficient for $ZnS_{(s)}$ precipitation that was five times greater than that for $FeS_{(s)}$, consistently with the experimental data. As a result, the majority of Zn^{2+} precipitated within the first half column (i.e., near the influent side) such that, towards the second half column, Zn^{2+} concentrations were sufficiently low as to allow $FeS_{(s)}$ precipitation to dominate. A cumulative mass analysis indicated that, throughout the duration of the test (i.e., 130 d), 1,000 to 1,200 mg SO_4^{2-} were reduced in the column, and approximately 275 mg Fe^{2+} and 350 mg Zn^{2+} were precipitated.

Fourth, using the model coupled to flow and contaminant transport, approximations of experimental data pertaining to three open-system bioreactor tests reported in the literature (each with a different solution residence time) were performed (Chapter 5). Since the bioreactors included a top liquid-gas interface, H_2S volatilization and the presence of a top, non SO_4^{2-} reducing layer were included in the simulations, which intended to approximate experimental effluent concentrations for SO_4^{2-} and Fe^{2+}. Adjusted Contois rate coefficients for decomposition of polysaccharides in freshly cut alfalfa resulted significantly higher than those adjusted for leaf mulch in Chapter 4. However, this finding was considered consistent with the reported C/N ratios of the materials, i.e., C/N = 13 for freshly cut alfalfa, and C/N = 21 for leaf mulch in Chapter 4. The model was capable of simulating the effect of variable residence time (i.e., 6.2, 3.1, and 31 d) on effluent concentrations for Fe^{2+} for all three bioreactors. However, in the case of SO_4^{2-} in Bioreactor 3 some discrepancy between simulated and experimental was observed. Due to the transverse and ascending pattern of flow and transport occurring in the bioreactors, $FeS_{(s)}$ precipitation was simulated as occurring not only near the solution inlet, or injection cell, but also near the solution outlet, i.e., the drain cell in the model. This finding may be considered relevant to other bioreactor, as well as larger-scale wetland systems, based on superficial drainage. The open system allowing the volatilization of H_2S retarded the precipitation of $FeS_{(s)}$ and resulted in greater effluent concentrations for Fe^{2+}. In addition, the open system had a significant impact on simulated effluent concentrations for SO_4^{2-} due to the presence of the top, non SO_4^{2-} reducing layer. As common to other open-systems (such as anaerobic wetlands for AMD remediation), the thickness of the top, non SO_4^{2-} reducing layer remained as an unknown,

such that parametric modeling was required. When simulating wetland systems, some degree of uncertainty induced by the unknown thickness of the top, non SO_4^{2-} reducing layer must be anticipated.

Fifth, the influence of aquifer heterogeneity on plume patterns and required thickness and length of PRBs was evaluated using stochastic modeling for different levels of aquifer heterogeneity, correlation structure anisotropy ratios, and distances from source zone to PRB (Chapter 6). For the highest level of aquifer heterogeneity evaluated in this study (σ_{lnK} = 1.6), strongly divergent and strongly convergent plumes developed in 24 % of all aquifers considered in this study, with ~ 12 % frequency of occurrence each. In terms of PRB thickness, a probabilistic factor of safety related to uncertainty in influent groundwater seepage velocities (FS_1) was quantified. The mean and standard deviation of 90th-percentile values of FS_1, i.e., $FS_{1,90}$ required for scaling the PRB thickness, increased significantly with increasing level of aquifer heterogeneity (i.e., as represented by the magnitude of the standard deviation of the logarithm of the aquifer hydraulic conductivity, σ_{lnK}), with mean values of 1.60, 1.91, 2.71, and 5.14 corresponding to σ_{lnK} values of 0.2, 0.4, 0.8, and 1.6, respectively. The correlation structure anisotropy ratio and the distance from the source zone to the PRB had comparatively minor impacts on $FS_{1,90}$, i.e., with mean values for $FS_{1,90}$ of 2.71, 2.87, and 3.74 corresponding to λ_x/λ_y values of 1.0, 1.5, and 3.0, respectively, and of 2.64, 2.71, and 2.74 corresponding to D_{PRB} values of 15 m, 30 m, and 45 m, respectively. In summary, for the highest level of heterogeneity in this study, i.e., σ_{lnK} = 1.6, $FS_{1,90}$ ranged from ~ 5.0 (mean) to ~ 10 (mean plus two standard deviations), and the trends for $FS_{1,90}$ versus σ_{lnK} compared well with previously published values based on a different

methodology. In terms of PRB length, a probabilistic factor of safety related to uncertainty in plume capture width at the location of the PRB, and defined as capture length ratio (CLR), was quantified. The mean and standard deviation of the CLR distributions obtained from the data increased with increasing level of aquifer heterogeneity (i.e., σ_{lnK}), with mean values for CLR of 1.09, 1.14, 1.24, and 1.54 corresponding to σ_{lnK} values of 0.2, 0.4, 0.8, and 1.6, respectively. The mean and standard deviation of the CLR distributions slightly decreased with increasing correlation structure anisotropy ratio, λ_x/λ_y, with mean values for CLR of 1.24, 1.20, and 1.16 corresponding to λ_x/λ_y values of 1.0, 1.5, and 3.0, respectively, a finding that is consistent with the fact that, as λ_y decreases, particle trajectories become less meandering resulting in shorter capture zone lengths. Also, the mean and standard deviation CLR increased with increasing distance from the source zone to the PRB, D_{PRB}, with mean values of 1.13, 1.24, and 1.33 corresponding to D_{PRB} values of 15 m, 30 m and 45 m, respectively, a finding that is consistent with the fact that locating the PRB further down-gradient with respect to the source zone results in a broader plume to be encompassed by the PRB. For σ_{lnK} = 1.6, the factor of safety CLR corresponding to the mean plus two standard deviations was on the order of 2.7. The importance of aquifer *in-situ* characterization a priori to designing a PRB was highlighted by the magnitude and significance of factors of safety for scaling the thickness and length of PRBs in heterogeneous aquifers obtained in this study. Also, in cases where aquifer heterogeneity is significant (e.g., $\sigma_{lnK} > 1.6$), the effect of the aquifer heterogeneity may be to the extent that the use of PRBs for *in-situ* remediation is rendered impractical, requiring the consideration of other remediation technologies.

Sixth, using the model coupled to flow and contaminant transport, approximations of trends in field derived data pertaining to the monitoring of the PRB located at the Nickel Rim mine site in Ontario (Canada) were performed with emphasis on the effect of seasonal temperature variability on AMD bioremediation and on evaluating and calibrating parameter values more representative of field conditions (Chapter 7). Simulated results were compared to measured field derived data pertaining to three monitoring events that occurred in the field at 13 months of PRB operation (1996), 26 months (1997), and 38 months (1998). Decomposition rate coefficients for compost, leaf mulch, and wood chips previously adjusted in Chapter 4 were reduced to account for overall larger particle sizes used in the PRB (i.e., 0.5 to 3.0 cm) when compared to the particle sizes used for the column tests. Based on the literature, rate coefficients for decomposition of organic materials are inversely proportional to the particle size. Vertically averaged *in-situ* groundwater temperatures ranged from ~ 3 ^{o}C (colder season) to ~ 15 ^{o}C (warmer season) and, for this reason, decomposition rate coefficients were adjusted for temperature. This adjustment was based on an exponential regression developed in this study in which rate coefficients go to zero as temperature goes to zero. In order for seasonality to be incorporated in the simulations, the RT3D source code was modified to allow time-dependant reaction rate constants originally not available. The occurrence of a succession of colder and warmer seasons (i.e., seasonality in temperature) resulted in a greater longevity of decomposable organic materials within the PRB. Leaf mulch and wood chips were estimated to last in the PRB for approximately 11 and for more than 13 years, respectively. The simulated percentages of decomposable polysaccharides remaining at 26 months were on the order of 50 and 73 % for leaf mulch

and wood chips, respectively. Seasonal temperature variability had a significant impact on the bioremediation of AMD in the PRB. Effluent mass fluxes exiting the PRB peaked during the colder season (3 °C) both for SO_4^{2-} (2,700 – 2,900 g/d) and for Fe^{2+} (30, 290, and 350 g/d for the first, second, and third cold seasons, respectively). These results highlighted the importance of considering the effects of temperature and seasonality on the performance of sulfate reducing PRBs, since although bacterial processes within the PRB were capable of achieving the remediation of the AMD plume during the warmer seasons, lower bacterial activity (i.e., decomposers and SRB) in response to the cold environment resulted in lower treatment efficiency during the colder seasons. This finding is expected to have significant practical relevance for all biological PRBs located in cold environments.

8.3. RECOMMENDATIONS

8.3.1. PRACTICAL IMPLICATIONS

Design of PRBs for AMD Remediation

The new model based on the serial application of Contois, Monod, and first-order kinetics with calibrated parameter values for modeling the bioremediation of AMD in sulfate reducing systems, and the extension of the model to the field scale, which included quantifying the influence of aquifer heterogeneity and of temperature and seasonality on PRB performance, are contributions from this research that may have a significant practical implication in terms of assisting in the design of sulfate reducing systems (including PRBs) for bioremediation of AMD. As shown in the flowchart of Fig. 1, the following steps can be anticipated when using the model:

- Characterization: AMD source zone and plume. Flow and transport parameters in the aquifer;
- Preliminary design of the PRB: location, length, thickness. Source materials and amounts of decomposable polysaccharides. Bacterial populations. Others (e.g., limestone);
- Selection of parameter values: Contois, Monod, and first-order parameter values. Temperature and seasonality.
- Model simulation: selection of relevant simulation cases. Selection of relevant time spans for simulation. Simulation;
- Verification of results: effluent contaminant concentrations and mass fluxes for all simulation cases. Longevity of decomposable polysaccharides and bioremediation. Effects of temperatures and seasonality;
- Refinement of the preliminary design and parameter values: location, thickness (residence time). Source materials and amounts of decomposable polysaccharides. Bacterial populations. Others (e.g., limestone). Sensitivity analysis;
- Model simulation. Convergence of the PRB design;
- Up scaling PRB dimensions due to aquifer heterogeneity: characterization of aquifer heterogeneity. Selection of appropriate factors of safety (thickness and length of the PRB). Final PRB dimensions.

8.3.2. SUGGESTIONS FOR FUTURE RESEARCH

For future research on the subject, the following suggestions can be made:

First, with respect to laboratory experiments aimed at providing experimental data for new model calibration (i.e., batch-equilibrium, column, or bioreactor tests). Perform experiments that include the measurement of:

- amounts of decomposable polysaccharides remaining with time and location;
- bacterial populations (i.e., decomposers and SRB) with time and location;
- quality and quantity of precipitated solid phases (i.e., sulfidic and carbonate minerals, among others) with time and location;
- sorption of metals (e.g., Fe^{2+}, Zn^{2+}, among others) to the organic materials with time and location, and
- gas phase concentrations of hydrogen sulfide (H_2S) and methane (CH_4) with time.

Second, with respect to monitoring field systems, i.e., such as pilot and full-scale PRBs, or large-scale columns and bioreactors:

- Monitoring schedule should include determination of effluent concentrations for both warm and cold seasons of the year, to assess the effect of seasonality.

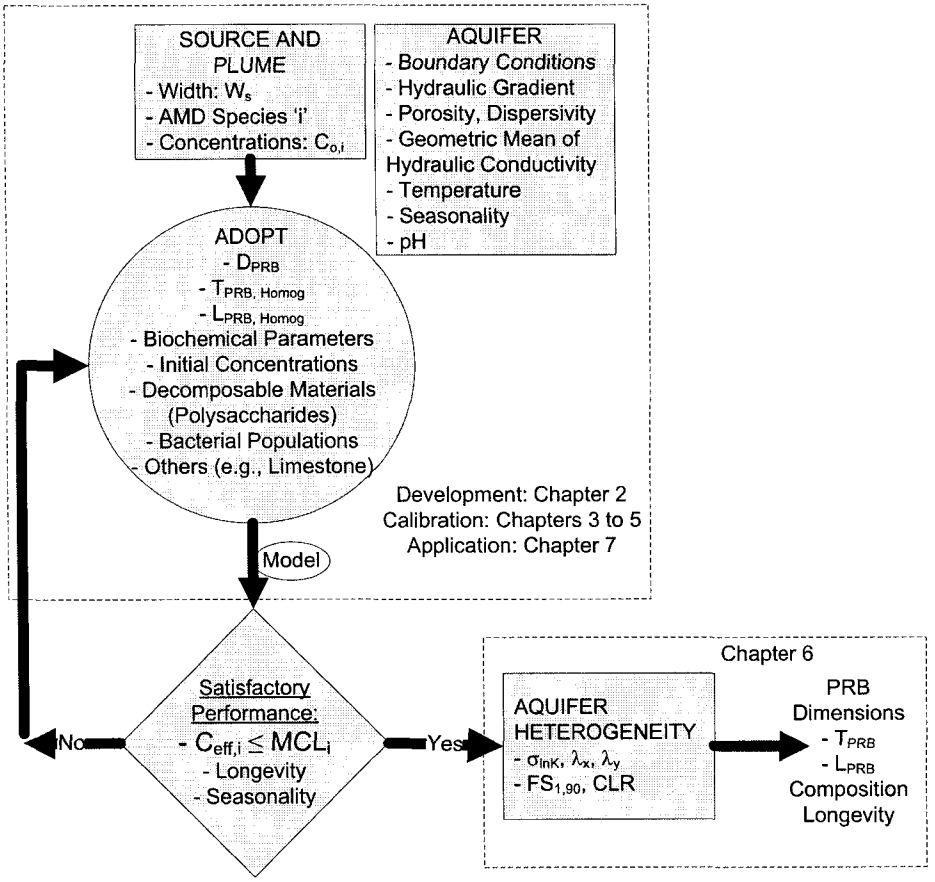

Figure 8.1 – Flowchart for designing PRBs for AMD remediation using the tools presented in this research.